Tip Flow Corrections for Horizontal Axis Wind and Tidal Turbine Rotors

Aidan Wimshurst
St John's College
University of Oxford

A thesis submitted for the degree of
Doctor of Philosophy
Hillary 2018

Acknowledgements

Firstly, I would like to thank my supervisor, Richard Willden, for his supervision and encouragement over the course of the DPhil. The rich and plentiful discussions on rotor aerodynamics and tidal energy have been fascinating and I am extremely grateful to have been able to work with him during my time at Oxford. I would also like to thank my examiners, Thomas Adcock and Timothy Stallard, for their careful and considered reading of my thesis, which considerably improved the quality and clarity of the content. I would also like to thank my colleagues in the Tidal Energy Research Group, for providing such a warm and welcoming research community. In particular I would like to thank: Christopher Vogel, Subhash Muchala, Susannah Cooke, William Hunter, Mohamad Bin Osman, Bowen Cao, Federico Zilic de Arcos, Ahmad Firdaus, Túlio Moreira and Andrea Schnabl for the many interesting technical discussions that we shared and for their invaluable feedback on my work. In addition, I would also like to thank my other colleagues in the wider Civil Engineering Research Group, particularly Jenkin Room 11, for providing such a warm and friendly working environment. In particular I would like to thank Maria Garcia-Espinosa, Christelle Abadie, Wing Nam (Coco) Yiu and Lucy Auton, for being the most wonderful friends and colleagues one could ask for.

Formally, I would like to thank the Engineering and Physical Sciences Research Council (EPSRC) and E.ON/Uniper, for joint funding the CASE Studentship award that funded this project. More specifically, I would like to thank my industrial liaisons, Clym Stock-Williams, Kester Gunn and Mark Dubal, for their extensive discussions and feedback on my work. Their industrial perspective considerably improved the applicability of many of the studies carried out in this project. I would also link to thank the Advanced Research Computing facility at the University of Oxford, for the help of their staff when running the plethora of simulations that were carried out in this project.

St John's College has provided a fun, friendly and exciting atmosphere during my time at Oxford and I would like to thank the college and all their staff for making this possible. I would also like to thank the college for providing financial support, so I could attend and present at the ISOPE conference in Rhodes. I am extremely grateful to have been given this opportunity.

In the wider university, I would like to thank all my fellow gymnasts at the Oxford University Gymnastics Club for the many fun and exciting times we shared together. In particular I would like to thank: Liza Hadley, Katrina Kelly, Jason Lee, Eric LeGresley, Mollie Clay, Rusheb Shah, Tom Nicholas, Caitlin O'Brien, Emma Fagan, Alex Koziell, James Tricker, Sam Barnett and Faez Kipli for some of my fondest memories of Oxford and for being such great friends. I would also like to thank my closest friends: Kane Morgan, Melissa Fryers, James Nichols, Rebecca Elstone, Matthew Maslin and Ettie Unwin for their friendship, laughter and continued support over the course of the DPhil. Finally, I would like to thank my parents, Claire and Anthony, and my brothers, Howard and Wesley, for their boundless support, encouragement and for being a source of constant inspiration to me.

Abstract

On the outboard sections of horizontal axis rotor blades (that are not enclosed within a duct or shroud), vorticity is shed into the wake of the rotor. The shed vorticity induces a downwash at the rotor plane and spanwise flow accelerations along the blade, which causes the blade loading to drop off as the tip is approached. These tip flow effects are currently not adequately accounted for by reduced order rotor models (such as the blade element momentum and actuator line methods) which are frequently used to represent wind and tidal turbine rotors in large simulations. Hence, the rotor thrust and torque may be considerably over-predicted by these models if they are not corrected appropriately for tip flow effects. In this thesis, the tip loss mechanism experienced by both wind and tidal turbine rotor blades is examined directly in a series of simulations, using computational fluid dynamics. Two different correction methods that can account for tip flow effects are then presented and critically evaluated. Both methods are shown to lead to a significant improvement in the accuracy of the computed blade loading, which is principally achieved by allowing the sectional force vector to reduce in magnitude and rotate towards the streamwise direction as the tip of the blade is approached.

Tip flow effects also reduce the strength of the suction peak developed on the suction surface of the blade. This reduction has considerable implications for the operation of tidal turbine rotors, since tidal turbine operation may be limited by cavitation inception and cavitation inception is most likely to initiate on the outboard sections of the rotor blade (where the static pressure reaches a minimum). In this thesis, a cavitation analysis of two different tidal turbine rotors is carried out. When tip flow effects are properly accounted for, cavitation inception is shown to be less likely at a given operating condition (tip-speed-ratio and submersion depth). Hence, industry standard cavitation analyses that are based on the blade element momentum method (and do not adequately account for tip flow effects) are shown to be currently overly-conservative.

In a separate study, tidal power extraction is examined in a computational domain where the sea bed slopes in the streamwise direction. When the sea bed slopes downwards in the streamwise direction, the velocity shear across the swept area of the rotor increases, increasing the power available for extraction. However, the increased velocity shear also increases the strength of the suction peak developed on the blade at top dead centre, so the device is more likely to cavitate at a given tip-speed-ratio. Conversely, when the sea bed slopes upwards in the streamwise direction, the incident velocity profile is more uniform, so the device is less likely to cavitate at a given tip-speed-ratio. Power extraction is also found to be more efficient on the upwards facing slope, as the flow through the swept area of the rotor is accelerated by the downstream flow passage constriction. At higher blockage ratios, the strength of the suction peak is further increased by the acceleration of the flow through the swept area of the rotor, so the device is even more likely to cavitate at a given tip-speed-ratio.

Contents

Nomenclature

Symbol	Unit	Definition
a_B	-	Axial induction factor local to the blade
$a_B{}'$	-	Swirl induction factor local to the blade
$\overline{a}$	-	Azimuthally-averaged axial induction factor
$\overline{a'}$	-	Azimuthally-averaged swirl induction factor
A	m^2	Disc or rotor area
B	-	Blockage ratio
c	m	Local chord length
c_1, c_2	-	Empirical coefficients
C_D	-	Drag coefficient
C_L	-	Lift coefficient
$C_{\dot{m}}$	-	Mass flow rate coefficient
C_s	-	Roughness constant
C_T	-	Thrust coefficient
$C_T{}'$	-	Alternative thrust coefficient
C_P	-	Power coefficient
$C_P{}'$	-	Alternative power coefficient
$C_{P,\max}$	-	Maximum power coefficient
C_{pre}	-	Static pressure coefficient
D	m	Diameter
	N/m	or drag force per unit span
$\boldsymbol{D}$	N/m	Sectional drag vector
E	-	Empirical coefficient
ΔE	W	Total energy flux removed from the flow
F	-	Prandtl correction factor
F_1	-	Tip flow correction factor
F_{ax}	$\mathrm{N/m}^2$	Axial force per unit span

F_{ta}	N/m^2	Tangential force per unit span
$F_{1,\text{ax}}$	-	Computed ratio of axial force per unit span
$F_{1,\text{ta}}$	-	Computed ratio of tangential force per unit span
Fr	-	Froude number
g	m^2/s^2	Acceleration due to gravity
g_1	-	Empirical function for tip flow correction
G	-	Cell growth ratio normal to the wall
Δh	m	Change in free surface height
h_{tip}	m	Tip submersion depth
H	m	Local depth
I	%	Turbulence intensity
k	m^2/s^2	Turbulent kinetic energy
k_{wall}	m^2/s^2	Turbulent kinetic energy on boundary cell face
K	-	Momentum loss factor
l	m	Turbulence length scale
L	L/m	Lift force per unit span
	m	or horizontal bed slope length
$\boldsymbol{L}$	N/m	Sectional lift vector
K_s	m	Roughness height
K_s^+	-	Dimensionless roughness height
LE	m	Chordwise cell dimension at the leading edge
$\dot{m}$	kg/s	Mass flow rate
$\hat{\boldsymbol{n}}$	-	Unit normal vector
N	-	Number of blades
N_c	-	Number of cells in the chordwise direction
N_{cells}	-	Number of cells in the inner domain
N_r	-	Number of cells in the radial direction
N_s	-	Number of cells in the spanwise direction
N_{surf}	-	Number of cells on the blade surface
N_x	-	Number of cells in the streamwise direction
N_θ	-	Number of cells around the circumference
p	N/m^2	Static pressure
p_{ATM}	N/m^2	Atmospheric pressure at sea level
p_{CFD}	N/m^2	Static pressure computed from simulation

p_{ref}	N/m^2	Reference static pressure
p_∞	N/m^2	Freestream static pressure
Δp	N/m^2	Static pressure drop across the disc
q	m/s	Velocity perturbation
Q	Nm	Torque
P	W	Power
r	m	Spanwise distance along the blade
Δr	m	Radial cell dimension at the disc edge
r_s	m	Sampling distance
$\boldsymbol{r}$	m	Position vector
R	m	Disc or rotor radius
R_o	m	Radius of the outer domain
Re	-	Reynolds number
Re_c	-	Chord-based Reynolds number
s	m	Tip-to-tip spacing between devices
S	m	Domain width
t	m	Blade thickness
T	N	Thrust
δT	N	Incremental disc thrust
TE	m	Chordwise cell dimension at the trailing edge
u_x	m/s	Velocity normal to the disc
u_{x0}	m/s	Undisturbed velocity normal to the disc
u_τ	m/s	Friction velocity
U_b	m/s	Bulk velocity
U_{ref}	m/s	Reference axial velocity
U_{rel}	m/s	Velocity magnitude relative to the rotor blade
U_x	m/s	Axial velocity
U_y	m/s	Lateral velocity
U_z	m/s	Vertical velocity
$\overline{U_x}$	m/s	Axial velocity averaged over a rotor revolution
U_∞	m/s	Freestream velocity
U^+	m/s	Velocity in wall units
x, y, z	m	Cartesian coordinates
Δx	m	Streamwise cell dimension at disc plane

y_0	m	Wall adjacent cell centroid height
y^+	-	Dimensionless wall normal distance
α	$^\circ$	Angle of attack
β	$^\circ$	Local twist angle of the aerofoil section
Δ_{tip}	m	Spanwise cell dimension at the blade tip
Δ_{grid}	m	Characteristic cell dimension
ϵ	-	Gaussian smearing parameter
Γ	m^2/s	Circulation strength
κ	-	Von Kármán constant
λ	-	Tip speed ratio
λ'	-	Alternative tip speed ratio
λ_r	-	Local speed ratio
μ	Ns/m^2	Dynamic viscosity
ν	m^2/s	Kinematic viscosity
ν_t	m^2/s	Kinematic eddy viscosity
η	-	Gaussian smearing distribution
ϕ	$^\circ$	Angle of local velocity relative to the rotor plane
θ	$^\circ$	Blade angle to top-dead-centre
	$^\circ$	or slope angle
	$^\circ$	or sectional force vector angle
ρ	kg/m^3	Fluid density
σ	-	Rotor solidity
τ_w	N/m^2	Wall shear stress
ω	s^{-1}	Specific dissipation rate
ω_{wall}	s^{-1}	Specific dissipation rate on boundary cell face
Ω	rad/s	Rotational speed
ζ	m	Distance to collocation point

Abbreviations/Acronyms

Abbreviation	Meaning
BEM	Blade element mometum
CfD	Contracts for Difference
CFD	Computational fluid dynamics
DNS	Direct numerical simulation
DNW	German-Dutch Wind tunnels
EMEC	European Marine Energy Centre
EU	European Union
GAMG	Generalised geometric-algebraic multi-grid
LLF	Large Low-speed facility
LMADT	Linear momentum actuator disc theory
NREL	National Renewable Energy Laboratory
MEXICO	Model Experiments in Controlled Conditions
NACA	National Advisory Committee for Aeronautics
OpenFOAM	Open Field Operation and Manipulation
PIV	Particle image velocimetry
RANS	Reynolds-averaged Navier-Stokes
RANS-BE	Reynolds-averaged Navier-Stokes embedded Blade Element
SIMPLE	Semi-implicit method for pressure linked equations
SST	Shear-stress transport
UK	United Kingdom

Chapter 1

Introduction

1.1 Renewable Energy Technologies

Growing concerns over climate change, fossil fuel consumption, energy demands and energy security has driven recent development in renewable energy technologies. To encourage the widespread adoption of these technologies, a variety of renewable energy policies have been introduced around the world. For example, the most ambitious renewable energy policy has been adopted by the European Union (EU), with the introduction of the Renewable Energy Directive in 2009 (European Parliament 2009). This directive requires 20% of the annual energy consumption of the EU (as a whole) to be derived from renewable sources by 2020. As part of this directive, each member state was set an individual target based on their existing renewable energy infrastructure and available resources. The United Kingdom (UK) for example, was set a target of deriving 15% of its gross energy consumption from renewable sources by 2020. All member states have made considerable progress towards their targets, with 9 states achieving their targets ahead of schedule in 2014 (Eurostat 2017).

Despite current trends in renewable energy production, considerable progress is still required if future renewable energy targets are to be met. Furthermore, many

countries have also adopted ambitious targets for the reduction of greehouse gas (GHG) emissions, due to concerns over anthropogenic climate change. The UK for example, is legally bound by the 2008 climate change act, requiring a reduction in the emissions of all 6 Kyoto greenhouse gases by 80% (relative to 1990 levels) by 2050 (Department of Energy and Climate Change 2008). Achieving such ambitious reductions necessitates a dramatic reduction in fossil fuel consumption, with a corresponding increase in low carbon energy production, in order to meet energy demands. However, a successful transition towards such a future energy supply is likely to require many different renewable energy sources and their associated technologies (Renewables Advisory Board 2008). Hence, extensive research and development is currently being carried out in many existing and emerging renewable energy technologies.

1.1.1 The Contribution of Tidal Stream Energy

Tidal energy is one potential contributor to a future energy supply dominated by renewable energy resources. It benefits from the predictability of the tides and high power density (particularly in constricted tidal straits and around headland sites) but suffers from intermittency and a challenging operating environment.

Early tidal power projects mainly used barrages to generate electricity from the tide. However, environmental concerns have limited the more widespread adoption of this technology. In particular, aquatic migration patterns, sediment transport and local ecosystems are likely to be adversely affected by the construction of a barrage (Kirby & Retiere 2009).

To mitigate these environmental impacts, tidal stream turbines are now being considered as a viable alternative. Tidal stream turbines extract power directly from the tidal current, rather than building up a water level difference across the turbines using a barrage. Hence, they appear to operate in the same manner as wind turbines (but installed underwater), as the flow can pass around the turbines as well as through

them. However, to extract significant power from the flow, many tidal stream devices will be required at a given site. These devices may still block a large proportion of the channel cross-section and lead to environmental consequences which are not yet well defined (Adcock et al. 2015, Fraser et al. 2017). Furthermore, only a limited number of sites around the world may be economically viable for tidal stream energy extraction. For example, in their resource assessment of the UK, Black and Veatch Ltd. (2011) only considered sites with mean undisturbed kinetic energy flux densities greater than 1.5kW/m^2 (mean flow velocities greater than 1.7m/s) to be economically viable for tidal stream energy extraction.

One benefit of having a limited number of feasible installation sites, is that the available resource can be estimated and quantified. For example, the Carbon Trust estimated that an annual resource of 20.6TWh could be feasibly extracted from the leading 30 sites in the UK (Black and Veatch Ltd. 2011). Based on the 336.4TWh of electricity generated in the UK in 2016 (Department of Energy and Climate Change 2017), tidal stream energy could therefore contribute up to 6.1% of the annual electricity generated in the UK. Hence, tidal stream energy could make a small but significant contribution to future electricity demands.

1.1.2 Tidal Stream Installations

In the last 10 years, several tidal stream demonstrator devices have been installed for field testing and data acquisition. Unlike the wind energy industry, the tidal energy industry does not appear to have converged to a single device design. The majority of device developers have adopted axial flow (propeller type) designs, such as the Atlantis Resources 1MW rated AR1000 (Fig. 1.1 (a)) and the Marine Current Turbines (acquired by Siemens then Atlantis) SeaGen 1.2MW turbine. Although less common, ducted and open centre devices such as the OpenHydro design (Fig. 1.1 (b)) have also been adopted by some companies.

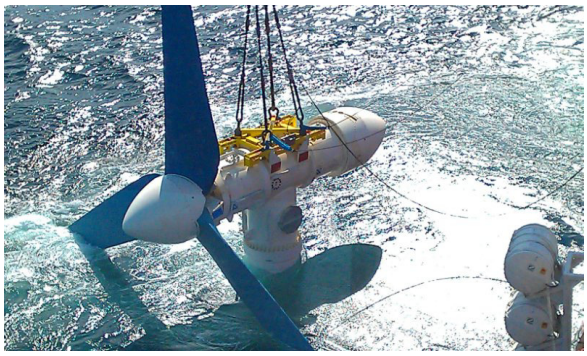

(a) Atlantis AR1000

(b) OpenHydro

Figure 1.1: Demonstrator devices installed at the European Marine Energy Centre (EMEC) in the Orkney Islands (Scotland) (EMEC 2016, OpenHydro 2017)

Device developers are now moving towards first generation arrays of devices, with installed capacities of 5-15MW. For example, Électricité de France (EdF) are planning to install 7 2MW OpenHydro devices at Paimpol-Bréhat (France) by the end of 2018, while Andritz Hydro Hammerfest and Atlantis Resources have deployed 4 1.5MW turbines in the inner sound of the Pentland Firth (Scotland), as part of the demonstration phase of the MeyGen Ltd. (2014) project (Phase 1a). Over the next decade, these arrays will increase in size until a significant capacity has been installed. For example, Phase 1 of the MeyGen Ltd. (2014) project has an approved capacity of 86MW, with an eventual capacity of 389MW planned for the end of the project.

1.1.3 Challenges for the Tidal Energy Industry

Considerable challenges remain before tidal stream power can make a worthwhile contribution to future energy demands. In particular, the levelised cost of energy (LCOE) for tidal stream turbines (at their current stage of development) is much higher than other competing renewable energy technologies. For example, the Low Carbon Innovation Coordination Group (2012) estimated that the current LCOE for tidal stream turbines is in the range of £200-300/MWh. In contrast, the UK government recently awarded contracts to DONG Energy (now Ørsted) and EDP

Renováveis to develop the 950MW Moray East and 1386MW Hornsea 2 offshore wind farms (respectively), at a strike price of £57.50/MWh, under the second round of the Contracts for Difference (CfD) scheme (Department for Business, Energy & Industrial Strategy 2017). This strike price is comparable with the current LCOE for combined cycle gas turbines (£56-58/MWh) (Department for Business, Energy & Industrial Strategy 2016*a*) and is also significantly lower than the recently confirmed deal for Hinkley Point C (a new nuclear power station) at £92.50/MWh (Department for Business, Energy & Industrial Strategy 2016*b*). Hence, a significant reduction in the LCOE is required for tidal stream turbines to become cost competitive.

The required reduction to the LCOE for tidal stream turbines can only be accomplished by increasing the annual energy output per MW of installed capacity (increasing the capacity factor at a given rated power) and by significantly reducing the capital and operating costs. While the annual energy output can be increased by improving the system reliability and availability, much of the cost reduction is expected to arise through economies of scale and supply chain optimisation (Low Carbon Innovation Coordination Group 2012). However, due to the harsh environmental conditions experienced by tidal turbines, considerable innovation is also required from device developers to improve device survivability and reduce the risk associated with device installation.

Due to the high cost of constructing, installing and monitoring full-scale demonstrator devices, hydrodynamic modelling has been used extensively by the tidal energy community over the past decade, to support device development. Many of these studies have shown that it is possible to increase the energy extracted per MW of installed capacity, through improved device and array design. Hydrodynamic modelling has also been used to quantify device loading under different environmental conditions, reducing the risk associated with device installation. As hydrodynamic modelling is the main focus of this thesis, a brief discussion of the key conclusions drawn from re-

cent hydrodynamic models will be presented in the next section, in order to motivate the work that follows.

1.2 Hydrodynamic Modelling of Tidal Energy Extraction

The standard approach in hydrodynamic modelling is to adopt an appropriate numerical model for the scale of interest and then adopt a low order model to capture the influence of the others (Adcock et al. 2015). This section provides a brief overview of basin scale modelling (where a low order array model is used), array scale modelling (where a low order device model is used) and device scale modelling (where simplified representations of the surrounding array and tidal basin are used).

1.2.1 Basin Scale

At the basin (or regional) scale, the aim of hydrodynamic modelling is to estimate the potential power that can be extracted from a given site and to minimise the overall environmental impact of device installation. Early estimates of the potential power that can be extracted were based on the mean undisturbed kinetic energy flux (see Black and Veatch Ltd. (2005) for example). However, to extract a significant fraction of the power that is available at a given site, a large number of tidal energy devices will be required, which results in a large thrust being applied to the flow. Under these conditions, the undisturbed kinetic energy flux is likely to give an inaccurate estimate of the potential power that can be extracted from a given site. This is because the thrust applied by the devices augments the natural resistance of the site (which is principally provided by bed friction and flow separations), which reduces the volume flow rate through the site. This results in a reduction in the available power, so that the maximum potential power that can be extracted from a given site is much lower

than the undisturbed kinetic energy flux (Garrett & Cummins 2005).

To develop an improved estimate of the maximum potential power that can be extracted from a given site, a variety of analytical models have been proposed to model the effect of device thrust on the site dynamics. Most of these analytical models are based on the 1D channel model of Garrett & Cummins (2005), where the flow through an idealised tidal channel is driven by a head difference between two large tidal basins. The thrust applied by the devices is uniformly distributed over the channel cross-section and is added to the undisturbed channel resistance (provided by bed friction and flow separations). Garrett & Cummins showed that (at most) the maximum average power that can be extracted from the channel is 24% of the product of the maximum head difference across the channel and the undisturbed volume flow rate through the channel. However, it should be noted that the maximum average power that can be extracted from the channel in practice will be much lower than the limit derived by Garrett & Cummins, principally due to leading order energy losses from support structure drag, wake mixing and viscous drag on the turbine blades. Furthermore, it is also unlikely that devices will be able to span the entire channel cross-section due to navigation constraints and the number of devices installed may also be deliberately limited in order to avoid significant environmental change.

While the 1D analytical models are useful for providing a preliminary estimate of the maximum power that is available for extraction, real tidal energy sites are usually modelled numerically. This is most often accomplished by solving the 2D depth-averaged shallow water equations in the region surrounding the site of interest. In these simulations, the resistance provided by the devices is usually modelled as either a local increase in bed friction (see Blunden & Bahaj (2006) or Vogel et al. (2013) for example) or a drop in static pressure head, using linear momentum actuator disc theory (LMADT) (Draper et al. 2010). When the data is available, turbine performance curves (thrust and power against depth-averaged velocity) have also

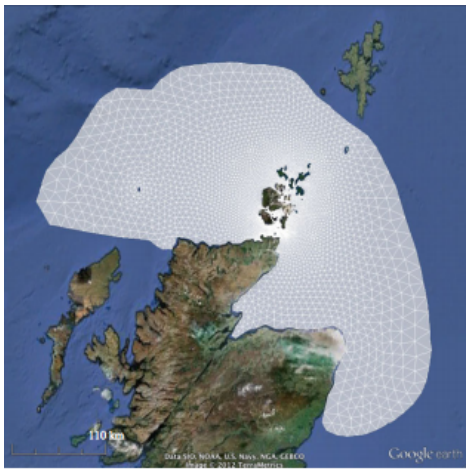

(a) Overall computational domain

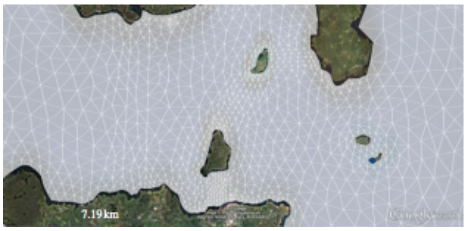

(b) Close-up view of the region around Stroma, Swona and South Ronaldsay where turbines are modelled.

Figure 1.2: Computational mesh used in the regional scale model of the Pentland Firth (Scotland) by Adcock et al. (2014), showing the overall domain (a) and a close-up view of the region where turbines are modelled (b).

been used by some authors (see Vogel (2014) for example). In addition to achieving a more realistic estimate of the power that is available for extraction than 1D analytical models, these 2D models include site specific details, such as the coastline geometry and local bathymetry. Hence, they can also be used to investigate changes in the local hydrodynamics that are induced by a given installation and form part of an environmental impact assessment (MeyGen Ltd. 2016). Several promising sites in the UK have been assessed using these methods, including the Portland Bill by Blunden & Bahaj (2006), the Anglesey Skerries by Serhadlioğlu et al. (2013) and the Pentland Firth by Adcock et al. (2014) (see Fig. 1.2).

1.2.2 Array Scale

In order to realise a significant fraction of the available tidal energy resource at a given site, multiple devices are likely to be grouped together to form arrays. With careful consideration of the array layout, it may be possible for individual devices within the array to interact constructively, improving the performance of the entire array. This

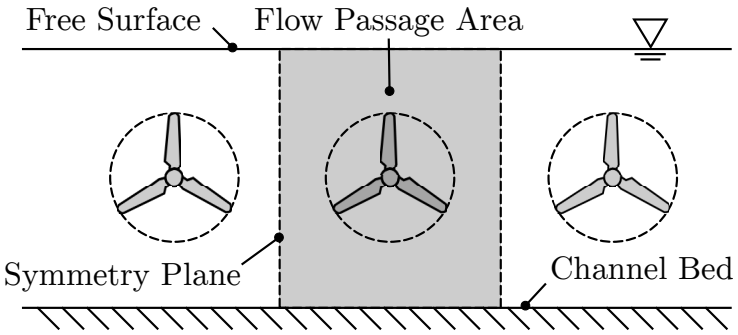

Figure 1.3: Schematic diagram of a cross-section through a tidal channel, normal to the flow direction. The local flow passage area is shaded in grey and the swept area of the rotor is identified with a dashed circle.

constructive interference requires careful consideration of the spacing between devices and the thrust applied by the individual devices within the array. While it may not be possible to achieve the optimum array layout in practice (due to shipping lanes, bathymetric features and the variable depth of the channel), recent hydrodynamic models of idealised tidal turbine arrays have produced many significant results. The key results from these studies will be summarised in the following sections.

1.2.2.1 Tidal Fences

For wind and tidal stream turbines, the incident flow can pass around the turbine as well as through the swept area of the rotor. As the thrust applied by the device increases, the flow is increasing diverted around the device and the mass flow rate through the swept area of the rotor reduces. Hence, there is an optimum point at which the power extracted from the flow (the product of the applied thrust and velocity through the swept area of the rotor) is maximised. Lanchester (1915) and Betz (1920) both showed (independently) that for an ideal energy extracting device (an actuator disc) operating in a completely unconstrained flow stream, the maximum power that can be extracted is 16/27 times the undisturbed kinetic energy flux passing through the swept area of the rotor. This maximum power is achieved when the upstream flow speed is reduced by 1/3 as it passes through the swept area of the

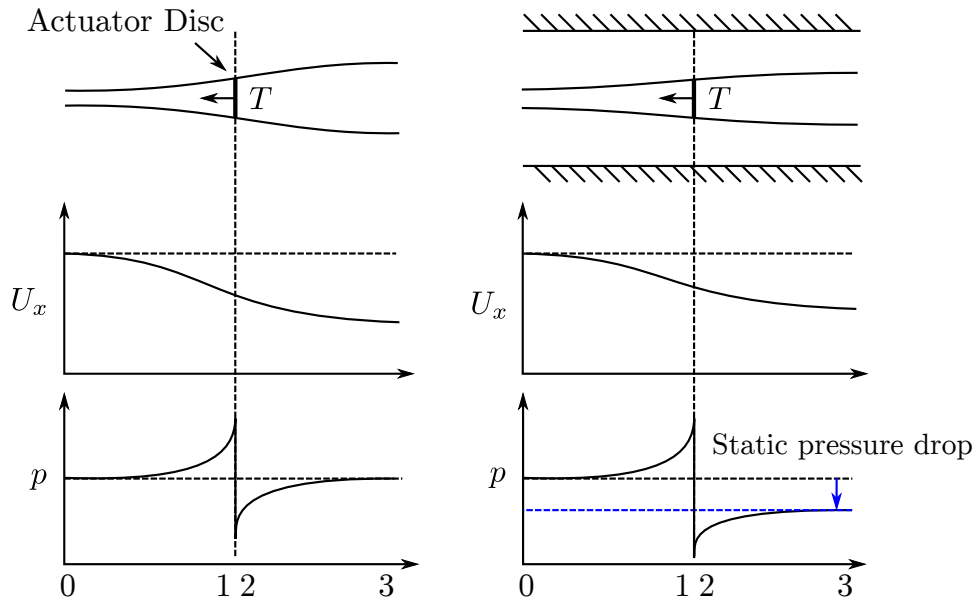

(a) Unblocked (b) Blocked

Figure 1.4: Streamwise variation of the axial velocity (U_x) and static pressure (p) through the centre of an actuator disc in (a) unblocked and (b) blocked conditions according to linear momentum actuator disc theory (Garrett & Cummins 2007). The static pressure has equalised between the core and bypass flow streams at station 3 but wake mixing must still occur downstream of station 3 (not shown).

rotor. Of course, the power that is extracted by real turbines is always lower than this limit due to viscous drag, rotation in the wake and electrical losses.

The Lanchester-Betz limit is only applicable to wind and tidal stream turbines that are operating in relative isolation from other devices and confining boundaries (such as the free surface and seabed). For an ideal energy extracting device operating in a confined channel, Garrett & Cummins (2007) showed that the maximum theoretical power coefficient increases above the Lanchester-Betz limit of 16/27 by a factor of $(1-B)^{-2}$, where B is the blockage ratio. The blockage ratio refers to the ratio of the frontal projected area of the device to the cross-sectional area of the local flow passage that the devices resides in, as shown in Fig. 1.3. The maximum theoretical power coefficient increases because of the mass flux constraint provided by the boundaries of the local flow passage that the device resides in (the seabed, free surface and the effective symmetry plane between neighbouring devices). More specifically, fluid

cannot be drawn in from the surrounding environment to raise the static pressure in the bypass flow (the flow which passes around the device) downstream of the device. Therefore, a static pressure drop is developed in the streamwise direction in response to the thrust that is applied to the flow by the device (see Fig. 1.4). Hence, the maximum theoretical power coefficient that be achieved by the device increases, as the device is able to extract energy from the static pressure head in the flow, in addition to the kinetic energy flux that is utilised by devices that operate in unconstrained flow conditions. In terms of device operation, this is equivalent to the flow through the swept area of the device accelerating at constant thrust, allowing more power to be extracted from the flow.

Although not accounted for in the analysis of Garrett & Cummins, the maximum theoretical power coefficient is also affected by channel aspect-ratio, asymmetric channel blockage and turbulent mixing downstream of the device (Nishino & Willden 2012*a*). It should also be noted that real tidal energy devices actually operate in an open channel flow, where the free-surface is exposed to constant atmospheric pressure and the flow is sub-critical. Under these conditions, the static pressure drop across the device leads to a drop in free surface height, which further accelerates the bypass flow around the device. The magnitude of the free surface deformation depends on the energy extracted from the flow (principally the thrust applied by the device) and the Froude number of the upstream flow. However, for the majority of tidal energy sites, the Froude number is < 0.2, and the thrust applied by the devices (under realistic blockage conditions) is sufficiently low that the deformation of the free surface can be neglected (Consul et al. 2013).

In order to maximise the power coefficient that can theoretically be achieved by tidal energy devices, the analysis carried out by Garrett & Cummins implies that the devices should be spaced as close together as possible, in order to maximise the blockage ratio. Furthermore, the optimum array configuration would be a single

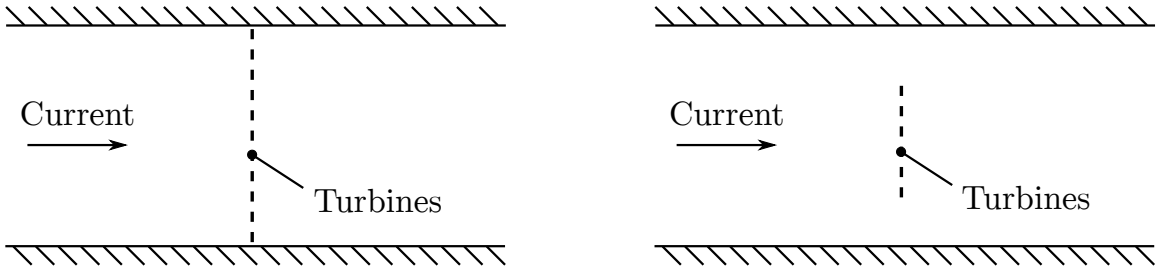

(a) Full Tidal Fence (b) Partial Tidal Fence

Figure 1.5: Schematic diagram of full and partial fences of tidal turbines (viewed from above).

continuous line of devices (a 'full tidal fence'), that stretches across the entire width of the channel and is aligned normal to the flow direction, as shown in Fig. 1.5 (a)). This configuration maximises the blockage experienced by each device and hence the power that can be extracted by the entire array. However, such a configuration is unlikely in practice, as it does not accommodate other users of the channel, the varying depth of the channel, or bathymetric features.

In practice, a line of turbines that does not block the entire width of the channel (a 'partial tidal fence') is a more realistic array configuration (see Fig. 1.5 (b)). Nishino & Willden (2012*b*) showed that for a partial tidal fence (with a fixed number of devices), the device power coefficient is maximised by a non-zero tip-to-tip spacing. The maximum power coefficient does not occur at zero tip-to-tip spacing (as in a full tidal fence) because the array thrust increases as the tip-to-tip spacing is reduced, which increasingly diverts the flow around the array and reduces the mass flow rate through the array. Hence, an optimum (non-zero) tip-to-tip spacing is required to maximise the power coefficient of devices operating in a partial tidal fence. This optimum spacing is a balance between increasing local blockage and reducing mass flow rate through the array, as the tip-to-tip spacing is reduced. Further computational studies have shown good agreement with the analytical model of Nishino & Willden, when the number of devices in the fence is sufficiently large (Nishino & Willden 2013).

Fig. 1.6 shows the results of an example simulation of a fence of 8 actuator discs

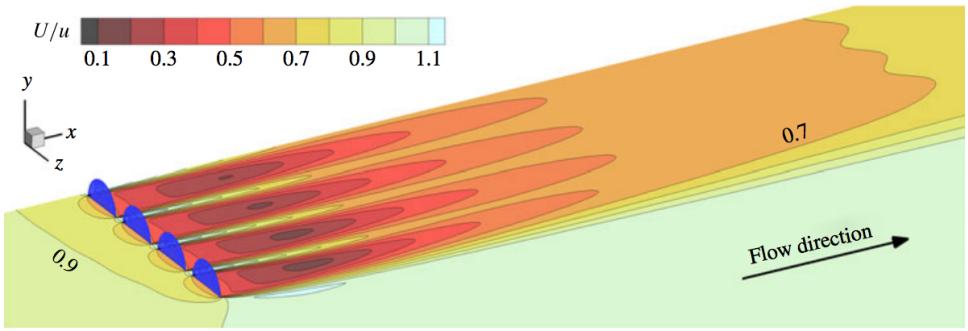

Figure 1.6: Streamwise velocity contours (at hub height) from a simulation by Nishino & Willden (2013) of a fence of 8 actuator discs (4 discs with a central symmetry plane). The discs have a tip-to-tip spacing of 1/4 of the disc diameter.

(4 discs with a symmetry plane), carried out by Nishino & Willden (2013). The contours of streamwise velocity clearly show that the mixing downstream of the individual devices occurs over a much shorter length-scale than the mixing between the array core flow and the array bypass flow. Hence, it may be reasonable to assume that these mixing processes occur independently (the scales are independent), as long as the fence is sufficiently long. However, when the tidal fence does not contain a large number of devices (a 'short partial fence'), the scale-separation assumption adopted in the analytic model of Nishino & Willden (2012*b*) is likely to be unreliable. To address this limitation, computational (Schluntz et al. 2014, Hunter et al. 2015) and experimental (Cooke et al. 2014, 2015) studies of short partial fences have been carried out, as a scale separation assumption is not required for these investigations. In an experimental investigation, Cooke et al. (2014) found that the power available to a fence of 8 porous discs was maximised by using low porosity (high thrust) discs, with a narrow (but non-zero) tip-to-tip spacing. Further increasing the disc thrust (by reducing the disc porosity) led to a drop off in power, as the flow rate through the entire array reduced. This experiment indicates that the same mechanism experienced by long partial fences is also experienced by short partial fences and the power coefficient can be maximised by carefully considering the tip-to-tip spacing and thrust of the devices.

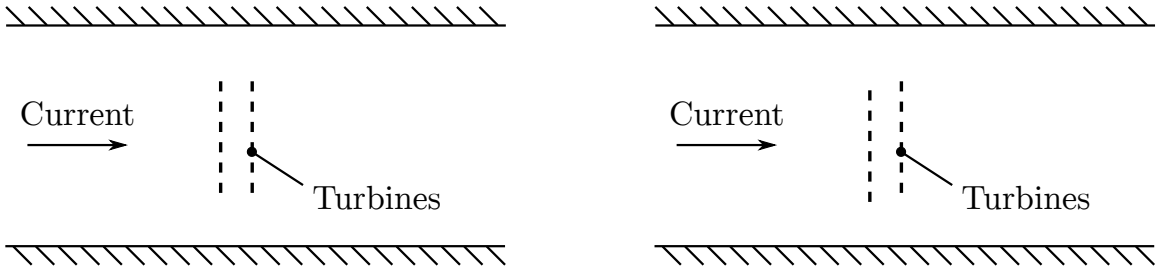

(a) Centred Rows (b) Staggered Rows

Figure 1.7: Schematic diagram of centred and staggered rows of tidal turbines (viewed from above).

1.2.2.2 Rows of Tidal Fences

At some tidal energy sites (particularly narrow channels), it may be necessary to use multiple rows of tidal fences to extract sufficient power from the flow. The hydrodynamically ideal array layout here would be to place the fences sufficiently far apart in the streamwise direction for full wake recovery between rows. However, to maintain a spatially compact array, it may not always be possible to space consecutive rows sufficiently far apart for full wake recovery. For these spatially compact arrays, Draper & Nishino (2014) showed that when the fences are aligned normal to the incident flow direction, higher maximum power coefficients can be achieved by staggered rows of devices (Fig. 1.7 (b)) than centred rows of devices (Fig. 1.7 (a)). This is because, in the staggered arrangement, the downstream devices encounter the high velocity bypass flow from the upstream devices, increasing the power that can be extracted at a given thrust. Conversely, in the centred arrangement, the downstream devices encounter the low velocity core flow from the upstream devices, reducing the power that can be extracted at a given thrust. The conclusions drawn by Draper & Nishino agree well with 3D RANS computations of various centred and staggered arrays of actuator discs performed by Malki et al. (2014) and Hunter et al. (2014).

When simulating arrays of turbines with multiple rows, accurate wake models are essential to predict the onset velocity and turbulence profiles encountered by

the downstream devices, in order to carry out an energy yield assessment for the entire array. As several energy yield assessments may be required at a given site (to compare different array layouts and onset flow orientations), low order wake models are essential to reduce the computational cost of each assessment. To develop accurate wake models, the wake behind a single rotor must be characterised first. Similarly to wind turbine rotors, the velocity deficit downstream of a single tidal turbine rotor is known to be a strong function of the device thrust and ambient turbulence (Stallard et al. 2013). However, as tidal channels are constrained in the vertical direction by the free surface and sea bed, the wake structure downstream of a single tidal turbine rotor is considerably different to the wake structure downstream of a wind turbine rotor. Hence, different wake models are required for tidal turbine rotors. Stallard et al. (2015) showed that the wake behind a single isolated tidal turbine rotor in a shallow turbulent flow follows a characteristic flow pattern. Immediately downstream of the rotor (the near wake), the time-averaged wake is relatively unconstrained and is almost axisymmetric. Moving downstream, the wake expands and transitions into a profile that can be described as a self-similar Gaussian in the lateral direction and a depth averaged profile in the vertical direction (when normalised by the upstream shear profile). In the far wake ($x/D > 8$), the velocity deficit is almost entirely two-dimensional, with the maximum velocity deficit being well approximated by a plane wake (proportional to $x^{-1/2}$, where x is the streamwise distance downstream of the rotor plane).

Once an accurate wake model has been developed for a single rotor, the wakes of several rotors can be combined to compute the inlet conditions for the downstream rotors. Several different methods have been adopted by the wind energy industry to combine the wakes of upstream rotors. These methods were recently compared by Machefaux et al. (2015) and Gunn et al. (2016) and include linear superposition, quadratic superposition and maximum deficit approaches. Linear superposition has

also been adopted by some authors for tidal turbine arrays (Stansby & Stallard 2016, Lande-Sudall et al. 2017) and has shown reasonable agreement both with experimental measurements and with Reynolds-averaged Navier-Stokes embedded blade element (RANS-BE) computations of the same arrays (Olczak et al. 2016). As an alternative to superposition methods, the RANS-BE method has been used by some authors to compute the combined wake of several rotors directly (by solving the RANS equations) (see Turnock et al. (2011) and Malki et al. (2014) for example). However, this approach is significantly more computationally expensive than the wake superposition methods.

1.2.3 Device Scale

The aim of hydrodynamic modelling at device scale is to maximise the power extracted by individual devices and to improve their survivability. This is usually achieved by developing algorithms to better design the devices themselves and by investigating the impact of the harsh environmental conditions (see Fig. 1.8) on device operation. To carry out these device scale investigations, simplifying assumptions must be made for the surrounding environment and the array that the device operates in. For example, the device is usually assumed to operate either in isolation (unblocked conditions) or in an infinitely long tidal fence (blocked conditions), which allows the blockage provided by the device to be specified for the investigation. The infinitely long fence assumption is usually considered a reasonable approximation to the operating conditions that are experienced by devices that are sufficiently far from the ends of long tidal fences. In addition, the thrust provided by the array is usually assumed to be small in comparison with the drag provided by the undisturbed channel (from bed friction and flow separations). Hence, the mass flow rate through the channel can be assumed to be constant, as the channel dynamics are unaffected by the presence of the devices (Garrett & Cummins 2007).

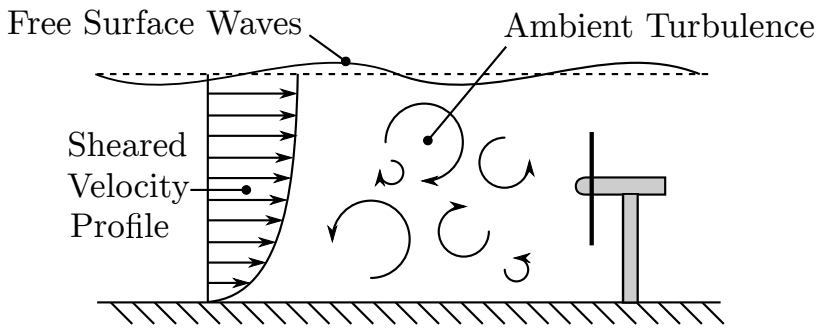

Figure 1.8: An illustration of the sheared velocity profile, ambient turbulence and free surface waves that all contribute to the unsteady loading on tidal energy devices.

1.2.3.1 Hydrodynamic Rotor Design Algorithms

The majority of the algorithms that have been adopted to design (wind and) tidal turbine rotor blades are based on the blade element momentum (BEM) method (see Batten et al. (2008) and Goundar & Ahmed (2013) for example). While these algorithms are useful for designing rotors for optimum operation in unblocked conditions, they are not sufficient to design optimal rotors for operation in blocked conditions. This is because they do not account for the additional acceleration of the flow through the rotor plane as blockage is increased (at constant tip-speed-ratio) and the increased rotor thrust that is required achieve the maximum power coefficient at higher blockage ratios (Schluntz & Willden 2015). To address this deficiency, McIntosh et al. (2011) proposed a new hydrodynamic rotor design algorithm, by embedding the blade element method within a 3D RANS solver (ANSYS Fluent). In this design algorithm, the 1D momentum equations (that are used in the standard BEM based design algorithm) are replaced by the 3D RANS equations, so the algorithm can account for blockage explicitly through the boundary conditions of the computational domain. This algorithm has subsequently been adopted by several authors including Belloni (2013), Schluntz & Willden (2015) and Hunter (2016) to design tidal turbine rotors for optimum operation under specific blockage conditions. When operating at their design blockage ratio, the rotors designed with this algorithm have been shown to

universally outperform rotors which were not specifically designed to operate at that blockage ratio (Schluntz & Willden 2015).

Despite the success of these blade element based algorithms, Hunter (2016) showed that the design of the root and tip sections is highly dependent on the empirical corrections that are used in the design algorithm to account for three-dimensional flow effects (such as the tip loss mechanism on the outboard blade sections). Hence, additional 3D blade resolved computations and experimental measurements are required to better understand the three-dimensional flow effects and incorporate them into the design process.

1.2.3.2 Velocity Shear

Field measurements at several prospective tidal energy sites have shown that the velocity profile exhibits high levels of shear and changes shape considerably over the tidal cycle (Gunn & Stock-Williams 2013, Mason-Jones et al. 2013). The sheared velocity profile results in a greater proportion of the incident kinetic energy flux residing near the top of the water column, so it is generally desirable to install devices as high up in the water column as possible. However, sufficient surface clearance must still be maintained for vessel navigation and to satisfy cavitation restrictions.

For device developers, the primary concern with the highly sheared velocity profile is the unsteady loading contribution, which arises as the blade passes through the low velocity fluid near the bottom of the water column followed by the high velocity fluid near the top of the water column. Individual blade pitch control has been proposed as one method that could be used to mitigate this unsteady loading contribution (Hu & Willden 2016). However, the control algorithms necessary to implement this load mitigation strategy have not yet been proposed.

1.2.3.3 Ambient Turbulence

Highly energetic and anisotropic turbulence has been measured at many prospective tidal energy sites. Milne et al. (2013) for example, measured streamwise turbulence intensities of 12-13% during non-slack flow in the Sound of Islay (Scotland, UK). From these measurements, Milne et al. computed integral length and time scales of 11-14m and 6s respectively (at maximum flow rate), indicating the presence of large coherent turbulent structures in the flow. Conversely, MacEnri et al. (2013) measured much lower turbulence intensities of 4-9% at Strangford Narrows (Northern Ireland, UK). They suggested that the lower turbulence intensity at this site is likely to be because the site is relatively sheltered from the open sea and does not feature many prominent bed and coastal features. Hence, ambient turbulence seems to be highly site dependent and will need to be characterised on a case-by-case basis.

High levels of ambient turbulence are generally undesirable for tidal energy devices, as ambient turbulence leads to an additional unsteady loading contribution that is difficult to mitigate with a control strategy. For this reason, devices are not likely be installed in the vicinity of prominent bed and coastal features that generate high levels of turbulence (Zangiabadi et al. 2015). Furthermore, the effect of ambient turbulence on the mean thrust and power developed by the rotor is not well understood. Mycek et al. (2014) and Blackmore et al. (2015) both found that the mean rotor thrust and power decreased slightly with increasing ambient turbulence intensity. However, a comprehensive explanation for this observation has not yet been proposed.

Despite the uncertainty in the behaviour of the mean thrust and power, the effect of ambient turbulence on wake recovery is well understood qualitatively and has been investigated both computationally (McNaughton 2013) and experimentally (Mycek et al. 2014). High levels of ambient turbulence facilitate a more rapid break down of the helical vortex structure downstream of the rotor and enhances mixing between

the core and bypass flow streams, leading to faster wake recovery.

1.2.3.4 Free Surface Waves

Tidal energy sites are typically characterised by energetic free surface waves. At the MeyGen site for example, significant wave heights of 1.25m-1.5m are typically observed, with typical wave periods of around 4s (MeyGen Ltd. 2011). While at the European Marine Energy Centre (EMEC), significant wave heights of 1.75-2m are typically observed, with typical wave periods of 5-10s (EMEC 2016). The primary concern for device developers is the additional unsteady loading contribution that arises from these surface waves, due to the wave induced velocity and pressure fluctuations. The wave induced dynamic pressure fluctuations reduce with increasing submersion depth and with increasing wavenumber, so devices installed near the free surface will be more strongly affected by surface waves than bed mounted devices.

To better understand the unsteady loading contribution, several experimental studies have been carried out with laboratory scale tidal turbine rotors in towing tanks (with applied surface waves). Galloway et al. (2010) and Luznik et al. (2013) both found that free surface waves had negligible affect on the mean thrust and power developed by their turbines. However, the unsteady loading contribution was found to be significant, with Galloway et al. reporting a fluctuation of 37% in thrust (about the mean) and 35% in power (about the mean) due to the surface waves. The surface waves used in this experiment were chosen to be representative of a wave climate with significant wave heights of around 1.6m in a water depth of 37m (similar to the EMEC site).

Fleming (2014) investigated the effect of wave height and wave length independently in a series of computational studies. With increasing wave height, the thrust and torque fluctuations were found to increase, as the wave induced velocity fluctuations increase in magnitude over the entire depth of the water column. The thrust and

torque fluctuations were also found to increase in magnitude with increasing wavelength, as the wave induced velocity fluctuations penetrate deeper into the water column and increase in magnitude over the rotor swept area.

1.3 Research Objectives

In this thesis, three specific objectives will be addressed that contribute towards the broader goals of the tidal energy industry that were discussed in the section 1.1.3. These objectives are defined and discussed in the following section.

1.3.1 Tip Flow Corrections for Horizontal Axis Rotors

For un-ducted horizontal axis rotors, the majority of the thrust and torque is generated by the outboard blade sections (typically from 70% to 95% of the span). Hence, accurately computing the loading on the outboard blade sections is of paramount importance if the performance and survivability of the rotor is to be predicted accurately. While reduced order rotor models (such as the blade element momentum and actuator line methods) give reasonably accurate predictions of the blade loading along the mid-span of the blade, the blade loading on the outboard sections is often over-predicted by these methods. This is because these methods do not sufficiently account for tip flow effects, which result in the blade loading dropping off as the tip of the blade is approached. Hence, a tip flow correction is required to prevent the blade loading from being significantly over-predicted by these methods.

In the wind energy industry, several tip flow corrections have already been proposed (see Lindenburg (2004), Shen et al. (2005), Sant (2007) for example). However, many of these corrections are purely empirical and they have not yet been extensively assessed and validated, despite their widespread adoption. Furthermore, tidal turbine rotors are likely to experience stronger tip flow effects than wind turbine rotors, due

to the greater planform area that can support spanwise flow. Hence, they are likely to require a more aggressive correction than is currently applied by the existing tip flow corrections.

The first objective of this thesis is to directly examine the tip loss mechanism experienced by two different un-ducted horizontal axis rotors (a wind turbine rotor and a tidal turbine rotor) to provide a general understanding of the tip loss mechanism. With this understanding, two different methods of correcting the blade loading for the tip loss mechanism will then be presented and critically evaluated. Both methods will be shown to yield a significant improvement in accuracy of the computed blade loading.

1.3.2 Cavitation Restrictions on Tidal Turbine Performance

To avoid structural damage, the latest guidelines for tidal turbine rotors states that cavitation inception must be avoided entirely during rotor operation (DNV GL 2015). However, there is currently no guidance for how this should be accomplished. The most direct approach would be to prevent the minimum static pressure from dropping below the vapour pressure of seawater. This can be accomplished by either limiting the maximum tip-speed-ratio of the rotor or by increasing the submersion depth of the rotor. However, these restrictions limit the maximum thrust and power that can be developed by the rotor. Furthermore, a large safety margin is likely to be required to account for the range of uncertainties in the hydrodynamic analysis, which further restricts the range of permissible tip-speed-ratios and submersion depths. By reducing the uncertainty in the cavitation analysis, it may be possible to reduce the safety margins that are placed on the rotor operating conditions, thus increasing the thrust and power that can be developed by the rotor.

Cavitation inception is likely to initiate on the outboard blade sections first, since the static pressure reaches a minimum here. However, the static pressure distribution

on the outboard blade sections is modified by blockage and tip flow effects. The magnitude of these changes is currently unknown, which results in significant uncertainty in the cavitation analysis and a large safety margin. Hence, the second objective of this thesis is to carry out a cavitation analysis that accounts for tip flow effects and blockage, in order to reduce the uncertainty in the cavitation analysis. This objective will be addressed by carrying out a series of blade resolved computations (that inherently include tip flow effects) over a range of blockage ratios and tip-speed-ratios.

1.3.3 Tidal Power Extraction on a Streamwise Bed Slope

Computational and experimental studies of tidal turbine rotors often assume that the sea bed is horizontal and uniform. However, at many sites that are currently under consideration for device installation, the sea bed is not uniform and slopes considerably in the streamwise and lateral directions. At the MeyGen site (Phase 1a) for example, the local depth varies from around 30m to around 35m in the immediate vicinity of the devices (over a few hundred metres) (MeyGen Ltd. 2016). While the effect of sloping bathymetry on the depth-averaged velocity can be readily captured in regional scale computations (by varying the local depth in the depth-averaged shallow water equations), the effect of sloping bathymetry on the local flow field at device scale is less well understood and is often ignored. Hence, the third objective of this thesis is to investigate the effect of a sloping sea bed on the local flow field in the immediate vicinity of a tidal energy device and the resulting impact on device performance. This information can then be used to better select device and equipment installation sites in the first place, by identifying areas where the local bathymetry is indicative of favourable flow conditions.

This objective will be addressed by carrying out a series of actuator disc and blade resolved computations in a domain that slopes in the streamwise direction. The device loading and near wake flow field will then be examined to demonstrate

the effect of the sloping sea bed on device performance.

1.4 Thesis Outline

The research objectives are addressed in 6 additional chapters.

Chapter 2 briefly summarises the numerical method adopted for the computations.

Chapter 3 introduces the actuator line and blade resolved rotor representation techniques. The methods are validated through comparison with experimental measurements of a 4.5m diameter wind turbine rotor (the MEXICO rotor).

Tip flow effects are investigated in detail in Chapter 4, by carrying out a series of actuator line and blade resolved computations. Two different methods of accounting for tip flow effects are presented and compared.

In Chapter 5, a cavitation analysis of two different tidal turbine rotor designs is carried out over a range of blockage ratios and tip-speed-ratios. Restrictions are placed on the minimum static pressure to avoid cavitation inception and the resulting limits on the rotor thrust and power are investigated.

In Chapter 6, actuator disc computations are carried out in a computational domain that slopes in the streamwise direction. Upwards facing, horizontal and downwards facing bed slopes are investigated and the power and thrust extracted by the disc on each bed slope is compared.

In Chapter 7, the actuator disc is replaced with a blade resolved rotor representation, so that the unsteady blade loading and near wake structure can be investigated in more detail.

In the final chapter of the thesis (Chapter 8), the main findings are summarised, conclusions are drawn and recommendations for future work are provided.

Chapter 2

Numerical Method

In this thesis, the Reynolds-averaged Navier-Stokes (RANS) equations are solved numerically using the computational fluid dynamics (CFD) solver OpenFOAM (version 2.3.1) to compute the flow field around wind and tidal turbine rotors. OpenFOAM uses a nominally second order accurate finite volume method to discretise the governing equations into a set of linear algebraic equations that can be solved numerically (the industry standard approach). As this procedure is well established in the scientific community, it will not be discussed in detail here. Instead, the reader is referred to either Jasak (1996) or Rusche (2002) where details of the discretisation and solution procedure adopted by OpenFOAM can be found.

OpenFOAM offers a variety of linear system solvers and discretisation schemes for the RANS equations. In this thesis, central differencing is used for the face interpolation of all the Laplacian and gradient terms (Versteeg & Malalasekera 1995), while a flux limited form of central differencing with the Sweby (1984) limiter, is used for the convection terms. A symmetric Gauss-Seidel solver is adopted for the solution of the momentum and turbulent scalar transport equations, while a generalised geometric-algebraic multi-grid (GAMG) method is adopted for the solution of the Poisson equation for pressure. A detailed discussion of these methods can

be found in Saad (1993). In both the steady and unsteady computations carried out in this thesis, the SIMPLE algorithm of Patankar (1980) is adopted to enforce the pressure-velocity coupling between the momentum equations and the continuity equation (within each time step).

The accuracy of the OpenFOAM code will be addressed in Chapter 3, by comparing the simulated results with experimental measurements of a 4.5m diameter wind turbine rotor. For further comparison, the simulated results will also be compared with similar computations of the same rotor carried out by Bechmann et al. (2011).

2.1 Turbulence Closure

The $k-\omega$ SST model remains the most popular turbulence model for wind and tidal turbine rotor computations, due to its comparatively superior performance prediction of flow over solid surfaces (such as the rotor blades, nacelle and support structure) and of flow separations (Bardina et al. 1997, Apsley & Leschziner 2000). For example, the $k-\omega$ SST model has been used to successfully compute the flow past the NREL Phase VI (Sørenson & Shen 2002) and MEXICO (Bechmann et al. 2011) experimental wind turbine rotors, showing good agreement with experimental measurements. Due to the importance of the solid boundaries investigated in this thesis (both from the turbine itself and the local bathymetry in the bed slope investigation), the $k-\omega$ SST model was deemed to be the most appropriate turbulence model and was therefore adopted for all the computations carried out in this thesis. A quantitative comparison of the accuracy of the k - ω SST model with other turbulence models was carried out by the author and can be found in Wimshurst & Willden (2016*a*).

In the k - ω SST model, two additional scalar transport equations are solved for k and ω (alongside the 3 momentum equations and the Poisson equation for pressure). These variables physically represent the energy and the scale of the turbulence

(respectively) and are a statistical representation of the turbulent fluctuations which are not explicitly resolved by the RANS equations. Once computed, these variables are used to compute the kinematic eddy viscosity ν_t and close the system of RANS equations via the Boussinesq (1878) hypothesis. For further details of the k - ω SST model, the reader is referred to Menter (1994).

2.2 Wall Modelling

In the near wall region, the spatial velocity gradients are large. Hence a fine grid resolution is required to accurately resolve them. With increasing Reynolds number the boundary layer thickness reduces, increasing the spatial gradients and the level of mesh resolution required to sufficiently resolve them (Schlichting & Gersten 2000). In some instances it may not be feasible to resolve these gradients and wall modelling approaches must be adopted instead. This section briefly discusses the wall modelling techniques adopted by OpenFOAM for RANS computations of high Reynolds number turbulent flow.

The wall modelling approaches are based on experimental measurements (Eckelmann 1974) and direct numerical simulations (DNS) (Moser et al. 1999) of fully developed turbulent channel flow, which have shown that the mean velocity component tangential to the wall approximately follows a universal profile with distance normal to the wall (von Kárman 1930), as shown in Fig. 2.1. Defining a dimensionless wall distance $y^+ = yu_\tau/\nu$, where y is the distance normal to the wall and $u_\tau = \sqrt{\tau_w/\rho}$ is the friction velocity (based on the wall shear stress τ_w), the tangential velocity component in the viscous sub-layer $U^+ = U/u_\tau$ varies linearly with distance from the wall,

$$U^+ = y^+ \qquad y^+ < 5. \tag{2.1}$$

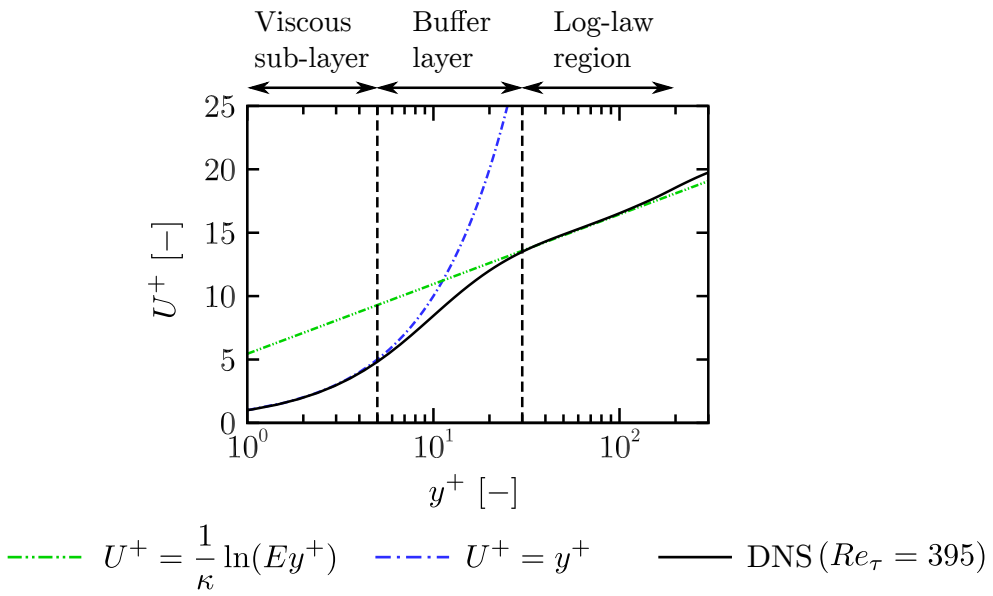

Figure 2.1: Dimensionless tangential velocity U^+ as a function of dimensionless wall distance y^+ computed using DNS of fully developed channel flow at a friction based Reynolds number $Re_\tau = yu_\tau/\nu = 395$ (Moser et al. 1999).

Whereas in the logarithmic law region, the tangential velocity component approximately follows a logarithmic profile,

$$U^+ = \frac{1}{\kappa}\ln(Ey^+) \qquad 30 < y^+ < 200 \tag{2.2}$$

where κ and E are empirical coefficients (0.41 and 9.8 respectively) (Versteeg & Malalasekera 1995). These measurements were carried out at a friction-based Reynolds number ($Re_\tau = yu_\tau/\nu$, where y is the half-depth of the channel) of 395, since it is not possible to carry out DNS simulations at higher Reynolds numbers with current computational resources. At higher Reynolds numbers that are typical of wind and tidal flows ($Re \sim 10^6 - 10^7$), the velocity profile is assumed to follow the same characteristic profile normal to the wall, with the exception of the distance that the lograrithmic law region extends into the bulk flow. Based on these observations (and assumptions), two different approaches can be adopted for RANS modelling of the near wall region. In the first approach, the wall adjacent cell centroids are placed in

the viscous sub-layer, with y^+ less than 5 over the entire surface. Hence, the velocity profile between the wall adjacent cell centroid and the wall can be assumed to be linear, following equation 2.1. This is often referred to as the wall resolved approach (Versteeg & Malalasekera 1995). One practical difficulty with the wall resolved approach is that the wall normal distance requirement often leads to high aspect ratio cells on the body surface. This can lead to numerical difficulties for the flow solver, particularly if the cells are also highly skewed due to the surface geometry (Jasak 1996).

In the second approach, the wall adjacent cell centroids are placed in the logarithmic law region, with y^+ greater than 30 but less than 200. Hence, the velocity profile between the wall adjacent cell centroid and the wall can be assumed to be logarithmic, following equation 2.2. This is often referred to as the wall function approach (Versteeg & Malalasekera 1995). Despite the reduced cell count and improved cell quality that can be achieved with this approach, the accuracy of the logarithmic velocity profile is likely to be unreliable in flows with high curvature, separation and reattachment (Ferziger & Perić 1995).

In this work, both the wall resolved and wall function approaches are used. For the computations of the 4.5m diameter wind turbine rotor in Chapter 3, a wall resolved approach is adopted. Conversely, a wall function approach is adopted for the full-scale tidal turbine rotor computations in Chapter 5 and 7.

For k and ω, OpenFOAM assigns appropriate boundary conditions based on the asymptotic behaviour of the scalar transport equation in the viscous sub-layer and logarithmic law regions (Kalitzin et al. 2005). With the wall adjacent cell centroid in the logarithmic law region, the turbulent kinetic energy is assigned a zero gradient boundary condition between the cell centroid and the boundary face ($\partial k/\partial n = 0$),

while the specific dissipation rate is assigned a fixed value of,

$$\omega_{\text{wall}} = \frac{u_\tau}{\sqrt{\beta^\star}\kappa y} \tag{2.3}$$

on the boundary cell face. Alternatively, if the wall adjacent cell centroid is placed in the viscous sub-layer, the turbulent kinetic energy and specific dissipation rate are assigned fixed values of,

$$k_{\text{wall}} = 0 \qquad \text{and} \qquad \omega_{\text{wall}} = 10\left(\frac{6\nu}{\beta_1 y^2}\right) \tag{2.4}$$

on the boundary cell face.

2.3 Rotor Rotation Techniques

Three different techniques are utilised to simulate the rotation of the rotor in this work. The first two methods resolve the geometry of the rotor directly, by fitting a block-structured mesh around the blades. These methods will be referred to as 'blade resolved' in this work. The third method replaces the blade geometry by equivalent virtual point forces, which are distributed along the blade span and are rotated through a stationary computational domain. This technique will be referred to as the 'actuator line' method and will be discussed in detail in Chapter 3. For both blade resolved approaches, the computational domain is divided into separate inner and outer domains and a separate block-structured mesh is created in each domain. As shown in Fig. 2.2, the inner domain is coin shaped, with a radius of $1.2R$ and length of $0.7R$ (where R is the rotor radius). This coin-shaped inner domain contains the rotor, nose cone and the front section of the nacelle. Conversely, the outer domain contains the rear section of the nacelle and the remainder of the computational domain (it extends up to the domain boundaries). By dividing the computational domain into separate inner and outer domains, the rotor can be rotated in isolation from the

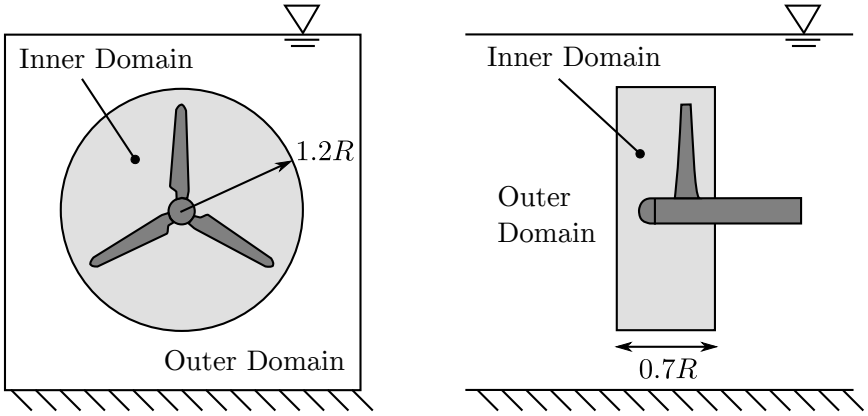

(a) Front View (b) Side View

Figure 2.2: Schematic diagram of the separation of the computational domain into separate inner and outer domains.

rest of the computational domain.

The inner and outer domain meshes are coupled together at a non-conformal cell interface on the surface of the coin, using the face interpolation algorithm of Farrell & Maddison (2011) that is available in OpenFOAM.

2.3.1 Multiple Reference Frame Approach

For the first blade resolved approach, both the inner and outer domain meshes remain stationary throughout the computation. However, in the inner domain the RANS equations are solved in a reference frame rotating with the rotor blades, while in the outer domain the RANS equations are solved in an inertially fixed reference frame (Luo et al. 1994). This approach is often called the Multiple Reference Frame (MRF) or Frozen Rotor approach and only produces a physical solution when the flow field (relative to the blade motion) is steady (Gosman 1998). For wind and tidal turbine rotor blades, this requires attached flow conditions with a uniform incident velocity profile and negligible tower interaction. The main advantage of the MRF approach is that a steady simulation can be carried out with a static mesh, leading to a dramatic reduction in total compute time (Gosman 1998). However, the MRF approach cannot

be used to accurately reproduce unsteady effects, such as blade rotation through a sheared velocity profile and blade-tower interaction. In this thesis, the MRF approach is adopted for the uniform flow computations of the 4.5m diameter wind turbine rotor in Chapter 3 and the uniform flow computations of the full-scale tidal turbine rotors in Chapter 5.

2.3.2 Sliding Mesh Approach

For the second blade resolved approach, the cells in the inner domain are physically rotated relative to the stationary outer domain by a fixed angular increment at the start of each time step. While this method is significantly more computationally demanding than the MRF approach, it does allow unsteady flow effects to be captured (Gosman 1998). The sliding mesh approach is adopted in Chapter 7 for the full-scale tidal turbine computations in sheared flow, in order to capture the unsteady blade loading as the blades rotate through the sheared velocity profile.

Chapter 3

Rotor Modelling and Methods

In this chapter, two different rotor representation techniques will be introduced for use in subsequent chapters. Their implementation and accuracy will be assessed through comparison with experimental data and with other computations carried out in the literature. The first technique resolves the geometry of the rotor blades directly, by fitting a block structured mesh around the blades. This technique will be referred to as the 'blade resolved' approach. The second technique uses the actuator line method of Sørenson & Shen (2002). In this approach, the rotor blade geometry is not resolved explicitly and is replaced by equivalent point forces, which rotate through a stationary computational domain in order to simulate the rotation of the rotor. Before carrying out the computations, the experimental data set that is used for validation will be briefly introduced and the actuator line and blade resolved techniques will be discussed in more detail.

3.1 MEXICO Experiments

In order to thoroughly validate the actuator line and blade resolved approaches, it is desirable to compare the spanwise variation of the blade loading and the near wake flow field with experimental measurements. Unfortunately, such measurements are

Figure 3.1: Photograph of the MEXICO rotor in the Large Low-speed facility (LLF) of the German-Dutch Wind Tunnels (DNW) in December 2006 (Schepers et al. 2012).

not taken in most experiments and the integrated thrust and torque are used for validation instead. In this thesis, the Model Experiments in Controlled Conditions (MEXICO) experiments were chosen to validate the actuator line and blade resolved approaches, as pressure tap measurements were taken along the blade span and could be used for validation. These measurements were taken concurrently with stereo particle image velocimetry (PIV) measurements of the near wake flow field, providing further data for validation.

The MEXICO experiments were designed with the aim of providing an extensive experimental data set that could be used to assess the accuracy of a variety of aerodynamic models. They were proposed as a successor to the Unsteady Aerodynamics Experiment (UAE) (Phase VI), which was conducted by the National Renewable Energy Laboratory (NREL) at the NASA AMES wind tunnel in the year 2000 (Hand et al. 2001). The MEXICO experiments were carried out in the open section of the Large Low-speed facility (LLF) of the German-Dutch Wind Tunnels (DNW) in December 2006 (Fig. 3.1). A large volume of data was recorded, which was subsequently analysed as an international collaborative project under IEA Task 29 Mexnext (Schep-

ers et al. 2012). The project highlighted several areas of uncertainty in the MEXICO experiments themselves, identified several inaccuracies in the aerodynamic codes and also proposed a second round of experiments to help address the uncertainties.

In June 2014, a second round of experiments were carried out on the MEXICO rotor. This new MEXICO project was carried out under the European aerospace program ESWIRP and aimed at complementing and reinforcing the original MEXICO experiments (Boorsma & Schepers 2014). At the time of this investigation, some preliminary measurements had been reported by Boorsma & Schepers (2014) and were used where available, as part of the validation exercise here.

3.1.1 Rotor Geometry

The MEXICO rotor is a 3 bladed 4.5m diameter horizontal axis wind turbine rotor with a hub diameter of approximately 0.54m. Each blade is constructed from three different aerofoil sections, with the DU91-W2-250 from 20% to 46% of the span, the RISØ-A1-21 from 54% to 66% of the span and the NACA 64-418 from 74% to 100% of the span (Schepers et al. 2012). These three blade sections are joined by proprietary transition pieces that blend the aerofoil sections together. The tip geometry extends outboard from 95% of the span towards the tip, and is swept and tapered. For the blade resolved computations, a computer aided design (CAD) file provided by the MEXICO project consortium was used to generate the mesh, such that the tip region and the transition pieces were reproduced accurately (Boorsma & Schepers 2009). However, for the actuator line computations, the aerodynamic behaviour of the transition pieces was unknown. Therefore the aerodynamic lift and drag coefficients were linearly interpolated from their neighbouring sections, following the approach of Shen et al. (2012).

The rotor was designed with the aim of maximising the chord-based Reynolds number of the outboard blade sections, while limiting the tip velocity to minimise

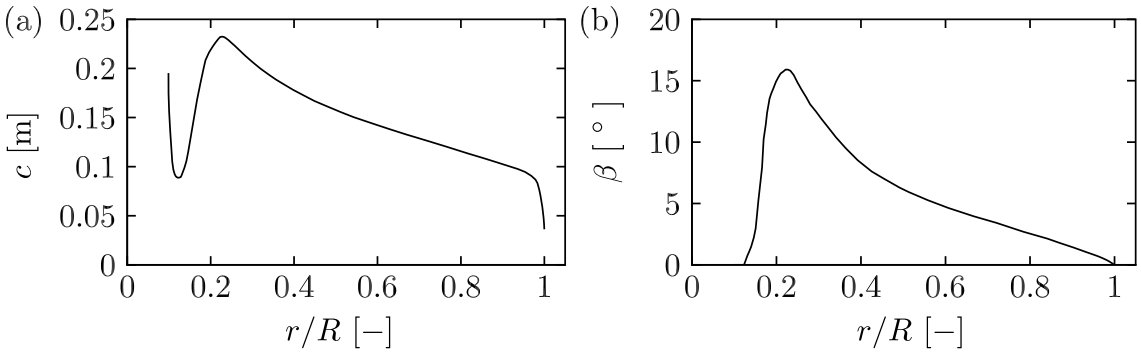

Figure 3.2: Approximate (a) chord and (b) twist distributions for the MEXICO rotor (Plaza et al. 2015).

compressibility effects (Schepers et al. 2012). As the diameter of the rotor was limited to 4.5m by the wind tunnel geometry, a rotational speed of 424.5 rpm was chosen in order to achieve a tip speed of 100.05 m/s. At 20°C room temperature (and a speed of sound of 343.2 m/s) this corresponds with a Mach number of 0.292. Schepers et al. (2012) reported negligible compressibility effects under these conditions and hence incompressible computations were deemed to be acceptable for this work.

Fig. 3.2 shows the approximate chord (c) and twist (β) distributions for the MEXICO rotor (Plaza et al. 2015). The design tip-speed-ratio of the rotor is 6.67, which is close to that of utility-scale wind turbines (typically 7-11). However, the chord-based Reynolds number along the majority of the span ($0.2 < r/R < 0.95$) is in the range of 0.4×10^6 to 0.7×10^6, so the flow is expected to be transitional near the leading edge of the blade. To mitigate the uncertainties associated with the transitional flow regime, zig-zag tape was applied on both the pressure and suction surfaces at a chordwise distance of 5% of the local chord length from the leading edge (to trip the boundary layer and force transition to turbulence). In all computations carried out here, the boundary layer was therefore assumed to be fully turbulent and the small transitional region upstream of the zig-zag tape was neglected.

3.1.2 Instrumentation and Measurements

148 Kulite pressure sensors were distributed over the pressure and suction surfaces of the blade, to measure the static pressure distribution. These sensors were clustered at 5 independent stations along the blade span (25%, 35%, 60%, 82% and 92% of the span), with 10-14 sensors at each station. These spanwise stations were specifically chosen to coincide with the well defined aerodynamic sections of the blade and avoid the transition sections. The pressure measurements were taken at a frequency of 5515Hz and then averaged over a period of 5 seconds (35 revolutions at a rotational speed of 424.5 rpm).

To carry out the PIV measurements, several overlapping PIV sheets were placed in a horizontal plane in the vicinity of the rotor, creating an extensive measurement region. As shown in Fig. 3.3, the measurement plane was located at the 9 o'clock position (when looking downstream at the rotor). The measurement area extended in the streamwise direction from $x = -2R$ upstream of the rotor to $x = 2.62R$ downstream of the rotor. In the lateral direction, the PIV sheets only covered the outboard sections of the blade and the tip region, from $y = 0.52R$ to $y = 1.2R$. In the measurement region, the instantaneous velocity field was recorded at several discrete snapshots in time, which correspond with the rotor occupying azimuthal positions of 0°, 20°, 40°, 60°, 80°, 100° and 120° (measured clockwise from top dead centre).

3.1.3 Experimental Data Set

The rotor was operated over a wide range of conditions in the experiments, in order to investigate a variety of aerodynamic effects. These conditions include: two different rotational speeds (324.5 rpm and 424.5 rpm), a range of tunnel velocities (10 m/s to 24 m/s), a range of blade pitch angles (from 5.3° towards stall to 1.7° towards feather) and a range of yaw angles (from +30° to -30°). In this investigation, only a small subset of the large volume of experimental data will be used to assess the accuracy of

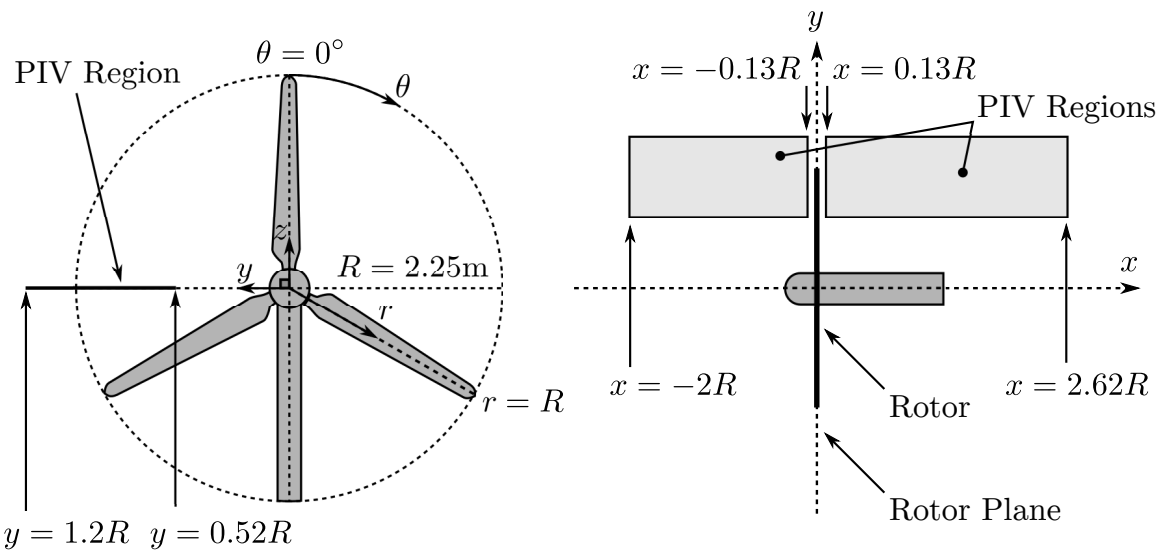

a) Front View b) Plan View

Figure 3.3: Schematic diagram showing the extent of the experimental PIV measurements from (a) the front view and (b) the plan view. The streamwise direction is in the x direction and the rotor rotates clockwise when viewed from the front. The tower diameter is 0.51m ($0.23R$) and its centreline is located 2.1m ($0.93R$) downstream of the rotor plane.

the actuator line and blade resolved computations. These conditions were primarily chosen to facilitate a direct comparison with similar computations carried out in the literature. A fixed rotational speed of 424.5 rpm was chosen, as PIV measurements were not available at 324.5 rpm. At this rotational speed, free stream tunnel velocities of 10, 15 and 24 m/s were chosen in order to achieve a wide range of tip-speed-ratios ($\lambda = 10.0, 6.67, 4.17$). For all computations, a fixed blade pitch angle of 2.3° towards stall was adopted and the rotor plane was aligned perpendicular to the incident flow direction (zero yaw angle).

3.1.4 Blockage Effects

The MEXICO rotor was placed in the open test section of the LLF between the nozzle and the collector, as shown in Fig. 3.4. As a result, the blockage provided by the rotor is difficult to precisely define, as the streamtube leaving the nozzle undergoes

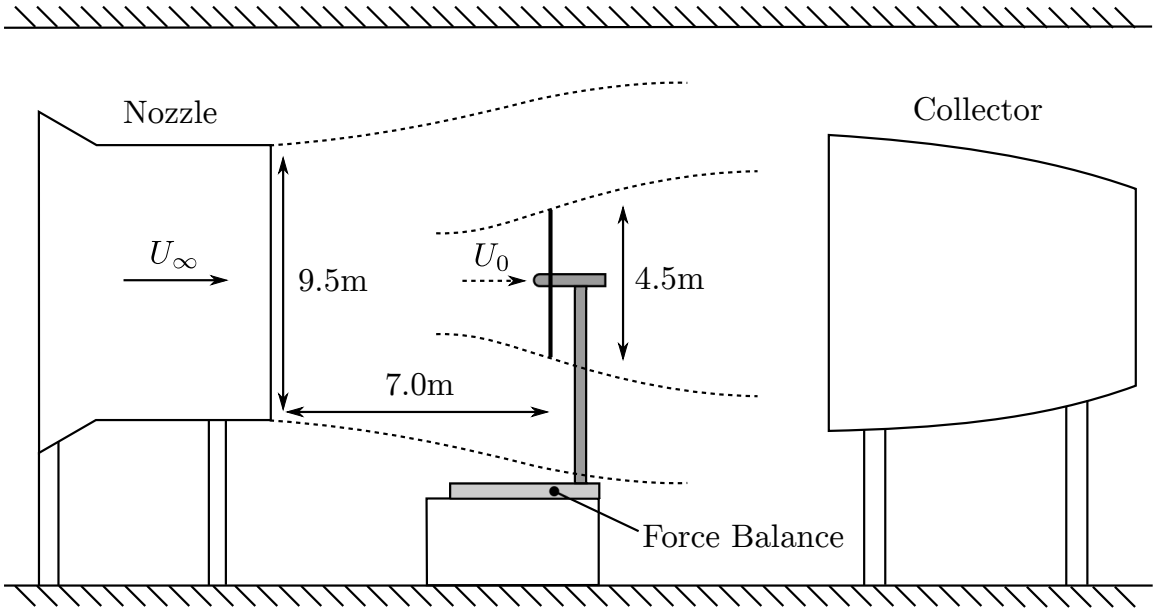

Figure 3.4: Schematic diagram of the Large Low-speed facility (LLF) of the German Dutch wind tunnels (DNW), showing the limited dimensions available for the tunnel (Schepers et al. 2012). U_∞ indicates the tunnel velocity and U_0 the axial velocity one diameter upstream of the rotor plane.

partial expansion before reaching the collector. To investigate the effect of the room geometry, Shen et al. (2012) carried out actuator line computations in a virtually unblocked domain with a blockage ratio (ratio of the rotor swept area to the cross-sectional area of the computational domain) of less than 1% and in a domain with the room geometry explicitly included. They found that the axial velocity at the rotor plane increased by a maximum of 3% when the geometry of the room was explicitly modelled. Hence, they concluded that blockage effects were insignificant and a blockage ratio of less than 1% could be assumed in future computations. In this investigation, a virtually unblocked domain (with a blockage ratio of 1%) was also adopted, to facilitate direct comparison with the blade resolved computations of Bechmann et al. (2011). To account for the neglected increase in axial velocity at the rotor plane from the room geometry, the axial velocity was normalised by the axial velocity one diameter upstream of the rotor plane (U_0 in Fig. 3.4), following Shen et al. (2012), rather than the freestream tunnel velocity (U_∞ in Fig. 3.4).

3.2 Blade Resolved Computations

This section begins by describing the meshing strategy adopted for the blade resolved computations and carrying out a mesh sensitivity study. The blade loading and the near wake flow field are then compared with the experimental measurements and the blade resolved computations of Bechmann et al. (2011).

3.2.1 Meshing Strategy

Based on the measured conditions in the LLF, the flow field approaching the rotor was assumed to be steady and uniform. This assumption allows rotational symmetry to be utilised, significantly reducing the computational cost of each simulation. Only a third of the rotor (a single blade and a section of the nacelle) was explicitly simulated and the computational domain took the form of a 120° wedge shape (as shown in Fig. 3.5), with periodic boundary conditions applied on the sides of the domain. Following Bechmann et al. (2011) and Shen et al. (2012), the support structure (0.51m diameter cylindrical tower with a spiral flange) was not included, since the tower centre is located 2.1m ($0.93R$) downstream of the rotor plane and its influence on the rotor plane flow is believed to be minimal (Herraez et al. 2012). The radius of the overall domain was set to $10R$, in order to achieve a blockage ratio of 1%.

The overall domain was subdivided into inner and outer domains, with separate block structured meshes in each region. The inner domain (with length $0.7R$ and radius $1.2R$) contained a single blade, the nose cone and a section of the nacelle, while the outer domain contained the domain boundaries and the remainder of the nacelle. This segregated meshing approach allows a refined block structured mesh to be fitted around the blade in the inner domain, without continuing the blocks through to the outer domain (which would have lead to a significant increase in the total cell count). Coupling between the two mesh regions was achieved at the non-conformal

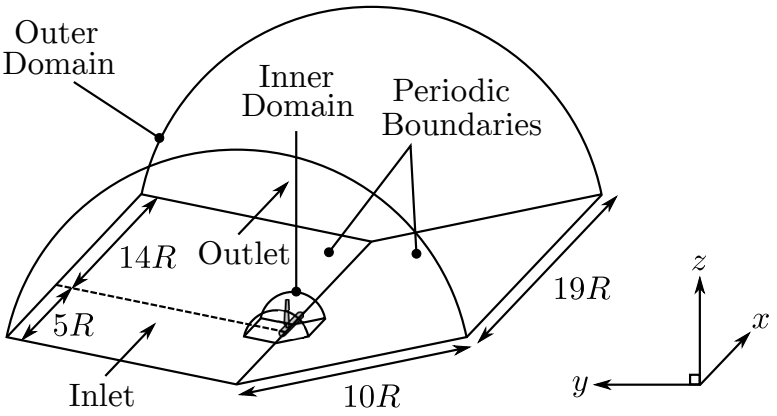

Figure 3.5: Schematic diagram of the computational domain and the coordinate system adopted for the computations, highlighting the separate inner and outer domains. The rotor rotates clockwise and the streamwise direction is in the x direction.

interface on the surface of the inner domain, with the face interpolation algorithm of Farrell & Maddison (2011) that is available in OpenFOAM.

In the inner domain, a C-C type blocking topology was fitted around the blade, as shown in Fig. 3.6. This topology was chosen to ensure high cell quality on the blade surface and to retain the rotational symmetry at the sides of the 120° wedge shaped domain, so that periodic boundary conditions can be applied. In addition, this blocking topology enables systematic control of the cells that capture the boundary layer in the wall normal, chordwise and spanwise directions. Along the blade span, several blocking slices were taken in order to capture the transition between the aerofoil sections and to increase the spanwise resolution near the root and tip. Finally, a Y block was inserted at the front of the nose cone in order to avoid generating highly distorted cells at the apex of the 120° wedge. In the outer domain, an O-grid type topology was fitted around the inner domain in order to expand the cells away from the inner domain in the radial direction.

At the domain inlet, uniform profiles of axial velocity (U_∞), turbulent kinetic energy (k) and specific dissipation rate (ω) were applied. The values chosen were based on the measured turbulence intensity of 0.48% in the LLF and an assumed length scale of 10% of the average blade chord. At the domain outlet, zero gradient

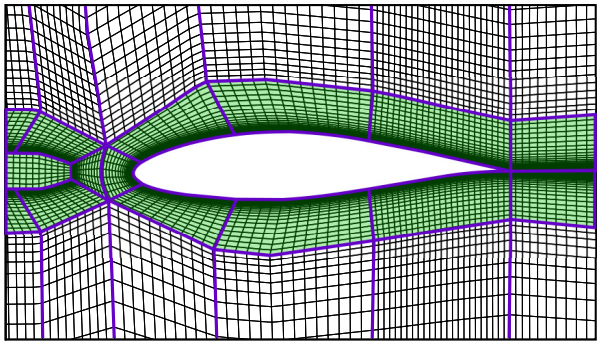

Figure 3.6: A horizontal slice through the coarse mesh of the MEXICO rotor blade (normal to the blade axis) at $r/R = 0.82$, showing the C-C type blocking topology around the NACA 64-418 aerofoil section. The blocking edges are highlighted in purple and the C-C type blocking topology is shaded in green.

boundary conditions were applied for all flow variables, except for the static pressure, which was assigned a fixed value of 0. On the outer (curved surface) of the domain, symmetry conditions were applied for all flow variables.

3.2.2 Mesh Sensitivity

An initial (coarse) mesh was generated using the blocking topology discussed in Section 3.2.1. To advise the initial distribution of cells in the chordwise and wall normal directions, some preliminary computations of the 2D NACA 64-418 aerofoil were carried out at a chord-based Reynolds number of 0.7×10^6 (which corresponds with the approximate chord-based Reynolds number of the full 3D rotor at $r/R = 0.82$ and a tip-speed-ratio of 6.67). In the spanwise direction, the initial distribution of cells was based on the distributions adopted for other wind turbines studies carried out in the literature (Sørenson & Shen 2002, Guntur & Sørensen 2015). This coarse mesh was then refined simultaneously in the chordwise, wall normal and spanwise directions to generate medium and fine meshes. Table 3.1 summarises the key parameters adopted to create these meshes, including the chordwise mesh spacing at the leading edge (LE), trailing edge (TE), the wall adjacent cell centroid height (y_0), the number of cells in the chordwise direction along the pressure and suction surfaces individually

(N_c), the growth ratio normal to the wall (G), the number of cells in the spanwise direction along the blade (N_s), the spanwise cell dimension at the blade tip (Δ_{tip}) and the total number of cells in the inner domain (N_{cells}). These meshes were simulated at tip-speed-ratios of 4.17, 6.67 and 10.0, in order to assess the sensitivity of the simulations to mesh refinement.

Table 3.1: Summary of the parameters adopted for the mesh sensitivity study, expressed in terms of the chord length $c_{0.82R} = 0.11$ m at $r/R = 0.82$.

Mesh	LE/$c_{0.82R}$	TE/$c_{0.82R}$	$y_0/c_{0.82R}$	N_c	G	N_s	$\Delta_{\text{tip}}/c_{0.82R}$	N_{cells}
Coarse	1.1e-2	9.9e-3	2.7e-4	58	1.2	130	2.0e-2	5,749,953
Medium	1.1e-2	4.5e-3	2.7e-4	78	1.1	188	1.4e-2	9,792,087
Fine	1.1e-2	2.2e-3	2.7e-4	98	1.075	210	9.9e-3	14,209,871

The wall adjacent cell centroid height (y_0) was set to ensure that the boundary layer was resolved through to the viscous sub-layer in all three meshes ($y^+ < 5$). Unfortunately, it was not possible to further reduce this wall normal distance and achieve $y^+ \sim 1$ without generating poor quality cells near the highly twisted blade root. Therefore, the cell growth ratio normal to the wall (G) was varied in the mesh sensitivity study instead, to ensure that there were sufficient cells normal to the wall to capture the boundary layer development.

Fig. 3.7 shows the static pressure coefficient (C_{pre}) in the chordwise direction, on several slices through the blade (normal to the blade axis) at the design tip-speed-ratio ($\lambda = 6.67$). The static pressure coefficient has been defined as,

$$C_{\text{pre}} = \frac{p - p_\infty}{\frac{1}{2}\rho\left(U_\infty^2 + (r\Omega)^2\right)} \tag{3.1}$$

where p is the local static pressure, p_∞ is the freestream static pressure, ρ is the density of air (1.225 kg/m^3) and Ω is the rotational speed of the rotor (424.5 rpm).

On the outboard stations ($r/R = 0.82, 0.92$), both sets of experimental measurements show good agreement with each other, leading to increased confidence in using

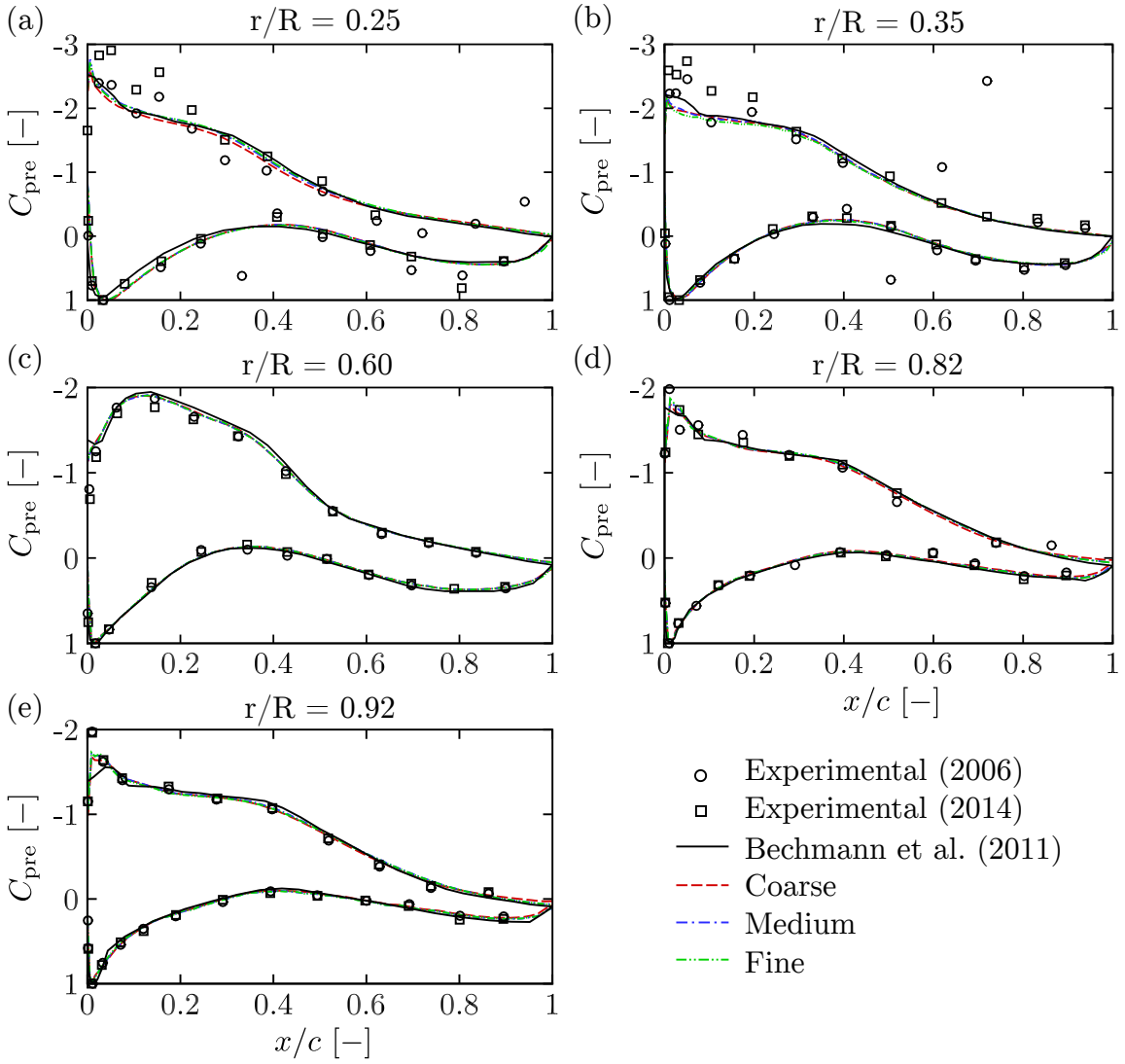

Figure 3.7: Static pressure coefficient distribution on several slices through the MEXICO rotor blade (normal to the blade axis) at a tip-speed-ratio of 6.67. 'Experimental (2006)' refers to the first round of experimental measurements presented by Schepers et al. (2012), whereas 'Experimental (2014)' refers to the second round of experimental measurements presented by Boorsma & Schepers (2014).

these measurements to assess the accuracy of the computations. However, on the inboard stations ($r/R = 0.25, 0.35$), the experimental measurements show much poorer agreement with each other, despite several faulty sensors being repaired after the first round of experiments in 2006 (Boorsma & Schepers 2014). Therefore the accuracy of the computations could not be confidently assessed on the inboard sections using the experimental measurements alone. Hence, a comparison with the computations

of Bechmann et al. (2011) was used to assess the accuracy of the blade resolved computations on the inboard sections instead.

As shown in Fig. 3.7, the coarse, medium and fine meshes show excellent agreement with each other and the computations of Bechmann et al. (2011), over all the considered spanwise stations at the design tip-speed-ratio ($\lambda = 6.67$). To provide an quantitative indication of the difference between the meshes, consider the difference in the local static pressure coefficient between the three meshes at the innermost radial station ($r/R = 0.25$). The maximum difference between the meshes at $r/R = 0.25$ is 0.12 and occurs at $x/c \approx 0.38$. Relative to the maximum suction pressure computed with the fine mesh at that radial location, the maximum difference between the meshes is only 4.8%. Elsewhere on the blade, the percentage difference between the coarse, medium and fines meshes is lower than 4.8% (noting that the maximum suction pressure varies with radial location). Therefore, the coarse mesh was deemed to have attained acceptable accuracy at this operating condition.

The coarse, medium and fines meshes also show good agreement for the high tip-speed-ratio case ($\lambda = 10.0$), as shown in Fig. 3.8. The maximum difference of 0.05 (4.2% of the maximum suction pressure computed with the fine mesh at that radial location) once again occurs at the innermost radial station ($r/R = 0.25$), near the leading edge on the suction surface ($x/c \approx 0.12$).

However, Fig. 3.9 shows that the coarse, medium and fine meshes do not show close agreement for the low tip-speed-ratio case ($\lambda = 4.17$). The region of relatively constant static pressure on the rear half on the suction surface shows that significant separation has occurred along the entire blade span and the rotor is heavily stalled. Hence, the differences between the coarse, medium and fine meshes shown in Fig. 3.9 are actually due to the steady flow solver (with the multiple reference frame approach for simulating rotation) being unable to capture the inherent unsteadiness in the separated regions (as the effective time step is too large), rather than insufficient

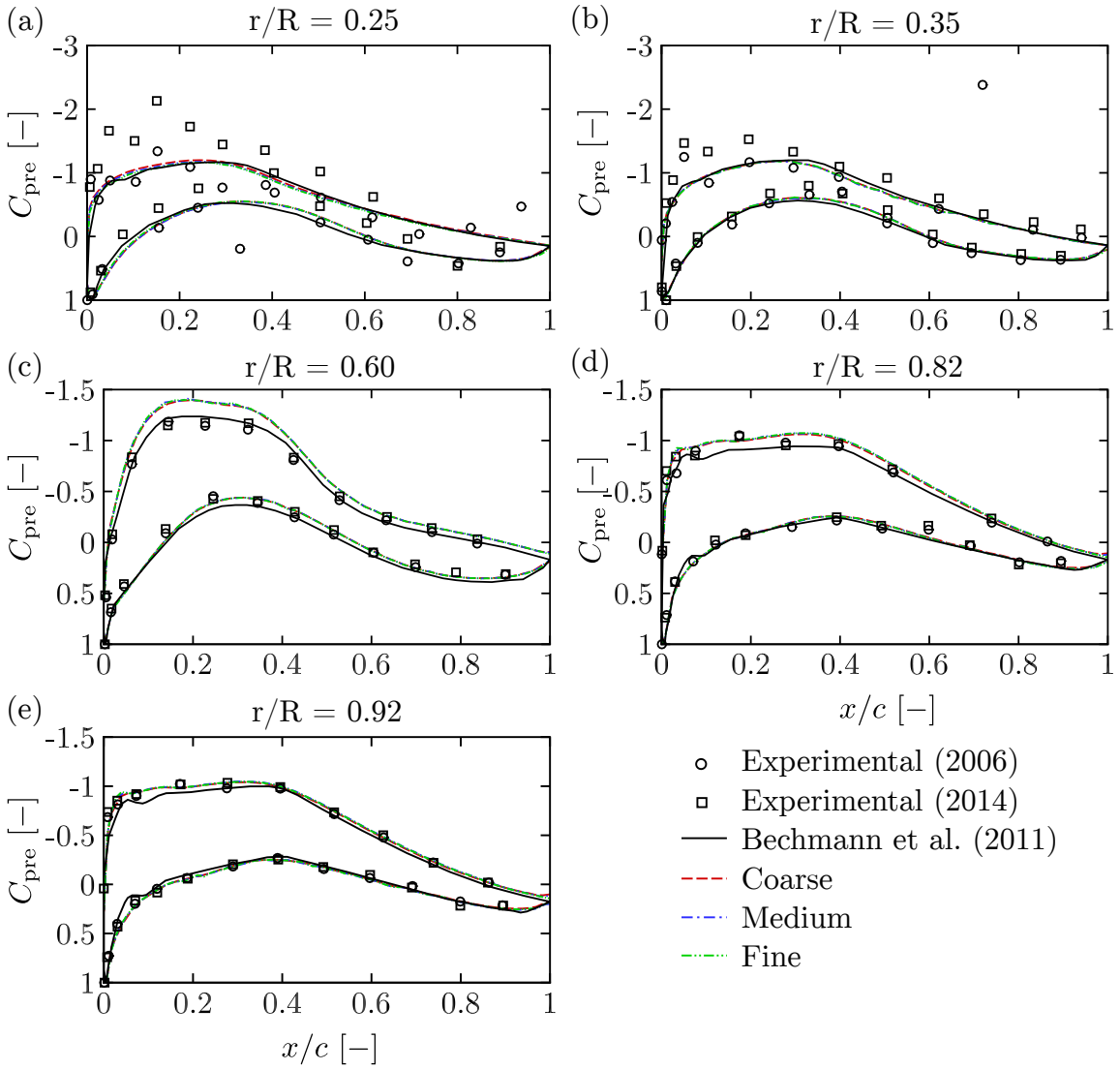

Figure 3.8: Static pressure coefficient distribution on several slices through the MEXICO rotor blade (normal to the blade axis) at a tip-speed-ratio of 10.0. 'Experimental (2006)' refers to the first round of experimental measurements presented by Schepers et al. (2012), whereas 'Experimental (2014)' refers to the second round of experimental measurements presented by Boorsma & Schepers (2014).

mesh resolution. Hence, the steady flow solver and level of spatial resolution adopted for these computations is only likely to be reliable before the onset of stall.

3.2.3 Spanwise Blade Loading

Fig. 3.10 shows the spanwise variation of the axial and tangential forces per unit span (F_{ax} and F_{ta} respectively), for comparison with the actuator line computations. The

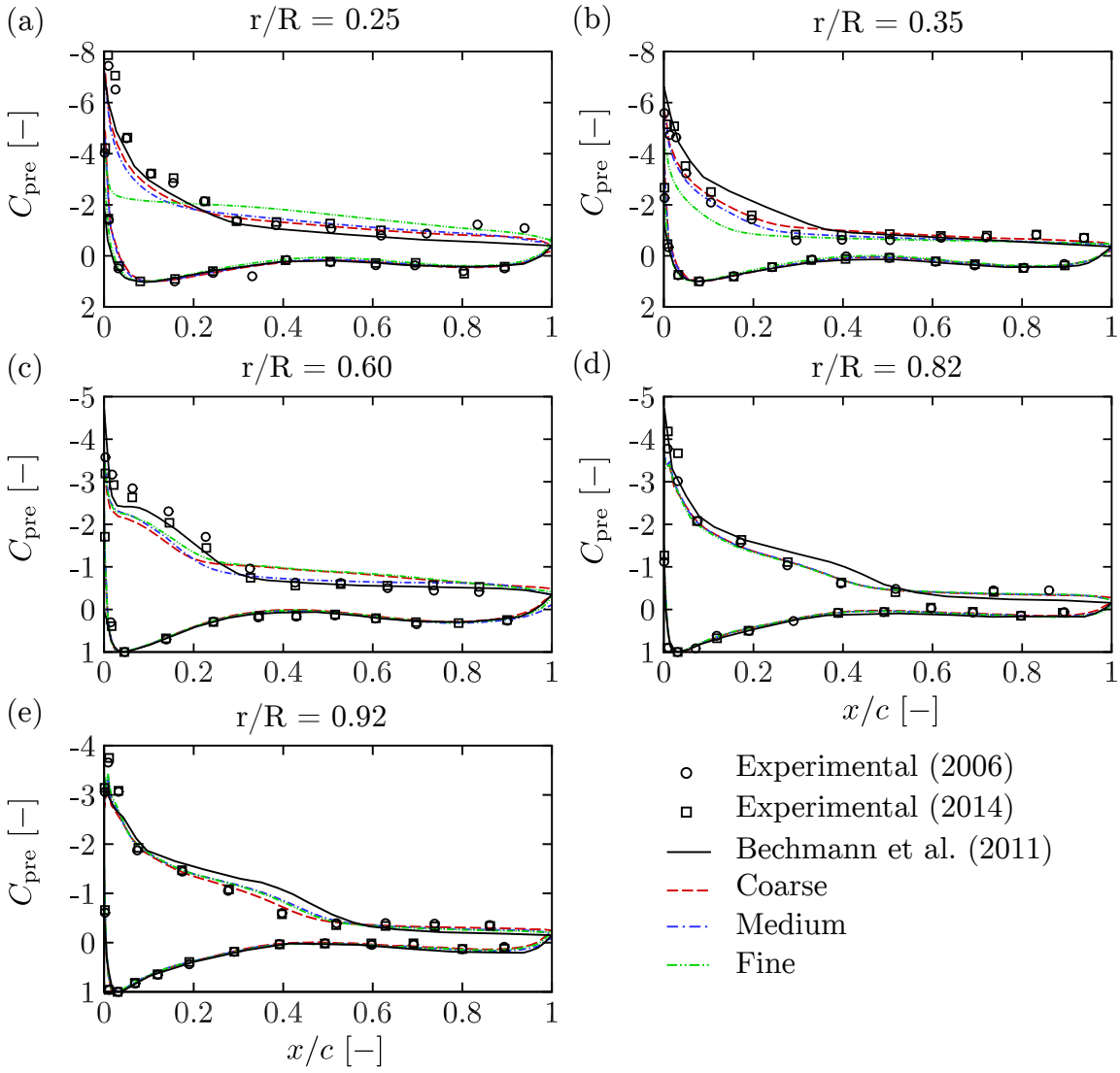

Figure 3.9: Static pressure coefficient distribution on several slices through the MEXICO rotor blade (normal to the blade axis) at a tip-speed-ratio of 4.17. 'Experimental (2006)' refers to the first round of experimental measurements presented by Schepers et al. (2012), whereas 'Experimental (2014)' refers to the second round of experimental measurements presented by Boorsma & Schepers (2014).

axial force per unit span refers to the thrust-producing force acting on each aerofoil section, whereas the tangential force per unit span refers to the torque-producing force acting on each aerofoil section.

At tip-speed-ratios of 6.67 and 10.0, the medium and fine meshes show close agreement along the entire span. The coarse mesh also shows good agreement at tip-speed-ratios of 6.67 and 10.0, with the exception of a slight under-prediction on the

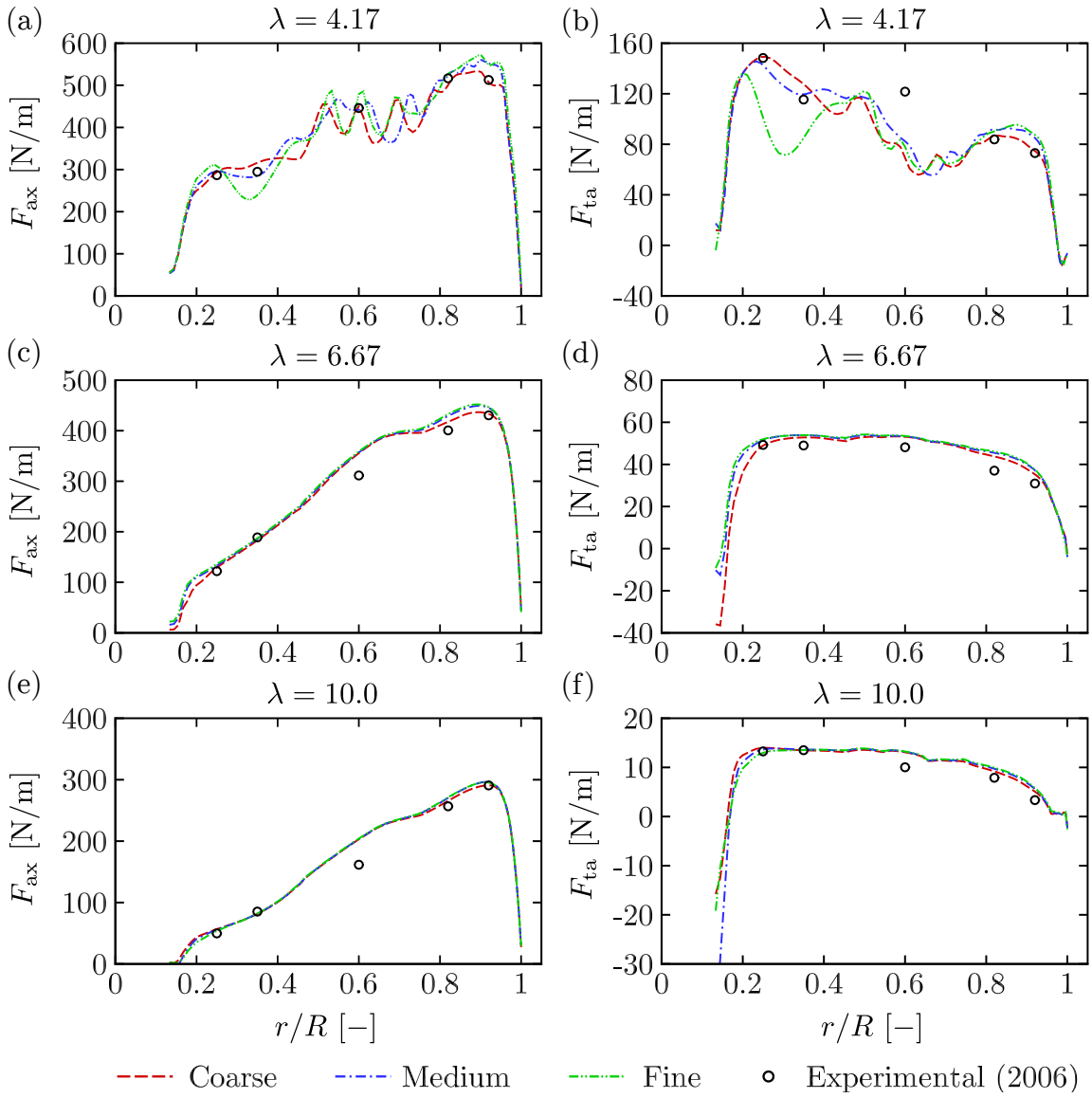

Figure 3.10: Axial and tangential forces per unit span at tip-speed-ratios of 4.17 (a and b), 6.67 (c and d) and 10.0 (e and f). 'Experimental (2006)' refers to the first round of experimental measurements presented by Schepers et al. (2012).

outboard sections ($0.8 < r/R < 0.95$). At a tip-speed-ratio of 10.0 for example, the coarse mesh under-predicts the axial force per unit span by 1.92% at $r/R = 0.9$ (when compared to the fine mesh) and the tangential force per unit span by 13.5%. Hence, the medium mesh was deemed to be sufficiently accurate for subsequent computations of the MEXICO rotor. At a tip-speed-ratio of 4.17, the meshes did not show close agreement, due to the limitations of the steady flow solver discussed previously in

Section 3.2.2.

Table 3.2 shows the rotor thrust and power coefficients (C_T and C_P respectively) which have been defined as,

$$C_T = \frac{T}{\frac{1}{2}\rho {U_\infty}^2 A} \tag{3.2}$$

$$C_P = \frac{Q\Omega}{\frac{1}{2}\rho {U_\infty}^3 A} \tag{3.3}$$

where A is the swept area of the rotor, T is the rotor thrust and Q is the rotor torque. The rotor thrust was computed by integrating the axial force per unit span along the blade span, while the rotor torque was computed by integrating the product of the tangential force per unit span and the spanwise distance (r) along the blade span. For the experimental values, Schepers et al. (2012) assumed a linear variation of the axial and tangential forces per unit span between the measurement stations (25%, 35%, 60%, 82% and 92% of the span), with a value of zero at the root and tip.

Table 3.2: Thrust and power coefficients for the MEXICO rotor (C_T and C_P respectively). The percentage differences (ΔC_T and ΔC_P) are expressed relative to the experimental values. Also shown for reference are the thrust and power coefficients computed using linear interpolation between the data points at $r/R = 0.25, 0.35, 0.6, 0.82$ and 0.92 (denoted by ${C_T}^\star$ and ${C_P}^\star$).

	λ	C_T	C_P	ΔC_T [%]	ΔC_P [%]	${C_T}^\star$	${C_P}^\star$
Experimental (2006)	6.67	0.710	0.398	-	-	-	-
Coarse	6.67	0.766	0.434	7.89	9.05	0.755	0.443
Medium	6.67	0.778	0.444	9.58	11.6	0.769	0.455
Fine	6.67	0.782	0.446	10.1	12.1	0.775	0.458
Bechmann et al. (2011)	6.67	0.802	0.456	13.0	14.6	-	-
Experimental (2006)	10.0	0.893	0.289	-	-	-	-
Coarse	10.0	1.000	0.322	12.0	11.4	0.979	0.342
Medium	10.0	1.012	0.334	13.3	15.6	0.987	0.351
Fine	10.0	1.020	0.336	14.2	16.3	0.988	0.353
Bechmann et al. (2011)	10.0	1.001	0.301	12.1	4.15	-	-

When compared with the experimental values, the computations carried out in this work and the computations carried out by Bechmann et al. (2011), all over-predict the thrust and power coefficients in the range of $10-20\%$, at both tip-speed-ratios. To help address this discrepancy, Bechmann et al. (2011) provided an additional estimate of the rotor thrust, by subtracting an estimate of the tower drag from the force balance measurement at the base of the tower (see Fig. 3.4). Unfortunately, the tower drag could only be estimated, due to the unknown axial velocity profile incident on the upper section of the tower (due to the rotor induction). Nevertheless, the rotor thrust coefficients estimated using this method (0.758 at $\lambda = 6.67$ and 0.957 at $\lambda = 10.0$) were much closer to the blade resolved computations. Furthermore, Schepers et al. (2012) showed that adopting a non-linear variation of the sectional forces between the spanwise stations resulted in an increase in the rotor thrust coefficient of up to 15% (a thrust coefficient of 0.796 at $\lambda = 6.67$ and 1.008 at $\lambda = 10.0$), which were much closer to the blade resolved values. Hence, a significant fraction of the discrepancy between the computations and the experimental values can be attributed to the integration procedure and the sparsity of the experimental pressure tap measurements.

Zhang et al. (2017) also suggested that the physical presence of the zig-zag tape on the MEXICO rotor blades, in addition to its primary function of forcing transition to turbulence, may lead to an artificial thickening of the boundary layer. The lower sectional lift coefficients and higher sectional drag coefficients induced by the increased boundary layer thickness could therefore also be a contributor to the discrepancy between the computations and experimental measurements.

Due to the uncertainties in the experimentally derived axial and tangential forces per unit span, the pressure tap measurements are a more reliable assessment of the accuracy of the computed blade loading. To complement these pressure tap measurements, an additional comparison of the near wake flow field and the experimental PIV measurements will be presented in the next section.

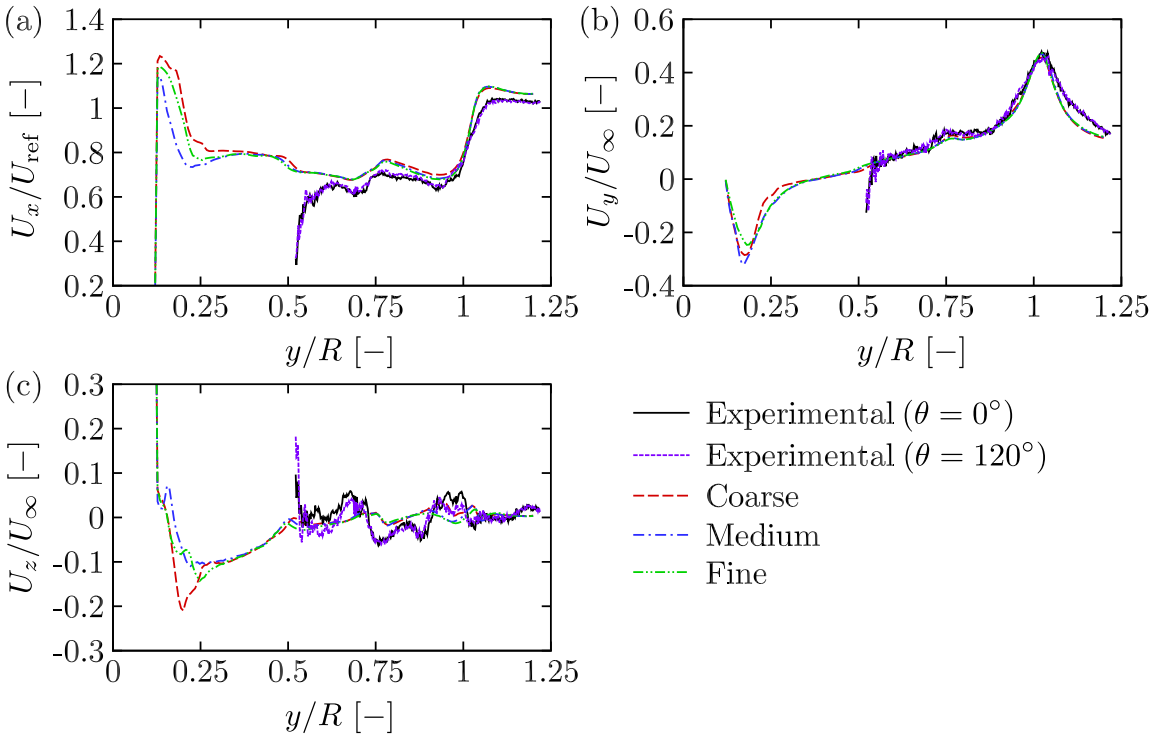

Figure 3.11: Instantaneous PIV traverse in the lateral direction $x = 0.3$m $(0.13R)$ downstream of the rotor plane for rotor azimuthal positions of 0° and 120°, at a tip-speed-ratio of 6.67. The reference velocity $U_{\text{ref}} = 14.3$ m/s for the experiments and $U_{\text{ref}} = 14.7$ m/s for the computations. The tunnel velocity $U_\infty = 15.0$ m/s. 'Experimental' refers to the first round of experimental measurements presented by Schepers et al. (2012).

3.2.4 Near Wake Flow Field

Fig. 3.11 shows the velocity components extracted along a radial traverse $x = 0.13R$ downstream of the rotor plane, for rotor azimuthal positions of 0° and 120°. These azimuthal positions were specifically chosen as an additional check of the experimental measurements, as they should be the same, due to rotational periodicity. Following the discussion in Section 3.4, the axial velocity has been normalised by a reference velocity (U_{ref}) taken one diameter upstream of the rotor plane (rather than the tunnel velocity), to account for the unknown expansion of the inlet flow leaving the nozzle.

As shown in Fig. 3.11, the coarse mesh predicts a slightly greater axial velocity on the outboard sections than the medium and fine meshes, which is consistent with the linear momentum change induced by the slightly lower axial force per unit span

(shown in Fig. 3.10). Otherwise, the coarse, medium and fine meshes show good agreement along the entire span, for all three velocity components. The discrepancies shown on the inboard region ($y/R < 0.3$) can be attributed to the unsteady root vortex, which cannot be reproduced accurately by the steady flow solver.

The experimental measurements show close agreement with each other along the entire traverse, leading to increased confidence in using these measurements to assess the accuracy of the blade resolved computations. The apparent discontinuity at $y/R = 0.52$ (which was not predicted by the blade resolved computations) has been attributed to errors in the correlation procedure at the edges of the PIV sheets by Schepers et al. (2012). Hence, the discontinuity was ignored in the comparison between the blade resolved computations and the experimental measurements.

Directly comparing the experimental measurements with the blade resolved computations reveals an inconsistency in the experimental measurements. The axial force per unit span is lower in the experiments than the blade resolved computations (see Fig. 3.10) and yet the axial velocity deficit in Fig. 3.11 is larger in the experimental measurements than in the blade resolved computations. Many of the computations presented in the final report of IEA Task 29 (Schepers et al. 2012) highlighted the same inconsistency in the experimental measurements, which provides further evidence that the experimentally derived blade forces are actually under-predicted. This discrepancy remains a significant source of uncertainty in the original MEXICO experiments and has been identified by Boorsma & Schepers (2014) as a key area to be addressed in the second round of MEXICO experiments.

Despite the uncertainties in the experimentally derived blade loading, the blade resolved computations undertaken here give good agreement with the blade resolved computations of Bechmann et al. (2011) and the experimental pressure tap measurements. Therefore, the blade resolved rotor representation technique is able to predict the performance of real horizontal axis rotors with good accuracy and will be used

for several subsequent investigations in this thesis.

3.3 Actuator Line Computations

The actuator line method was originally proposed by Sørenson & Shen (2002) to study wind turbine wake dynamics. By using a discrete blade representation, the actuator line method is able to capture the tip vortices and helical wake structure downstream of the rotor, which is not possible using azimuthally-averaged actuator disc type methods. Since its proposal, the method has been successfully applied to several laboratory-scale and utility-scale wind turbines, demonstrating reasonably accurate prediction of the blade loading and near wake structure. For example, the NREL Phase VI rotor (Schluntz & Willden 2015), the Nordtank 500 kW turbine (Sørenson & Shen 2002), the 2MW Tjæreborg turbine (Mikkelsen 2003) and the NREL 5MW virtual turbine (Martínez-Tossas et al. 2015) have all been studied using the actuator line method. Although less common, the actuator line method has also been used to study tidal turbines. Churchfield et al. (2013) and Schluntz et al. (2014) both used the actuator line method to compare different tidal turbine array layouts. The principle advantage of the actuator line method in these studies is the reduced computational cost, as the rotor blade boundary layers are not directly resolved. The reduced computational cost allows multiple rotors to be studied concurrently, which is (generally) not possible with a blade resolved approach.

3.3.1 Numerical Method

In the actuator line method, the physical rotor blades are replaced by equivalent point forces that are distributed along the blade span. The location of the point forces are often called 'collocation points' in the literature, as both the blade forces and local flow field are computed at the same location. Typically the collocation points are placed at

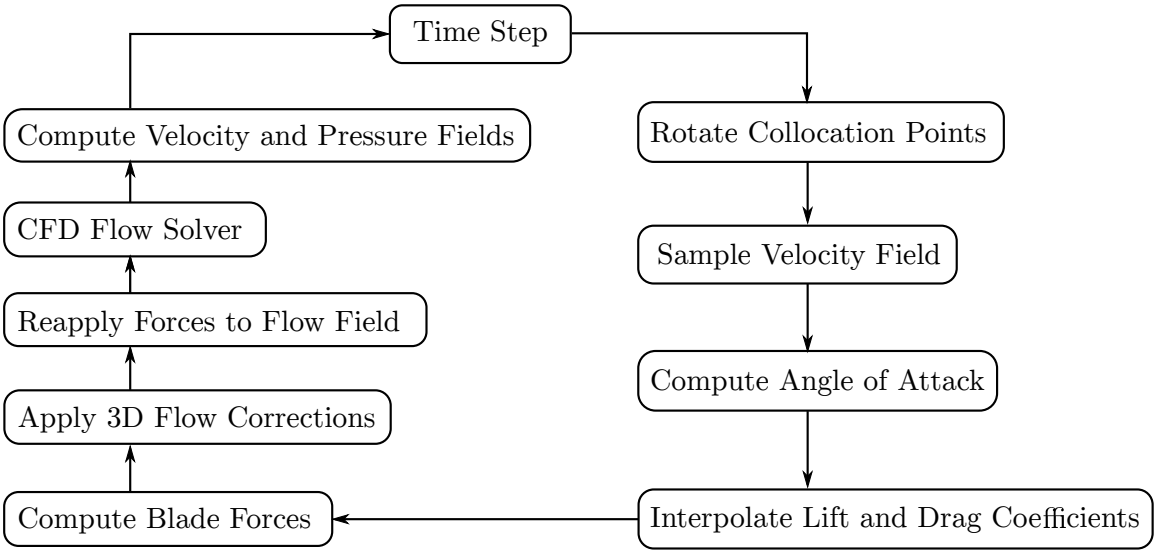

Figure 3.12: A flow chart summarising the main stages in the actuator line method.

the blade quarter chord and are clustered in the spanwise direction towards the blade root and tip. These collocation points are rotated through a static computational domain to simulate the rotation of the rotor, without resolving the physical geometry of the blade.

Fig. 3.12 shows a flow chart to summarise the key stages in the actuator line method. At the start of each time step, the collocation points are rotated about the rotor apex by a fixed angular increment, to update the location of the virtual blades. The velocity field is then extracted from the CFD solver and interrogated to determine the local velocity vector at the new location of each collocation point. From the local velocity vector, the angle of attack (α) and relative velocity magnitude (U_{rel}) are computed using the blade element diagram shown in Fig. 3.13. Having computed the angle of attack, the lift and drag coefficients (C_L and C_D respectively) are interpolated from a set of tabulated aerodynamic data (a 2D aerofoil polar) that is specific to each aerofoil section along the blade span. The tabulated aerodynamic data is computed beforehand in a separate set of 2D computations or experiments, thus avoiding the need to resolve the rotor blade itself in the actuator line computations.

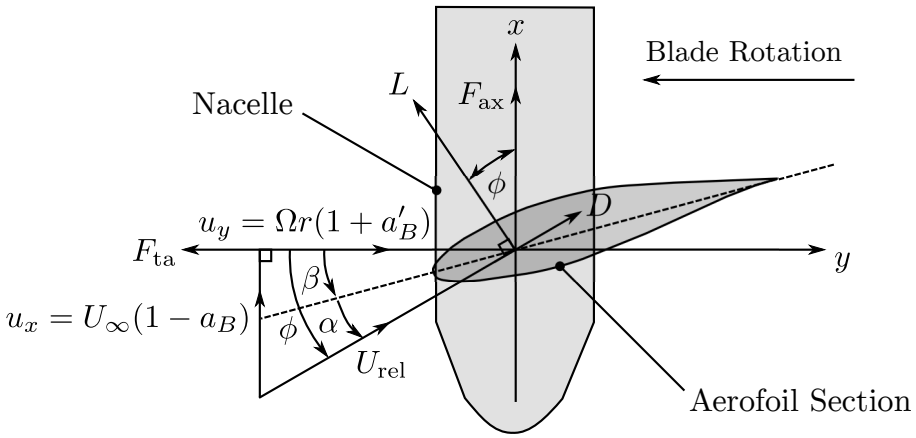

Figure 3.13: Blade element diagram for an aerofoil section at a spanwise distance r along the blade. ϕ represents the angle of the incident flow vector relative to the rotor plane, β the sum of the local twist angle and the blade pitch angle, a_B the axial induction factor and a'_B the swirl induction factor.

Once the lift and drag coefficients have been computed, the lift and drag forces per unit span (L and D) can be computed at each collocation point using equations 3.4 and 3.5 (where c is the local chord length).

$$L = C_L \left(\frac{1}{2} \rho {U_{\text{rel}}}^2 c \right) \tag{3.4}$$

$$D = C_D \left(\frac{1}{2} \rho {U_{\text{rel}}}^2 c \right) \tag{3.5}$$

Having computed the lift and drag forces per unit span, the sectional force vector at each collocation point ($\boldsymbol{F}_{\text{blade}}$) can be assembled from the scalar lift and drag forces per unit span and the unit vectors in the direction of the lift ($\boldsymbol{e}_L$) and drag ($\boldsymbol{e}_D$) forces.

$$\boldsymbol{F}_{\text{blade}} = L\boldsymbol{e}_L + D\boldsymbol{e}_D \tag{3.6}$$

The sectional force vector is mapped back to the flow field and returned to the CFD flow solver. To complete the time step, the RANS equations are solved by the CFD flow solver using the updated sectional force vector to yield the new velocity field. In the next time step, the collocation points are rotated to their new location and the process is repeated until the flow field and the blade forces are both sufficiently

converged.

To compute the total thrust and torque acting on the rotor, the lift and drag forces per unit span are first resolved in the streamwise direction and the direction of blade rotation to compute the axial and tangential forces per unit span (F_{ax} and F_{ta} respectively).

$$F_{\text{ax}} = L\cos(\phi) + D\sin(\phi) \tag{3.7}$$

$$F_{\text{ta}} = L\sin(\phi) - D\cos(\phi) \tag{3.8}$$

The axial force per unit span can then be integrated along the span to compute the blade thrust, while the product of the tangential force per unit span and the spanwise distance r can then be integrated along the span to compute the blade torque.

The accuracy of the actuator line method is dependant on 2 main stages in the algorithm: the method used to reapply the forces to the flow field and the three-dimensional flow corrections that are applied to the blade forces. These aspects of the actuator line method will now be discussed in more detail to motivate the work that follows.

3.3.2 Blade Load Smearing

Applying the blade forces at discrete points in the computational domain (the collocation points) results in steep velocity gradients, which may lead to numerical instabilities. To mitigate these instabilities, Sørenson & Shen (2002) used a Gaussian distribution (η) to smear the blade forces over multiple cells.

$$\eta = \frac{1}{\epsilon^3 \pi^{3/2}} \exp\left(\frac{-\zeta^2}{\epsilon^2}\right) \tag{3.9}$$

ζ represents the distance between the collocation point and the cell centroid and ϵ is a numerical parameter that controls the width of the Gaussian distribution.

The total force vector applied to the fluid ($\boldsymbol{F}$) is subsequently calculated from the convolution of the blade force vector ($\boldsymbol{F}_{\text{blade}}$) and the Gaussian distribution (η),

$$\boldsymbol{F} = \sum_{i=0}^{N} \int_{0}^{R} \boldsymbol{F}_{\text{blade}} \eta(|\boldsymbol{x} - r\boldsymbol{e}_i|) \mathrm{d}r \tag{3.10}$$

where N is the number of blades and $\boldsymbol{e}_i$ is the unit vector in the spanwise direction along blade i.

Mathematically, the convolution operation ensures that when the force is smeared, the total force applied to the fluid is consistent with the discrete force representation. However, due to the discretised finite volume formulation of the RANS equations, several authors have reported that the accuracy of the computed blade loading is dependant on ϵ.

Martínez-Tossas et al. (2015) showed that when ϵ is decreased, the same total body force is applied over a smaller volume of cells, which increases the force per unit volume applied to each cell. Hence, the angle of attack and relative velocity magnitude are reduced at each collocation point, which reduces the lift and drag forces per unit span acting on the blade. Furthermore, if either ϵ is too small or the local cell size is too large, then the volume force will be applied to a single cell, leading to the same discontinuity that smearing the forces aims to avoid.

In early investigations carried out in the literature, ϵ was often selected as an integer multiple of the characteristic local cell size Δ_{grid} (cube root of the cell volume or cell dimension in the streamwise direction) in order to mitigate the numerical oscillations that arise when the blade forces are smeared over an insufficient number of cells. Table 3.3 summarises the ranges of ϵ that have been investigated in the literature and the minimum values recommended to avoid excessive numerical oscillations.

Shives & Crawford (2013) and Jha et al. (2013) suggested that ϵ should be based on the region of space that represents the physical rotor blade instead, rather than the local cell size. The mesh should then be carefully constructed with a sufficiently small

Table 3.3: Summary of the range of ϵ investigated by several independent studies in the literature and the minimum values recommended to maintain numerical stability.

Author	Turbine	Range	Minimum
Mikkelsen (2003)	Tjæreborg 2MW	1-4 Δ_{grid}	-
Troldborg (2009)	Tjæreborg 2MW	1.5-3 Δ_{grid}	1.5 Δ_{grid}
Ivanell et al. (2009)	Tjæreborg 2MW	1-3 Δ_{grid}	1 Δ_{grid}
Shen et al. (2012)	MEXICO 25kW	2-3 Δ_{grid}	-
Churchfield et al. (2013)	Proprietary 550kW	2 Δ_{grid}	2 Δ_{grid}
Martínez-Tossas et al. (2015)	NREL 5MW Virtual	1-10 Δ_{grid}	2 Δ_{grid}

cell size to achieve a stable computation for this value of ϵ. However, no universal consensus has been reached for how ϵ should be specified or the distribution that should be adopted along the blade. In this chapter, the significance of ϵ will be quantified in Section 3.3.8, by comparing several uniform distributions of ϵ.

3.3.3 Three-dimensional Flow Corrections

The blade element aspect of the actuator line method is based on the flow independence principle, as the forces acting on each blade section are computed using only the flow components in the plane of the aerofoil section (neglecting the spanwise flow component). This assumption often leads to acceptable accuracy along the mid-span of the blade. However, near the blade root and on the outboard sections near the blade tip, three-dimensional flow effects become increasingly significant and the blade loading is often not accurately predicted by blade element based methods. To account for these inaccuracies, three-dimensional flow corrections are often applied. In this section, the main classes of three-dimensional flow correction will be briefly introduced, to motivate the computations that follow.

3.3.3.1 Rotational Augmentation and Stall Delay

Experimental measurements from as early as 1945 have shown that the inboard sections of rotating blades experience stall at a greater angle of attack than non-rotating 2D aerofoil sections (Himmelskamp 1945). Such observations have also been made in several recent blade resolved computations (Shen & Sørensen 1999, Sørensen et al. 2002, Guntur & Sørensen 2015). Snel & Van Holten (1994) proposed a physical explanation for these observations. Under strongly retarded flow conditions (such as separated flow), a significant spanwise flow component develops on the suction surface near the blade root, due to centrifugal forcing. This spanwise flow component results in a Coriolis force in the chordwise direction, which acts as a favourable pressure gradient. Hence, the separation point is shifted in the chordwise direction towards the trailing edge and the onset of stall is delayed to higher angles of attack. In addition, the displacement thickness of the separated region is reduced, leading to higher lift coefficients. This phenomena is often referred to as 'rotational augmentation', resulting in 'stall delay' in the literature.

Several semi-empirical corrections have been proposed to account for the effect of rotational augmentation. The majority of these models were developed by computing solutions to simplifications of the integral boundary layer equations for a rotating blade (Snel & Van Holten 1994, Du & Selig 1998). While a general consensus exists for the increase in the maximum lift coefficient due to rotational augmentation, the behaviour of the drag coefficient is less clear. For example, the models of Snel & Van Holten (1994) and Lindenburg (2004) do not modify the drag coefficient at all, whereas the model of Du & Selig (1998) predicts a decrease in drag coefficient and the model of Chaviaropoulos & Hansen (2000) predicts an increase.

For the actuator line computations in this investigation, a rotational augmentation correction is not included. This is because the computations are all undertaken before the onset of stall and therefore the effect of rotational augmentation on the lift and

drag coefficients on the blade inboard sections is likely to be small.

3.3.3.2 Finite Number of Blades

When carrying out a steady flow analysis of horizontal axis rotors, some computational methods (such as the blade element momentum method) azimuthally-average the momentum equations to reduce the computational cost of the simulations. The azimuthally-averaged momentum equations can be solved to yield the azimuthally-averaged axial and swirl velocities that balance the applied thrust and torque. These azimuthally-averaged velocities are conventionally expressed as azimuthally-averaged axial and swirl induction factors ($\bar{a}$ and $\bar{a'}$ respectively) at the rotor plane. However, the blade element method (that is often coupled to the momentum equations to compute the blade forces) requires the axial and swirl induction factors that are local to the blade section (a_B and a'_B) and not the azimuthal-averages. Hence, a correction factor (F) is required to compute the local values from the azimuthal averages.

$$F = \frac{\overline{a}}{a_B} = \frac{\overline{a'}}{a'_B} \tag{3.11}$$

For a theoretical rotor with an infinite number of blades $F = 1$, as the azimuthal-average and the local induction factors are identical. However, physical observations of real rotors (with a finite number of blades) suggest that the induction in the vicinity of the blades should be greater than between the blades. In general F should therefore be less than or equal to 1. However, the exact behaviour of F remains unknown for real rotors. Prandtl (in an appendix to the dissertation of Betz (1919)) proposed an approximation for F, by modelling the wake downstream of the rotor by a series of vertical impermeable material sheets,

$$F = \frac{2}{\pi} \cos^{-1} \left[\exp \left(-\frac{N}{2} \left(1 - \frac{\lambda_r}{\lambda} \right) \sqrt{1 + \lambda^2} \right) \right] \tag{3.12}$$

where $\lambda_r = \omega r / U_\infty$ is the local speed ratio and N is the number of blades. Glauert (1935) proposed a simplified version of Prandtl's correction factor, in order to facilitate its inclusion in blade element momentum codes.

$$F = \frac{2}{\pi} \cos^{-1} \left[\exp \left(-\frac{N(R-r)}{2r \sin(\phi)} \right) \right] \tag{3.13}$$

For the actuator line computations carried out in this work, a finite blade correction factor (F) is not required. This is because the induction factors that are computed from the sampled flow field (a_B and a'_B) are already local to the blade section.

3.3.3.3 Tip Flow Effects

On the outboard sections of horizontal axis rotor blades (that are not enclosed in a duct or shroud), vorticity is shed into the wake. The shed vorticity induces a downwash at the rotor plane and spanwise flow accelerations on the pressure and suction surfaces of the blade (inboard on the suction surface and outboard on the pressure surface). The induced downwash and the spanwise flow accelerations modify the static pressure distribution on the surface of the blade, so that the blade loading drops off as the tip of the blade is approached. Unfortunately, the blade element method does not directly account for these tip flow effects, as the spanwise flow component is neglected and the induced downwash is not accounted for. Hence, a correction is required to account for these neglected tip flow effects. Without a tip flow correction, the axial and tangential forces per unit span are often over-predicted, resulting in a significant over-prediction of the rotor thrust and torque due to the large moment arm of the outboard blade sections.

Two main methods have been adopted in the literature to account for tip flow effects on the outboard blade sections. Either the 2D lift and drag polars are corrected directly, or the sectional blade forces are corrected before they are applied to the flow

field. Table 3.4 summarises the main tip flow correction factors (denoted by F_1) that have been proposed in the literature, along with the variable (either sectional forces or lift and drag coefficients) that they are applied to. In this chapter, the correction factor of Shen et al. (2005) will be adopted, to allow direct comparison with the actuator line computations of Shen et al. (2012). However, in Chapter 4, both the method of correcting the lift and drag polars and the method of correcting the sectional forces will be considered, and an assessment of their accuracy will be carried out. In addition, the tip loss mechanism itself will be examined in more detail, so that more accurate tip flow corrections may be proposed in future that better capture the tip flow physics.

Table 3.4: Summary of the tip flow correction factors (F_1) that have been proposed in the literature and the quantities that they are applied to. AR is the blade aspect ratio, $C_{L,\text{inv}}$ is the 2D inviscid lift coefficient and $C_{L,2D}$ is the 2D viscous lift coefficient for that aerofoil section.

Author	F_1	Application
Lindenburg (2003)	$1 - \left(\frac{\Omega r}{U_{\text{rel}}}\right)^2 \exp\left[-2\text{AR}\left(\frac{C_{L,\text{inv}} - C_{L,2D}}{C_{L,\text{inv}}}\right)\right]$	C_L
Shen et al. (2005)	$\frac{2}{\pi}\cos^{-1}\left[\exp\left(-g_1\frac{N(R-r)}{2r\sin(\phi)}\right)\right]$ $g_1 = \exp\left(-0.125(N\lambda - 21.0)\right) + 0.1$	$F_{\text{ax}},\ F_{\text{ta}}$
Sant (2007)	$\frac{2}{\pi}\cos^{-1}\left[\exp\left(-18\frac{1-r/R}{r/R}\right)\right]$	$C_L,\ C_D$

3.3.4 Lift and Drag Polars

Fig. 3.14 shows the lift and drag polars for the DU91-W2-250, RISØ-A1-21 and NACA 64-418 aerofoils that were used for the actuator line computations of the MEXICO rotor in this chapter. These polars were derived from experimental measurements that were carried out as part of the MEXICO project and were chosen in

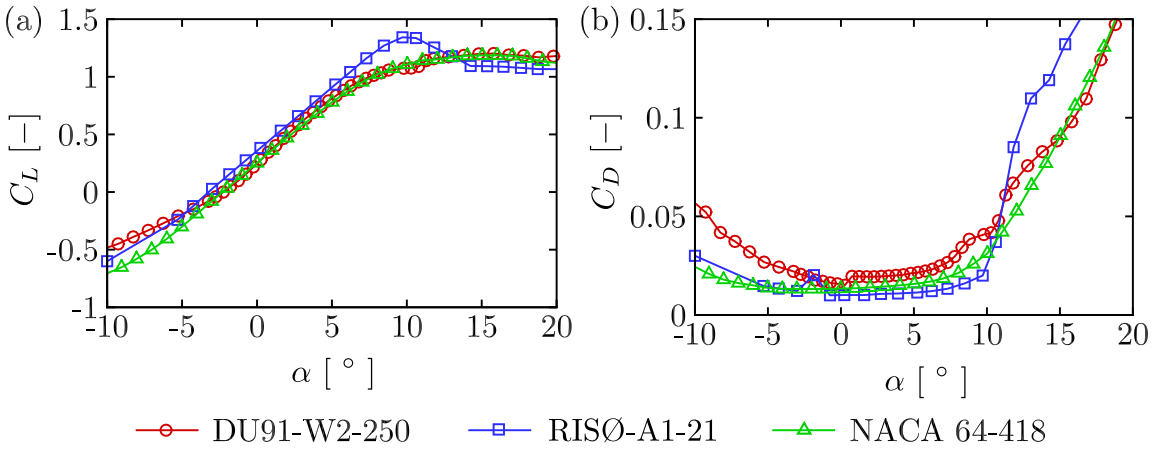

Figure 3.14: Experimental (a) lift and (b) drag polars for the DU91-W2-250, RISØ-A1-21 and NACA 64-418 aerofoils, at chord based Reynolds numbers of 0.5×10^6, 1.6×10^6 and 0.7×10^6 respectively. The data points have been extracted from Boorsma & Schepers (2014).

preference to computationally derived polars, to facilitate a direct comparison with the actuator line computations of Shen et al. (2012) (who also adopted the experimentally derived polars). In the experiments, zig-zag tape was applied at a distance of 5% of the chord length from the leading edge on both the pressure and suction surfaces of all three aerofoils (forcing premature transition to turbulence), to be consistent with the complete MEXICO rotor (which also used zig-zag tape).

3.3.5 Actuator Line Code

The actuator line code used in this investigation was originally developed by Hunter et al. (2014) as a shared object library that was incorporated into OpenFOAM through the `fvOptions` framework. This code was subsequently modified by the author to add the capability for variable Gaussian smearing and three-dimensional flow corrections. The actuator line code uses the vortex equivalence approach of Schluntz & Willden (2014) to sample the flow field and compute the relative velocity magnitude (U_{rel}) and angle of attack (α) at each collocation point. In the vortex equivalence approach, the flow field around collocation point m is modelled as the superposition of a uniform

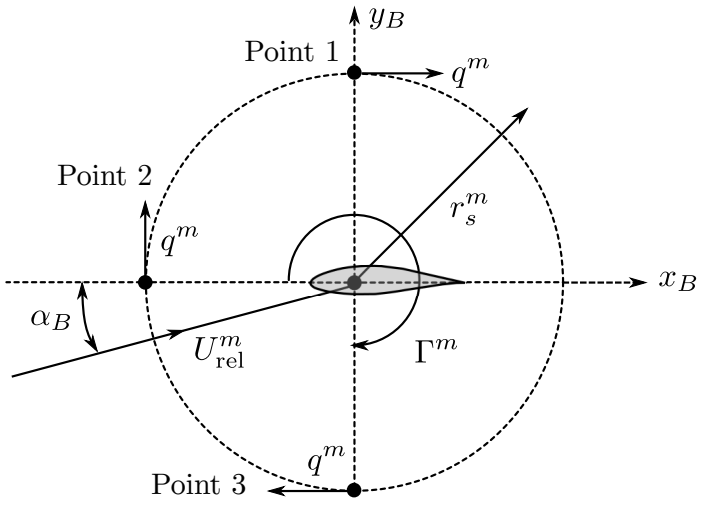

Figure 3.15: Diagram of the local coordinate system and the location of the sampling points around collocation point m, in the vortex equivalence approach. The x_B axis is parallel with the local chord line and the y_B axis is perpendicular to the local chord line. The origin is taken at the collocation point, which is positioned at the aerofoil quarter chord ($x/c = 0.25$).

free stream U_{rel}^m and a point vortex with circulation strength Γ^m, as shown in Fig. 3.15. Three sampling points are then selected on a circle of radius r_s^m around the collocation point, outside the region of the local flow field distortions. Schluntz & Willden (2014) determined a distance of one chord length to be sufficiently far from the collocation point to minimise the local flow field distortions.

The point vortex (with circulation strength Γ^m) induces a velocity perturbation q^m at each of the sampling points.

$$q^m = \frac{\Gamma^m}{2\pi r_s^m} \tag{3.14}$$

At each of the sampling points, the local velocity vector ($\boldsymbol{U}_B = (U_B, V_B, W_B)$) is interpolated from the surrounding cell centroids (which are outside the region of the local flow field distortions). Three equations with three unknowns can then be written for the angle of attack α^m, relative velocity magnitude U_{rel}^m and perturbation velocity q^m.

$$U^m_{B,1} = U^m_{\text{rel}} \cos(\alpha_m) + q^m \tag{3.15}$$

$$V^m_{B,2} = U^m_{\text{rel}} \sin(\alpha_m) + q^m \tag{3.16}$$

$$U^m_{B,3} = U^m_{\text{rel}} \cos(\alpha_m) - q^m \tag{3.17}$$

The subscripts 1, 2, 3 in equations 3.15, 3.16 and 3.17 refer to the sampling point locations in Fig. 3.15. Schluntz & Willden (2014) subsequently showed that the system of equations has the following solution for the perturbation velocity, relative velocity magnitude and angle of attack.

$$q^m = \frac{1}{2}\left(U^m_{B,1} - U^m_{B,3}\right) \tag{3.18}$$

$$U^m_{\text{rel}} = \sqrt{\left(V^m_{B,2} - \frac{1}{2}\left[U^m_{B,1} - U^m_{B,3}\right]\right)^2 + \left(\frac{1}{2}\left[U^m_{B,1} + U^m_{B,3}\right]\right)^2} \tag{3.19}$$

$$\alpha^m = \sin^{-1}\left(\frac{V^m_{B,2} - \frac{1}{2}\left[U^m_{B,1} - U^m_{B,3}\right]}{U^m_{\text{rel}}}\right) \tag{3.20}$$

3.3.6 Time Stepping

The actuator lines were rotated by a fixed angular increment of 0.4° each time step, with 10 iterations of the SIMPLE algorithm within each time step. These parameters were determined from a convergence study of the integrated blade loading. 22 rotor revolutions were found to be sufficient to achieve steady state convergence of the integrated blade loading and near wake flow field.

3.3.7 Meshing Strategy

The shape of the computational domain was constructed to be as consistent as possible with the blade resolved computations of the MEXICO rotor, with the exception that the full 360° cylindrical domain was modelled, rather than a 120° wedge shaped section. A block structured mesh was fitted around the nacelle, with an O-grid type

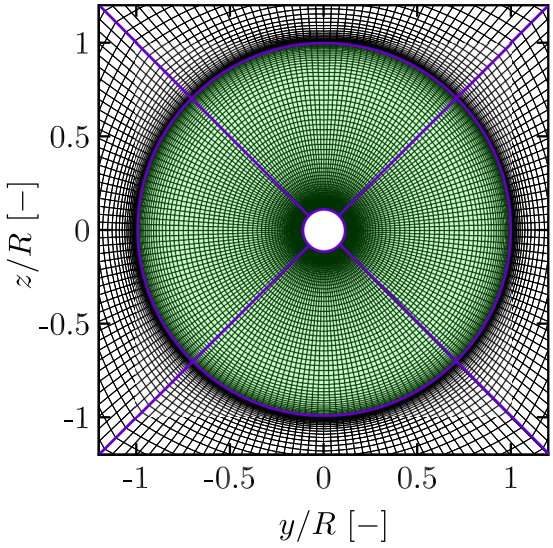

Figure 3.16: A slice through the coarse mesh (normal to the incident flow direction) at the rotor plane ($x = 0$), showing the O grid type blocking topology around the central nacelle. The blocking edges are highlighted in purple and the cells that make up the rotor swept area are shaded in green.

topology, as shown in Fig. 3.16. This topology facilitates independent control of the mesh resolution in the axial, radial and circumferential directions.

An initial (coarse) mesh was generated with a similar level of resolution to the actuator line computations carried out by Shen et al. (2012). This mesh was then simultaneously refined in the axial, radial and circumferential directions to generate medium and fine meshes. Table 3.5 shows a summary of the parameters adopted for the coarse, medium and fine meshes. Δx represents the streamwise cell dimension at the rotor plane, N_x the number of cells in the axial direction in the rotor vicinity ($-R < x < 3R$), N_r the number of cells along the blade span, N_θ the number of cells along the circumference of the O-grid and N_{cells} the total number of cells in the computational domain. The thrust and power coefficients (C_T and C_P respectively) computed at a tip speed ratio of 6.67, are also shown in Table 3.5 for reference.

A mesh sensitivity study was carried out using these three meshes, to identify an appropriate level of resolution for subsequent computations. For this study, ϵ was assigned a value of 0.101m along the entire span (0.75 times the average blade chord),

Table 3.5: Summary of the parameters adopted for the mesh sensitivity study. Percentage differences in the thrust and power coefficients (ΔC_T and ΔC_P respectively) have been expressed relative to the fine mesh.

Mesh	Δx	N_x	N_r	N_θ	N_{cells}	C_T	C_P	ΔC_T [%]	ΔC_P [%]
Coarse	$R/30$	120	69	198	3,006,960	0.7791	0.4816	-0.05	-0.27
Medium	$R/40$	160	89	248	6,112,696	0.7792	0.4821	-0.04	-0.17
Fine	$R/50$	200	109	312	11,270,480	0.7795	0.4829	-	-

for all three meshes. This value was chosen based on an independent investigation of the effect of ϵ, which will be presented in section 3.3.8.

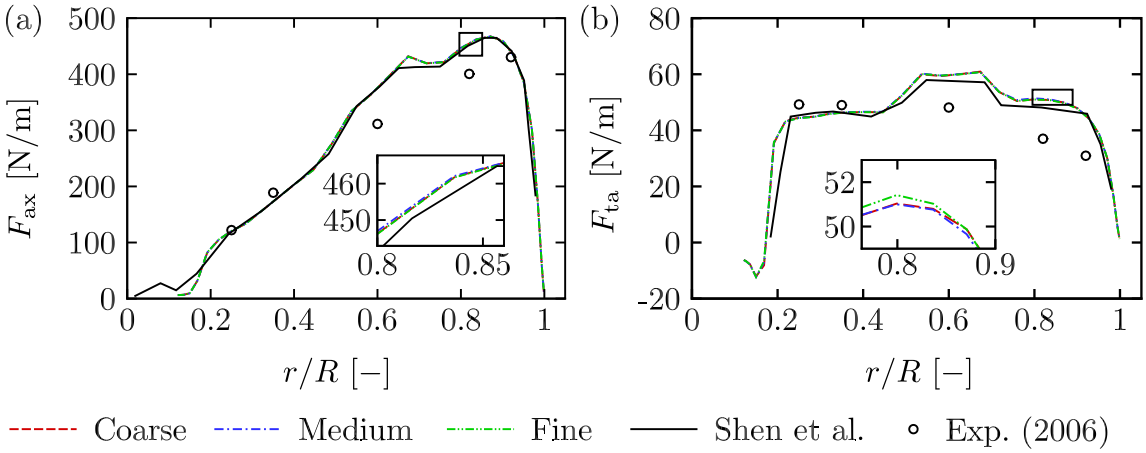

Figure 3.17: Axial (a) and tangential (b) forces per unit span at a tip speed ratio of 6.67. 'Exp. (2006)' refers to the first round of experimental measurements presented by Schepers et al. (2012).

Fig. 3.17 shows the axial and tangential forces per unit span, computed with the three meshes at a tip speed ratio of 6.67. At $r/R = 0.8$, the axial force per unit span computed with the coarse mesh was within 0.831 N/m (0.19%) of the fine mesh and the tangential force per unit span was within 0.42 N/m (0.82%) of the fine mesh. Furthermore, the thrust coefficient computed with the coarse mesh was within 0.05% of the fine mesh and the power coefficient was within 0.27%. Based on these observations, the coarse mesh was deemed to be sufficiently well converged (in terms of the blade loading) and was adopted for the remaining computations.

3.3.8 Blade Load Smearing

The effect of ϵ on the axial and tangential forces per unit span was investigated by carrying a series of actuator line computations with a range of uniform distributions of ϵ (where ϵ is constant along the blade span). Table 3.6 shows a summary of the values of ϵ that were investigated, in terms of both the local cell size (Δ_{grid}) and the average chord length (c_{avg}). The values of ϵ were chosen to cover the approximate range of values adopted by other investigations in the literature.

Table 3.6: A summary of the uniform distributions of ϵ that were investigated, expressed in terms of the average blade chord $c_{\text{avg}} = 0.1343$m and the characteristic cell dimension $\Delta_{\text{grid}} = \Delta x = R/30 = 0.075$m at the rotor plane. The percentage differences have been expressed relative to $\epsilon = 1.0c_{\text{avg}}$.

Distribution	ϵ/c_{avg}	$\epsilon/\Delta_{\text{grid}}$	C_T	C_P	ΔC_T [%]	ΔC_P [%]
Uniform	0.50	1.12	0.7751	0.4694	-0.60	-3.08
Uniform	0.75	1.34	0.7791	0.4816	-0.09	-0.56
Uniform	1.00	1.79	0.7798	0.4843	-	-
Uniform	1.25	2.24	0.7796	0.4846	-0.03	0.06
Uniform	1.50	2.69	0.7792	0.4854	-0.08	0.23

In addition to the uniform distributions, two non-uniform distributions of ϵ were also investigated. ϵ was related to the local chord length in the first distribution and the local lift coefficient in the second distribution. However, when compared with the uniform distributions presented here, these non-uniform distributions did not lead to a significant improvement in the accuracy of the computed blade loading. Hence they are not described in this thesis. The interested reader is referred to Wimshurst & Willden (2016*b*) instead, where the non-uniform distributions are presented.

As shown in Table 3.6, the thrust and power coefficients drop off sharply when adopting the smallest value of ϵ (which corresponds with the narrowest Gaussian distribution). This sharp reduction arises because the effect of reducing ϵ is to apply the same total body force over a smaller volume of cells, which increases the force

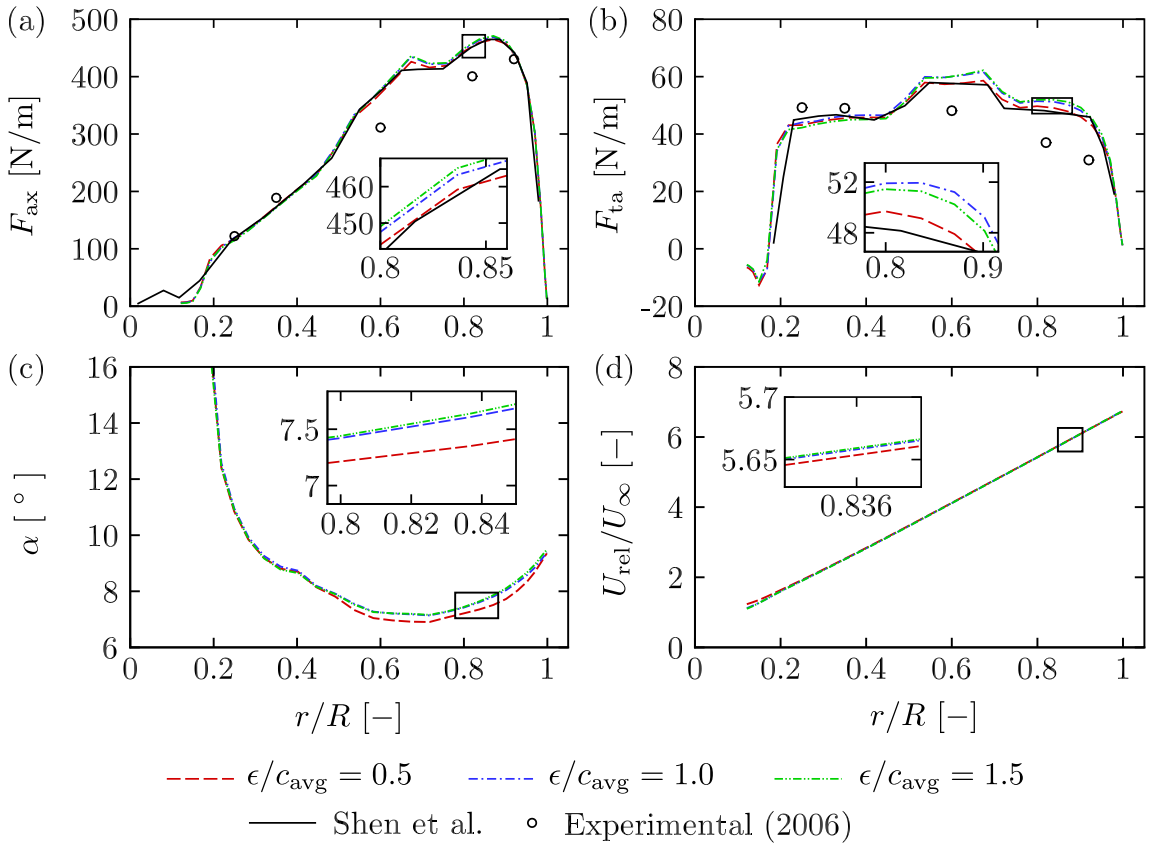

Figure 3.18: (a) Axial force per unit span, (b) tangential force per unit span, (c) angle of attack and (d) relative velocity magnitude, for the coarse mesh at a tip speed ratio of 6.67, for different uniform distributions of ϵ. The computed results for $\epsilon/c_{avg} = 0.75$ and $\epsilon/c_{avg} = 1.25$, have been omitted for clarity. 'Experimental (2006)' refers to the first round of experimental measurements presented by Schepers et al. (2012).

per unit volume applied to the cells. With increasing force per unit volume, the local velocity and angle of attack reduce at each collocation point, which leads to lower lift and drag forces per unit span acting on the blades. This reduction in lift and drag forces per unit span is manifested as a reduction in both the axial and tangential forces per unit span, as shown in Fig. 3.18.

For the wider Gaussian distributions ($\epsilon = 1.0c_{avg}, 1.25c_{avg}, 1.5c_{avg}$), Table 3.6 shows that the thrust and power coefficients are in close agreement, with differences of $\sim 0.1\%$. Hence, the rotor thrust and power coefficients are relatively unaffected by the value chosen for ϵ, as long as ϵ is sufficiently large (in this case greater than $\epsilon = 0.75c_{avg}$). Furthermore, as the undesirable numerical oscillations reduce as ϵ is

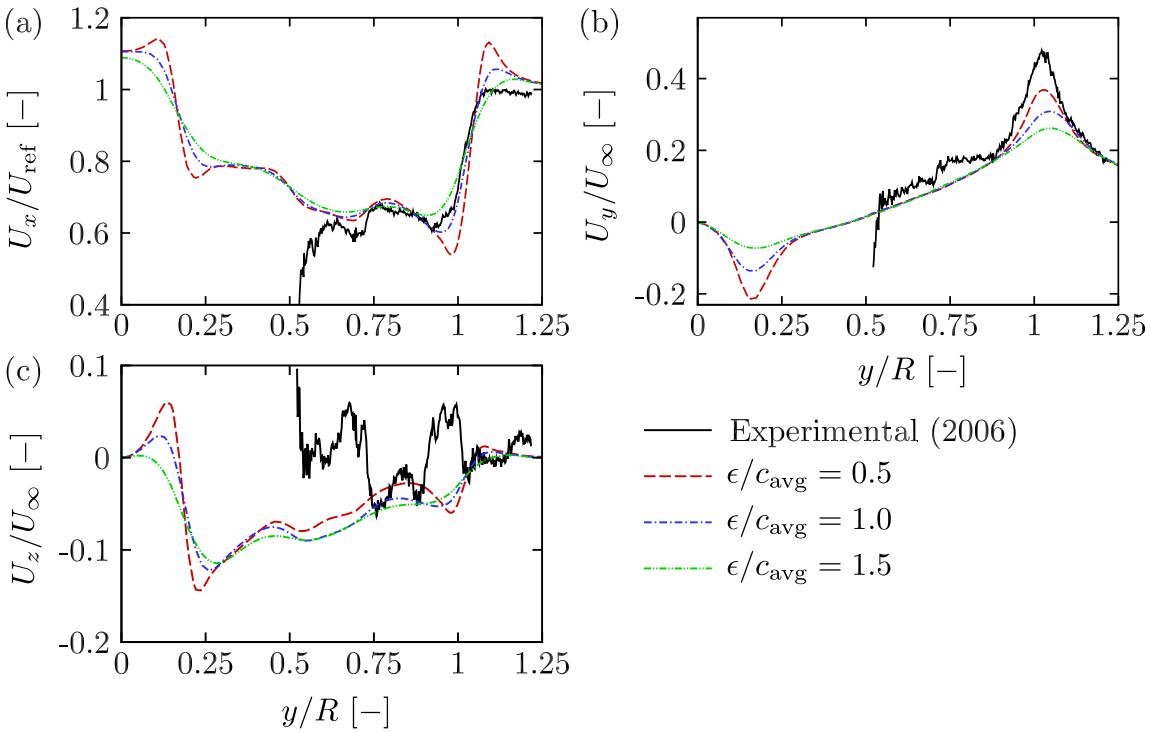

Figure 3.19: Instantaneous PIV traverse in the lateral direction $x = 0.13R$ downstream of the rotor plane for a rotor azimuthal positions of 0°, at a tip speed ratio of 6.67. The reference velocity $U_{\text{ref}} = 14.3$ m/s for the experiments and 14.7 m/s for the computations. The tunnel velocity $U_\infty = 15.0$ m/s. 'Experimental (2006)' refers to the first round of experimental measurements presented by Schepers et al. (2012).

increased, a wider Gaussian distribution would appear to always be preferable. However, as shown in Fig. 3.19, the strength of the root and tip vortices reduce as the width of the Gaussian distribution is increased, because the body force is smeared over more cells. Hence, a compromise is required between the accuracy of the blade loading and the resolution of the near wake structure. For the coarse mesh adopted in this study, a medium width distribution with $\epsilon = 0.75c_{\text{avg}}$ was deemed to be a good compromise.

3.4 A Comparison of Rotor Models

Fig. 3.20 shows a comparison of the axial and tangential forces per unit span computed with the actuator line and blade resolved approaches, at a tip speed ratio of

6.67. The blade resolved computations should be interpreted as the target solution here (rather than the experimental measurements), due to the previously discussed uncertainties in the experimentally derived axial and tangential forces per unit span (see section 3.2.4). On the inboard region of the blade ($r/R < 0.4$), the actuator line computations under-predict both the axial and tangential forces per unit span. As will be shown in the next chapter, this can be partly attributed to an under-prediction of the angle of attack by the vortex equivalence method (the method used to sample the flow field).

Along the mid-span of the blade ($0.5 < r/R < 0.65$), the actuator line computations over-predict both the axial and tangential forces per unit span. This can be partly attributed to the lift and drag polars that were used for the RISØ-A1-21 aerofoil in the actuator line computations, as the chord-based Reynolds number of the 2D aerofoil experiments (1.6×10^6) was far higher than that experienced by the mid-span of the MEXICO rotor blade ($\sim 0.5 \times 10^6$). With a higher chord-based Reynolds number, the boundary layer thickness is reduced, leading to greater lift coefficients and lower drag coefficients, as shown in Fig. 3.21. By adopting 2D computational polars at a more appropriate chord-based Reynolds number of 0.5×10^6, a slight improvement in the axial and tangential forces per unit span was obtained, as shown in Fig. 3.20. Shen et al. (2012) also concluded that the experimentally derived polars for the RISØ-A1-21 aerofoil were inappropriate for the MEXICO rotor computations and reported a similar improvement in the axial and tangential forces per unit span by adopting modified polars.

On the outboard regions of the blade ($r/R > 0.8$), the actuator line computations considerably over-predict the tangential force per unit span. This over-prediction arises because tip flow effects are not adequately accounted for by the tip flow correction factor of Shen et al. (2005) in these computations. In Chapter 4, the flow around the tip of the blade will examined in more detail and be used to propose a

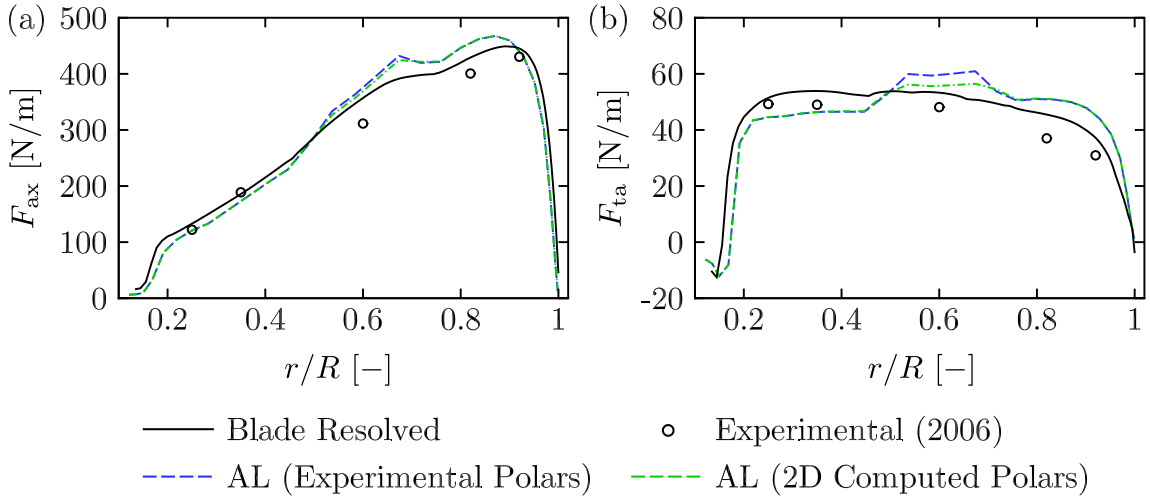

Figure 3.20: (a) Axial and (b) tangential forces per unit span computed with the actuator line and blade resolved approaches at a tip speed ratio of 6.67. For the blade resolved computations, the medium mesh is shown, whereas for the actuator line computations, the coarse mesh is shown, with a constant distribution of $\epsilon = 0.75c_{\text{avg}}$. The experimental polars for the RISØ-A1-21 were taken at $Re_c = 1.6 \times 10^6$, while the 2D computed polars for the RISØ-A1-21 were taken at $Re_c = 0.5 \times 10^6$. 'Experimental (2006)' refers to the first round of experimental measurements presented by Schepers et al. (2012).

more accurate tip flow correction for the MEXICO rotor computations.

3.5 Summary

Actuator line and blade resolved rotor representation techniques have been validated against experimental measurements of the MEXICO rotor. The blade resolved computations show excellent agreement both with the experimental measurements and with similar blade resolved computations performed by Bechmann et al. (2011), leading to increased confidence in the accuracy of this rotor representation technique. The actuator line computations show excellent agreement with similar actuator line computations carried out by Shen et al. (2012), leading to increased confidence in the implementation of this technique. However, the actuator line computations did not show comprehensive agreement with the blade resolved computations along the entire blade span. This discrepancy has been attributed to a combination of the lift and

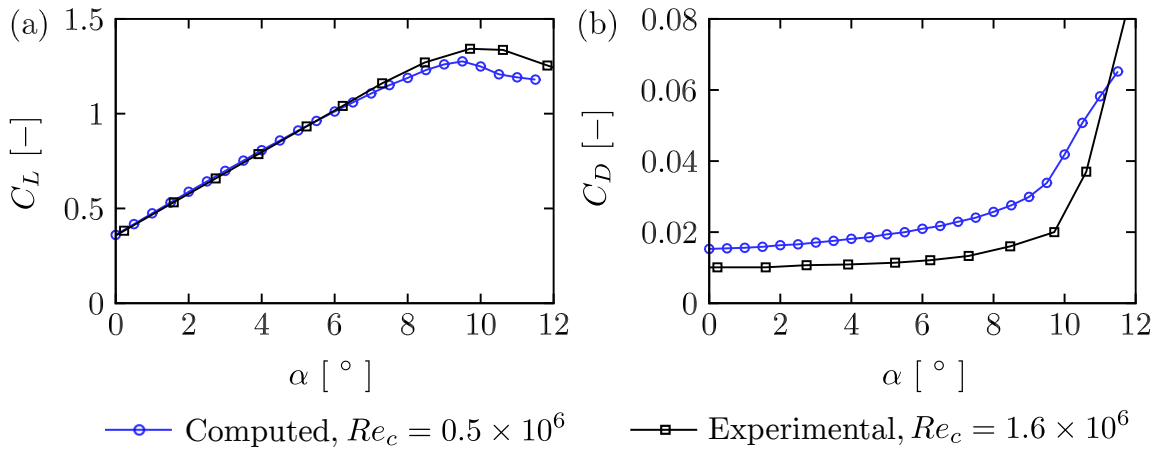

Figure 3.21: A comparison of computed and experimentally derived lift and drag coefficients for the RISØ-A1-21 aerofoil at chord based Reynolds numbers of 0.5×10^6 and 1.6×10^6 respectively.

drag polars that were used along the mid-span of the blade and the tip flow correction that was adopted on the outboard region of the blade. The effect of the (artificial) blade load smearing was also investigated and found to have relatively little effect on the accuracy of the computed blade loading in comparison with the aerofoil polars and the tip flow correction.

A few areas of uncertainty in the experimental measurements were also identified in this chapter. These same uncertainties have also been highlighted by the MEXICO project consortium as key areas to be addressed in the second round of MEXICO experiments (Boorsma & Schepers 2014). The main uncertainty was an apparent under-prediction of the sectional blade loading, which may be partially attributed to the chordwise and spanwise integration of the pressure tap measurements and partly to the effect of the zig-zag tape.

Chapter 4

Tip Flow Corrections for Horizontal Axis Rotors

The blade loading on the outboard sections of horizontal axis rotors (that are not enclosed within a duct or shroud) drops off as the tip is approached. Reduced order rotor models (such as the blade element momentum and actuator line methods) cannot accurately predict this drop off in their original formulation, as the blade loading acting on each aerofoil section is computed using only the flow components in the plane of the aerofoil section, and the spanwise flow component (normal to the aerofoil section) is neglected. Along the mid-span of the blade this is a reasonable approximation. However, on the outboard sections of the rotor blade, the spanwise flow component is significant and is a critical component of the tip loss mechanism. Hence, reduced order rotor models require a correction to account for the effect of the neglected spanwise flow component, so that the blade loading can drop off as the tip is approached. However, the mechanism that causes the blade loading to drop off is not well understood and a general consensus has not yet been reached for how the reduced order rotor models should be corrected. Furthermore, the accuracy of the adopted correction is of paramount importance, since the outboard blade sections

are the dominant contributors to the total rotor thrust and torque. Hence, there is a need for improved understanding of the mechanism that causes the blade loading to drop off as the tip is approached, so that better informed tip flow corrections can be developed.

In this chapter, blade resolved simulations of the MEXICO rotor (introduced in Chapter 3) and Rotor 2 (the high solidity tidal rotor introduced in Chapter 5) will be used to directly observe the tip loss mechanism. Following these observations, two different methods that can be used to correct the blade loading for tip flow effects will then be presented and evaluated. In the first method, the lift and drag polars (that are used as a sub-grid model to compute the blade forces) are corrected directly. In the second method, the lift and drag polars are left uncorrected, while the sectional blade forces are modified directly using a correction factor. To complete the chapter, both of these methods will be applied to actuator line computations of the MEXICO rotor, so that the results can be compared and contrasted.

4.1 The Tip Loss Mechanism

Moving outboard from the root section of a rotor blade towards the tip, the static pressure difference between the pressure and suction surfaces generally increases (assuming only modest blade taper), due to the increased dynamic pressure that is incident on the blade. This might imply that the greatest static pressure difference (and hence the maximum blade loading) occurs at the very tip of the blade. However, at the very tip of the blade, the static pressure must equalise between the pressure and suction surfaces. As a result, an additional static pressure gradient is generated in the spanwise direction on the outboard blade sections. This static pressure gradient causes the static pressure to increase on the suction surface as the tip of the blade is approached (an adverse pressure gradient) and decrease on the pressure surface as the

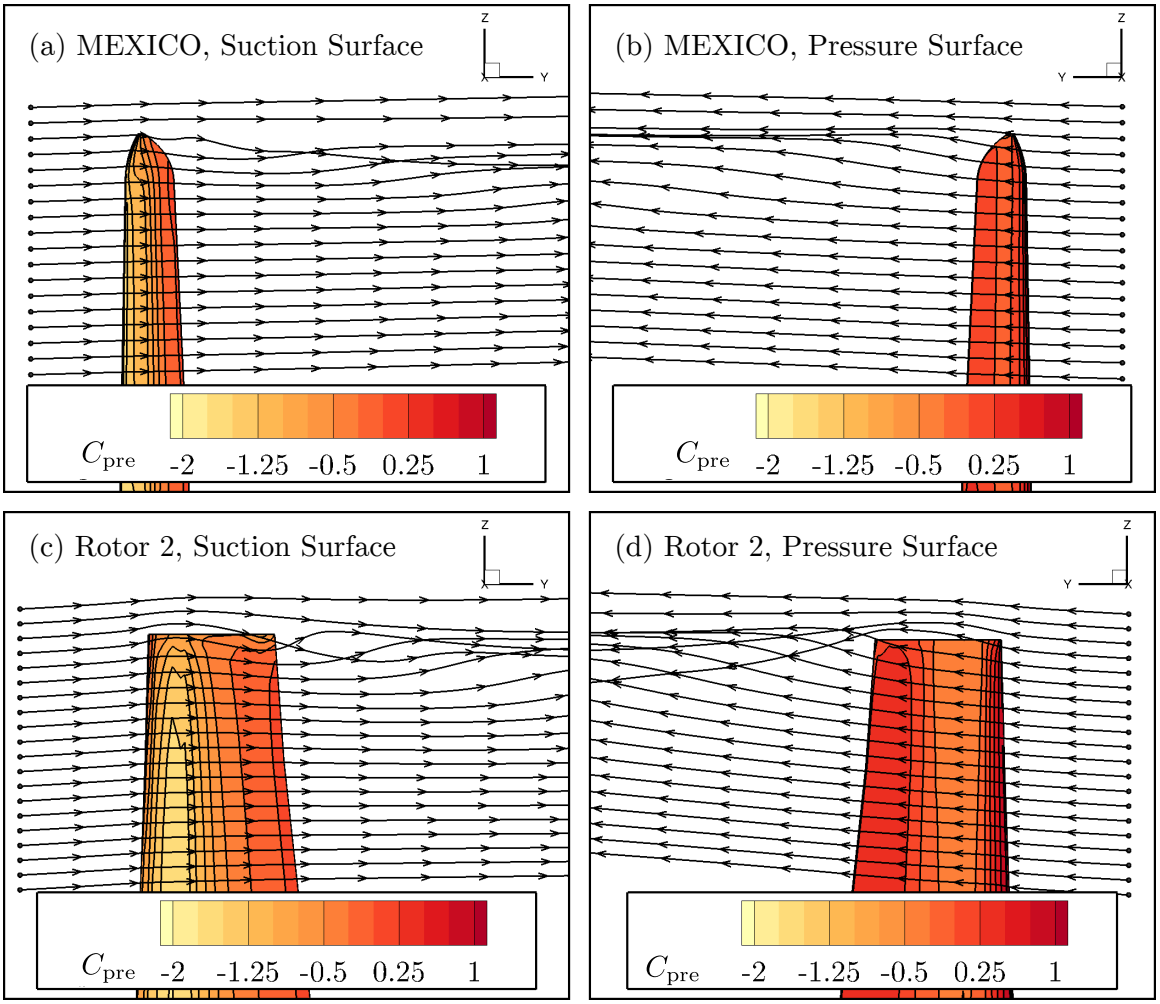

Figure 4.1: Contours of static pressure coefficient (C_{pre}) on the outboard sections of the MEXICO rotor (a and b) and Rotor 2 (c and d). The streamlines were released $R/10$ upstream of the rotor blade, in the plane of rotor rotation.

tip of the blade is approached (a favourable pressure gradient). Hence, the maximum static pressure difference between the pressure and suction surfaces actually occurs slightly inboard from the tip of the blade and the blade loading drops off as the tip is approached.

These static pressure changes can be observed qualitatively in Fig. 4.1, which shows contours of static pressure coefficient (C_{pre}) on the pressure and suction surfaces of the MEXICO rotor and Rotor 2 (the high solidity tidal rotor). In Fig. 4.1, the

static pressure coefficient has been defined as,

$$C_{\text{pre}} = \frac{p - p_\infty}{\frac{1}{2}\rho\left[U_\infty^2 + (\Omega r)^2\right]} \tag{4.1}$$

where p is the static pressure, p_∞ is the freestream static pressure, ρ is the fluid density, r is the spanwise distance from the axis of rotation, U_∞ is the freestream velocity and Ω is the rotational speed of the rotor.

As shown in Fig. 4.1, the favourable pressure gradient on the pressure surface causes the incident flow to accelerate in the spanwise direction (defining positive spanwise flow acceleration as increasing spanwise flow velocity towards the tip), driving the flow outboard and bending the streamlines towards the tip. Conversely, the adverse pressure gradient on the suction surface causes the incident flow to decelerate in the spanwise direction (the spanwise flow velocity decreases as the tip is approached), driving the flow inboard and bending the streamlines away from the tip. Hence, a rotational flow component is generated around the tip of the blade, driving the fluid outboard on the pressure surface, around the tip and inboard on the suction surface. This rotational flow component is convected downstream of the blade into the wake as shed vorticity.

Conceptually, the shed vorticity has two main effects on the blade loading developed at the rotor plane. These effects are shown schematically in Fig. 4.2. Firstly, the shed vorticity induces a downwash at the rotor plane, which reduces the angle of attack on the outboard blade sections. The reduced angle of attack then reduces the sectional lift and drag coefficients developed by the outboard blade sections, by modifying the static pressure distribution. Unfortunately, is not straightforward to extract the induced downwash directly from the local velocity field because it is not possible to accurately determine the axial and swirl induction factors local to the blade section. Hence, the induced downwash will be identified indirectly in Section 4.1.1 instead, by observing the changes in the static pressure distribution on the blade

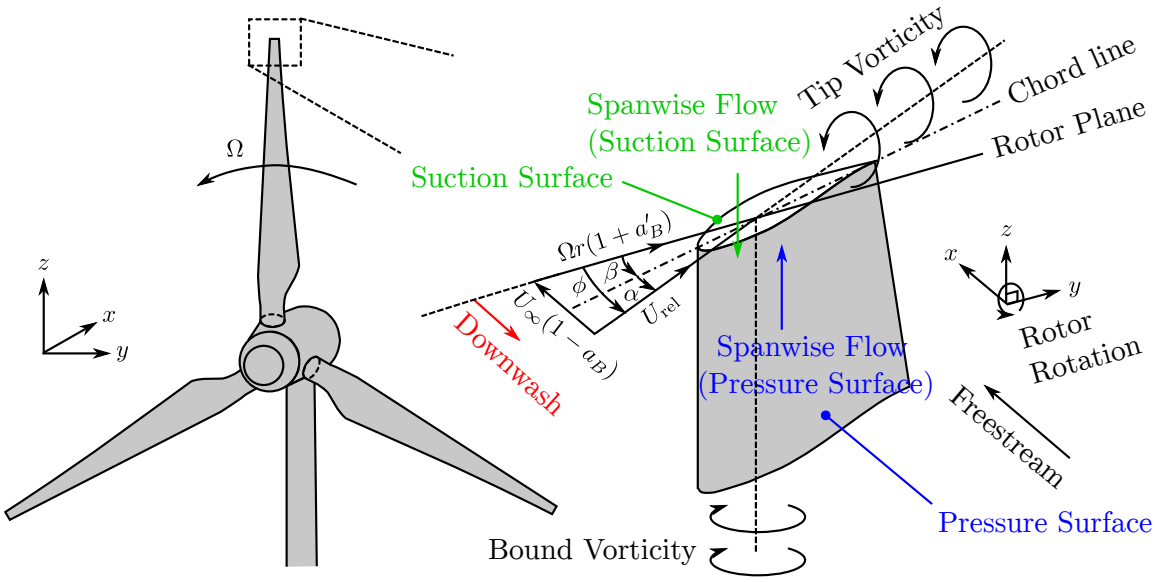

Figure 4.2: Schematic diagram of the effect of the shed vorticity on the outboard blade sections. The induced downwash is highlighted in red, the spanwise flow acceleration on the pressure surface is highlighted in blue and the spanwise flow acceleration on the suction surface is highlighted in green.

surface.

The second effect of the shed vorticity is the spanwise flow accelerations that are induced on the outboard blade sections. Unlike the induced downwash, the spanwise flow accelerations can be identified directly from the local flow field. Fig. 4.3 shows contours of the spanwise velocity component (U_r) on two slices through the computational domain (normal to the blade axis) at $r/R = 0.9$ and $r/R = 0.95$ (noting that the tip geometry of the MEXICO rotor extends outboard from $r/R = 0.95$ to the tip of the blade). In general, the spanwise flow that is induced on the outboard blade sections is outboard on the pressure surface and inboard on the suction surface (as positive U_r indicates outboard flow and negative U_r indicates inboard flow). Fig. 4.3 also shows that the strength of the spanwise flow varies along the aerofoil chord. Starting at the leading edge, the spanwise velocity is continuous between the pressure and suction surfaces. Hence, the difference in spanwise velocity between the pressure and suction surfaces is small and little vorticity is generated. Moving in the chordwise

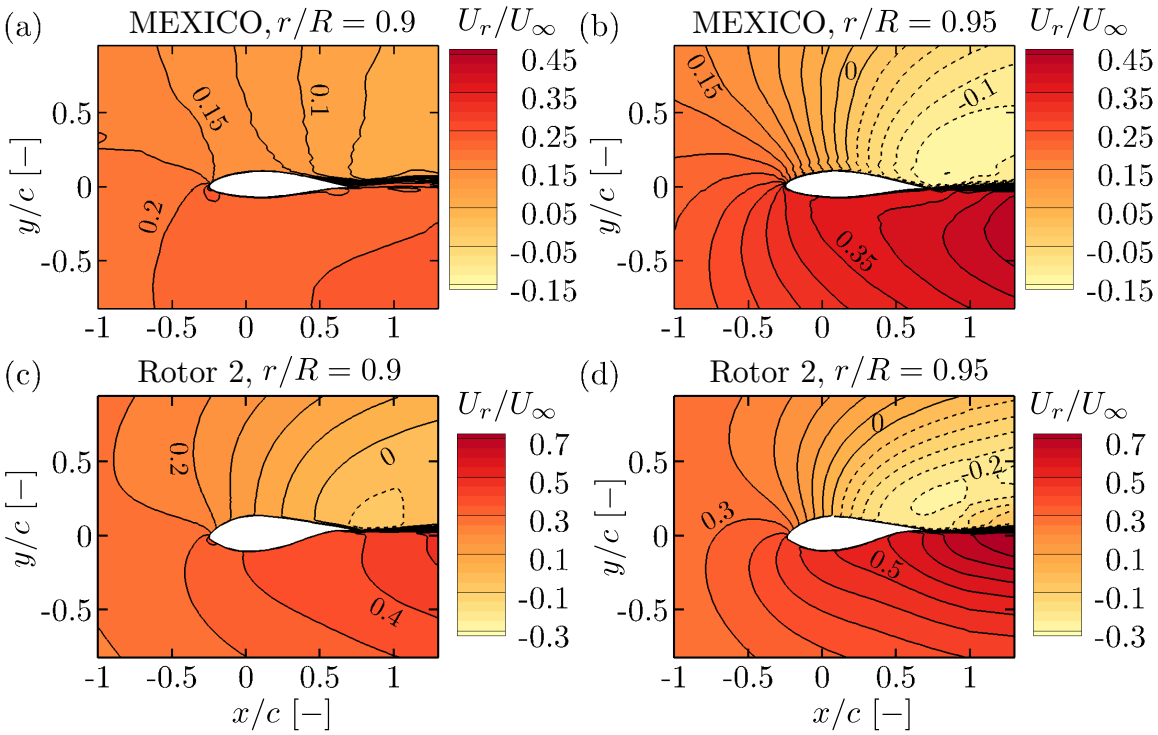

Figure 4.3: Contours of spanwise velocity (U_r) on a slice through the blade (normal to the blade axis) at $r/R = 0.9$ (a and c) and $r/R = 0.95$ (b and d). Positive contours are shown with solid lines, while negative contours are shown with dashed lines.

direction towards the trailing edge, the strength of the spanwise flow increases, with the flow being driven increasingly outboard on the pressure surface and increasingly inboard on the suction surface. Therefore, the difference in spanwise velocity between the pressure and suction surfaces increases in the chordwise direction, resulting in a build up of vorticity, which is eventually shed from the blade at the trailing edge.

The spanwise flow accelerations that are induced by the shed vorticity are balanced (through spanwise momentum conservation) by the spanwise pressure gradients that are developed on the outboard blade sections. With a reduced static pressure difference between the pressure and suction surfaces, the blade loading drops off as the tip is approached. However, the manner in which the loading drops off is dependent on the blade geometry and therefore varies between rotors. This drop off in the blade loading is critical for developing accurate tip flow corrections. Hence, the manner in which the blade loading drops off will be examined in more detail in the

next section.

4.1.1 Static Pressure Changes on the Blade Surface

In order to examine the changes in blade loading that occur when moving outboard towards the tip of the blade, Fig. 4.4 shows the static pressure coefficient distribution on four slices through the blade of the MEXICO rotor (normal to the blade axis) at $r/R = 0.8$, 0.9, 0.95 and 0.98. The static pressure coefficient distribution for the 2D NACA 64-418 aerofoil (computed in Chapter 3) is also shown for comparison, over a range of angles of attack (α). To facilitate a direct comparison between the 2D and 3D computations, the static pressure has been normalised by the (approximate) dynamic pressure incident on each aerofoil section. Hence, the static pressure coefficient has been defined using equation 4.1, but with $\Omega = 0$ for the 2D aerofoil computations.

At $r/R = 0.8$, tip flow effects are small, so the static pressure coefficient distribution can be used as a reference when moving outboard towards the tip of the blade. Furthermore, the local flow conditions at $r/R = 0.8$ can be assumed to be 2D (in the plane of the aerofoil section) with reasonable accuracy, since the (3D) extracted static pressure coefficient distribution shows close agreement with the 2D static pressure coefficient distribution at an angle of attack of somewhere between 6° and 7°. The agreement between the (3D) extracted and the 2D static pressure coefficient distributions at $r/R = 0.8$ is close over the majority of the chord length, except for the rear half of the suction surface ($x/c > 0.4$). At $x/c = 0.7$ for example, the suction developed on the 3D rotor blade is even weaker than the suction developed by the 2D NACA 64-418 aerofoil at an angle of attack of 0°. Since, tip flow effects are small at $r/R = 0.8$, the source of the discrepancy between the 2D and the (3D) extracted static pressure coefficient distributions over the rear half of the suction surface remains unclear. Nevertheless, the discrepancy between the 2D and the (3D) extracted static pressure coefficient distributions at $r/R = 0.8$ will not affect the observation

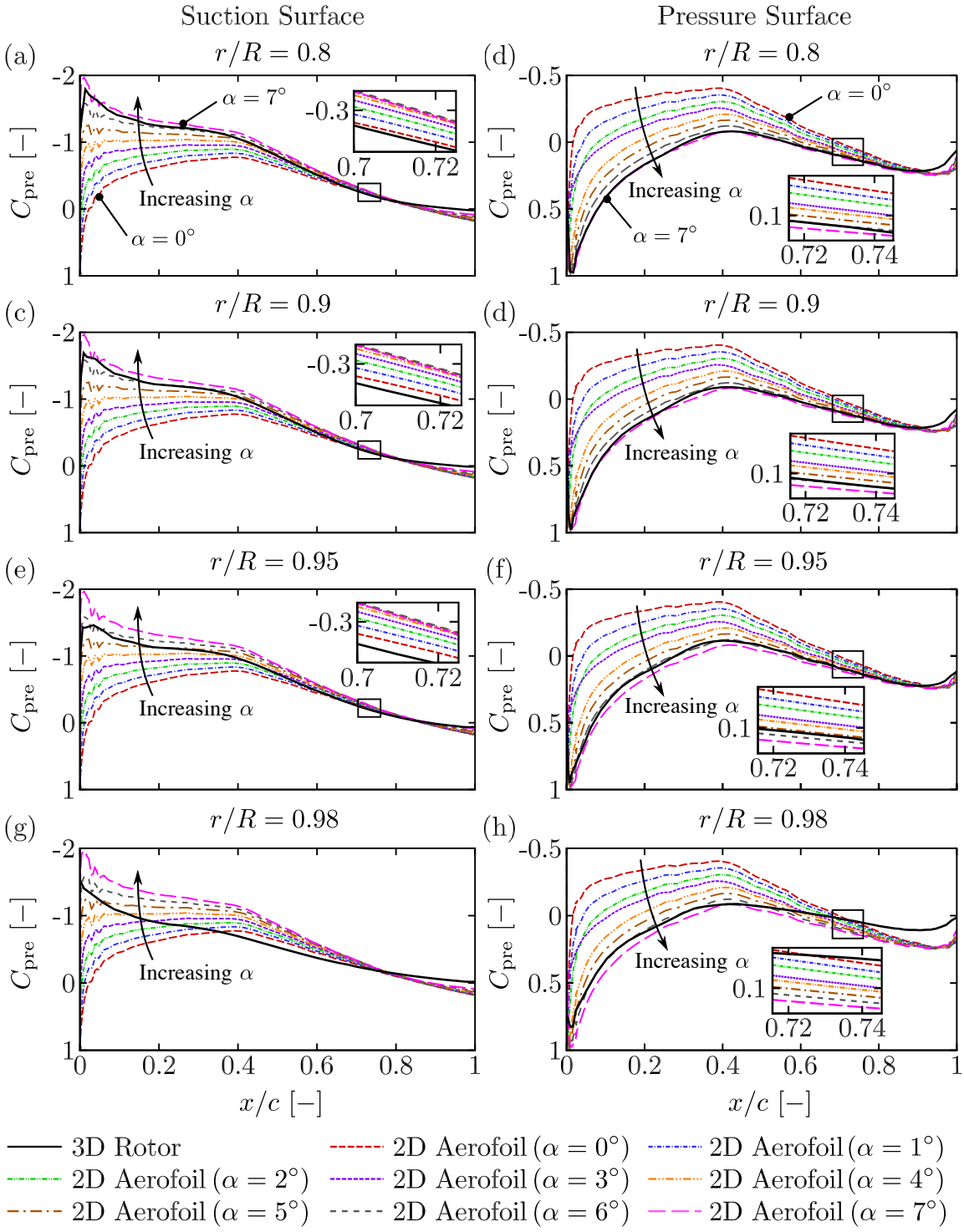

Figure 4.4: Static pressure coefficient distribution on four slices through the blade of the MEXICO rotor, normal to the blade axis. The 2D static pressure distributions were taken from a series of computations of the 2D NACA 64-418 aerofoil.

of tip flow effects on the more outboard stations ($r/R = 0.9, 0.95, 0.98$), since this station is used as a reference for comparison when moving outboard towards the tip of the blade.

Moving outboard to $r/R = 0.9$, the effect of the induced downwash and spanwise flow acceleration on the pressure and suction surfaces can be observed by comparing the (3D) extracted static pressure coefficient distribution with the inboard static pressure coefficient distribution at $r/R = 0.8$. On the suction surface of the blade, the static pressure at $r/R = 0.9$ has increased relative to the static pressure at $r/R = 0.8$, over the entire chord length of the extracted aerofoil section. This reduction in suction is generated by a combination of downwash (reducing the angle of attack) and the inboard transport of momentum from the shed vorticity, which can be seen in Fig. 4.1. The inboard transport of momentum decelerates the velocity magnitude, which increases the static pressure on the suction surface of the blade. Conversely, on the pressure surface of the blade, the static pressure starts to decrease over the entire chord length of the aerofoil section. This reduction in static pressure is generated by a combination of downwash and the outboard transport of momentum (or outboard acceleration) by the shed vorticity, which can also be seen in Fig. 4.1.

Moving outboard to $r/R = 0.95$, the static pressure coefficient distribution shows an even more significant departure from the inboard static pressure coefficient distribution than at $r/R = 0.9$. Near the leading edge of the suction surface, the static pressure increases and the (3D) extracted static pressure coefficient distribution now approximately follows the static pressure coefficient distribution of the 2D NACA 64-418 aerofoil at an angle of attack of somewhere between 5° and 6°. Meanwhile on the pressure surface, the static pressure reduces over the entire surface and the static pressure coefficient distribution near the leading edge now more closely follows the static pressure distribution of the 2D NACA 64-418 aerofoil at an angle of attack of 6°. Between $r/R = 0.9$ and 0.95, the (leading edge based) angle of attack therefore

appears to reduce by around 1°. As the twist angle of the rotor blade reduces by around 0.6° between these locations, the angle of the incident flow vector to the rotor plane (ϕ) reduces by around 1.6° between $r/R = 0.9$ and 0.95. This reduction in the angle of the incident flow vector can be attributed to the increased downwash from the shed vorticity, as the strength of the induction from the tip vorticity increases as the tip of the blade is approached.

In addition to the strength of the downwash, the strength of the spanwise flow acceleration on the pressure and suction surfaces increases when moving outboard towards the tip of the blade. Unfortunately, the combined effect of downwash and spanwise flow acceleration cannot be accurately assessed on the outermost station at $r/R = 0.98$, due to the tip geometry employed by the MEXICO rotor (which extends outboard from $r/R = 0.95$). Nevertheless, Fig. 4.4 shows that the static pressure coefficient distribution at $r/R = 0.98$ departs significantly from the general shape of the 2D NACA 64-418 static pressure coefficient distribution (over all angles of attack), which indicates that the flow induced by the tip geometry is complex and requires careful separate examination (which is not the emphasis of the work carried out here).

To confirm that the observed tip flow effects are not unique to the MEXICO rotor, the static pressure coefficient distribution on the surface of Rotor 2 will now be examined. Fig. 4.5 shows the static pressure coefficient distribution on four slices through the blade of Rotor 2 (normal to the blade axis), at $r/R = 0.8, 0.9, 0.95$ and 0.98. In these plots, the static pressure coefficient distribution for the 2D RISØ-A1-24 aerofoil is also shown for comparison, over a range of angles of attack.

Despite the different aerofoil profiles adopted by the MEXICO rotor and Rotor 2, tip flow effects lead to the same qualitative changes in the static pressure distribution as the tip of the blade is approached. At $r/R = 0.8$ for example, the (3D) extracted static pressure coefficient distribution shows good agreement with the 2D static pres-

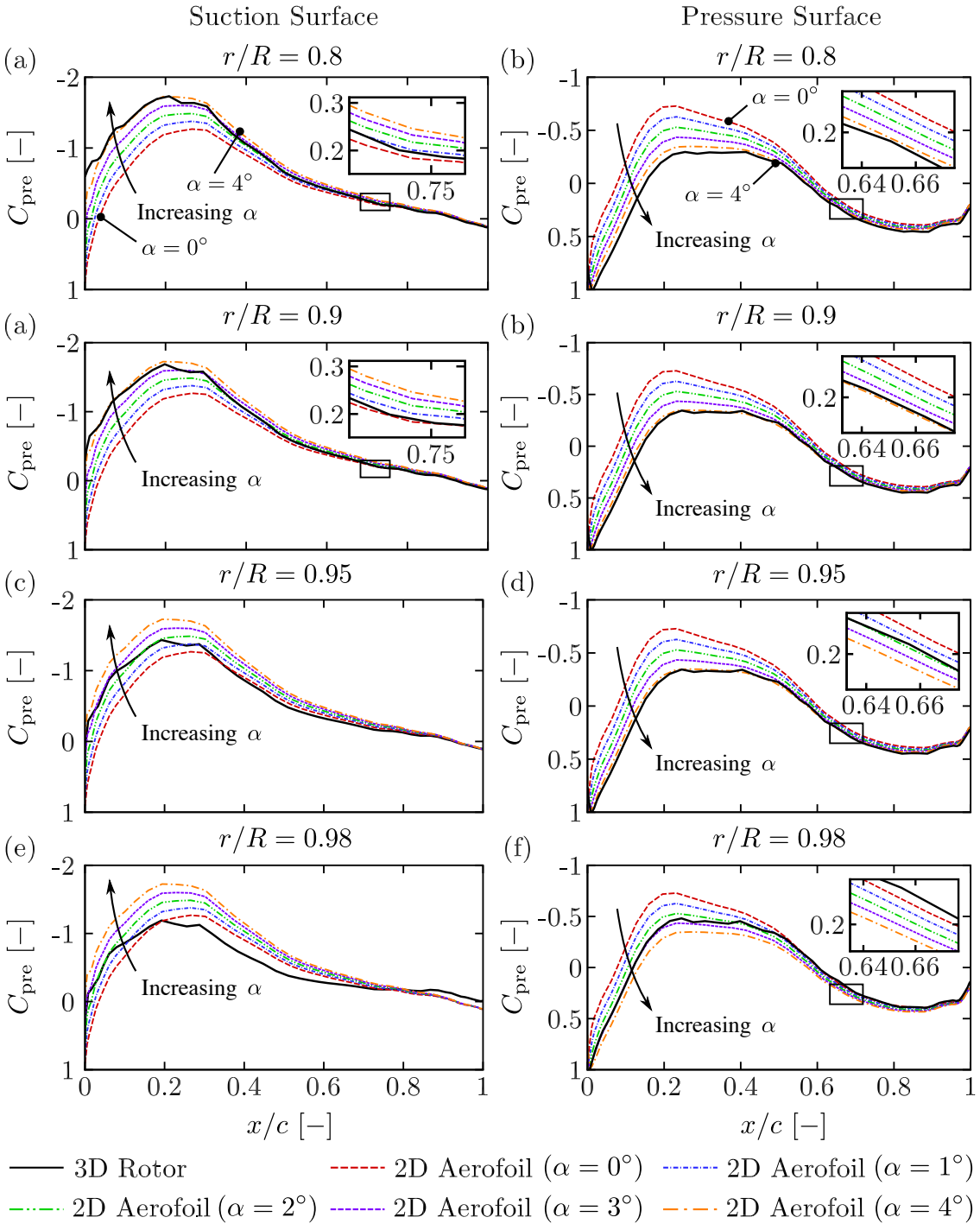

Figure 4.5: Static pressure coefficient distribution on four slices through the blade of Rotor 2, normal to the blade axis. The 2D static pressure coefficient distributions were taken from a series of computations of the 2D RISØ-A1-24 aerofoil.

sure coefficient distribution at an angle of attack of somewhere between 4° and 5°, over the majority of the aerofoil surface. Moving outboard, the induced downwash from the shed vorticity leads to a reduction in the angle of the incident flow vector to the rotor plane (ϕ), which is reflected in a reduction of the (leading edge based) angle of attack. At $r/R = 0.9$ for example, the static pressure coefficient distribution near the leading edge of Rotor 2 approximately follows the 2D static pressure coefficient distribution at an angle of attack of somewhere between 3° and 4°. Moving outboard to $r/R = 0.95$, the static pressure coefficient distribution near the leading edge now more closely follows the 2D static pressure coefficient distribution at an angle of attack of somewhere between 2° and 3°. As the twist angle of the aerofoil sections is constant between $r/R = 0.9$ and $r/R = 0.95$ ($\beta = 2.6°$), the angle of the incident flow vector to the rotor plane (ϕ) therefore appears to reduce by around 1° when moving outboard from $r/R = 0.9$ to $r/R = 0.95$ on Rotor 2.

The shape of the (3D) extracted static pressure coefficient distribution also starts to depart from the shape of the 2D static pressure coefficient distributions when moving outboard towards the tip of the blade. By $r/R = 0.95$, the static pressure over the rear half ($x/c > 0.4$) of the pressure surface has reduced significantly (relative to the inboard station at $r/R = 0.8$), while the static pressure over the rear half of the suction surface has increased significantly. These changes are caused by the spanwise flow accelerations on the pressure and suction surfaces of the blade, which can be seen in Fig. 4.1. By $r/R = 0.98$ it is clear that the (3D) extracted static pressure coefficient distribution no longer follows the 2D static pressure coefficient distributions along the entire chord length, at any angle of attack. It follows that tip flow corrections which only modify the angle of attack (such as Prandtl type corrections (Betz 1919)) will always be insufficient to capture the static pressure changes induced by the shed vorticity on the outboard blade sections and additional corrections are required to accompany them. These corrections will be discussed further in Section 4.3.

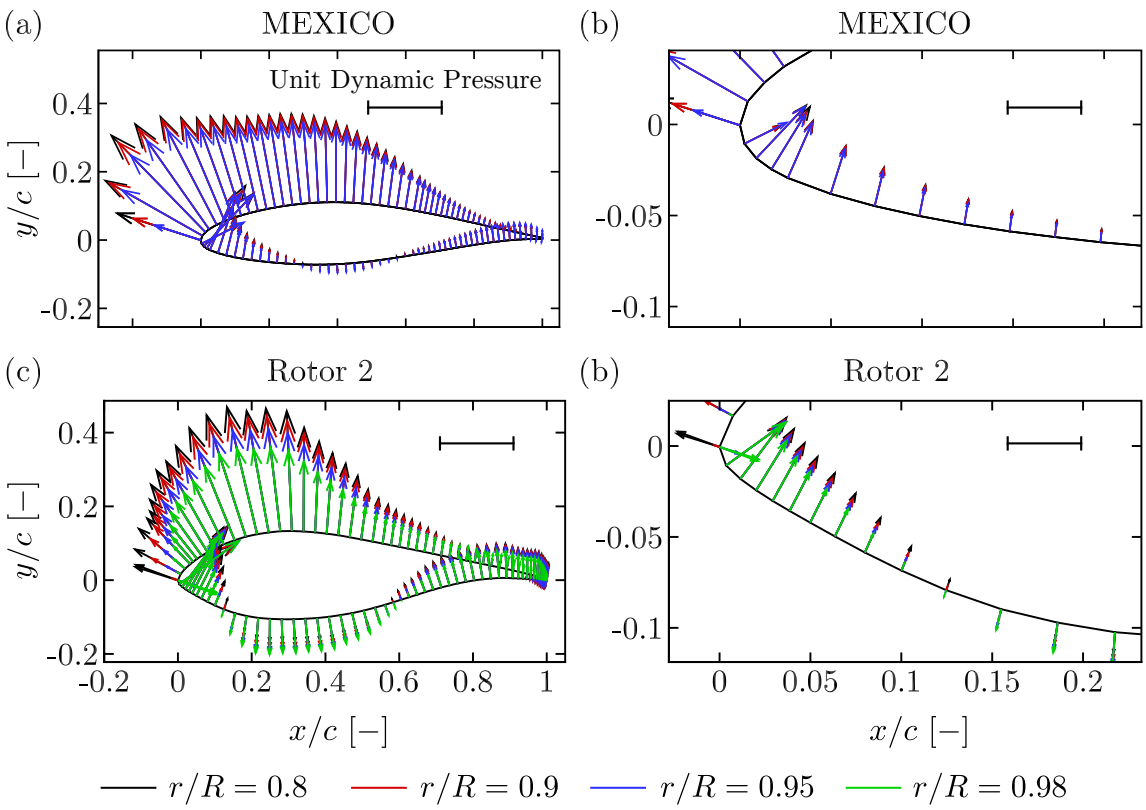

Figure 4.6: Vector plots of the static pressure coefficient distribution on slices through the blade of the MEXICO rotor (a and b) and the Rotor 2 (c and d), normal to the blade axis. Close-up views of the leading edge are shown in (b) and (d). The vectors are scaled by unit incident dynamic pressure, $\frac{1}{2}\rho(U_\infty^2 + (r\Omega)^2)$. The vectors at $r/R = 0.98$ are not shown for the MEXICO rotor, as this region is part of the tip geometry.

4.1.2 Surface Pressure Vectors

In order to identify the consequences of the changing static pressure distribution on the sectional blade loading, Fig. 4.6 shows vector plots of the static pressure coefficient vector (the static pressure coefficient multiplied by the unit normal vector) for the MEXICO rotor and Rotor 2. In these plots, vectors pointing out of the surface indicate a negative static pressure coefficient (suction), while vectors pointing into the surface indicate a positive static pressure coefficient (positive pressure). The x and y axes are aligned parallel and perpendicular to the local chord line (respectively) and the pitch angle of the outboard blade sections of both rotors is relatively small (between 0.3° and 2.7°). Hence, the $-x$ and $+y$ axes approximately correspond with

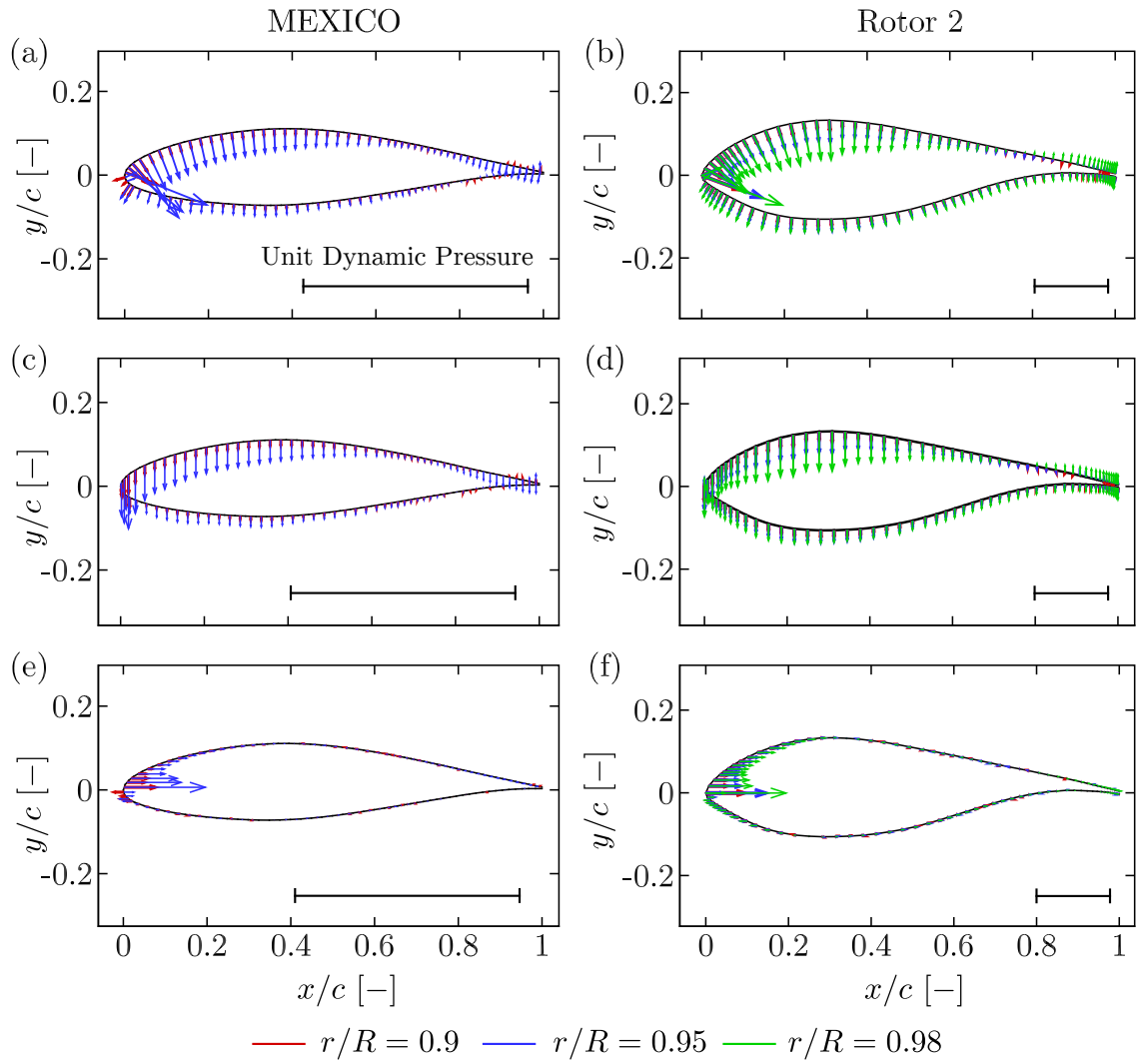

Figure 4.7: Vector plots of the difference in static pressure coefficient vector between each radial station and the inboard radial station at $r/R = 0.8$. The complete vector is shown in (a) and (b), the component normal to the chordline is shown in (c) and (d) and the component parallel to the chordline is shown in (e) and (f). The vectors are scaled by unit incident dynamic pressure, $\frac{1}{2}\rho(U_\infty^2 + (r\Omega)^2)$. The vectors at $r/R = 0.98$ are not shown for the MEXICO rotor, as this region is part of the tip geometry.

the torque and thrust-producing directions (respectively).

To accompany these plots, Fig. 4.7 shows vector plots of the difference in static pressure coefficient vector between each radial station and an inboard radial station ($r/R = 0.8$) where the induction from the shed vorticity is small. The components of these vectors that are parallel and perpendicular to the local chordline are also

shown in Fig. 4.7, to help identify the regions of the aerofoil surface that contribute to the changes in the sectional thrust and torque-producing forces. Fig. 4.7 shows that both the thrust and torque-producing forces drop off as the tip of the blade is approached (an increase in positive x direction force is a reduction in torque, while an increase in negative y direction force is a reduction in thrust). While the sectional torque reduction is highly localised to the region around the leading edge of the suction surface, the sectional thrust reduction is more evenly distributed over the entire aerofoil surface, with contributions from both the pressure and suction surfaces.

To quantitatively observe the effect of the changing static pressure distribution on the sectional blade loading, Fig. 4.8 shows the cumulative integral (in the chordwise direction) of the incremental thrust and torque-producing forces acting on each aerofoil section. These incremental forces were computed on a cell by cell basis by summing the surface pressure and wall shear force vectors and then resolving the resultant vector in the thrust and torque-producing directions. At $r/R = 0.8$, 279.6 N/m (83%) of the total thrust-producing force per unit span (334.9 N/m) on the MEXICO rotor blade is generated by the suction surface. This contribution is distributed over the entire suction surface and is stronger near the leading edge (due to the blade suction peak). The regions near the leading and trailing edges of the pressure surface also contribute to the thrust-producing force (as indicated by the increasing cumulative integral). However, their contribution to the thrust-producing force (28.1 N/m for $x/c < 0.1$ and 21.6 N/m for $x/c > 0.6$) is much smaller than the contribution provided by the suction surface.

The torque-producing force is more concentrated than the thrust-producing force, with 56.6 N/m (out of a net total of 36.4 N/m) being generated over the leading 25% of the suction surface of the MEXICO rotor blade at $r/R = 0.8$. A small positive contribution to the torque-producing force is also generated near the trailing edge of the pressure surface (2.2 N/m from $0.6 < x/c < 1.0$). However, over the remainder of

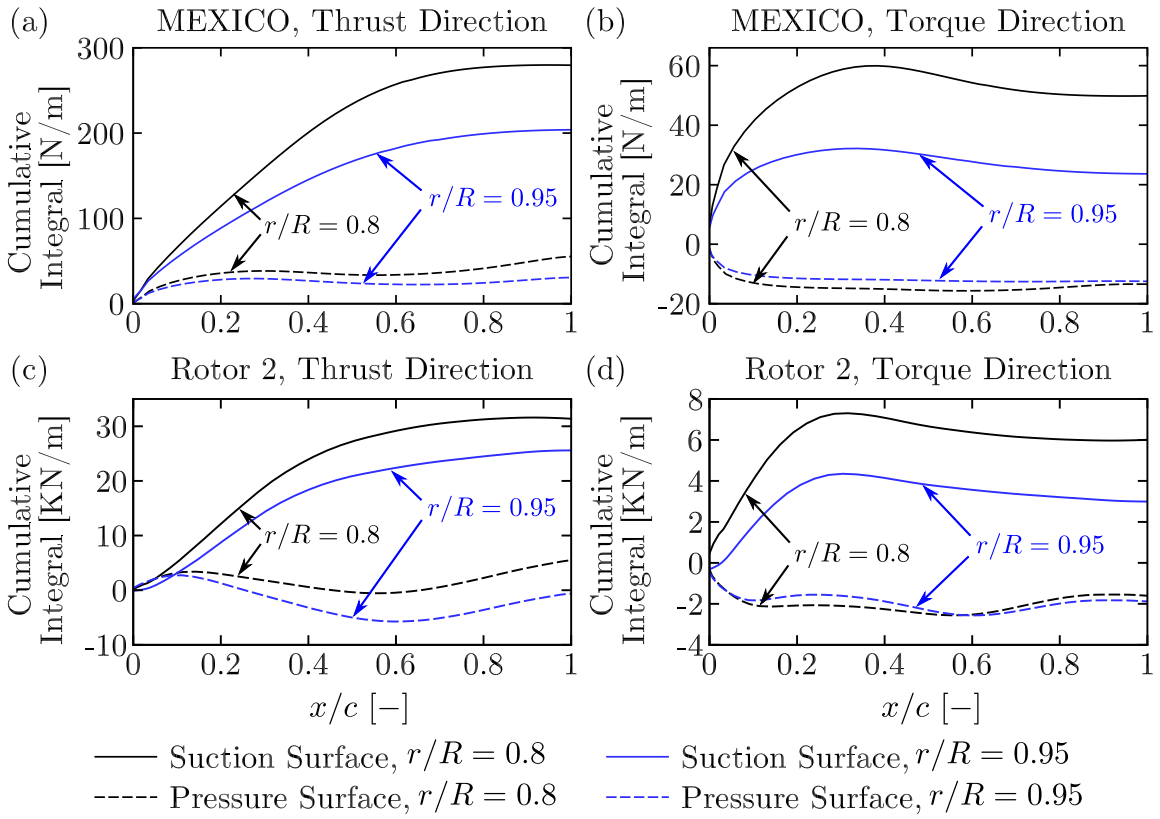

Figure 4.8: Cumulative integral in the chordwise direction of the incremental thrust and torque-producing forces on a slice through the blade of the MEXICO rotor and Rotor 2 (normal to the blade axes), at $r/R = 0.8$ and $r/R = 0.95$.

the pressure and suction surfaces, the surface force distribution provides a negative contribution to the torque-producing force (as indicated by the decreasing cumulative integral).

The relative spanwise reduction in the sectional thrust and torque-producing forces can also be computed from Fig. 4.8, by comparing the cumulative integrals on the inboard ($r/R = 0.8$) and outboard ($r/R = 0.95$) stations. For both rotors, the relative reduction in torque-producing force (69% for the MEXICO rotor and 76% for Rotor 2) is much larger than the relative reduction in thrust-producing force (30% for the MEXICO rotor and 33% for Rotor 2), when moving outboard from $r/R = 0.8$ to $r/R = 0.95$. Furthermore, the majority of this reduction can be attributed to the suction surface, as the cumulative integral of the torque-producing force on the pressure surface remains relatively unchanged when moving outboard.

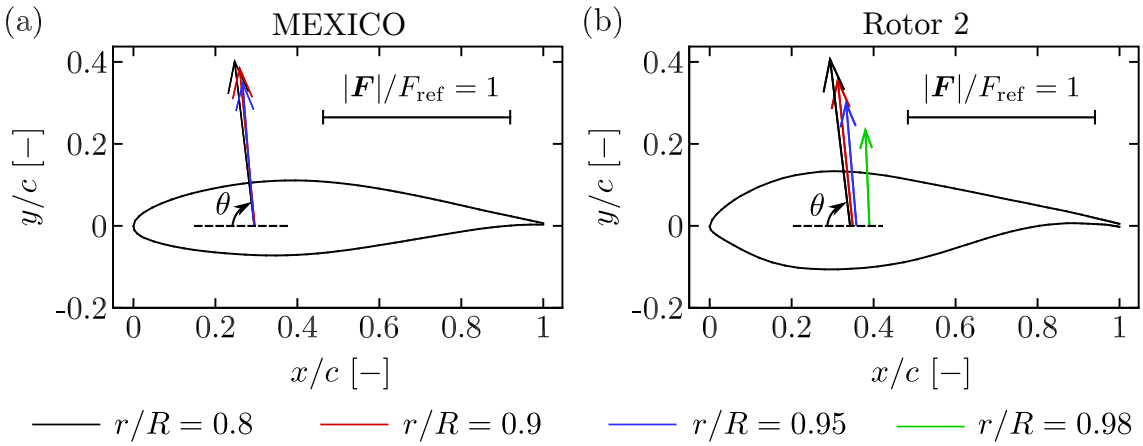

Figure 4.9: Vector plots of the sectional force vector acting on selected outboard sections of the MEXICO rotor and Rotor 2 in a global coordinate system (relative to the rotor plane and not the local chord line). The vectors have been placed with their origin at the (calculated) centre of pressure of their respective aerofoil sections. Here θ represents the angle of the sectional force vector relative to the rotor plane and is measured in a clockwise sense, with 0° at the 9 o'clock position. The aerofoil sections are pitched nose-down relative to the rotor plane, with twist angles shown in Table 4.1. The vectors are scaled on the reference force $F_{\text{ref}} = \frac{1}{2}\rho(U_\infty^2 + (r\Omega)^2)c$. The vector at $r/R = 0.98$ is not shown for the MEXICO rotor, as this region is part of the tip geometry.

The implications of these observations will be discussed in more detail in the next section.

4.1.3 Force Vector Rotation

The static pressure distributions in Fig. 4.6, together with the wall shear stress distributions, were integrated in the chordwise direction to compute the total sectional force vector ($\boldsymbol{F}$) acting on each of the outboard stations. The total sectional force vectors are shown in Fig. 4.9 and have been placed at the (calculated) centre of pressure of their respective aerofoil sections. To aid with the interpretation of Fig. 4.9, Table 4.1 shows the magnitude of the total sectional force vector ($|\boldsymbol{F}|$), the angle of the sectional force vector relative to the rotor plane (θ) and the chordwise location of the centre of pressure (x_p).

Fig. 4.9 shows that (for both rotors) the total sectional force vector reduces in

Table 4.1: Magnitude of the sectional force vector ($|\boldsymbol{F}|$), angle of the sectional force vector to the rotor plane (θ), chordwise position of the centre of pressure (x_p) and the twist angle of the aerofoil sections relative to the rotor plane (β). θ and β are measured in a clockwise sense, with 0° at the 9 o'clock position. Therefore β is negative as the aerofoil sections are pitched in an anti-clockwise sense (nose-down) relative to the rotor plane. The reference force $F_{\text{ref}} = \frac{1}{2}\rho(U_\infty^2 + (r\Omega)^2)c$. The tabulated values at $r/R = 0.98$ are not shown for the MEXICO rotor, as this region is part of the tip geometry.

Rotor	r/R [-]	$\lvert\boldsymbol{F}\rvert/F_{\text{ref}}$ [-]	θ [°]	x_p/c [-]	β [°]
MEXICO rotor	0.8	0.876	84.0	0.295	-2.54
MEXICO rotor	0.9	0.838	85.1	0.296	-1.41
MEXICO rotor	0.95	0.757	86.1	0.294	-0.83
Rotor 2	0.8	0.887	83.1	0.343	-2.81
Rotor 2	0.9	0.774	84.2	0.349	-2.59
Rotor 2	0.95	0.651	85.2	0.358	-2.59
Rotor 2	0.98	0.507	87.5	0.390	-2.59

magnitude and rotates (in a clockwise sense) towards the streamwise direction as the tip of the blade is approached. These changes follow directly from the changing shape of the static pressure distribution in Fig. 4.7. More specifically, since the strength of the suction developed on the suction surface and the pressure developed on the pressure surface both reduce as the tip of the blade is approached, the sectional force vector must reduce in magnitude. Additionally, the large reduction in suction generated near the leading edge of the suction surface of the aerofoil leads to the torque-producing force dropping off more rapidly than the thrust-producing force, which causes the sectional force vector to rotate away from the rotor plane, towards the streamwise direction.

For some rotors in the literature, the torque-producing force per unit span has even been observed to tend to zero before the very tip of the blade, particularly at high tip-speed-ratios (Hansen & Johansen 2004, Ferrer & Munduate 2007). Under these conditions, the outboard blade sections are actually applying a braking force to the

rotor. To achieve such a negative torque-producing force per unit span, the sectional force vector must rotate past 90°, which is only possible if the torque-producing force per unit span drops off faster than the thrust-producing force per unit span as the tip of the blade is approached. Hence, the sectional force vector must be reducing in magnitude and rotating towards the streamwise direction as the tip of the blade is approached, which is consistent with the observations presented in this work.

Fig. 4.9 also shows that, as another consequence of the changing static pressure distribution, the centre of pressure moves in the chordwise direction (towards the trailing edge) as the tip of the blade is approached. While the magnitude of this movement is far greater for Rotor 2 than the MEXICO rotor, the magnitude of the movement is still small for both rotors (except in the very distorted flow region near the very tip of the blade). More specifically, the centre of pressure on the blade of Rotor 2 only moves by 1.5% of the chord length when moving outboard from $r/R = 0.8$ to $r/R = 0.95$. Hence, it is likely that this movement of the centre of pressure will not be of primary importance in the subsequent analysis of the rotor and can be neglected.

The reduction in magnitude and rotation of the sectional force vector can also be interpreted in terms of lift and drag vectors components. To facilitate the following explanation, Fig. 4.10 shows a blade element diagram with lift and drag vector components that are exerted on an inboard and an outboard section of the rotor blade. Here the inboard section represents a section far from the blade tip (say $r/R = 0.8$) where the induction from the shed vorticity (both induced downwash and spanwise flow acceleration) is negligible, while the outboard section represents a section near the tip of the blade (say $r/R = 0.95$) where the induction from the shed vorticity is more significant.

There are three possible scenarios that are consistent with the observed variation of the blade loading on the outboard blade sections. They are all shown in Fig. 4.10.

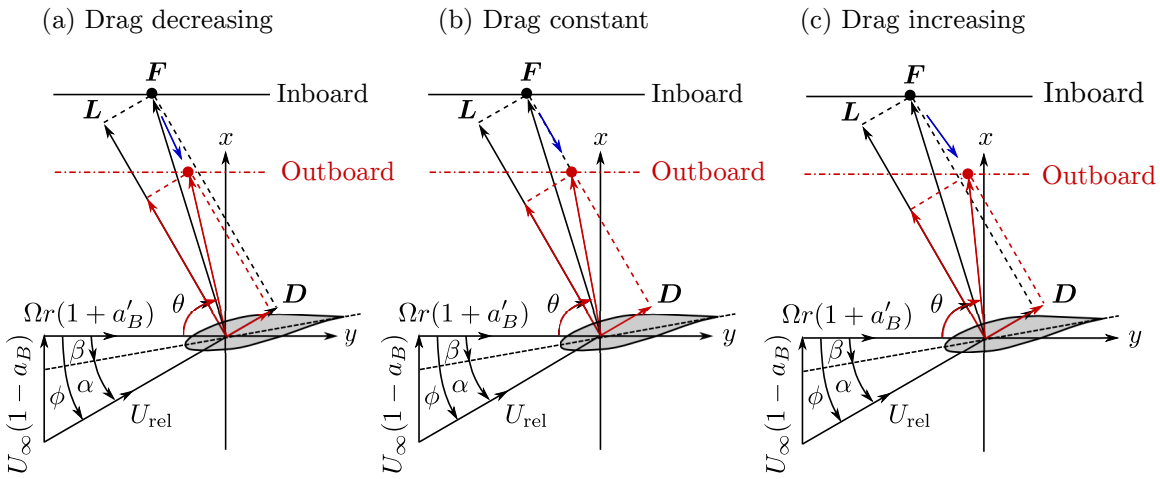

Figure 4.10: Blade element diagram for an inboard section of the rotor blade (black lines) where the induction from the shed vorticity is negligible and an outboard section of the rotor blade (red lines) where the induction from the shed vorticity is significant. The blue arrow indicates the change in the the sectional force vector ($\boldsymbol{F}$) between the inboard and outboard sections. The sectional drag force per unit span may (a) decrease, (b) remain constant or (c) increase, depending on the degree of rotation of the sectional force vector.

In order for the sectional force vector to reduce in magnitude and rotate towards the streamwise direction, the sectional lift force per unit span ($\boldsymbol{L}$) must reduce. However, the sectional drag force per unit span ($\boldsymbol{D}$) may decrease, remain constant, or increase, depending on the degree of rotation. While all three scenarios are permissible and consistent with the observed behaviour of the sectional force vector (clockwise rotation), the degree of rotation (and therefore the behaviour of the sectional drag coefficient) is currently unknown. Hence, it is not possible to strictly classify the behaviour of the drag coefficient on the outboard sections of all rotors as either Fig. 4.10 (a), (b) or (c), since all three scenarios are permissible with a clockwise rotation and a reduction in magnitude of the sectional force vector. However, the majority of rotors investigated in the literature exhibit an increase in the sectional drag coefficient on the outboard blade sections (see Johansen & Sørenson (2004) and Shen et al. (2009) for example). This will also be shown to be the case for the MEXICO rotor in Section 4.2.3. Hence, the rotation of the sectional force vector corresponds with Fig. 4.10 (c) for these rotors.

Fig. 4.10 can also be used to better understand and classify different tip flow correction methods. For example, tip flow corrections that only reduce the angle of attack (such as Prandtl style corrections), reduce both the lift and drag coefficients as the tip of the blade is approached (assuming of course that the aerofoil is not stalled and $\alpha > 0$). As the drag coefficient is reduced, these correction methods implicitly assume that the reduction in magnitude and rotation of the sectional force vector corresponds with Fig. 4.10 (a). Hence, these methods will be insufficient for correcting the blade loading if the rotation of the sectional force vector (for a given rotor that is to be corrected) is much greater and actually corresponds with Fig. 4.10 (b) or (c). In a similar manner, tip flow correction methods that only reduce the lift coefficient or the circulation strength implicitly assume that the rotation of the sectional force vector corresponds with Fig. 4.10 (b), as the drag coefficient is not corrected by these methods. Hence, these methods will also be insufficient for correcting the blade loading if the rotation of the sectional force vector (for a given rotor that is to be corrected) is much greater and actually corresponds with Fig. 4.10 (c). The two correction methods that are presented and evaluated in the next section correct the lift and drag vector components independently. Hence, the rotation of the sectional force vector is not constrained to Fig. 4.10 (a), (b) or (c) and the sectional force vector can be accurately corrected, regardless of the degree of rotation exhibited by a given rotor.

4.2 Lift and Drag Polar Replacement

The first method that can be used to account for the tip loss mechanism is to replace the original (2D) lift and drag polars with new polars that are extracted directly from either experimental measurements or blade resolved computations of the complete (3D) rotor. In this approach, the rotor blade is divided into several independent

stations along the blade span and a separate polar is extracted at each station. As the polars are allowed to vary along the span, three-dimensional flow effects can be captured directly within the set of extracted polars. The main benefit of this approach is that different three-dimensional flow effects can all be captured within the same set of polars, so the effect of rotational augmentation on the inboard sections (discussed in Chapter 3) can be captured, in addition to the tip loss mechanism.

In this section, the original (2D) lift and drag polars that were used for the actuator line computations of the MEXICO rotor in Chapter 3, are replaced by a separate set of polars that are extracted directly from the blade resolved computations of the MEXICO rotor (which were also carried out in Chapter 3). This section begins by describing the method used to extract the polars from the blade resolved computations. The extracted polars are then compared with the original (2D) polars, to identify the three-dimensional flow effects. To complete the section, the extracted polars are then used in a set of actuator line computations of the MEXICO rotor, to quantify the improvement in the thrust and torque producing forces that can be achieved using this tip flow correction method.

4.2.1 Extracting Lift and Drag Polars from Blade Resolved Computations

In order to extract lift and drag polars from blade resolved computations of the complete (3D) rotor, the spanwise distribution of the angle of attack (α), relative velocity magnitude (U_{rel}), lift coefficient (C_L) and drag coefficient (C_D) are required along the entire blade span, for a range of tip-speed-ratios. To compute these quantities, the spanwise distribution of the axial and tangential forces per unit span (F_{ax} and F_{ta} respectively) are first extracted from the blade resolved computations, by integrating the wall shear stress and surface pressure distributions in the chordwise direction. Once the angle of attack is determined, the lift and drag forces per unit span (L and

D) can then be computed by resolving the axial and tangential forces per unit span normal to and parallel with the incident flow direction.

$$L = F_{\text{ax}} \cos(\phi) + F_{\text{ta}} \sin(\phi) \tag{4.2}$$

$$D = F_{\text{ax}} \sin(\phi) - F_{\text{ta}} \cos(\phi) \tag{4.3}$$

The lift and drag coefficients can then be evaluated from the lift and drag forces per unit span by using the relative velocity magnitude (U_{rel}).

$$C_L = \frac{L}{\frac{1}{2}\rho {U_{\text{rel}}}^2 c} \tag{4.4}$$

$$C_D = \frac{D}{\frac{1}{2}\rho {U_{\text{rel}}}^2 c} \tag{4.5}$$

Hence, to extract lift and drag polars from the blade resolved computations of the MEXICO rotor, only the angle of attack and relative velocity magnitude need to be extracted, as the axial and tangential forces per unit span were already extracted in Chapter 3. However, the spanwise distribution of the angle of attack and relative velocity magnitude are not straightforward to extract from blade resolved computations of a complete (3D) rotor, due to the wake induction at the rotor plane and the flow field distortions from the physical presence of the blade. The angle of attack and relative velocity magnitude are even more challenging to extract from experimental measurements, as the local flow field is often not available and must be deduced from static pressure measurements on the blade surface (Yang et al. 2011).

To work around these difficulties, three main methods have been proposed in the literature to extract the spanwise distribution of the angle of attack and relative velocity magnitude: the inverse blade element momentum method (Guntur et al. 2011), the inverse free wake method (Sant et al. 2006) and the azimuthal-average induction factor method (Johansen & Sørenson 2004). The inverse blade element momentum method cannot be used in this work, as the lift and drag polars are

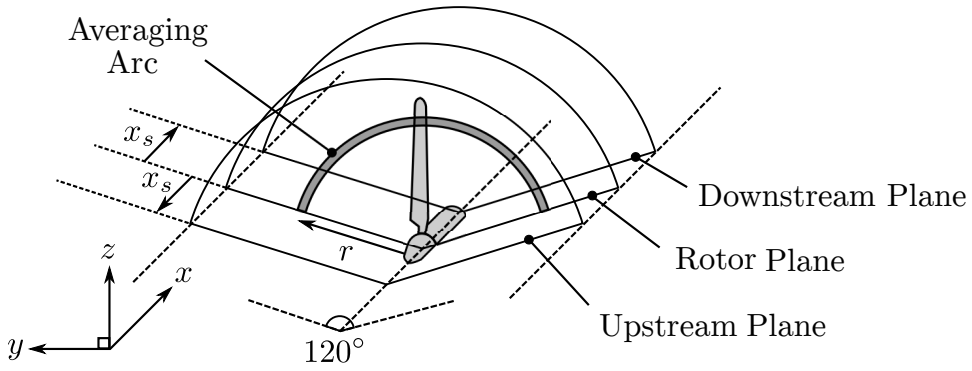

Figure 4.11: Schematic diagram of the azimuthal-average induction factor method. The averaging planes are placed at a distance x_s upstream and downstream of the rotor plane and the arc has radius r. The arc is infinitesimally thin (its thickness has been exaggerated in the diagram for clarity) and spans an angle of 120° when the rotor computations are azimuthally periodic.

required as part of the method and these have not yet been computed. Conversely, the inverse free wake method requires an artificial model of the wake to be constructed, in order to compute the wake induction at the rotor plane. As the local flow field has already been computed as part of the blade resolved computations, an artificial wake model would not be appropriate for this investigation. Therefore, the azimuthal-average induction factor method was deemed to be the most appropriate method for this investigation. It will be briefly described in the next section, before being applied to the blade resolved computations of the MEXICO rotor.

4.2.2 Azimuthal-Average Induction Factor Method

As shown in Fig. 4.11, the azimuthal-average induction factor method of Johansen & Sørenson (2004) places two planes normal to the incident flow direction, at a distance x_s upstream and downstream of the rotor plane. The velocity field at the rotor plane ($x = 0$) is assumed to be the average of these two planes, in order to remove the physical presence of the blades and the local flow field distortions from the boundary layer. The axial and swirl induction factors (a and a') are computed on this plane from the axial and swirl velocities (U_x and U_θ), which are extracted from the flow

field.

$$a = \frac{U_\infty - U_x}{U_\infty} \tag{4.6}$$

$$a' = -\frac{U_\theta}{\Omega r} \tag{4.7}$$

To compute the angle of attack and relative velocity magnitude at a spanwise distance r from the rotor apex, the azimuthal-average axial and swirl induction factors ($\overline{a}$ and $\overline{a'}$) are computed by averaging the axial and swirl induction factors (a and a') in the azimuthal direction along an arc with radius r. Since the blade resolved computations carried out in Chapter 3 were azimuthally periodic, the averaging arc spans an angle of 120° in this investigation.

Having completed the averaging, the induction factors that are local to the blade section (a_B and a'_B) are then computed from the azimuthal-averages, by using a finite blade correction factor F (discussed previously in Section 3)).

$$a_B = \frac{\overline{a}}{F} \tag{4.8}$$

$$a'_B = \frac{\overline{a'}}{F} \tag{4.9}$$

Finally, the blade element diagram in Fig. 3.13 can be used to compute the angle of attack and relative velocity magnitude from the induction factors that are local to the blade section (a_B and a'_B).

$$\alpha = \tan^{-1}\left[\frac{U_\infty(1-a_B)}{\Omega r(1+a'_B)}\right] - \beta \tag{4.10}$$

$$U_{\text{rel}} = \sqrt{\left[U_\infty(1-a_B)\right]^2 + \left[\Omega r(1+a'_B)\right]^2} \tag{4.11}$$

The azimuthal-average induction factor method has been applied by Shen et al. (2009), Branlard (2011) and Bechmann et al. (2011), with little consideration for the effect of the sampling plane distance (x_s) and the choice of finite blade correction

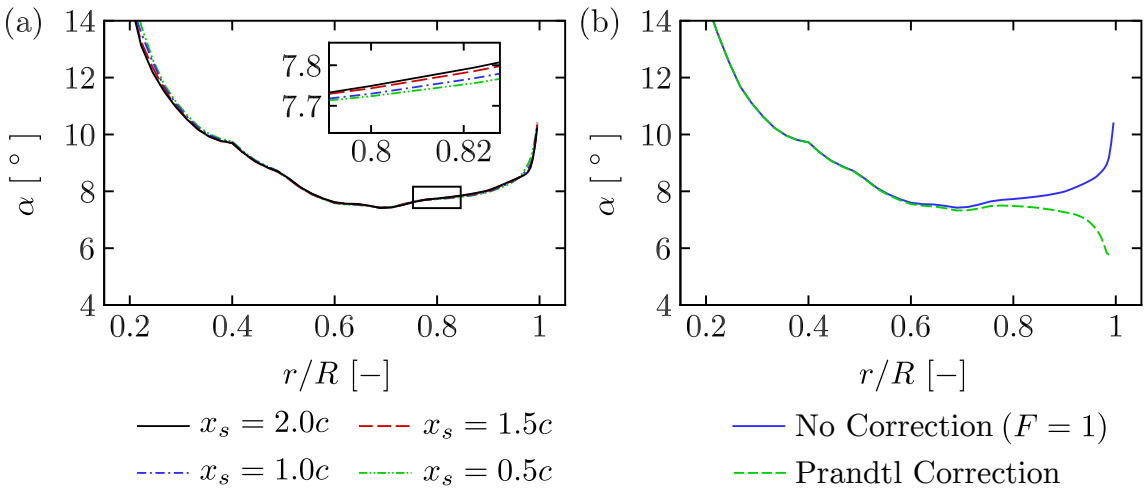

Figure 4.12: Angle of attack variation with (a) sampling plane distance and (b) with and without the finite blade correction factor of Prandtl.

factor (F). Due to near wake expansion, the sampling planes should ideally be as close to the rotor plane as possible ($x_s \to 0$). However, Schluntz & Willden (2014) showed that for distances less than 1 chord length, local flow field distortions from the proximity of the boundary layer become significant. Therefore, sampling distances less than 1 chord length may lead to inaccuracies in the averaging process. To investigate the sensitivity of the angle of attack to sampling plane distance, Fig. 4.12 (a) shows the spanwise variation of the angle of attack, for sampling plane distances of 0.5, 1.0, 1.5 and 2.0 chord lengths.

On the outboard blade sections, the angle of attack was found to be relatively insensitive to the sampling plane distance. At $r/R = 0.8$ for example, reducing the sampling plane distance from two chord lengths to half a chord length only changed the angle of attack by 0.03° (0.3%). Therefore, a sampling plane distance of one chord length was deemed to be appropriate for extracting the lift and drag polars in this investigation.

Before assessing the effect of the finite blade correction factor (F) in equations 4.8 and 4.9, the reader should recall that the exact behaviour of F remains unknown for real rotors and that all functions proposed for F in the literature are only approx-

imations. For this reason, the azimuthal-average induction factor method is often employed in the literature without a finite blade correction factor (the azimuthal-average and local induction factors are assumed to be the same).

Fig. 4.12 (b) compares the angle of attack distribution computed with and without a finite blade correction factor. Where a finite blade correction factor has been used, the Prandtl correction factor (Betz 1919) has been used for F in equations 4.8 and 4.9. Conversely, where a finite blade correction factor has not been used, F has been set to 1 in equations 4.8 and 4.9.

As the tip of the blade is approached, the Prandtl correction factor forces $a_B \to 1$ and $\phi \to 0°$ (Shen et al. 2005). It should be noted that this asymptotic behaviour is also exhibited by other finite blade correction factors proposed in the literature (such as the Glauert (1935) and Goldstein (1929) correction factors) and is not unique to the Prandtl correction factor. However, Shen et al. (2005) pointed out that the axial induction factor should not tend to exactly 1 at the blade tip, as this implies that the flow is purely tangential to the rotor plane ($\phi = 0°$) and the tip vortex cannot be convected downstream. In reality, the angle of attack distribution will therefore be somewhere in between the angle of attack distributions shown in Fig. 4.12 (b). However, as discussed in Section 4.1.1, the exact angle of attack distribution near the tip is not straightforward to compute, as the flow is highly three-dimensional.

For the remainder of this chapter, the angle of attack and relative velocity magnitude distributions are computed without a finite blade correction factor ($F = 1$). This is primarily because the angle of attack distribution gives much closer agreement with the angle of attack distribution computed in the actuator line computations (this will be shown directly in Fig. 4.15). As the aim of this study is to use the extracted lift and drag polars as inputs for actuator line computations of the same rotor, achieving a similar angle of attack distribution between the two methods was deemed to be essential to ensure that the blade forces are reproduced correctly.

4.2.3 Extracted Lift and Drag Polars

Fig. 4.13 shows the lift and drag polars that were extracted using the azimuthal-average induction factor method, at several stations along the span of the MEXICO rotor blade. 5 different tip-speed-ratios were used for extraction, leading to 5 different angles of attack (and their corresponding lift and drag coefficients) at each spanwise station. Linear interpolation was used between the computed angles of attack to determine the intermediate lift and drag coefficients. The polars have been separated into inboard (a and b), mid-span (c and d) and outboard (e and f) sections, in order to facilitate direct comparison with the corresponding 2D polars for these aerofoil sections. In addition to the experimental polars, 2D computationally derived polars for the DU91-W2-250, RISØ-A1-21 and NACA 64-418 aerofoils have also been included in Fig. 4.13 for further comparison. These computationally derived polars were carried out at the same chord-based Reynolds number as the experimental measurements, except for the RISØ-A1-21 aerofoil, which was carried out at a lower chord-based Reynolds number (0.6×10^6) to better match the chord-based Reynolds number of the 3D rotor blade.

A direct comparison of the polars extracted from the 3D blade resolved computations and the 2D polars allows the main three-dimensional flow effects to be identified. For example, on the outboard blade sections (from $r/R = 0.82$ to 0.94), the tip loss mechanism causes the lift coefficient to decrease while the drag coefficient increases, as the tip of the blade is approached. This is consistent with the total sectional force vector reducing in magnitude and rotating towards the streamwise direction as the tip of the blade is approached. On the inboard sections (from $r/R = 0.30$ to 0.40), the extracted lift coefficient continues to increase far above the 2D experimental lift coefficient before significant stall is encountered. This increase is characteristic of rotational augmentation and stall delay (as discussed in Chapter 3 Section 3.3.3.1) and agrees qualitatively with the polars extracted from other rotors in the literature

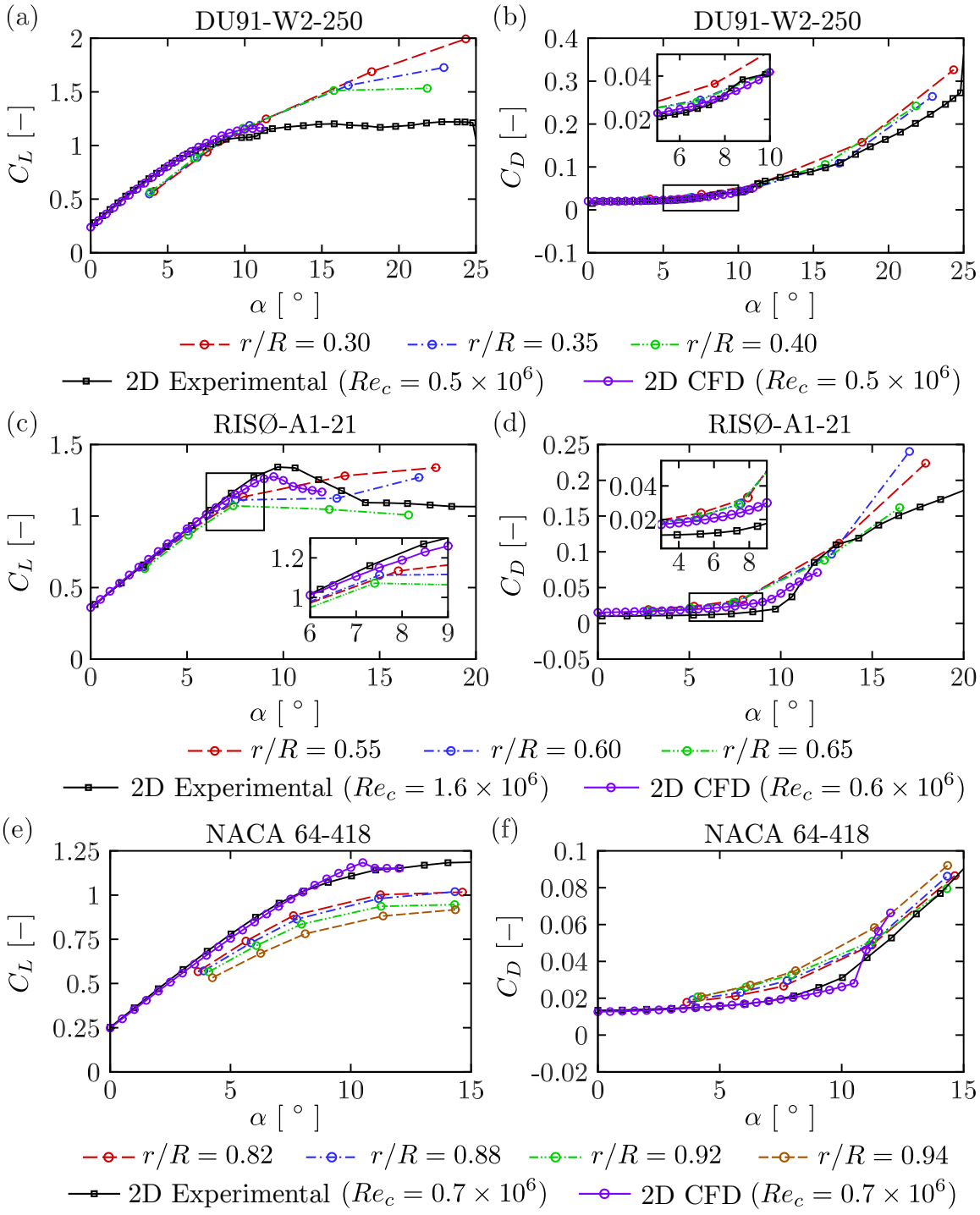

Figure 4.13: Lift and drag polars extracted from blade resolved computations of the MEXICO rotor. The DU91-W2-250 aerofoil extends from $r/R = 0.20$ to 0.46, the RISØ-A1-21 aerofoil extends from $r/R = 0.54$ to 0.66 and the NACA 64-418 aerofoil extends from $r/R = 0.74$ to 1.0.

(Sørensen et al. 2002, Bechmann et al. 2011). Along the mid-span of the blade (from $r/R = 0.54$ to 0.66), the RISØ-A1-21 aerofoil sections are sufficiently far from the root and tip for three-dimensional flow effects to be insignificant. As a result, the extracted lift and drag polars show close agreement with the 2D computational polars before the onset of stall. However, it should be noted that the peak lift coefficients for the RISØ-A1-21 aerofoil sections (at an angle of attack of around 10°) are not well resolved by the extracted polars. This could be remedied in future by increasing the number of data points (tip-speed-ratios) around the peak that the polars are extracted from.

4.2.4 Corrected Actuator Line Computations

Having extracted lift and drag polars from the blade resolved computations, three different sets of actuator line computations were carried out at tip-speed-ratios of 6.67 and 10.0. The first set of computations used the 2D computationally derived lift and drag polars and did not include any corrections. These computations will be used as a reference case to assess the relative improvement achieved by the other computations. The second set of computations also used the 2D computationally derived lift and drag polars but with the semi-empirical correction factor of Shen et al. (2005) applied to the blade forces. For now, this set of computations will be used to represent the standard approach that is adopted in the literature to account for tip flow effects in the actuator line method. This method of correcting the actuator line method will be revisited and discussed in more detail in Section 4.3. The third set of computations used the lift and drag polars that were extracted from the blade resolved computations in Section 4.2.3. As this set of polars already includes three-dimensional flow effects, no additional corrections were applied. Fig. 4.14 shows the axial and tangential forces per unit span computed by the three sets of actuator line computations.

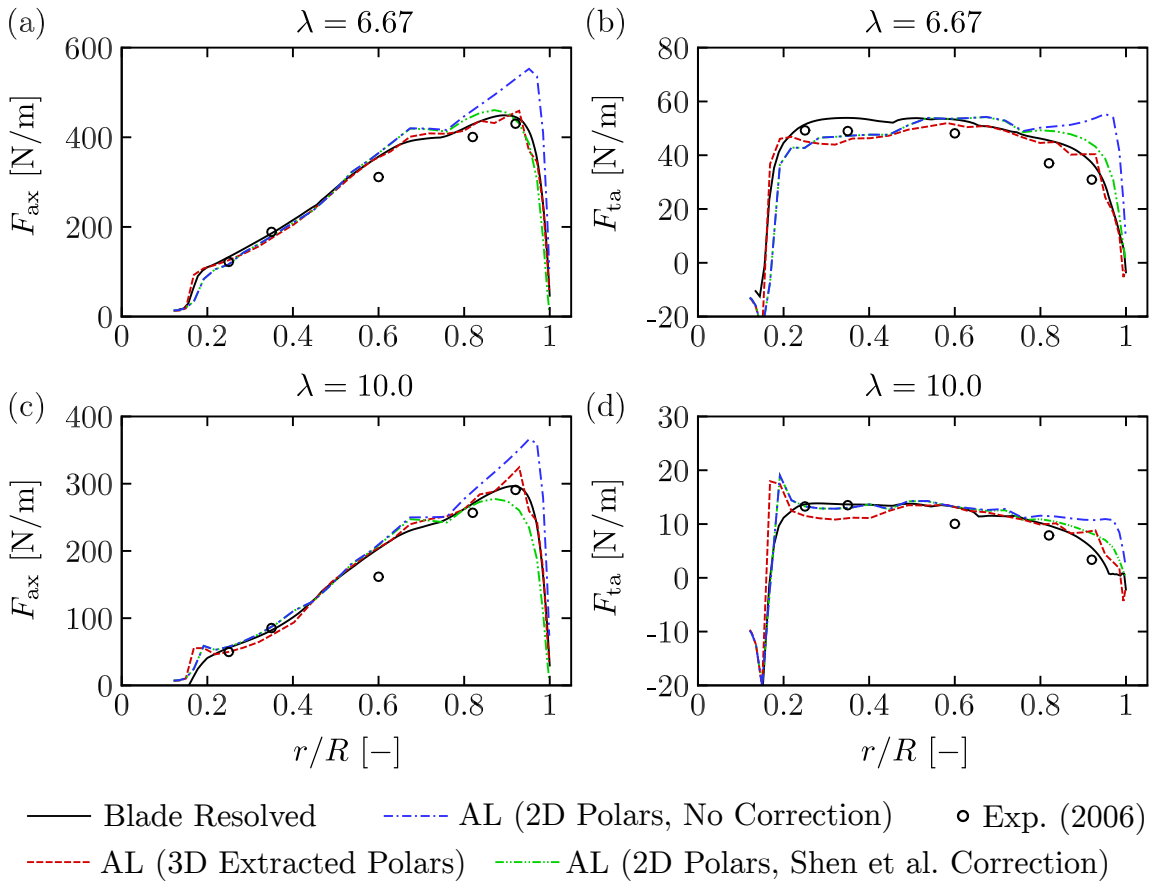

Figure 4.14: Axial and tangential forces per unit span for the MEXICO rotor at tip-speed-ratios of 6.67 (a and b) and 10.0 (c and d). 'AL' refers to actuator line whereas 'BR' refers to blade resolved. 'Exp. (2006)' refers to the first round of experimental measurements presented by Schepers et al. (2012).

As shown in Fig. 4.14, the axial and tangential forces per unit span are both considerably over-predicted on the outboard blade sections ($r/R > 0.8$) when the uncorrected 2D lift and drag polars are adopted. For example, at $r/R = 0.9$ the axial force per unit span is over-predicted by 67.0 N/m (14.9%) and the tangential force per unit span is over-predicted by 12.3 N/m (30.7%), at a tip-speed-ratio of 6.67. With the semi-empirical correction factor of Shen et al. included, the axial force per unit span over-prediction at $r/R = 0.9$ reduces to 6.3 N/m (1.4%), while the tangential force per unit span over-prediction reduces to 6.2 N/m (15.4%). However, this correction is still sub-optimal as the correction factor of Shen et al. (2005) (in its original formulation) is isotropic and does not allow the sectional force vector

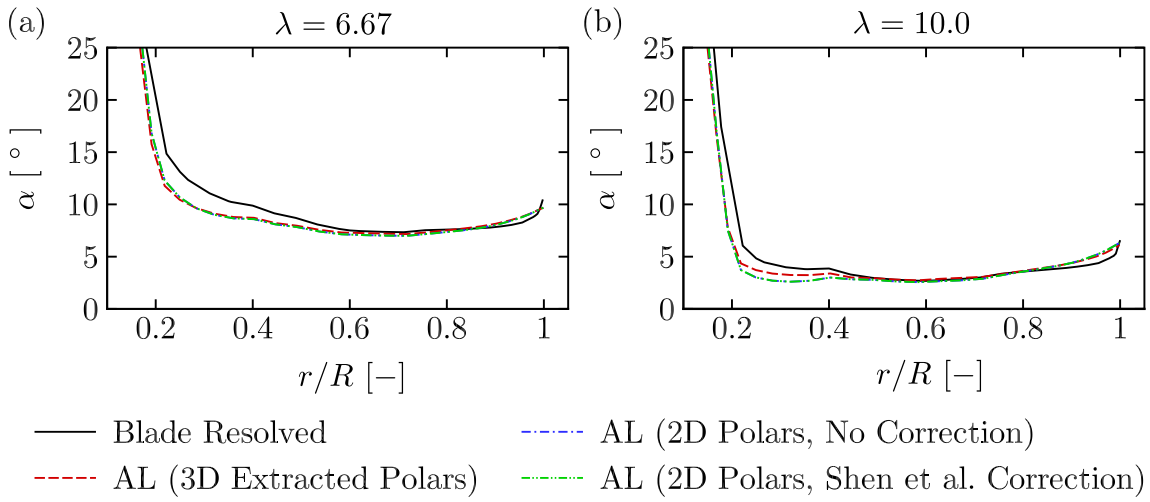

Figure 4.15: Angle of attack distribution for the MEXICO rotor at tip-speed-ratios of 6.67 and 10.0. The blade resolved data is taken from post-computation analysis using the azimuthal-average induction factor method, whilst the actuator line data is computed from the blade element diagram during the computation.

to rotate towards the streamwise direction. The closest agreement with the blade resolved computations is achieved by the actuator line computations with the (3D) extracted polars. When these extracted polars are adopted, the axial force per unit span at $r/R = 0.9$ is only over-predicted by 1.9 N/m (0.4%), while the tangential force per unit span is only over-predicted by 0.4 N/m (0.9%). This additional improvement is enabled by the anisotropic nature of the polars that are extracted from the blade resolved computations. More specifically, the sectional force vector can reduce in magnitude and rotate towards the streamwise direction as the tip of the blade is approached, as the lift coefficient decreases while the drag coefficient increases on the outboard blade sections.

Despite the improved agreement that the actuator line computations achieve on the outboard blade sections by using the (3D) extracted polars, the axial and tangential forces per unit span are under-predicted on the inboard blade sections ($r/R < 0.4$). As shown in Fig. 4.15, this can be attributed to the actuator line computations under-predicting the angle of attack on the inboard blade sections. At $r/R = 0.25$ for example, the actuator line computations predict an angle of attack

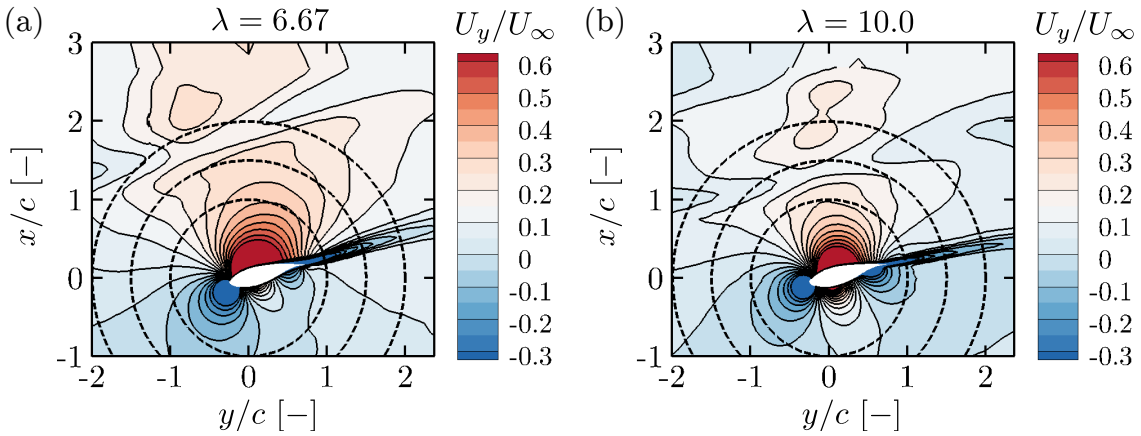

Figure 4.16: Contour plots of the lateral velocity component U_y (relative to the blade) on a horizontal slice through the blade at $r/R = 0.25$, for tip-speed-ratios of 6.67 and 10.0. The dashed lines indicate concentric circles of radius 1, 1.5 and 2 chord lengths, centred on the local quarter chord. The non-conformal cell interface at the edge of the inner domain is located at $x/c = 2.68$. The coordinate system is global (not relative to the local aerofoil section), the freestream velocity is in the positive x direction and the rotor plane is located at $x/c = 0$.

that is approximately 2.6° (20.0%) lower than the blade resolved computations at a tip-speed-ratio of 6.67 and 1.79° (37.1%) lower at a tip-speed-ratio of 10. On the inboard sections, the angle of attack error arises because the wake of the upstream blade passes in close proximity to the downstream blade, as shown in Fig. 4.16. The passing wake leads to local flow field distortions in the immediate vicinity of the blade (less than 2 chord lengths away). Hence, the assumption of a uniform free stream and a point vortex (adopted in the vortex equivalence approach for sampling the flow field) is no longer accurate and the angle of attack is under-predicted. This error could potentially be mitigated by reducing the sampling distance (r_s) near the blade root. However, due to the relatively small contribution of the inboard sectional loads to the overall rotor thrust and power, this was not pursued further in this investigation.

In order to demonstrate the cumulative effect of the error in the spanwise loading distributions, Table 4.2 shows the computed thrust and power coefficients (C_T and C_P respectively) for the MEXICO rotor. Here the thrust and power coefficients are defined as,

$$C_T = \frac{T}{\frac{1}{2}\rho {U_\infty}^2 A} \tag{4.12}$$

$$C_P = \frac{P}{\frac{1}{2}\rho {U_\infty}^3 A} \tag{4.13}$$

where T is the total integrated rotor thrust, P is the total integrated rotor power, ρ is the density of air (1.225 kg/m^3) and A is the swept area of the rotor.

Table 4.2: Thrust and power coefficients for the MEXICO rotor at tip-speed-ratios of 6.67 and 10.0. The percentage differences have been expressed relative to the blade resolved computations. AL refers to actuator line.

	λ [-]	C_T [-]	C_P [-]	ΔC_T [%]	ΔC_P [%]
Blade Resolved	6.67	0.776	0.446		
AL (3D Extracted Polars)	6.67	0.771	0.427	-0.64	-4.26
AL (2D Polars, Shen et al. Correction)	6.67	0.774	0.468	-0.26	+4.93
AL (2D Polars, No Correction)	6.67	0.828	0.495	+6.70	+10.99
Blade Resolved	10.0	1.004	0.3226		
AL (3D Extracted Polars)	10.0	1.024	0.3395	+1.99	+5.24
AL (2D Polars, Shen et al. Correction)	10.0	1.002	0.3674	-0.20	+13.89
AL (2D Polars, No Correction)	10.0	1.108	0.3988	+10.36	+23.62

The actuator line computations with the original uncorrected (2D) polars over-predict the thrust coefficient by 6.70% at a tip-speed-ratio of 6.67 and by 10.36% at a tip-speed-ratio of 10.36. The power coefficient over-prediction is even greater, with an over-prediction of 10.99% at a tip-speed-ratio of 6.67 and an over-prediction of 23.62% at a tip-speed-ratio of 10.0. The error is particularly large for these computations because of the significant over-prediction of the axial and tangential forces per unit span on the outboard blade sections (see Fig. 4.14). The outboard blade sections are the dominant contributors to the total thrust and torque, due to the moment arm of the aerofoil sections and the increased dynamic pressure incident on the aerofoil sections from the rotational velocity component. Hence, errors in the spanwise loading distribution are magnified in the thrust and power coefficients.

With the correction factor of Shen et al. (2005) applied to the original (2D) polars (the standard approach adopted in the literature), the error in the thrust and power coefficients is reduced significantly. For example, the error in the power coefficient is reduced by 6.06% at a tip-speed-ratio of 6.67 and by 9.73% at a tip-speed-ratio of 10.0. However, it should be noted that this correction factor is (currently) calibrated to the NREL Phase IV and the Swedish WG 500 rotors. Hence, the improvement can only be considered coincidental at this stage, until the correction factor is re-calibrated to the MEXICO rotor in section 4.3.

The closest agreement with the blade resolved computations is achieved by the actuator line computations that adopt the lift and drag polars extracted from the blade resolved computations. This is predominantly due to the close agreement achieved on the outboard sections of the blade. The small remaining discrepancy in the power coefficient (4.26%) is due to the under-prediction of the tangential force per unit span on the inboard blade sections. This in turn is due to the angle of attack under-prediction shown in Fig. 4.15. Hence, further improvements to the method that is used to determine the angle of attack on the inboard sections may lead to even closer agreement with the blade resolved computations in future.

4.3 Tip Flow Correction Factors

As an alternative to replacing the original (2D) lift and drag polars with a set of lift and drag polars that are extracted directly from either blade resolved simulations or experimental measurements, a tip flow correction factor can be used. In this approach, the original (2D) lift and drag polars are left uncorrected, while the axial and tangential forces per unit span are multiplied by a correction factor before they are applied to the flow field. The correction factor reduces in magnitude as the tip of the blade is approached, so the blade loading is forced to drop off on the outboard

blade sections. This method is appealing as the angle of attack and relative velocity magnitude do not have to be extracted from either blade resolved computations or experimental measurements of the 3D rotor. Furthermore, the correction factor is straightforward to implement in a variety of low order rotor models that use the blade element method to compute the blade loading.

Several tip flow correction factors have already been proposed in the literature (see Lindenburg (2004), Shen et al. (2005) and Sant (2007) for example). However, they are often purely empirical and their relative accuracy has not yet been assessed, particularly when applied to rotors that were not used in their original calibration. In this work, the tip flow correction factor of Shen et al. (2005) will be adopted, since it is the most widely used in the wind energy industry.

The aim of this section is to assess the accuracy of the tip flow correction factor of Shen et al. and improve its calibration, by using the blade resolved computations of the MEXICO rotor that were presented in Chapter 3. In the next section, the same tip flow correction factor will then be applied to the two different tidal turbine rotor designs that are introduced in Chapter 5 (Rotor 1 and Rotor 2), in order to assess its applicability to higher solidity tidal turbine rotors that typically operate at lower tip-speed-ratios.

4.3.1 Tip Flow Correction Factor of Shen et al.

The semi-empirical tip flow correction factor (F_1) proposed by Shen et al. (2005) takes the following form,

$$F_1 = \frac{2}{\pi}\cos^{-1}\left[\exp\left(-g_1\frac{N(R-r)}{2r\sin(\phi)}\right)\right] \tag{4.14}$$

where N represents the number of blades, ϕ the angle of the incident flow vector to the rotor plane, r the spanwise distance along the blade from the axis of rotation and R the rotor radius. The functional form of F_1 was originally chosen by Shen et al. to

closely follow the Glauert (1935) correction factor, which was originally derived using an idealised model of the rotor wake. This functional form also provides the desired asymptotic behaviour at the root ($F_1 \rightarrow 1$) and tip ($F_1 \rightarrow 0$) of the blade, so that (when multiplied by F_1) both the axial and tangential forces per unit span are forced to zero as the tip is approached. Furthermore, for a rotor with an infinite number of blades ($N \rightarrow \infty$) or running at an infinite tip-speed-ratio ($\sin(\phi) \rightarrow 0$), $F_1 \rightarrow 1$ so the rotor behaviour tends towards that of an actuator disc. The only difference with the functional form of the Glauert correction factor is the empirical parameter g_1, which is calibrated to experimental data.

$$g_1 = \exp\left(-c_1(N\lambda - c_2)\right) + 0.1 \tag{4.15}$$

$\lambda = \Omega R/U_\infty$ represents the tip-speed-ratio of the rotor and c_1 and c_2 are empirical coefficients (0.125 and 21.0 respectively) that were originally calibrated by Shen et al. to experimental data from the NREL Phase VI rotor at a tip-speed-ratio of 3.79 and the Swedish WG 500 rotor at a tip-speed-ratio of 14.0. These two rotors were originally chosen to cover a wide range of tip-speed-ratios. However, Shen et al. note that more experimental and computational data is still required to improve the applicability of g_1 to other rotors. In this investigation, blade resolved computations of the MEXICO rotor will be used to provide additional data points for the intermediate tip-speed-ratios (6-10) and improve the calibration of the correction factor.

In the original implementation of the correction factor, Shen et al. multiply both the axial and the tangential forces per unit span by the same correction factor F_1. Hence, the axial and tangential forces per unit span are both forced to drop off at the same rate as the tip of the blade is approached. With this implementation of the correction factor, the sectional force vector reduces in magnitude but cannot rotate towards the streamwise direction as the tip of the blade is approached. To allow the sectional force vector to rotate towards the streamwise direction and better follow

the observed drop off in blade loading, the correction factor F_1 will be calibrated separately in the axial and tangential directions in this work.

4.3.2 Calibrating the Correction Factor

To calibrate the correction factor of Shen et al. to the MEXICO rotor, the axial and tangential forces per unit span were first extracted from the (uncorrected) actuator line (F_{ax}^{AL} and F_{ta}^{AL}) and blade resolved (F_{ax}^{BR} and F_{ta}^{BR}) computations of the MEXICO rotor. The ratio of these two sets of forces represents the fractional reduction in the axial and tangential forces per unit span due to tip flow effects that are not captured by the (uncorrected) actuator line method.

$$F_{1,\text{ax}} = \frac{F_{\text{ax}}^{BR}}{F_{\text{ax}}^{AL}} \tag{4.16}$$

$$F_{1,\text{ta}} = \frac{F_{\text{ta}}^{BR}}{F_{\text{ta}}^{AL}} \tag{4.17}$$

Having computed each of these ratios, a function of the form given by F_1 (equation 4.14) was fitted to each ratio using a least-squares regression analysis, with the distribution of ϕ taken from the actuator line computations. Only the data on the outboard blade sections was used for the regression analysis ($r/R > 0.8$), as the correction factor is only intended to capture the three-dimensional flow effects associated with the tip loss mechanism on the outboard blade sections. Furthermore, the very tip of the blade ($r/R > 0.95$) was excluded from the regression analysis, as the data was found to be unreliable here due to the tip geometry. Fig. 4.17 shows the computed ratios ($F_{1,\text{ax}}$ and $F_{1,\text{ta}}$) and the best fit to the data, at tip-speed-ratios of 7 and 10, to demonstrate the process.

The data fits were all partially restricted by the functional form of F_1. At a tip-speed-ratio of 10 in particular, the tangential force per unit span (from the blade resolved computations) tends to zero before the very tip of the blade. Such a situation

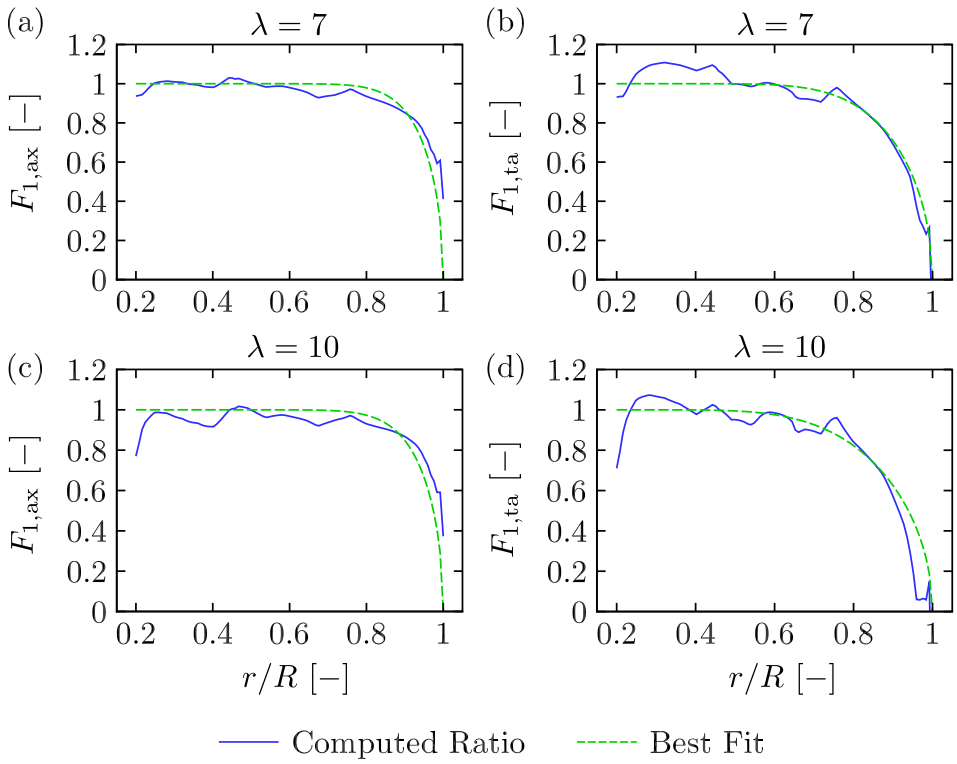

Figure 4.17: Curve fits of the computed data to the function F_1 in the axial and tangential directions, at tip-speed-ratios of 7 and 10.

can arise physically for $r/R < 1$ as $L\sin(\phi) - D\cos(\phi) \to 0$ as $\phi \to 0$. This behaviour is more likely to occur at high tip-speed-ratios, as ϕ reduces with increasing tip-speed-ratio. Despite this observation, the computed ratio cannot be captured exactly with the current functional form of F_1, as F_1 only tends to zero at the very tip of the blade. Hence, an alternative form of F_1 may lead to a better fit of the computed ratios, particularly at high tip-speed-ratios.

4.3.3 Strength of the Correction Factor

The best fit of the function F_1 to the computed ratios ($F_{1,\mathrm{ax}}$ and $F_{1,\mathrm{ta}}$) at each tip-speed-ratio results in a unique value of g_1 in the axial and tangential directions (here denoted $g_{1,\mathrm{ax}}$ and $g_{1,\mathrm{ta}}$ respectively). g_1 can be physically interpreted as the strength of the correction factor, with a smaller value of g_1 resulting in a smaller value of F_1 and hence a stronger correction, as shown in Fig. 4.18. A smaller value of g_1 therefore

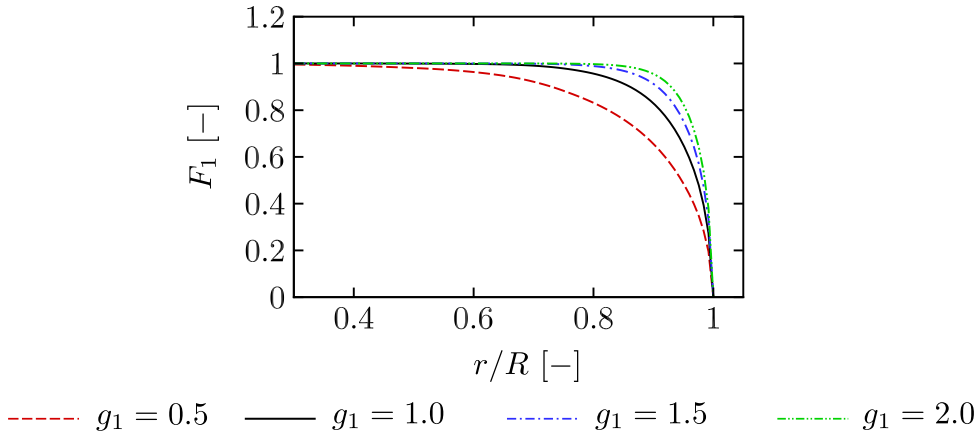

Figure 4.18: Variation of F_1 with g_1 at a tip-speed-ratio of 7.

implies that tip flow effects are more significant and a stronger correction is required.

Fig. 4.19 shows the computed values of $g_{1,\mathrm{ax}}$ and $g_{1,\mathrm{ta}}$, plotted against the product of the tip-speed-ratio and number of blades $N\lambda$ (which represents the blade passing frequency), to allow direct comparison with equation 4.15. Two new curve fits have also been included in Fig. 4.19. Curve fit 1 was performed by fitting equation 4.15 to the MEXICO data points alone (excluding the data point at $N\lambda = 30$ due to aforementioned difficulties in the curve fitting process at high tip-speed-ratios). This curve fit represents the approach that might be taken to calibrate the tip flow correction to a specific rotor. Curve fit 2 was performed by fitting equation 4.15 to the MEXICO data points (excluding $N\lambda = 30$), the NREL Phase VI rotor and the Swedish WG 500 rotor. This curve fit represents the approach that might be taken to move towards a more general tip flow correction that can be applied to new rotors, using all the available data. Unfortunately, curve fit 2 does not give good agreement with the MEXICO data points. This is because the NREL Phase VI rotor data point (at $N\lambda = 7.58$) leads to a significant distortion of the curve fit at higher tip-speed-ratios. Hence, more experimental and computational data is clearly required before a more general form of $g_{1,\mathrm{ax}}$ and $g_{1,\mathrm{ta}}$ can be proposed.

In the axial direction, the original curve fit adopted by Shen et al. (2005) shows good agreement with the computed data points for the MEXICO rotor. Hence, the

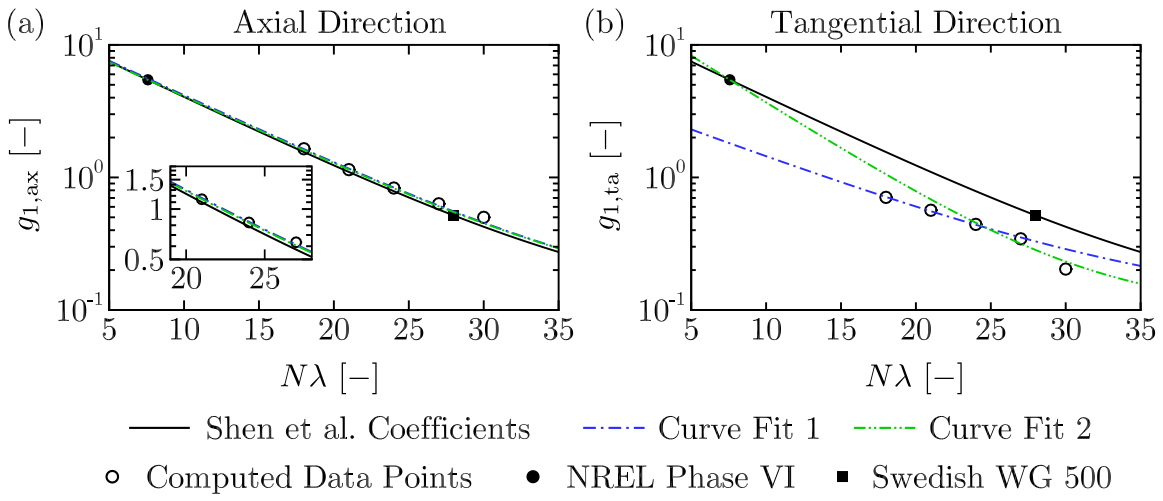

Figure 4.19: Computed values of g_1 in the (a) axial and (b) tangential directions. Curve Fit 1 was performed using the computed data points for the MEXICO rotor alone (excluding the data point $N\lambda = 30$). Curve Fit 2 was performed using the computed data points for the MEXICO rotor (excluding the data point $N\lambda = 30$), the NREL Phase VI rotor and the Swedish WG 500 rotor data points. The MEXICO rotor has 3 blades ($N = 3$), the NREL Phase VI rotor has 2 blades ($N = 2$) and the Swedish WG 500 rotor has 2 blades ($N = 2$).

original curve fit would be a reasonable first approximation for correcting the axial force per unit span. It follows that an alternative functional form of F_1 is required to further improve the axial force per unit span, as further calibrating the current functional form of F_1 will only result in limited improvement.

For the MEXICO rotor, the computed values of g_1 are much lower in the tangential direction than the axial direction. Hence, a much stronger correction is required in the tangential direction than the axial direction. As discussed earlier in Section 4.1.3, this is because the total sectional force vector reduces in magnitude and rotates towards the streamwise direction as the tip of the blade is approached, so the tangential force per unit span drops off more aggressively than the axial force per unit span. The original correction factor proposed by Shen et al. does not allow the total sectional force vector to rotate, as the same correction is applied to the axial and tangential forces per unit span. Hence, the original curve fit considerably over-predicts the required values of $g_{1,\mathrm{ta}}$ for the MEXICO rotor. An alternative curve fit is clearly

required in the tangential direction to avoid this over-prediction and account for the anisotropy of the total sectional force vector (curve fit 1 being the most appropriate here).

Table 4.3 shows the empirical coefficients (c_1 and c_2) that correspond with the curve fits in Fig. 4.19. With reference to equation 4.15, c_1 represents the gradient of g_1 and c_2 represents the horizontal shift along the $N\lambda$ axis. In the axial direction, the computed values of c_1 and c_2 from curve fit 1 and 2 are within 2.8% of 2.4% of the values proposed by Shen et al.. These observations suggest that an isotropic correction factor would be a reasonable first approximation for correcting the axial force per unit span (and hence the rotor thrust). However, the large discrepancy in the tangential direction shows that an anisotropic correction is essential to accurately correct the tangential force per unit span (and hence the rotor torque).

Table 4.3: Empirical coefficients for the functions $g_{1,\mathrm{ax}}$ and $g_{1,\mathrm{ta}}$.

	$g_{1,\mathrm{ax}}$		$g_{1,\mathrm{ta}}$	
	c_1	c_2	c_1	c_2
Shen et al.	0.125	21.0	0.125	21.0
Curve Fit 1	0.1219	21.52	0.0984	13.026
Curve Fit 2	0.1215	21.39	0.1652	17.732

4.3.4 Corrected Actuator Line Computations

Fig. 4.20 shows the axial and tangential forces per unit span computed with the actuator line method and the three sets of empirical coefficients presented in Table 4.3. The actuator line computations with no correction factor have also been included for reference, along with the blade resolved computations, which represent the target values. In the axial direction, all three sets of empirical coefficients result in a similar reduction in the axial force per unit span, with a maximum difference of 1.4% between the values at $r/R = 0.9$. This observation confirms that the original empirical

coefficients of Shen et al. would be a reasonable first approximation to correcting the axial force per unit span. However, the axial force per unit span still does not match the blade resolved computations exactly. As discussed in Section 4.3.3, this is due to the functional form of F_1, which cannot exactly fit the computed data on the outboard blade sections.

With the original empirical coefficients of Shen et al., the tangential force per unit span is over-predicted over the entire range of computed tip-speed-ratios. For example, at $r/R = 0.9$ and $\lambda = 7$, the tangential force per unit span is over-predicted by 21.3%. These over-predictions are due to the values of $g_{1,\mathrm{ta}}$ being too large for the MEXICO rotor and the sectional force vector being unable to rotate sufficiently towards the streamwise direction. By adopting lower values of $g_{1,\mathrm{ta}}$ and allowing the sectional force vector to rotate, curve fits 1 and 2 achieve a further reduction in the tangential force per unit span, resulting in much closer agreement with the blade resolved computations. For example, at $r/R = 0.9$ and $\lambda = 7$, the tangential force per unit span is now only over-predicted by 1.3% using curve fit 1 and 3.9% by curve fit 2, which highlights the potential improvement that can be attained by calibrating g_1 separately in the axial and tangential directions.

Fig. 4.21 demonstrates the resulting error in the thrust and power coefficients that is incurred by inaccurately predicting the spanwise loading distributions. At a tip-speed-ratio of 7, the actuator line computations with no correction over-predict the thrust coefficient by 8.7% and the power coefficient by 15.1%. The inclusion of the tip correction factor reduces this discrepancy significantly in all cases. At a tip-speed-ratio of 7, the thrust coefficient is now only over-predicted by a maximum of 1.4% by the corrected actuator line computations. With the original empirical coefficients of Shen et al., the power coefficient is over-predicted by 6.3% at a tip-speed-ratio of 7. This represents a considerable improvement over the original over-prediction of 15.1%. However, curve fits 1 and 2 achieve an ever closer agreement with the blade

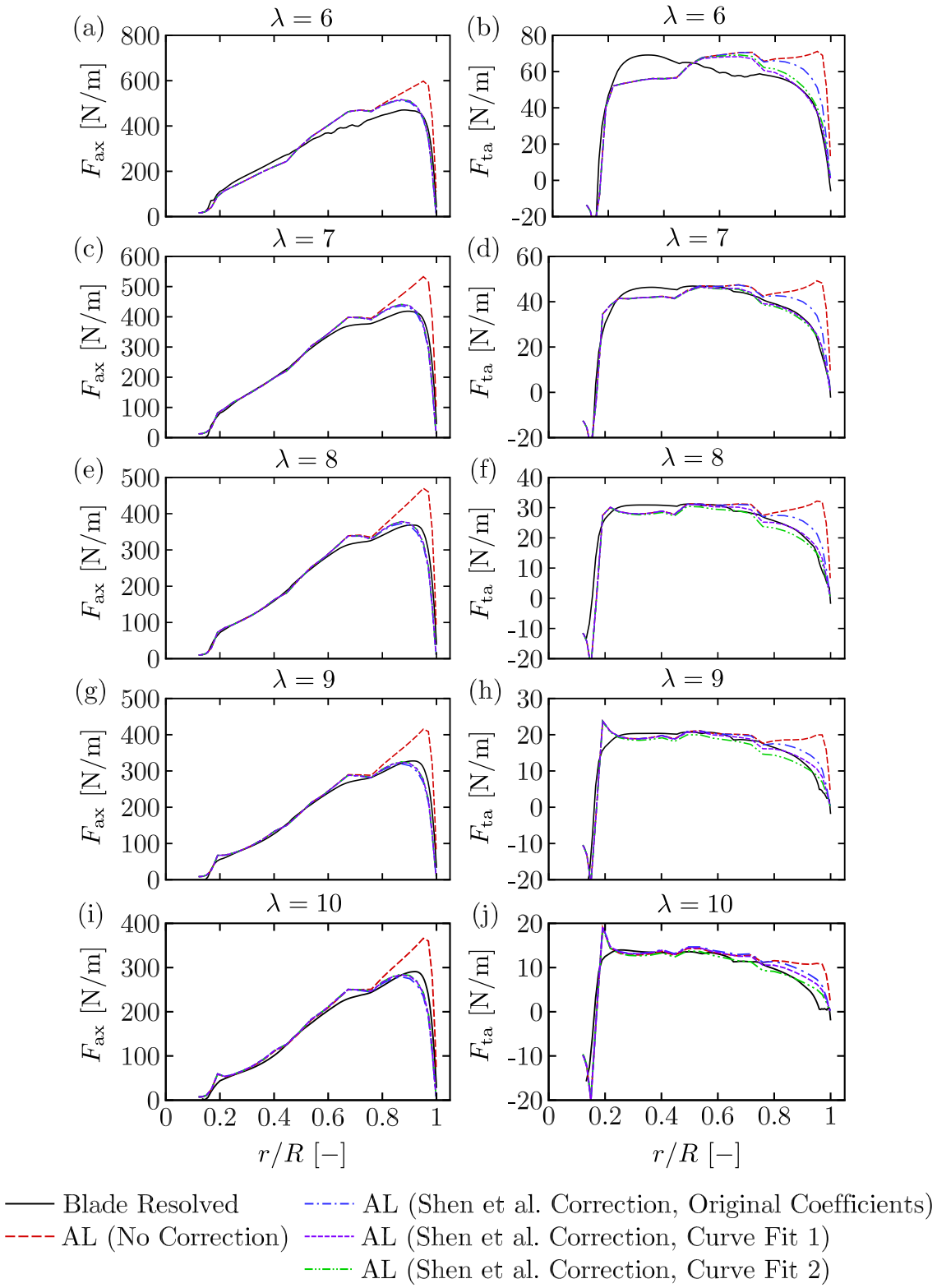

Figure 4.20: Axial and tangential forces per unit span for tip-speed-ratios of 6, 7, 8, 9 and 10, using the actuator line (AL) and blade resolved approaches.

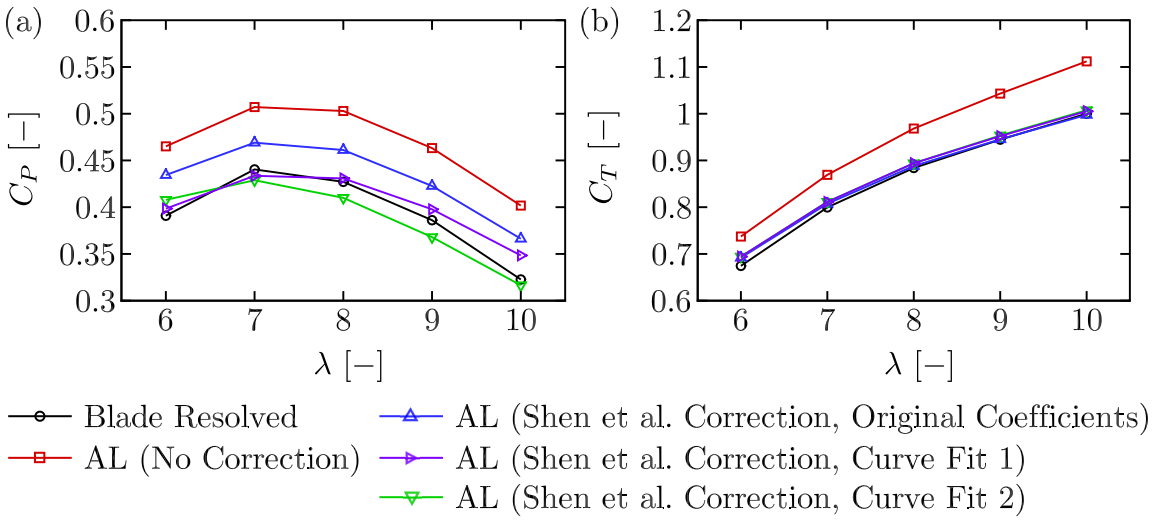

Figure 4.21: Power and thrust coefficients for the MEXICO rotor, computed with the actuator line and blade resolved approaches. AL refers to actuator line.

resolved computations, by accounting for the anisotropy of the sectional force vector. At a tip-speed-ratio of 7, the power coefficient is now only under-predicted by 1.6% by curve fit 1 and 2.7% by curve fit 2. The small remaining under-prediction can be attributed to the under-prediction of the tangential force per unit span on the inboard sections of the blade (which can be seen in Fig. 4.20).

At high tip-speed-ratios, the power coefficient computed with the corrected actuator line computations shows a less comprehensive agreement with the blade resolved computations. By observing the tangential force per unit span in Fig. 4.20, this can be attributed to the functional form of F_1 being unable to capture the spanwise variation of the blade loading near the tip. Hence, an alternative functional form of F_1 may lead to further improvement in the computed power coefficients at high tip-speed-ratios.

4.4 Tip Flow Corrections for Tidal Turbines

Tidal turbine blades are usually thicker and have a higher aspect ratio than wind turbine blades, in order to support higher thrust. With greater chord lengths (and

often blunt tip geometries) the strength of the shed vorticity and the spanwise flow accelerations that are induced along the blade are likely to be much stronger than on typical wind turbine blades. Hence, the blade loading on high solidity tidal turbine rotors is likely to drop off at a different rate to low solidity wind turbine rotors as the tip is approached. Furthermore, tidal turbine rotors operate over a lower range of operational tip-speed-ratios (typically 4-6) than utility-scale wind turbine rotors (typically 7-11), in order to avoid the onset of cavitation. Hence, the tip flow corrections that were originally developed for wind turbines may need to be re-calibrated if they are to be applied successfully to tidal turbine rotors.

In this section, the two tidal turbine rotors that are introduced and described in Chapter 5 (Rotor 1 and Rotor 2) will be used to re-calibrate the tip flow correction factor of Shen et al.. Having re-calibrated the correction factor, new actuator line computations will be undertaken to demonstrate the resulting improvement that can be achieved by re-calibrating the correction factor specifically to tidal turbine rotors.

4.4.1 Re-calibrating the Correction Factor

To re-calibrate the correction factor to Rotor 1 and Rotor 2, (uncorrected) actuator line computations were carried out over a range of tip-speed-ratios (4.5-7 for Rotor 1 and 4-6 for Rotor 2) in a virtually unblocked domain (a blockage ratio of 0.01). The computed axial and tangential forces per unit span (F_{ax}^{AL} and F_{ta}^{AL}) were then used in combination with the blade resolved computations (presented in Chapter 5) to compute values of $g_{1,\mathrm{ax}}$ and $g_{1,\mathrm{ta}}$ at each tip-speed-ratio (using the procedure described in section 4.3.2). Fig. 4.22 shows the values of $g_{1,\mathrm{ax}}$ and $g_{1,\mathrm{ta}}$ that were computed for Rotor 1 and Rotor 2, along with the values that were computed for the MEXICO rotor in Section 4.3.3, for further comparison.

Both Rotor 1 and Rotor 2 exhibit lower values of g_1 in the tangential direction than the axial direction, indicating that a stronger correction is required to the tan-

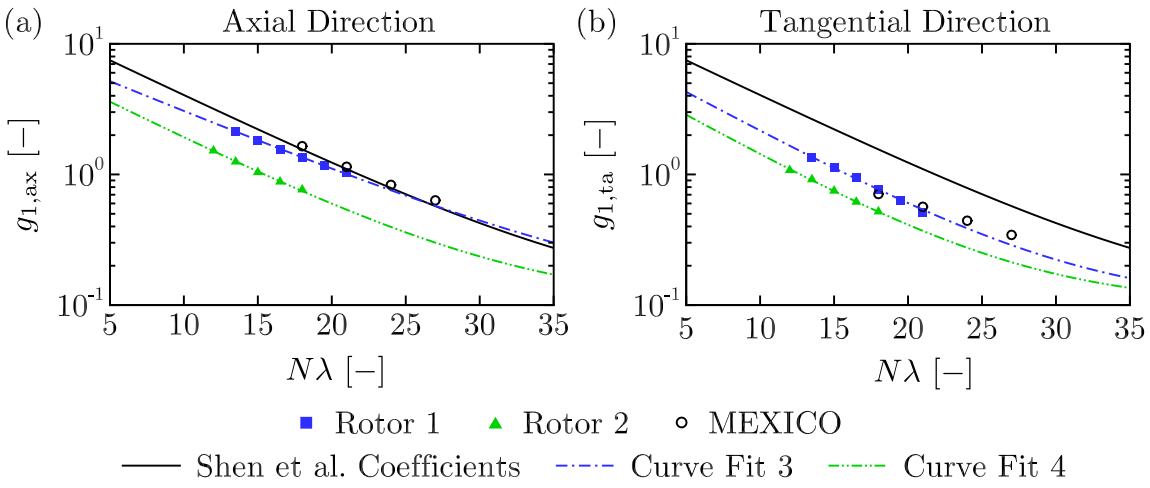

Figure 4.22: Computed values of g_1 in the axial and tangential directions for Rotor 1 and Rotor 2. Curve Fit 3 was performed using the data points for Rotor 1. Curve Fit 4 was carried out using the data points for Rotor 2.

gential force per unit span than the axial force per unit span. This behaviour is also exhibited by the MEXICO rotor and arises because the sectional force vector reduces in magnitude and rotates towards the streamwise direction as the tip of the blade is approached.

Fig. 4.22 also shows that Rotor 1 (the low solidity rotor) experiences a similar reduction in axial and tangential forces per unit span to the MEXICO rotor. This is because Rotor 1 was originally designed for unblocked conditions and hence has a similar chord and twist distribution to the MEXICO rotor. However, Rotor 2 (the high solidity rotor) experiences a much stronger reduction in axial and tangential forces per unit span than both Rotor 1 and the MEXICO rotor. This is because tip flow effects are stronger for high solidity rotors, so they require a more aggressive correction. Hence, Fig. 4.22 suggests that the strength of the tip flow correction (g_1) should be dependent on the blade geometry, in addition to the parameter representing the blade passing frequency ($N\lambda$). However, g_1 does not contain any blade shape functional dependency and there is insufficient data to propose such a dependency at this stage (more rotors need to be analysed).

As an alternative approach, two separate curve fits were carried out for $g_{1,\mathrm{ax}}$ and

$g_{1,\mathrm{ta}}$ instead. These curve fits are specific to Rotor 1 and Rotor 2 and are referred to as 'Curve Fit 3' and 'Curve Fit 4' respectively, in Fig. 4.22. With this approach, the blade shape dependency is directly captured in the empirical coefficients c_1 and c_2 that are generated by this curve fitting process. Table 4.4 shows the empirical coefficients that are generated for Rotor 1 and Rotor 2, which will be used to carry out corrected actuator line computations in the next section.

Table 4.4: Empirical coefficients for $g_{1,\mathrm{ax}}$ and $g_{1,\mathrm{ta}}$.

	$g_{1,\mathrm{ax}}$		$g_{1,\mathrm{ta}}$	
	c_1	c_2	c_1	c_2
Shen et al.	0.125	21.00	0.125	21.00
Rotor 1	0.108	20.90	0.141	15.15
Rotor 2	0.130	14.65	0.145	12.00

4.4.2 Corrected Actuator Line Computations

Fig. 4.23 shows the axial force per unit span, the tangential force per unit span and the angle of the sectional force vector to the rotor plane, computed with the actuator line method and the three sets of empirical coefficients presented in Table 4.4, at a tip-speed-ratio of 5. In the axial and tangential directions, the actuator line computations with the original coefficients of Shen et al. give a slightly closer agreement with the blade resolved computations than the uncorrected computations. However, the angle of the sectional force vector is not improved with this calibration. This is because the same correction factor is applied in the axial and tangential directions and hence only the magnitude of the sectional force vector is reduced. With the new calibration, both the axial and tangential forces per unit span achieve an even closer agreement with the blade resolved computations. In addition, the angle of the sectional force vector also achieves a slightly closer agreement, as a stronger

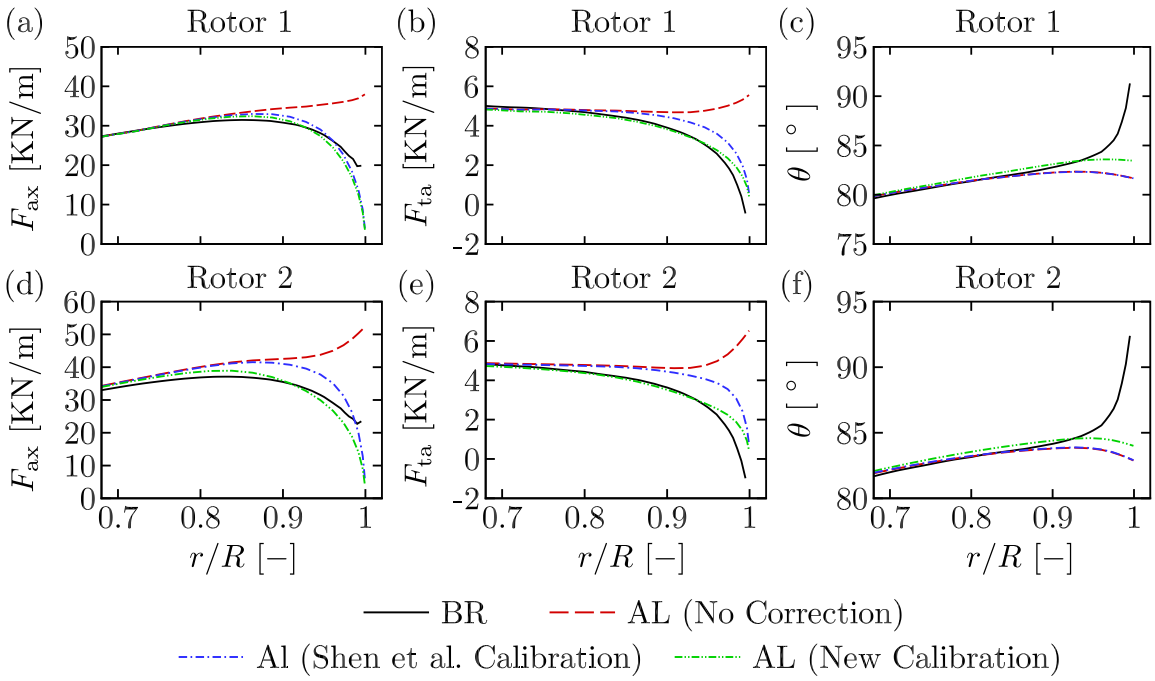

Figure 4.23: Axial force per unit span (a and d), tangential force per unit span (b and e) and angle of the sectional force vector to the rotor plane (c and f), for Rotor 1 and Rotor 2 at a tip-speed-ratio of 5. BR refers to the blade resolved computations and AL refers to the actuator line computations.

correction is applied in the tangential direction than the axial direction. However, despite these improvements, the angle of the sectional force vector still does not match the blade resolved computations sufficiently near the blade tip. This is because the angle of the sectional force vector is limited by the functional form of F_1, which cannot increase above 90°, regardless of its calibration. This limitation is likely to become particularly problematic at higher tip-speed-ratios, as the angle of the incident flow to the rotor plane (ϕ) is already small and hence the initial angle of the sectional force vector is close to 90°.

Fig. 4.24 shows the thrust and power coefficients for Rotor 1 and Rotor 2. With no correction factor applied, the thrust and power coefficients are significantly over-predicted over the entire range of computed tip-speed-ratios. For example, at a tip-speed-ratio of 5, C_P is over-predicted by 11.7% for Rotor 1 and 20.3% for Rotor 2. With the tip correction factor of Shen et al. applied, the error is significantly

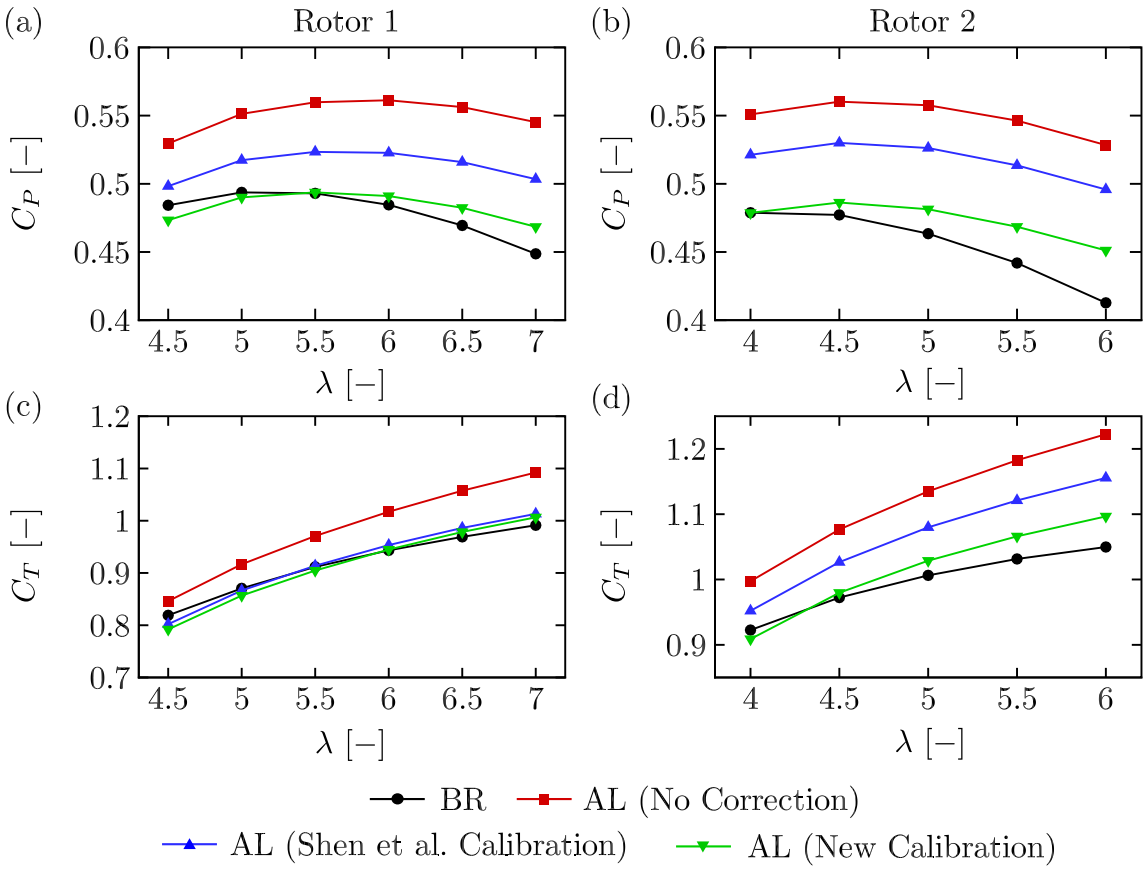

Figure 4.24: Power and thrust coefficients for Rotor 1 and Rotor 2 using the blade resolved (BR) and actuator line (AL) approaches.

reduced in all cases. For example, at a tip-speed-ratio of 5, C_P is only over-predicted by 4.78% for Rotor 1 and 13.5% for Rotor 2 when using the original calibration of Shen et al.. Further improvement to the thrust and power coefficients is achieved by using the new calibration presented in this work. At a tip-speed-ratio of 5, C_P is now only under-predicted by 0.75% for Rotor 1 and over-predicted by 3.86% for Rotor 2.

4.5 Limitations of the Near-Tip Analysis

The near-tip analysis presented in this chapter has a limited range of applicability. Firstly, the flow field incident on the outboard blade sections must be locally steady, as the interaction of the spanwise pressure gradients with the unsteady response of

the outboard aerofoil sections remains unknown. Hence, conditions where the flow is highly sheared across the swept area of the rotor, the channel cross-section is highly anisotropic and/or tower shadow effects are strong, are inappropriate for the current near-tip analysis. Furthermore, at high blockage ratios the spanwise pressure gradients on the outboard blade sections and the trajectory of the shed vorticity are modified by the domain boundaries and effective symmetry plane between neighbouring devices. The degree of blockage at which these affects become significant is currently unknown. Hence for flow conditions where any of these effects are likely to be significant, blade resolved computations are essential until the behaviour of the tip loss mechanism is better understood. For example, the computations of the tidal turbine rotor carried out in Chapter 7 are clearly inappropriate for a tip flow corrected reduced order model (such as the actuator line method), due to the strong velocity shear, high blockage ratio and square channel cross-section required for the investigation. Hence, blade resolved computations will be carried out in Chapter 7 instead, as tip flow effects can be captured under these unsteady conditions.

4.6 Summary

In this chapter, a mechanism has been proposed to account for the drop off in blade loading that occurs as the tip of a rotor blade is approached (the tip loss mechanism). The shed vorticity on the outboard blade sections induces a downwash at the rotor plane and spanwise flow accelerations along the blade surfaces (outboard on the pressure surface, around the tip and inboard on the suction surface). This induction modifies the static pressure distribution on the blade surface, so that both the thrust and torque-producing forces drop off as the tip of the blade is approached. However, the torque-producing force drops off faster than the thrust-producing force, so the sectional force vector reduces in magnitude and rotates towards the streamwise di-

rection as the tip of the blade is approached. This is equivalent to the lift coefficient decreasing while the drag coefficient increases, on the outboard blade sections.

Two different methods were introduced that can be used to account for the drop off in blade loading as the tip of the blade is approached. Both methods can achieve a similar level of accuracy and account for the same tip flow mechanism. In the first method, the lift and drag polars (which are conventionally derived from 2D experiments or computations) are replaced by a set of lift and drag polars that are extracted directly from either blade resolved computations or experimental measurements of the complete (3D) rotor. These extracted polars vary along the blade span, which enables three-dimensional flow effects to be captured within the set of polars. In the second method, the sectional blade forces (computed from the 2D lift and drag polars) are corrected using a semi-empirical correction factor, before they are applied to the flow field. Both methods considered in this chapter can account for the anisotropy of the changes in the sectional force vector, which allows them to achieve a much closer agreement with the blade resolved computations than when an isotropic tip flow correction is used. However, further calibration is still required if these methods are to accurately predict the performance of a variety of rotor designs. Tidal turbine rotors in particular, have thicker blades and can support stronger spanwise flow than low solidity wind turbine rotors, so they are likely to require a stronger tip flow correction.

Chapter 5

Cavitation Restrictions on Tidal Turbine Performance

There is a general desire to increase the design tip-speed-ratio of tidal turbine rotors, which is often around 4-6 and is much lower than the design tip-speed-ratio of utility-scale wind turbines (7-11). Higher design tip-speed-ratios increase the maximum theoretical power coefficient that can be achieved by the rotor and also reduce the maximum torque load, so a lighter drive train can be adopted (Ning & Dykes 2014). While the tip-speed-ratio of utility-scale wind turbines is mainly limited by noise constraints, the tip-speed-ratio of tidal turbine rotors is mainly limited by cavitation. More specifically, recent design guidelines for tidal turbines state that cavitation must be avoided completely during rotor operation (DNV GL 2015). To satisfy this requirement and avoid cavitation inception, restrictions must be placed on either the tip-speed-ratio or submersion depth of the rotor, with a large safety margin to account for the uncertainties in the analysis. These restrictions ultimately limit the thrust and power that can developed by the rotor and the energy extracted by MW of installed capacity. Hence, it is desirable to quantify the restrictions that cavitation inception places on the submersion depth and tip-speed-ratio of the rotor, so that the

safety margin can be relaxed and the thrust and power can be increased.

The majority of the cavitation analyses that have been carried out in the literature use the blade element method to carry out a sectional analysis of the minimum static pressure along the blade span (see Batten et al. (2008) and Buckland et al. (2013) for example). While these methods are computationally efficient, it has been shown in Chapter 4 that blade element based methods (currently) do not adequately account for tip flow effects. Tip flow effects increase the static pressure developed on suction surface of the blade, so the rotor is less likely to cavitate at a given tip-speed-ratio and submersion depth. As tip flow effects are (currently) not adequately accounted for by blade element based methods, the strength of the suction peak on the outboard blade sections is over-predicted by these methods and the resulting restrictions that are applied to the tip-speed-ratio and submersion depth of the rotor are overly-conservative. In this chapter, a cavitation analysis will be carried out using a series of blade resolved computations instead, since tip flow effects are inherently captured by these computations. The results will be compared with a separate cavitation analysis that is carried out with a blade element based method, to quantify the discrepancies.

Unlike utility-scale wind turbines, tidal turbines are likely to be installed close together in short fences and arrays (Adcock et al. 2015, Vennel et al. 2015). In these configurations, the blockage experienced by the devices is much higher than when they are installed in isolation, resulting in a greater static pressure drop across the rotor plane at a given tip-speed-ratio. Hence, the rotors in these closely packed layouts experience a modified static pressure distribution on the blade surface. In particular, they experience stronger suction peaks than rotors which are installed in isolation, so they are more likely to cavitate at a given tip-speed-ratio and submersion depth. In this chapter, the blade resolved computations will also be used to quantify the changes that must be made to the tip-speed-ratio and submersion depth restrictions, in order to avoid cavitation inception under blocked conditions.

5.1 Rotor Designs

Two different rotors designs will be used for the cavitation analysis in this chapter. These rotors were originally designed by Schluntz & Willden (2015) and will be referred to as 'Rotor 1' and 'Rotor 2' respectively. The design algorithm adopted by Schluntz & Willden (2015) varies the chord and twist distributions along the blade span, in order to achieve a target angle of attack distribution and a target local thrust coefficient distribution at the design tip-speed-ratio. The target angle of attack distribution is usually taken as the angle of attack that maximises the lift to drag ratio of each aerofoil section along the blade span. However, the target local thrust coefficient is more difficult to prescribe, as the optimum local thrust coefficient (and its distribution along the span) remains unknown under blocked conditions (Belloni 2013). Therefore, Schluntz & Willden (2015) investigated several target local thrust coefficients and the optimum rotor design was taken as that which maximised the power coefficient.

Rotor 1 and Rotor 2 are first generation tidal turbine rotor designs, which have only been designed for hydrodynamic performance. As structural and cavitation analyses have not yet been carried out on these rotors, Schluntz & Willden used a single aerofoil profile along the entire span. The RISØ-A1-24 aerofoil was chosen as it is often claimed to be a realistic choice for tidal turbine applications. Its high thickness to chord ratio (to withstand the higher fluid loading experienced by tidal turbines), gradual stall transition and broad suction peak (to provide cavitation resistance) make it particularly appealing for tidal turbine applications (Ahmed 2012). However, its relatively low maximum lift to drag ratio (57 at a Reynolds number of 1.6×10^6) limits the maximum power coefficient that can be generated by the rotor. Hence, the next generation of rotor designs may adopt different aerofoil profiles along the blade span (with higher maximum lift to drag ratios), in order to increase the maximum power coefficient of the rotor. However, separate calculations will be required to ensure that

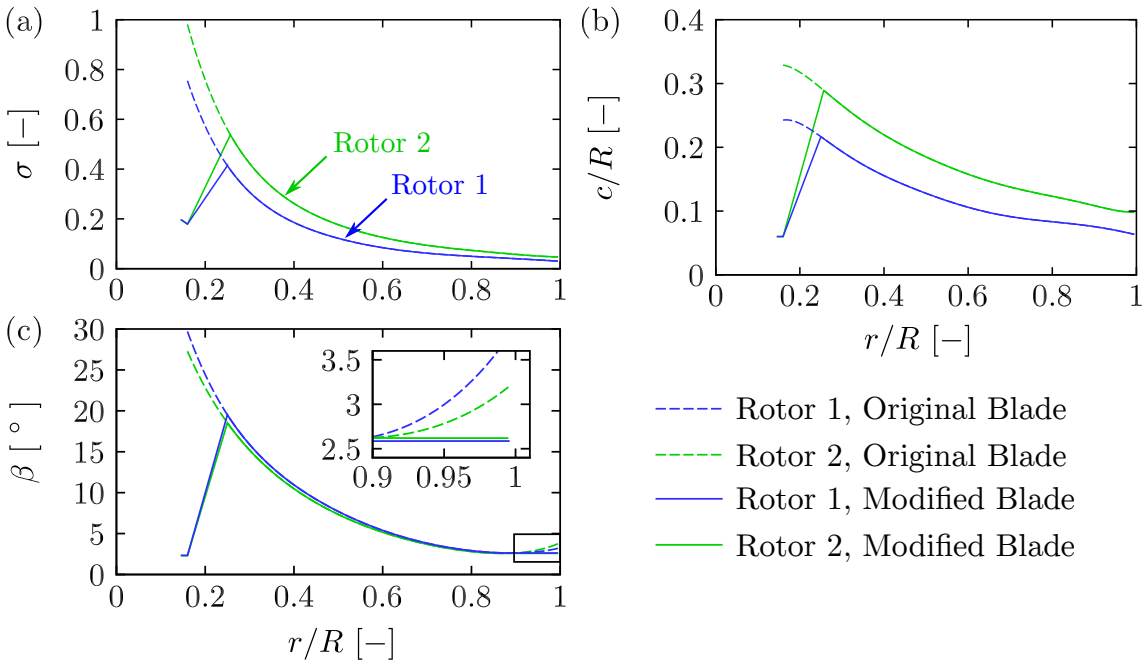

Figure 5.1: (a) Solidity, (b) chord, and (c) twist distributions for Rotor 1 and Rotor 2. $R = 10$m for both rotors. Modifications to the blade root and tip sections adopted in the present work, are also shown.

the structural integrity of the rotor is not compromised by these designs and the rotor is not likely to cavitate (due to the sharper suction peaks that are usually exhibited by aerofoils with higher maximum lift to drag ratios).

Fig. 5.1 shows the solidity (σ), chord (c) and twist (β) distributions for Rotor 1 and Rotor 2. In this work, the local solidity refers to the local chord length as a fraction of the local circumference at radius r,

$$\sigma(r) = \frac{Nc}{2\pi r} \tag{5.1}$$

where N is the number of blades.

Both Rotor 1 and Rotor 2 were designed to achieve their maximum power coefficients at a tip-speed-ratio of 5. However, Rotor 1 was designed to achieve its maximum power coefficient at a tip-speed-ratio of 5 in a virtually unblocked domain (a blockage ratio of 0.0001), while Rotor 2 was designed to achieve its maximum power coefficient at a tip-speed-ratio of 5 in a more highly blocked domain (a block-

age ratio of 0.197). At higher blockage ratios, greater thrust is required to maximise the power coefficient. As Rotor 1 and Rotor 2 have the same design tip-speed-ratio of 5, Rotor 2 has a greater chord length and slightly lower twist angle than Rotor 1 along the entire span. This allows Rotor 2 to naturally apply the greater levels of thrust that are required to maximise the power coefficient at higher blockage ratios, without spinning the rotor faster. A more complete discussion of the effect of rotor design on the thrust and power that can be developed by the rotors will be presented in Section 5.4.3.

Before creating the rotor geometries and setting up the simulations for the cavitation analysis, the original rotor designs of Schluntz & Willden (2015) were modified in order to make them more realistic. The modified blade geometries are also shown in Fig. 5.1.

In order to maintain a constant angle of attack and local thrust coefficient along the entire blade span, the original designs of Schluntz & Willden require high solidity and twist near the root of the blade. For Rotor 2 in particular, the solidity approaches 1.0 near the root, which may be problematic when pitch control is utilised. Pitch control is used by the majority of full-scale tidal turbines for power capping and in some cases to avoid yawing the entire device when the flow direction reverses (see the SeaGen S for example (MacEnri et al. 2013)). Hence, to make the designs more realistic, the root section was modified inboard of $r/R = 0.25$, by blending the RISØ-A1-24 aerofoil into a cylinder. As the root sections generate comparatively little power and cavitation inception is most likely to occur on the outboard sections of the blade, this modification was not likely to significantly impact the results of this investigation.

The design algorithm adopted by Schluntz & Willden (2015) included a Glauert (1935) tip correction factor. In their implementation, the Glauert tip correction factor was used to reduce the axial induction factor on the outboard blade sections, which

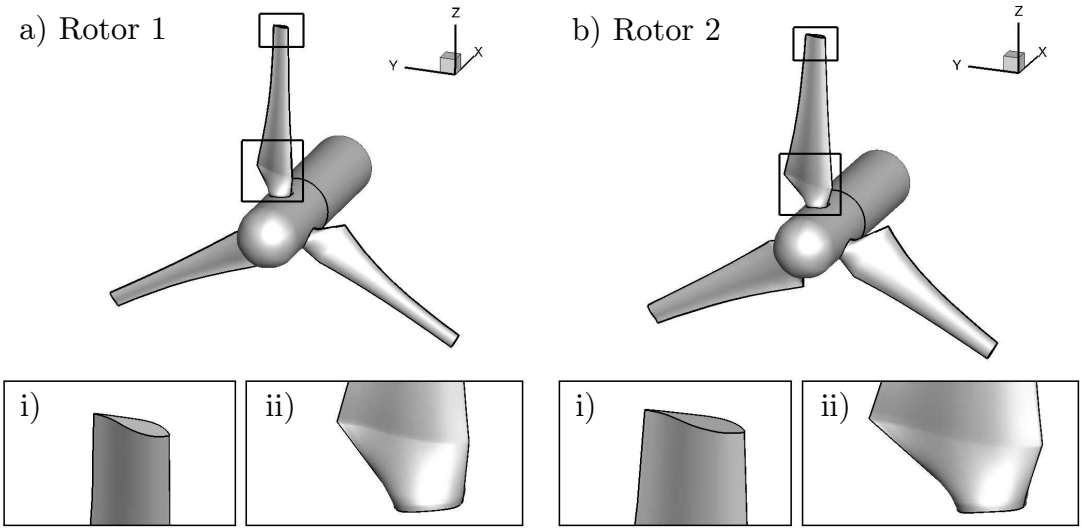

Figure 5.2: Comparison of the surface geometry of (a) Rotor 1 and (b) Rotor 2, with close up views of the (i) tip and (ii) root sections.

increased the angle of the incident flow velocity relative to the rotor plane (ϕ). As a result, the twist angle of both rotor designs increased (towards feather) in the tip region ($r/R > 0.9$), in an attempt to maintain a constant angle of attack along the span. However, it has been shown in this thesis (in Chapter 4) that the angle of attack actually reduces when approaching the tip of the blade, due to the induced downwash from the shed vorticity. Therefore, the twist angle of the blade should actually be reducing as the tip of the blade is approached (if the goal of the design algorithm is to maintain a constant angle of attack). Unfortunately, it is not possible to calculate the exact variation of the angle of attack as the tip is approached, due to the three-dimensional nature of the flow and therefore the optimum twist distribution cannot be specified. In this investigation, the twist angle of the blade is held constant outboard of $r/R = 0.9$ instead and the shape of the tip geometry is left to a separate investigation.

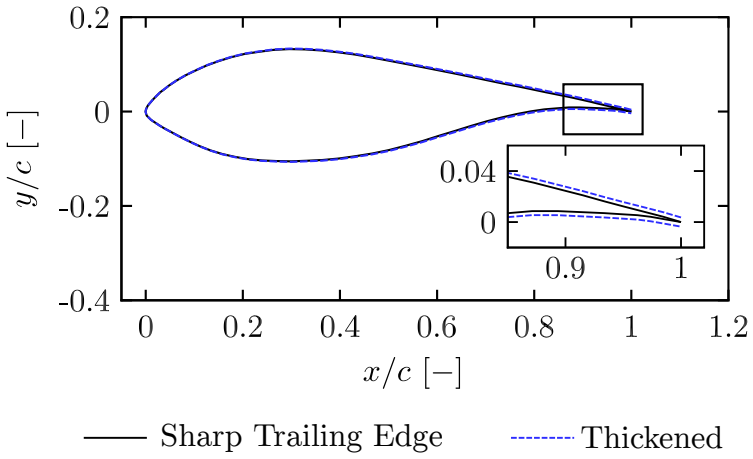

Figure 5.3: A comparison of the RISØ-A1-24 aerofoil geometry with sharp and thickened trailing edges.

5.1.1 Turbine Geometry

A comparison of the complete surface geometries of Rotor 1 and Rotor 2 is shown in Fig. 5.2. The blades were constructed using the modified chord and twist distributions shown in Fig. 5.1 and the approximate coordinates of the RISØ-A1-24 aerofoil from Bertagnolio et al. (2001). Both rotors have 3 blades and were assigned a diameter (D) of 20m. A cylindrical nacelle with a diameter of 3m ($0.15D$), length 10m ($0.5D$) and a hemispherical nose cone, was also included in the turbine designs. These dimensions were specifically chosen to replicate the typical dimensions of many of the full-scale tidal demonstrator devices that have already been installed (Belloni 2013). To reduce the computational cost of the blade resolved simulations, a support structure was not included in the turbine geometry.

5.1.2 Aerofoil Modifications

The nature of the trailing edge of the RISØ-A1-24 aerofoil was not specified in the original report produced by Bertagnolio et al. (2001). Therefore, a sharp trailing edge was assumed initially to create the aerofoil shape. This aerofoil was subsequently thickened using the method of Herrig et al. (1951), to produce a more realistic shape

for the 3D rotor geometries. Fig. 5.3 compares the RISØ-A1-24 aerofoil shape with sharp and thickened trailing edges. It has been claimed that the method of Herrig et al. (1951) does not significantly alter the aerodynamic performance of the aerofoil (McNaughton 2013). To identify and quantify the nature of the changes induced by thickening the aerofoil, a direct comparison of the aerodynamic performance of the RISØ-A1-24 aerofoil with sharp and thickened trailing edges was carried out. Steady flow RANS computations were carried out at a chord-based Reynolds number of 1.6×10^6 and an inlet turbulence intensity of 0.7%, to match the conditions in the VELUX wind tunnel that was used for the experimental measurements (Bertagnolio et al. 2001). The computations were carried out over a range of angles of attack from 0° to 11.5°, in increments of 0.5°.

Fig. 5.4 shows the lift coefficient (C_L), drag coefficient (C_D) and lift to drag ratio (C_L/C_D) for the RISØ-A1-24 aerofoil with sharp and thickened trailing edges. At low angles of attack (below approximately 8°), the computational data gives good agreement with the experimental measurements for both the sharp and thickened trailing edges. Neither geometry can be concluded to give universally better agreement with the experiments because the sharp trailing edge under-predicts both lift and drag at low angles of attack but over-predicts lift and drag at high angles of attack (and visa-versa for the thickened trailing edge). It is therefore likely that the geometry of the RISØ-A1-24 aerofoil used in the experiments of Bertagnolio et al. (2001), is somewhere between the approximate geometries computed here. At high angles of attack (greater than 8°), both sharp and thickened trailing edges give greater lift coefficients and lower drag coefficients than the experimental measurements, indicating that the onset of separation had been delayed in the computations. This is most likely a limitation of the RANS turbulence modelling approach and the steady flow solver adopted for these computations. Nevertheless, at low angles of attack (below 8°) and around the peak lift to drag ratio (7°), the lift and drag coefficients are well predicted.

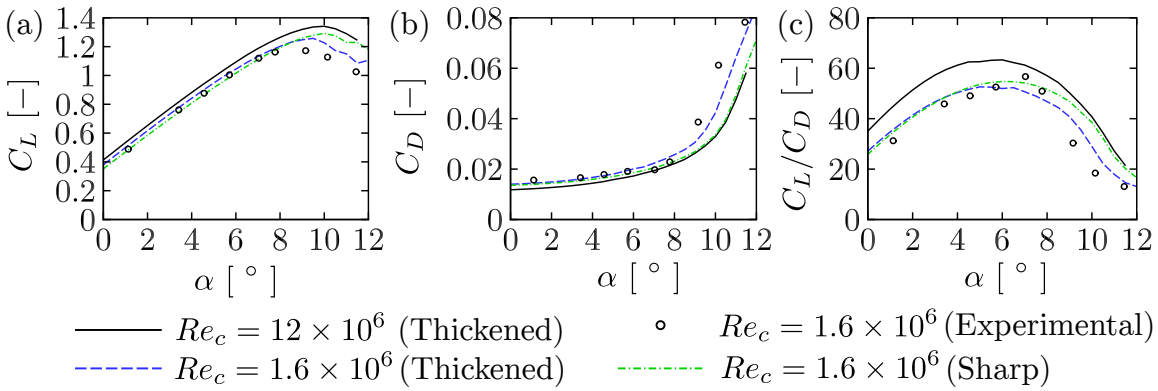

Figure 5.4: (a) Lift coefficient, (b) drag coefficient and (c) lift to drag ratio for the RISØ-A1-24 aerofoil with sharp and thickened trailing edges.

Therefore, a 3D rotor based on the thickened RISØ-A1-24 aerofoil geometry is likely to yield a reasonably accurate prediction of the thrust and power coefficients around the maximum power coefficient.

For operating conditions that are typical of full-scale tidal turbine operation, the chord-based Reynolds number is significantly higher than the chord-based Reynolds number used in the experimental measurements of the RISØ-A1-24 aerofoil (1.6×10^6). More specifically, for a freestream velocity of 2.0 m/s and a tip-speed-ratio of 5, the chord-based Reynolds number is approximately 12×10^6 at a spanwise distance of $r/R = 0.8$ along Rotor 2. To assess the likely impact of the higher chord-based Reynolds number on rotor performance, Fig. 5.4 also shows the lift coefficient, drag coefficient and lift to drag ratio of the thickened aerofoil at a chord-based Reynolds number of 12×10^6. For all angles of attack, the higher chord-based Reynolds number results in greater lift coefficients and lower drag coefficients, due to the reduced boundary layer thickness. Furthermore, the peak lift to drag ratio (approximately 63) is slightly greater than the peak lift to drag ratio at the lower chord-based Reynolds number (approximately 57 in the experiments) and also occurs at a slightly lower angle of attack (approximately 6° rather than 7°). The full-scale rotor designs are therefore likely to achieve their peak power coefficients at a slightly greater tip-speed-ratio than they was originally designed for (approximately 5.0).

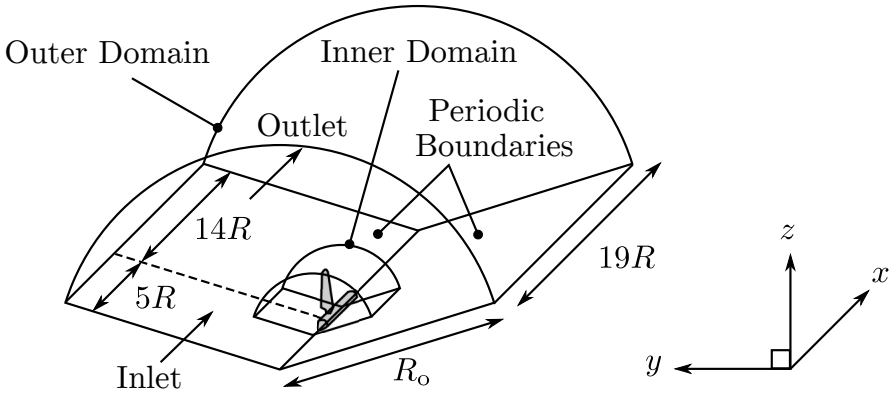

Figure 5.5: Diagram of the computational domain, highlighting the separate inner and outer domains. The streamwise direction is in the x direction and the rotor rotates clockwise (when viewed from the front). The radius of the outer domain (R_o) is varied to set the cylindrical blockage ratio.

5.2 Computational Domain and Meshing Strategy

The blade resolved computations in this chapter were carried out over a range of tip-speed-ratios (4-7) and cylindrical blockage ratios (0.01, 0.065, 0.0982 and 0.197) in steady uniform flow. It will be shown later in Chapter 7 that the static pressure distribution and blade loading in a rectangular domain are well predicted by a cylindrical domain with equivalent area blockage, as long as the device is not close to the domain boundaries and the bypass flows are not highly asymmetric. As shown in Fig. 5.5, rotational symmetry was utilised to reduce the computational cost of each simulation, by adopting a 120° wedge shaped computational domain (rather than a complete circular cylinder), with rotationally periodic boundary conditions applied on the sides. The overall domain was divided into separate inner and outer domains and independent meshes were generated in each region. This segregated approach for meshing the computational domain has two main advantages over a single connected domain. Firstly, a refined block-structured mesh can be fitted around the blade in the inner domain, without continuing the blocks through to the outer domain (which would lead to an extremely high cell count). Secondly, the cylindrical blockage provided by the rotor can be varied by modifying the radius of the outer domain (R_o),

without modifying the mesh structure around the blade in the inner domain. To simulate cylindrical blockage ratios of 0.01, 0.065, 0.0982 and 0.197 (respectively), outer domain radii of $10R$, $3.9R$, $3.19R$ and $2.25R$ were adopted for the computations.

In all computations, the inner domain was assigned a streamwise length of $0.7R$ and radius $1.2R$. It contained a single blade, the hemispherical nose cone and a section of the nacelle. The outer domain contained the remainder of the nacelle and the domain boundaries. These meshes were connected at a non-conformal interface on the surface of the inner domain wedge and were coupled together with the face interpolation algorithm of Farrell & Maddison (2011) that is available in OpenFOAM (version 2.3.1).

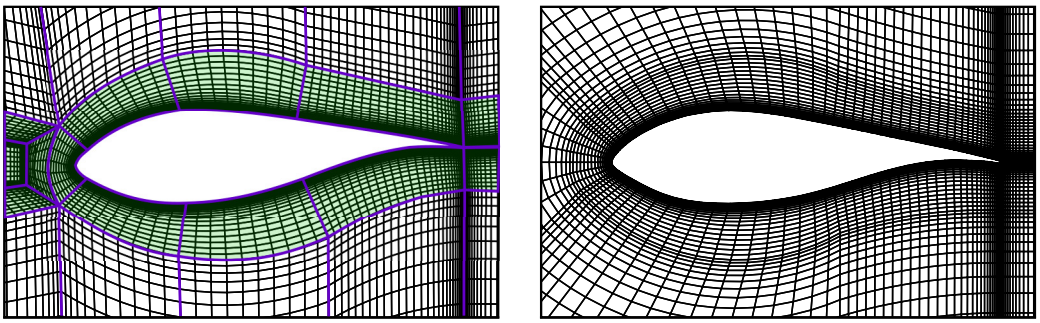

(a) 3D Rotor ($r/R = 0.8$) (b) 2D Aerofoil

Figure 5.6: (a) A slice through the 3D rotor mesh normal to the blade axis at $r/R = 0.8$ and (b) the 2D aerofoil mesh that was used to investigate the accuracy of the wall modelling approach. The green shaded area highlights the C-C blocking topology, while the purple lines indicate the blocking edges in the 3D rotor mesh.

As shown in Fig. 5.6 (a), a C-C type blocking topology was fitted around the blade in the inner domain. This topology was chosen in order to retain the rotational symmetry between the sides of the 120° wedge shaped domain and allow periodic boundary conditions to be applied. Several blocking slices were taken along the blade, in order to control the spanwise resolution near the blade root and tip. Finally, a Y block was inserted at the front of the nose cone, in order to avoid generating highly distorted hexahedral cells at the apex of the 120° wedge.

5.2.1 Boundary Conditions

At the inlet, uniform profiles of velocity ($U_\infty = 2.0$ m/s), turbulent kinetic energy (k) and specific dissipation rate (ω) were applied. The values of turbulent kinetic energy and specific dissipation rate were computed based on a turbulence intensity (I) of 10% and a length scale (l) of 0.7 times an assumed hub-height of 20m (mid-depth of the channel).

$$k = \frac{3}{2} I^2 U_\infty^2 \tag{5.2}$$

$$\omega = \frac{\sqrt{k}}{l} \tag{5.3}$$

These values of turbulence intensity and turbulence length scale were chosen to mimic the high levels of turbulence found in real tidal channels, following the recommendations by Gant & Stallard (2008). However, in uniform flow computations the applied turbulence intensity decays between the inlet and the rotor plane, due to a lack of shear to sustain the turbulence. In this investigation, the turbulence intensity decay was found to be small (from 10% to 9.908%) and it was therefore deemed unnecessary to modify the inlet boundary condition to achieve a turbulence intensity of exactly 10% at the rotor plane. At the outlet, zero gradient boundary conditions were applied for the velocity and turbulence scalars (k and ω), while the static pressure was assigned a fixed value of 0. On the curved outer surface of the wedge shaped domain, zero gradient boundary conditions were applied for all flow variables (a slip condition).

5.2.2 Wall Modelling

An additional aim of the blade resolved computations carried out in this chapter was to attain an appropriate level of mesh of resolution (in the inner domain) that could be used for the subsequent sliding mesh computations that are carried out in sheared

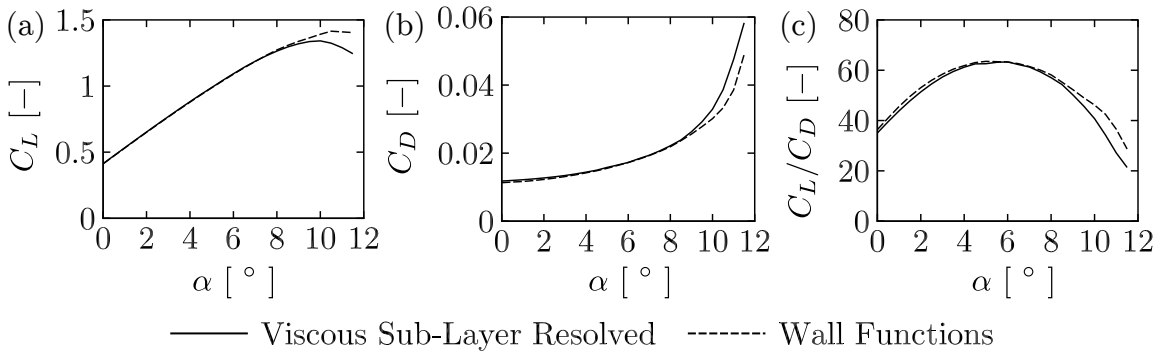

Figure 5.7: Lift coefficient (a), drag coefficient (b) and lift to drag ratio (c) for the RISØ-A1-24 aerofoil at a chord-based Reynolds number of 12×10^6, with wall function based and viscous sub-layer resolved meshes.

flow in Chapter 7. The sliding mesh computations require the complete rotor to be simulated, rather than just a single blade (as investigated in this chapter). Therefore, the total cell count for the sliding mesh computations increases by a factor of at least 3, when compared to the multiple reference frame (MRF) computations that are carried out in a periodic domain in this chapter. Furthermore, the sliding mesh computations also require an unsteady simulation, due to the sheared velocity profile. Hence, the computational expense of the sliding mesh computations is considerably greater than the MRF computations carried out in this chapter, providing further motivation for adopting an efficient level of mesh resolution in the inner domain. For this reason, it was deemed to be infeasible to resolve the rotor blade boundary layers through to the viscous sub-layer ($y^+ < 5$). More specifically, the inner domain mesh was found to require approximately 15 million cells (for a single blade) in order to attain sufficiently high cell quality for stable computations (when a viscous sub-layer resolved mesh was adopted). Therefore, in order to facilitate a tractable computation, the meshes adopted in this chapter placed the wall adjacent cell centroid in the logarithmic law region instead ($30 < y^+ < 300$). The velocity profile between the wall adjacent cell centroid and the wall was then modelled using the standard wall functions described in Chapter 2.

To investigate the limitations of the wall modelling approach, a comparison was

made of the aerodynamic performance of the RISØ-A1-24 aerofoil (in 2D) with viscous-sub layer resolved ($y^+ < 5$) and wall function ($30 < y^+ < 300$) based meshes. The mesh structure for the 2D meshes was specifically constructed to closely resemble the mesh structure on a slice through the 3D rotor blade (normal to the blade axis) at $r/R = 0.8$ (see Fig. 5.6). The computations were carried out over a range of angles of attack from 0° to 11.5°, in increments of 0.5°. Fig. 5.7 shows the lift coefficient (C_L), drag coefficient (C_D) and lift to drag ratio (C_L/C_D), for the viscous sub-layer resolved and wall function based meshes. For angles of attack below 8°, the lift and drag coefficients are both well predicted by the wall function based mesh. As a result, the peak lift to drag ratio (at approximately 6°) is also well predicted and hence the 3D rotor mesh is expected to predict the peak power coefficient well at the design tip-speed-ratio.

However, the wall function based mesh over-predicts the lift coefficient and under-predicts the drag coefficient at high angles of attack (above 8°). This discrepancy can be attributed to a delayed separation onset by the wall function based mesh, which arises from an over-prediction of the wall shear stress. Due to the lift coefficient over-prediction and drag coefficient under-prediction at high angles of attack, the 3D rotor mesh is expected to over-predict power and over-predict thrust at low tip-speed-ratios. However, this is not likely to significantly impact the results of this investigation, since cavitation inception is more likely to occur at high tip-speed-ratios (which are well predicted by the wall function based mesh).

5.3 Mesh Sensitivity

An initial mesh was generated for Rotor 2 (the higher solidity rotor design), with the distribution of cells in the chordwise and wall normal directions based on the distribution of cells adopted in the 2D computations of the RISØ-A1-24 aerofoil. In

the spanwise direction, the initial distribution of cells was based on the distribution of cells adopted for the blade resolved computations of the MEXICO rotor in Chapter 3. This initial (coarse) mesh was then selectively refined in the chordwise, wall normal and spanwise directions simultaneously, to generate medium and fine meshes. These three meshes were compared to identify an appropriate level of resolution to accurately compute the blade loading (and hence the static pressure distribution for the cavitation analysis). The comparisons were carried out in the highest blockage domain ($B = 0.197$), at a tip-speed-ratio of 5 (close to the maximum power coefficient). A summary of the key parameters used to define the block-structured meshes is provided in Table 5.1. LE refers to the chordwise cell dimension at the leading edge, TE the chordwise cell dimension at the trailing edge, y_0 the wall adjacent cell centroid height, N_c the number of cells in the chordwise direction along the pressure and suction surfaces individually, G the cell growth ratio normal to the wall, N_s the number of cells in the spanwise direction along the blade, Δ_{tip} the spanwise cell dimension at the blade tip, N_{surf} the number of cells on the pressure and suction surfaces individually and N_{cells} the total number of cells in the (120° wedge shaped) inner domain.

Table 5.1: Summary of the mesh parameters adopted for the coarse, medium and fine meshes, expressed in terms of the chord length at $r/R = 0.8$ ($c_{0.8R} = 1.23$m) and the chord length at the blade tip ($c_{\text{tip}} = 0.985$m).

Mesh	LE/$c_{0.8R}$	TE/$c_{0.8R}$	$y_0/c_{0.8R}$	N_c	G	N_s	$\Delta_{\text{tip}}/c_{\text{tip}}$	N_{surf}	N_{cells}
Coarse	1.63e-2	3.25e-3	5.69e-4	58	1.2	68	4.1e-2	3,944	1,466,268
Medium	1.63e-2	1.63e-3	5.69e-4	78	1.1	88	2.0e-2	6,864	2,913,968
Fine	1.63e-2	8.13e-4	5.69e-4	98	1.075	108	1.0e-2	10,584	4,998,728

Fig. 5.8 shows the axial and tangential forces per unit span (F_{ax} and F_{ta} respectively) computed with the coarse, medium and fine meshes. In general, the coarse, medium and fine meshes all show close agreement along the entire span. For example, at $r/R = 0.8$ the axial force per unit span is only 0.48% lower when computed with

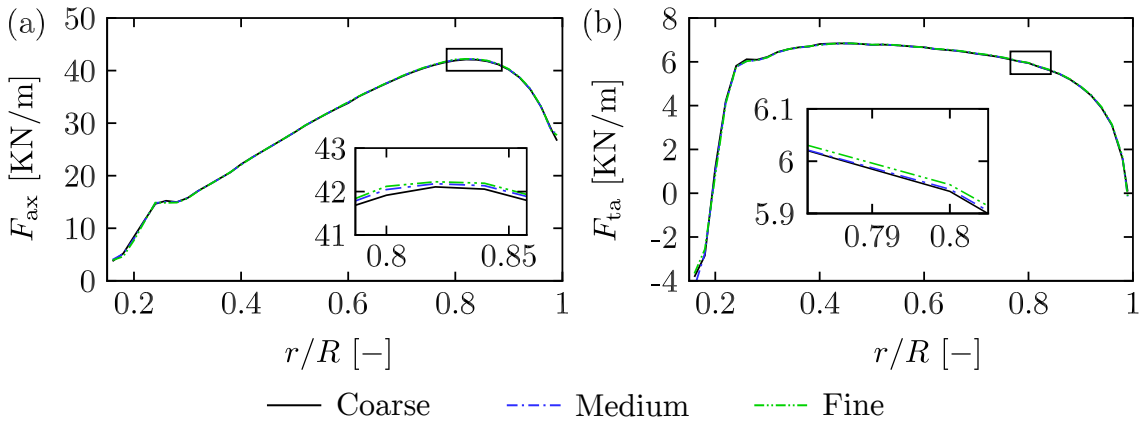

Figure 5.8: (a) Axial and (b) tangential forces per unit span for Rotor 2 in the blocked domain ($B = 0.197$) at a tip-speed-ratio of 5 for the coarse, medium and fine meshes.

the coarse mesh rather than with the fine mesh. Meanwhile, the tangential force per unit span is only 0.22% lower when computed with the coarse mesh than with the fine mesh.

The resulting difference in the rotor thrust and power coefficients (C_T and C_P respectively) between the three meshes, is shown in Table 5.2. The thrust and power coefficients have been computed using equations 5.4 and 5.5, where T is the rotor thrust, P is the rotor power, ρ is the density of seawater (1025 kg/m^3), U_∞ is the (uniform) freestream velocity and A is the swept area of the rotor.

$$C_T = \frac{T}{\frac{1}{2}\rho U_\infty^2 A} \tag{5.4}$$

$$C_P = \frac{P}{\frac{1}{2}\rho U_\infty^3 A} \tag{5.5}$$

Table 5.2: Thrust and power coefficients for the coarse, medium and fine meshes at a tip-speed-ratio of 5. The change in thrust and power coefficients (ΔC_T and ΔC_P) for the coarse and medium meshes have been expressed relative to the fine mesh.

Mesh	C_P	C_T	ΔC_P [%]	ΔC_T [%]
Coarse	0.62465	1.17126	-0.19	-0.20
Medium	0.62568	1.17353	-0.03	-0.009
Fine	0.62585	1.17363	-	-

Table 5.2 shows that the thrust coefficient computed using the coarse mesh is only 0.20% lower than the thrust coefficient computed using the fine mesh. In addition, Table 5.2 also shows that the power coefficient is only 0.19% lower when computed with the coarse mesh than when computed with the fine mesh. These results indicate that the coarse mesh is sufficiently converged in terms of the integrated blade loading. In addition, Fig. 5.8 shows that the coarse mesh is also sufficiently converged in terms of the spanwise distribution of the blade loading. Hence, the coarse mesh was deemed to be sufficient for all further computations using Rotor 2.

Having decided that the coarse level of resolution was sufficient for Rotor 2, a similar block-structured mesh was constructed for Rotor 1, using the same mesh parameters adopted for the coarse mesh of Rotor 2. This mesh was used for all further computations of Rotor 1.

5.4 Blade Resolved Cavitation Analysis

The precise onset of cavitation is difficult to predict exactly, since it depends on the the local static pressure in the fluid, the amount of dissolved air in the fluid and the time taken for the cavitation nuclei to grow to a sufficient size (Carlton 1994). Hence, cavitation inception is often assumed to occur when the minimum static pressure in the fluid drops below the vapour pressure of the fluid (for simplicity). This approach was also adopted in this work, since the aim of the study was to avoid cavitation inception altogether, rather than modelling the physical process of cavitation itself.

However, the static pressure distribution extracted from the blade resolved computations does not include hydrostatic and atmospheric components at this stage, as they were not computed directly in the simulations. Therefore, the computed static pressure cannot be compared directly with the vapour pressure of seawater to assess the likelihood of cavitation inception. In this work, the hydrostatic and atmospheric

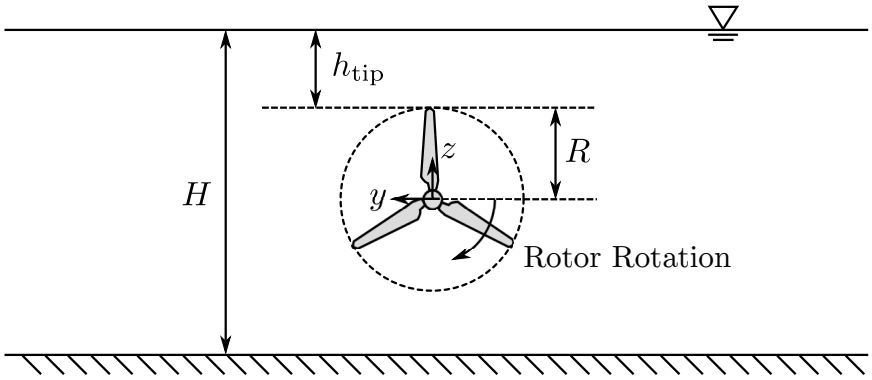

Figure 5.9: Schematic diagram of the domain adopted to add hydrostatic and atmospheric pressure components to the blade resolved computations (that were carried out in cylindrical domains). The streamwise (x) direction is into the page and the z coordinate is measured vertically upwards from the centre of the nacelle. H is the depth of the fluid.

pressure components are added during the post-processing stage, using the schematic diagram in Fig. 5.9. In Fig. 5.9, the tip of the rotor (at top-dead-centre) is assumed to be submerged a vertical distance h_{tip} below the surface of a rectangular channel, with an equivalent area blockage ratio to the computed cylindrical channels. This modelling assumption is likely to be acceptable (this will be shown explicitly in Chapter 7) as long as the rotor is not installed close to the free surface or the vertical blockage is much higher than the lateral blockage. Under these asymmetric conditions, the bypass flow and the static pressure distribution on the blade surface are likely to vary considerably over the rotor revolution (the bypass flow being more strongly accelerated above the rotor when close to the free surface). This asymmetry over the rotor revolution is not captured by the computations in the cylindrical domain. Hence, to compute the correct static pressure distribution under asymmetric loading conditions, the computations would have to be carried out directly in the desired rectangular domain.

In Fig. 5.9, the blade is assumed to be located at top dead centre, since the hydrostatic pressure contribution is a minimum here and hence cavitation inception is most likely to occur. At real tidal energy sites, the minimum allowable tip submer-

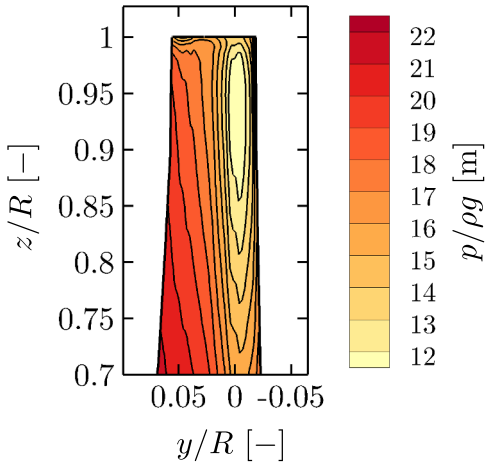

Figure 5.10: Contours of static pressure on the suction surface of Rotor 1 at a tip-speed-ratio of 5.0, a blockage ratio of 0.01 and a tip submersion depth of 8m. The streamwise (x) direction is into the page and the rotor rotates clockwise.

sion depth (below lowest astronomical tide) h_{tip}, is likely to be set by local shipping requirements. For instance, the minimum allowable tip submersion depth at the MeyGen site (Phase 1a) is 8m (MeyGen Ltd. 2014). Following the restrictions at the MeyGen site, a tip submersion depth of 8m will also be adopted for the cavitation analysis in this work.

Using the coordinate system and notation adopted in Fig. 5.9, the static pressure in the fluid (p) can be assembled (during the post-processing stage) from the computed (p_{CFD}), atmospheric ($p_{\text{Atm}} = 101325$ Pa) and hydrostatic components.

$$p = p_{\text{CFD}} + p_{\text{Atm}} + \rho g(h_{\text{tip}} + R - z) \tag{5.6}$$

The resulting static pressure distribution on the blade surface is complex, since it contains several competing contributions. As an example of this distribution, Fig. 5.10 shows the static pressure on the suction surface of the blade of Rotor 1, at a tip-speed-ratio of 5. The strength of the suction peak generally increases with distance from the hub, due to the increasing dynamic pressure that is incident on the blades from the rotational velocity component and the reducing hydrostatic pressure contribution. However, tip flow effects lead to a reduction in the strength of the

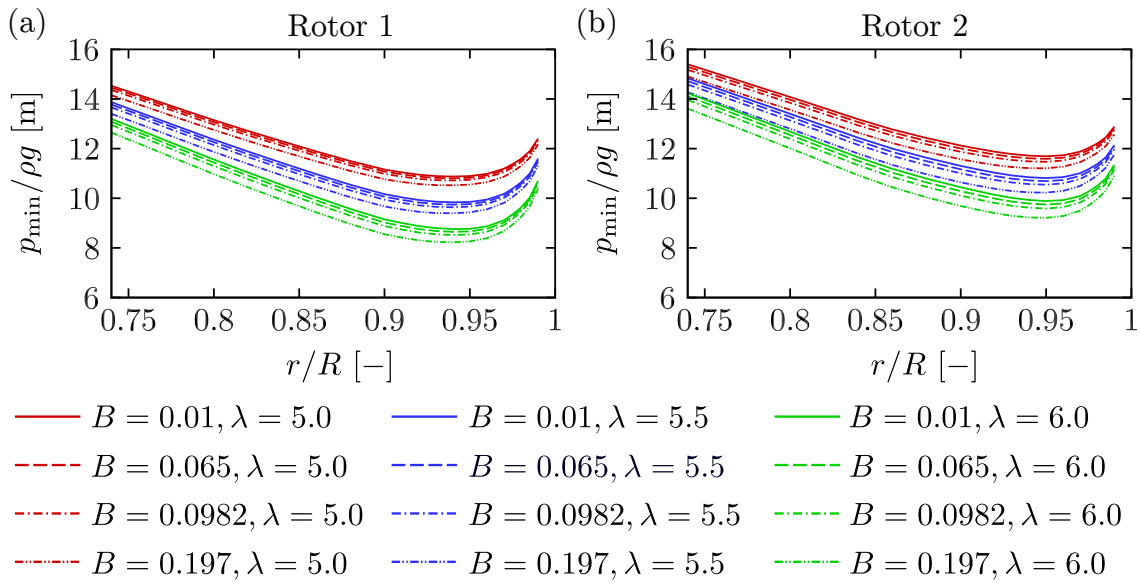

Figure 5.11: Spanwise variation of the minimum static pressure ($p_{\min}$) acting on each aerofoil section, expressed in terms of a pressure head. The tip submersion depth $h_{\text{tip}} = 8$m.

suction peak as the tip of the blade is approached. Hence, the minimum static pressure does not occur at the very tip of the blade but slightly inboard from the tip, at $r/R \approx 0.94$.

To assess the spanwise variation of the minimum static pressure in more detail, the rotor blade was divided into several independent (2D) sections along the blade span (normal to the blade axis). The minimum static pressure was extracted from each of these sections to give the spanwise variation of the minimum static pressure ($p_{\min}$) shown in Fig. 5.11. With increasing tip-speed-ratio, the rotational velocity component incident on the rotor increases, which increases the strength of the blade suction peak and reduces the minimum static pressure. Hence, the rotor is pushed closer towards cavitation with increasing tip-speed-ratio. Fig. 5.11 also shows that increasing the blockage ratio (at constant tip-speed-ratio) reduces the minimum static pressure on the blade surface, which pushes the rotor closer towards cavitation. This reduction arises because the axial velocity through the swept area of the rotor increases with blockage ratio (at constant tip-speed-ratio). As the axial velocity increases, the angle

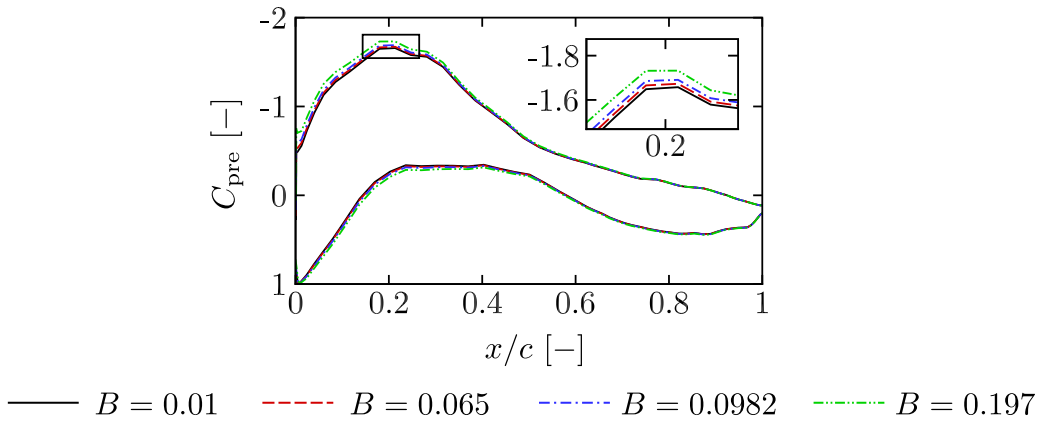

Figure 5.12: Static pressure coefficient in the chordwise direction on a slice through Rotor 1 (normal to the blade axis) at $r/R = 0.94$, for a range of blockage ratios. The tip-speed-ratio $\lambda = 5$.

of attack and relative velocity magnitude increase, which increases the strength of the suction peak. For a more direct comparison, Fig. 5.12 shows the static pressure coefficient on a slice through the blade of Rotor 1 at $r/R = 0.94$ and a tip-speed-ratio of 5, over a range of blockage ratios. Here the static pressure coefficient has been defined as,

$$C_{\text{pre}} = \frac{p_{\text{CFD}} - p_\infty}{\frac{1}{2}\rho\left[U_\infty^2 + (\Omega r)^2\right]} \tag{5.7}$$

where Ω is the rotational speed of the rotor, r is the spanwise distance along the blade, U_∞ is the freestream velocity and p_∞ is the freestream static pressure. Fig. 5.12 shows that increasing the blockage ratio directly increases the strength of the suction peak, which pushes the rotor closer towards cavitation.

Fig. 5.11 also allows the rotor designs to be compared. At the same tip-speed-ratio and blockage ratio, Rotor 1 experiences a lower minimum static pressure than Rotor 2, so Rotor 1 is closer to cavitation. This is because Rotor 1 has a shorter chord length and higher twist angle than Rotor 2, so it exerts less thrust on the flow at the same blockage ratio and tip-speed-ratio. With less thrust exerted on the flow, the axial velocity through the swept area of the Rotor 1 is greater than

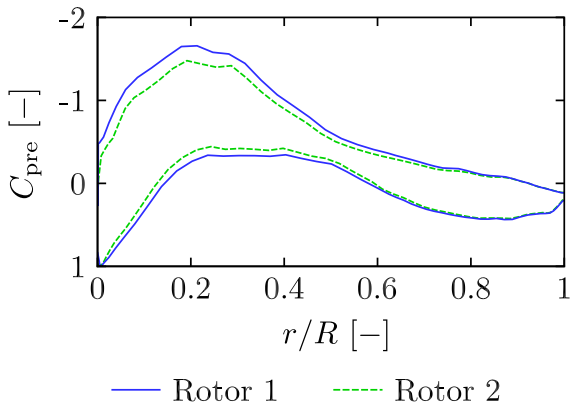

Figure 5.13: Static pressure coefficient in the chordwise direction on a slice through the blade of Rotor 1 and Rotor 2 (normal to the blade axis) at $r/R = 0.94$. The blockage ratio $B = 0.01$ and the tip-speed-ratio $\lambda = 5$.

Rotor 2. It can be inferred (by considering a velocity triangle) that Rotor 1 therefore experiences a greater angle of attack and relative velocity magnitude than Rotor 2 at the same blockage ratio and tip-speed-ratio. Hence, Rotor 1 experiences a stronger suction peak than Rotor 2, as shown in Fig. 5.13. Due to its stronger suction peak, Rotor 1 will cavitate at a lower tip-speed-ratio than Rotor 2 (when operating at the same blockage ratio). Therefore, in order to avoid cavitation inception, Rotor 1 will be forced to either operate over a more restricted range of tip-speed-ratios or at a greater submersion depth.

5.4.1 Tip-Speed-Ratio and Submersion Depth Restrictions

Device developers may choose to either limit the maximum operational tip-speed-ratio of devices or increase their submersion depth, in order to increase the minimum static pressure and avoid cavitation inception. In order to specify such restrictions, Fig. 5.14 shows the minimum static pressure experienced by both rotor designs over the entire range of tip-speed-ratios, for two different submersion depths. Fig. 5.14 (a) shows the minimum static pressure experienced by both rotors with a tip submersion depth of 8m, while Fig. 5.14 (b) shows the minimum static pressure experienced by both rotors with the tip submersion depth reduced to 0m. A tip submersion

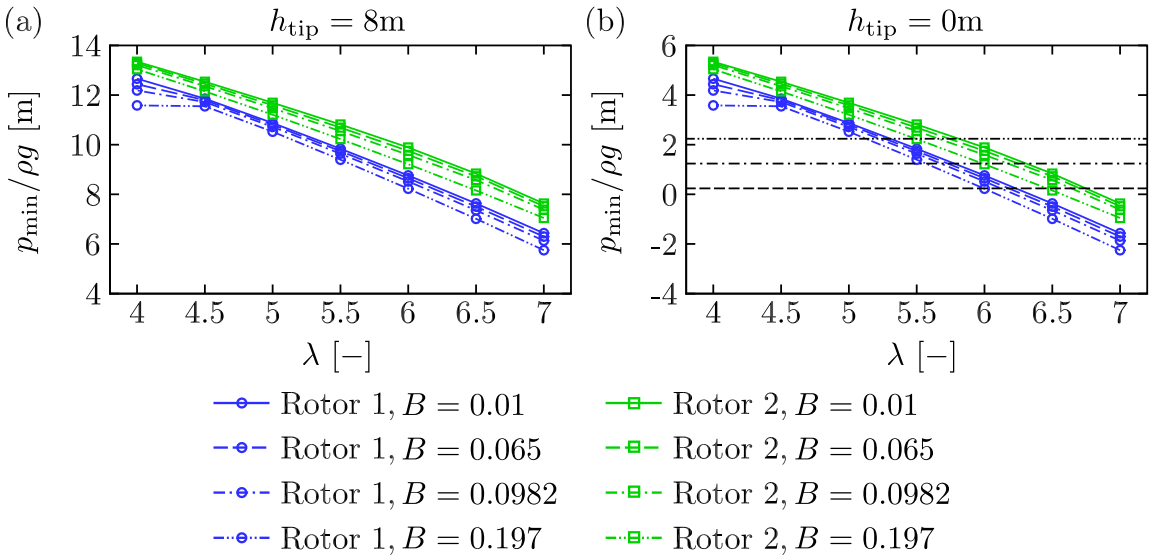

Figure 5.14: Minimum static pressure head on the blade suction surface for tip submersion depths of (a) 8m and (b) 0m. The horizontal dashed, dashed dotted and dashed double dotted lines indicate safety margins of 0m, 1m and 2m respectively, relative to the vapour pressure head of seawater (0.24m).

depth of 8m is likely to be typical for bed mounted devices, such as those installed at the MeyGen Ltd. (2014) site (Phase 1a). However, some rotors may be installed below a floating support structure (such as the Scotrenewables SR250), with a much shallower submersion depth. To address this case, Fig. 5.14 (b) shows the minimum static pressure experienced by both rotors when the tip submersion depth is reduced to 0m. This submersion depth was specifically chosen to investigate the limiting case where the hydrostatic pressure contribution is minimised and the rotors are most likely to cavitate. In practice, as the tip submersion depth is reduced to 0m (at constant blockage ratio), the bypass flow above the rotor is rapidly accelerated, while the bypass flow below the rotor is decelerated. This anisotropy will modify the static pressure distribution on the outboard blade sections (at top-dead-centre) and hence the onset of cavitation. A separate detailed analysis is clearly required to compute this limiting case. However for the simplified analysis carried out in this work, anisotropic blockage effects are neglected and the 0m case is only used as a demonstration of the effect of reducing the hydrostatic pressure contribution.

At a tip submersion depth of 8m, neither rotor is likely to cavitate over the entire range of computed tip-speed-ratios because the minimum static pressure head is greater than the vapour pressure head of seawater (approximately 0.24m at 15°C). However, with a tip submersion depth of 0m, cavitation inception is likely to occur if the minimum static pressure drops below the horizontal dashed line in Fig. 5.14 (b) (which corresponds with the vapour pressure head of seawater). Furthermore, if the submersion depth is fixed (perhaps due to the nature of the support structure), then the intersection between the computed curves and the horizontal dashed line in Fig. 5.14 (b) represents the maximum tip-speed-ratio that should be permissible before cavitation inception is likely to occur.

Traversing to the left along the horizontal dashed line in Fig. 5.14 (b), shows that increasing the blockage ratio from 0.01 to 0.197 reduces the maximum permissible tip-speed-ratio by 0.24 for Rotor 1 and 0.27 for Rotor 2. This is because the strength of the suction peak increases with blockage ratio (see Fig. 5.12) and hence the tip-speed-ratio of the rotor has to reduce in order to limit the strength of the suction peak and avoid cavitation. However, if the submersion depth is not fixed and it is desirable to maintain the same range of operational tip-speed-ratios (when the blockage ratio is increased from 0.01 to 0.197), then the rotor submersion depth would have to increase by 0.53m to maintain the same minimum static pressure at a tip-speed-ratio of 6.

Traversing along the horizontal dashed line (between rotor designs) shows that at a blockage ratio of 0.197, the maximum permissible tip-speed-ratio for Rotor 2 is 0.48 higher than for Rotor 1. As shown in Fig. 5.13, this is because Rotor 2 experiences a weaker suction peak than Rotor 1 at the same tip-speed-ratio. Hence, Rotor 2 can be operated at higher tip-speed-ratios before cavitation inception is likely to occur. Alternatively, if the submersion depth is not fixed, then the submersion depth of Rotor 1 would have to be increased by 0.98m to attain the same minimum static pressure as Rotor 2 at a tip-speed-ratio of 6.0.

5.4.2 Factors Affecting Cavitation

Free surface waves, ambient turbulence and the sheared axial velocity profile lead to unsteady velocity and static pressure fluctuations that have not been modelled in the computations carried out in this chapter. These unsteady fluctuations may lead to cavitation inception, even if the minimum static pressure under steady conditions is greater than the vapour pressure of seawater. For example, the highly sheared velocity profile (that is present at many tidal energy sites) leads to an increase in the axial velocity and angle of attack near the top of the water column. As the angle of attack and relative velocity magnitude increase, the strength of the suction peak increases, which pushes the blade closer to cavitation than it would be in uniform flow. The presence of free surface waves leads to a transient submersion depth, which locally reduces the hydrostatic pressure contribution (during wave troughs) and pushes the rotor closer to cavitation. Free surface waves also induce a dynamic pressure fluctuation which reduces with increasing depth and increasing wavenumber. This dynamic pressure fluctuation leads to a dynamic aerofoil response, which may locally reduce the static pressure on the surface of the blade below the vapour pressure of sea water, increasing the likelihood of cavitation inception.

The presence of the support structure (not included in the computations in this chapter) also leads to a periodic dynamic pressure fluctuation. As the blade passes in front of the support structure, the presence of the support structure locally increases the static pressure on the blade surface (Muchala 2017). If the support structure is surface piercing, then the blade suction peak at top-dead-centre will be reduced by the presence of the support structure, reducing the likelihood of cavitation inception. Conversely, bed mounted support structures are not likely to modify the likelihood of cavitation inception, since the hydrostatic pressure contribution is much larger at bottom-dead-centre and the blade is not likely to cavitate here anyway.

As these unsteady fluctuations have not been modelled in the computations carried

out in this chapter, a hydrodynamic safety margin is required. For consistency with the preceding analysis, this safety margin will be specified as an increase in the minimum allowable static pressure head under steady flow conditions. This additional static pressure head is required to prevent the fluid from cavitating as a result of the unsteady fluctuations arising from free surface waves, ambient turbulence and velocity shear. Rather than suggesting an appropriate value for the safety margin, the effect of specifying such a safety margin on the range of operating conditions that can be achieved by the rotor will be demonstrated instead. This is because appropriate safety margins are likely to be dependent on the wave climate and degree of velocity shear at a given site. Hence, device developers are likely to specify safety margins on a site-specific basis or be forced to specify a more universal safety margin that is overly conservative. While an additional safety margin may still be required to account for other effects such as marine fouling, these effects have not been considered in this work.

When the submersion depth is large, the minimum static pressure (under steady conditions) may already be sufficiently large that an additional static pressure head is not required to account for the unsteady pressure fluctuations. For example, even if the minimum static pressure head is locally reduced by 5m in Fig. 5.14 (a) (by unsteady fluctuations), both Rotor 1 and Rotor 2 are not likely to cavitate over the entire range of operating conditions. Hence, if the required safety margin is less than 5m, then no restriction on the rotor operating conditions is required at a tip submersion depth of 8m.

However, for devices installed closer to the free surface, an increase in the minimum allowable static pressure (under steady conditions) is essential to prevent the device from cavitating. The horizontal dashed dotted and dashed double dotted lines in Fig. 5.14 (b) indicate additional static pressure heads of 1m and 2m respectively, that could be selected as an appropriate safety margin (depending on the local en-

vironmental conditions). If the submersion depth of the device is fixed, the chosen safety margin will considerably restrict the maximum permissible tip-speed-ratio that can be achieved by the rotor. For example, applying a safety margin of 1m to Rotor 1 at $B = 0.197$, reduces the maximum permissible tip-speed-ratio by 0.42. This restriction has considerable consequences for the thrust and power coefficients that can be achieved by the rotor, as will be demonstrated in Section 5.4.3.

However, if the submersion depth of the device is not fixed, Fig. 5.14 can alternatively be used to select an appropriate submersion depth that does not restrict the range of operational tip-speed-ratios and includes the required safety margin. For example, to maintain a safety margin of 2m and achieve a tip-speed-ratio of 7 at a blockage ratio of 0.197, Rotor 1 requires a minimum submersion depth of 4.5m (2.0m + 0.25m - -2.25m), while Rotor 2 requires a minimum submersion depth of only 3.2m (2.0m + 0.25m - -0.95m). However, it is not necessarily desirable to increase the submersion depth of the device in preference to limiting the range of operational tip-speed-ratios. This is because the velocity profile at some tidal energy sites is highly sheared, with a greater proportion of the incident kinetic energy flux residing near the top of the water column. Hence, reducing the submersion depth at these sites results in a lower potential for energy extraction, despite not having to limit the tip-speed-ratio to avoid cavitation inception.

For many tidal energy devices (particularly bed mounted devices), the installation depth of the device is fixed by the support structure (once installed), while the submersion depth varies over the tidal cycle. For these devices, a practical design approach that can be adopted is to identify the lowest astronomical tide and highest tidal current at a given installation site (since these are the conditions where the device is most likely to cavitate). After applying an appropriate hydrodynamic safety margin to account for the dynamic pressure fluctuations, a combination of the design tip-speed-ratio and installation depth can be selected to optimise performance,

noting the shut down speed (from the cavitation analysis) that is required to avoid cavitation.

5.4.3 Rotor Performance

If the submersion depth of the rotor is fixed, then a tip-speed-ratio restriction may be necessary to avoid the onset of cavitation. However, this tip-speed-ratio restriction may significantly reduce the maximum thrust and power coefficients that can be achieved by the rotor, particularly at higher blockage ratios. Fig. 5.15 shows the thrust and power coefficients for Rotor 1 and Rotor 2 as a function of tip-speed-ratio and mass flow rate coefficient ($C_{\dot{m}}$), where the thrust and power coefficients have been defined using equations 5.4 and 5.5, respectively. The mass flow rate coefficient is defined in equation 5.8 and represents the ratio of the mass flow rate through the swept area of the rotor to the mass flow rate through the swept area of the rotor without the rotor present (indicated by the subscript 0).

$$C_{\dot{m}} = \frac{\int_A (\rho U_x)\,\mathrm{d}A}{\int_A (\rho U_{x0})\,\mathrm{d}A} \tag{5.8}$$

With this definition, the mass flow rate coefficient can also be interpreted as $1-\bar{a}$, where $\bar{a}$ is the spatial average of the axial induction factor over the rotor swept area. To assist in the ensuing analysis, a polynomial curve fit has been used to estimate the maximum power coefficient in each domain and the approximate tip-speed-ratio that it occurs at. The maximum power coefficients are also shown in Fig. 5.15 and are connected by a black dashed line.

Fig. 5.15 shows that increasing the blockage ratio at constant tip-speed-ratio (following the solid black line) leads to greater thrust and power coefficients for both rotor designs. This increase occurs because the bypass flow (the flow which does not pass through the rotor swept area) is increasingly accelerated by the domain boundaries as the blockage ratio is increased. The increased acceleration of the bypass

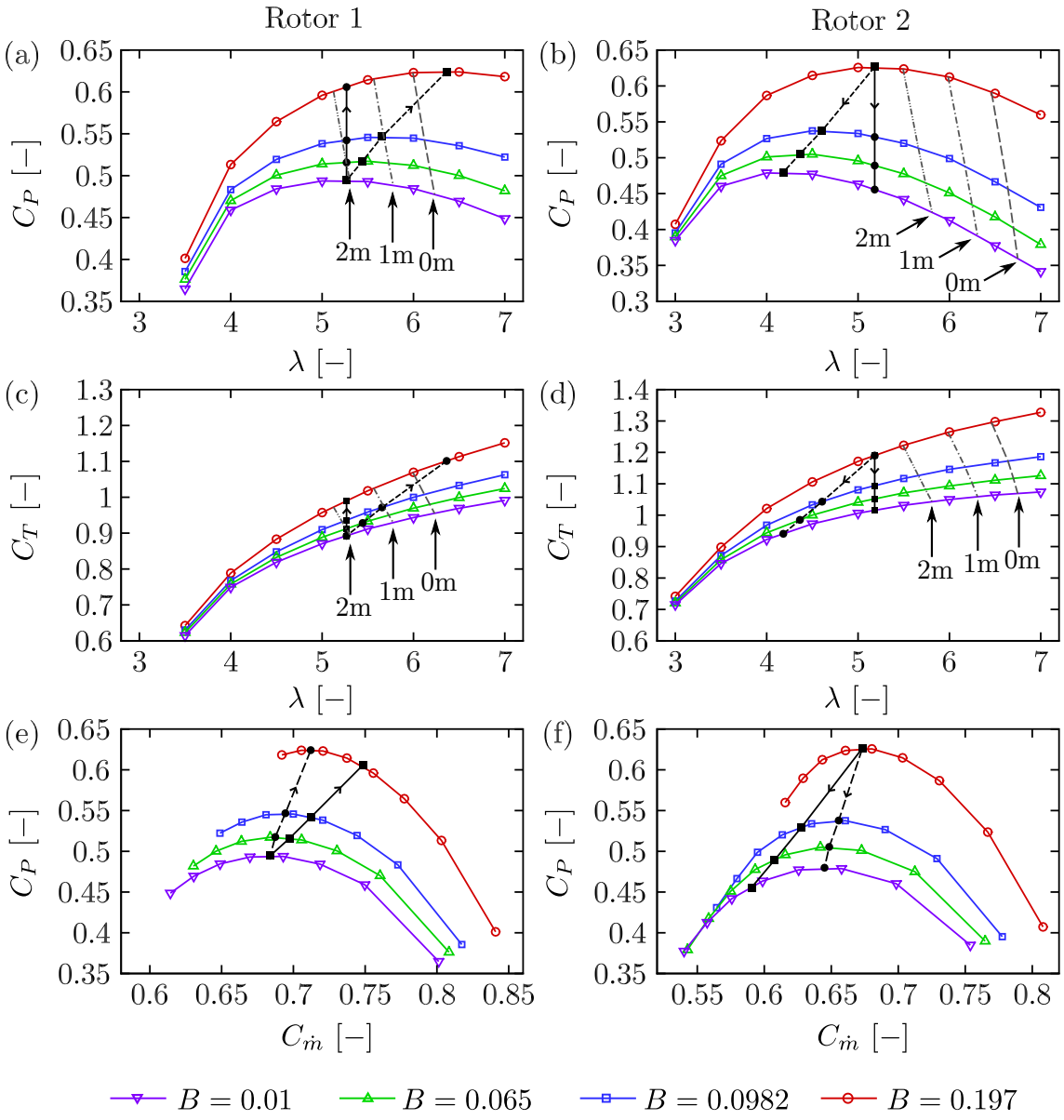

Figure 5.15: Power and thrust coefficients for Rotor 1 and Rotor 2 over a range of blockage ratios and tip-speed-ratios. The black solid lines indicate constant tip-speed-ratio operation, while the black dashed lines indicate the approximate trajectory required to achieve the maximum power coefficient at each blockage ratio. The grey lines indicate the maximum permissible tip-speed-ratios for a device with a tip submersion depth of 0m and safety margins of 0m, 1m and 2m.

flow leads to a greater static pressure drop across the bypass flow passage and hence also across the core flow passage (as the static pressure must equalise between the core and bypass flow streams both far upstream and downstream of the rotor). With

an increased static pressure drop across the core flow passage, a greater mass flow rate is drawn through the rotor swept area. As the rotor is operating at the same tip-speed-ratio, the acceleration of the core flow increases the (azimuthally-averaged) angle of attack and relative velocity magnitude incident on the blades. Hence, the rotor exerts more thrust on the flow and is able to extract more power at the same tip-speed-ratio.

However, operating at constant tip-speed-ratio while increasing the blockage ratio does not lead to the maximum power coefficient that is available in the higher blockage domains. This is because the mass flow rate through the rotor swept area increases as the blockage ratio increases. Hence, the (azimuthally-averaged) angle of attack increases above the (azimuthally-averaged) angle of attack that maximises the lift to drag ratio of the aerofoil sections. To achieve the maximum power coefficients that are available in the higher blockage domains (traversing along the black dashed line in Fig. 5.15), a higher tip-speed-ratio is required. Increasing the tip-speed-ratio increases the thrust applied to the flow by the rotor, which diverts a greater fraction of the incident flow into the bypass flow passage and reduces the mass flow rate through the rotor swept area. Hence, the (azimuthally-averaged) angle of attack reduces back towards the (azimuthally-averaged) angle of attack that maximises the lift to drag ratio of the aerofoil sections. This allows the power coefficient to be maximised in the higher blockage domains and is only possible by increasing the rotor thrust.

However, if the maximum permissible tip-speed-ratio is limited (due to the cavitation restrictions discussed in Section 5.4.2), it may not be possible to increase the rotor thrust and maximise the power coefficient by increasing the tip-speed-ratio. For example, the grey solid, dashed and dashed dotted lines in Fig. 5.15 indicate the maximum permissible tip-speed-ratio of the rotor when the tip submersion depth of the rotor is 0m (the limiting case when the blade tip is touching the surface) and safety margins of 0m, 1m, and 2m of static pressure head (respectively) are applied to the

minimum static pressure. These lines directly correspond with the horizontal safety margin lines in Fig. 5.14 (b). In order to avoid the onset of cavitation, operating conditions to the right of these lines are not permitted.

The performance of Rotor 2 will not be affected by a safety margin of 2m or less, since the maximum power coefficient in each domain occurs at a tip-speed-ratio that is lower than the maximum permissible tip-speed-ratio (to the left of the grey lines). This is because Rotor 2 can apply the higher levels of thrust that are required to maximise the power coefficient naturally (due to its greater solidity), so it does not need as high a tip-speed-ratio as Rotor 1 to apply the necessary thrust. Conversely, Rotor 1 may not be able to achieve the maximum power coefficient that is available in the higher blockage domains, as it requires higher tip-speed-ratios to apply the necessary thrust. In the highest blockage domain ($B = 0.197$) for example, Rotor 1 can achieve a maximum power coefficient of 0.624 at a tip-speed-ratio of 6.36. However, with a safety margin of 2m, this tip-speed-ratio is beyond the maximum permissible tip-speed-ratio and hence the tip-speed-ratio is limited to 5.13 instead. With this tip-speed-ratio restriction, the maximum power coefficient is limited to 0.601 (a performance decrement of 0.023 or 3.69%). In the highest blockage domain considered in this work ($B = 0.197$), it follows that due to the cavitation restriction on the rotor tip-speed-ratio, Rotor 2 (the high solidity rotor) will always outperform Rotor 1, unless Rotor 1 is sufficiently submerged that a tip-speed-ratio restriction is not necessary. This is because Rotor 2 achieves its maximum power coefficient at a lower tip-speed-ratio than Rotor 1 and the cavitation restriction itself occurs at a higher tip speed for Rotor 2.

5.5 Blade Element Computations

In this section, an additional cavitation analysis will be carried out using a blade element based method. The results will be compared with the cavitation analysis carried out in Section 5.4, in order to identify and quantify the discrepancies arising from tip flow effects that are not adequately accounted for in the blade element method.

The blade element method adopted in this section is embedded in a 3D RANS solver (using the approach described by McIntosh et al. (2011)) and will be referred to as the RANS-BE method in this work. In the RANS-BE method, the flow field local to the blade elements is computed directly from the 3D RANS equations, rather than a 1D momentum balance. This formulation allows the RANS-BE method to directly account for the effects of channel blockage, flow deflection by the nacelle and ambient turbulence on the induction at the rotor plane. The forces that are developed on the blade elements are then applied back to the 3D flow field in the form of a static pressure drop and added swirl momentum on the cell faces that make up the actuator disc.

The RANS-BE approach was chosen in preference to a purely analytical blade element momentum (BEM) method, in order to minimise the modelling differences between the blade resolved and blade element approaches and isolate the differences caused by tip flow effects. For example, the nacelle geometry was made to match the blade resolved computations exactly in the RANS-BE computations. By modelling the relatively large nacelle explicitly (15% of the rotor diameter), flow deflection can be captured in the RANS-BE approach, which is generally not possible with the analytical BEM method. For further consistency with the blade resolved computations, the outer domain was set to be cylindrical with a radius of $10R$ (a blockage ratio of 0.01).

The RANS-BE method of McIntosh et al. (2011) accounts for the finite number of

blades in the azimuthally-averaged analysis by using a Glauert (1935) correction factor (which is the standard approach in blade element based analyses). The Glauert correction factor increases the axial induction factor as the tip of the blade is approached, which reduces the angle of the incident flow vector to the rotor plane (ϕ) and the angle of attack (α). With a reduced angle of attack, the strength of the suction peak on the outboard blade sections reduces and the onset of cavitation is delayed, as the minimum static pressure in the fluid has increased. Hence, the Glauert correction does partially account for some tip flow effects (specifically the induced downwash) that lead to a reduction in the strength of the suction peak on the outboard blade sections and a delay in the onset of cavitation. However, as discussed in Chapter 3, the Glauert correction does not account for the induced downwash exactly, as the function was derived using a simplified model of an idealised rotor wake. In addition, the Glauert correction also does not account for the spanwise flow accelerations on the pressure and suction surfaces of the blade (which are induced by the shed vorticity). Hence, the complete tip loss mechanism is not necessarily accounted for with sufficient accuracy in blade element based cavitation analyses, when only a Glauert correction is used. In the next section, the discrepancy between the blade resolved and RANS-BE cavitation analyses will be identified and quantified, in order to demonstrate the significance of the tip loss mechanism in the cavitation analysis of tidal turbine rotors.

5.5.1 Blade Element Based Cavitation Analysis

To carry out a cavitation analysis using the results of the RANS-BE computations, the spanwise variation of angle of attack (α) and relative velocity magnitude (U_{rel}) were extracted from the converged RANS-BE computations. The angle of attack distribution was then used to infer the spanwise variation of the minimum static pressure coefficient (C_{pre}), by looking up the minimum static pressure coefficient (at

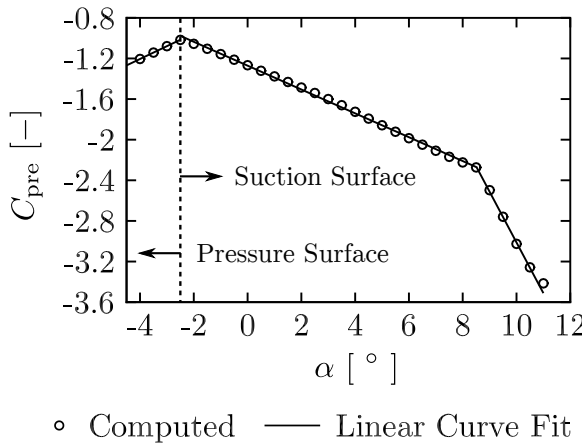

Figure 5.16: Minimum static pressure coefficient on the surface of the RISØ-A1-24 aerofoil at a chord-based Reynolds based of 12 million. Points (on and) to the left of the vertical dashed line indicate that the minimum static pressure occurs on the pressure surface, while points to the right of the vertical dashed line indicate that the minimum static pressure occurs on the suction surface.

each angle of attack) from the corresponding 2D aerofoil computations that were used to compute the lift and drag polars. Fig. 5.16 shows the variation of the minimum static pressure coefficient with angle of attack, that was used in this analysis.

Hydrostatic and atmospheric pressure components were then added to compute the spanwise variation of the minimum static pressure along the blade at top dead centre.

$$p = p_{\mathrm{Atm}} + \rho g(h_{\mathrm{tip}} + R - r) + C_{\mathrm{pre}}(\alpha(r)) \left[\frac{1}{2}\rho U^2_{\mathrm{rel}}(r)\right] \tag{5.9}$$

Fig. 5.17 shows the spanwise variation of the minimum static pressure computed with the RANS-BE and blade resolved approaches. Along the mid-span of the blade ($r/R < 0.9$), the blade resolved and RANS-BE approaches show close agreement, as tip flow effects are small in this region of the blade. However, near the tip of the blade (where the static pressure reaches a minimum and cavitation inception is most likely to occur) tip flow effects are more significant and the blade resolved and RANS-BE approaches do not show close agreement. More specifically, the RANS-BE computations predict a lower minimum static pressure than the blade resolved computations,

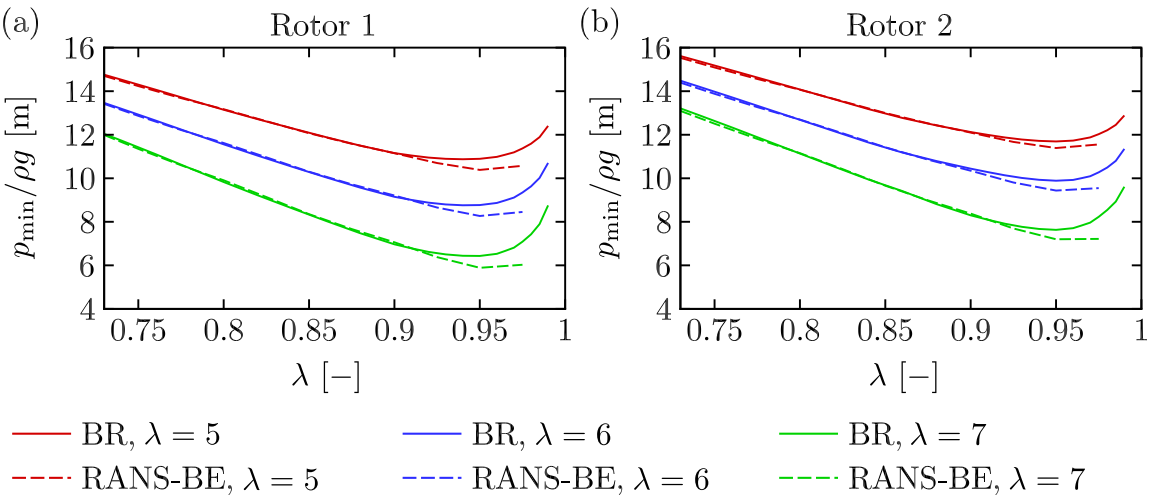

Figure 5.17: Spanwise variation of the minimum static pressure acting on each aerofoil section, expressed in terms of a static pressure head. BR stands for blade resolved.

so the rotor is closer to cavitation at a given tip-speed-ratio and submersion depth. The inaccuracy in the RANS-BE computations arises because the Glauert correction is not sufficient to account for the entire tip loss mechanism. As discussed in Chapter 4, the spanwise flow accelerations on the pressure and suction surfaces of the blade lead to a further reduction in the strength of the suction peak (above that which is induced by the downwash), increasing the minimum static pressure in the fluid and pushing the rotor further away from cavitation. While the Glauert correction may be able to partially account for the induced downwash (which reduces the angle of attack and the strength of the suction peak), it cannot account for the spanwise flow accelerations. Hence, blade element based cavitation analyses that only use the Glauert correction will always be overly conservative, unless an additional correction is employed.

Fig. 5.18 compares the magnitude of the minimum static pressure computed using the RANS-BE and blade resolved approaches. At the same tip-speed-ratio, the RANS-BE approach predicts a minimum static pressure head that is approximately 0.4m lower than the blade resolved approach. Hence, the devices could actually be installed 0.4m higher up in the water column than computed with the RANS-BE

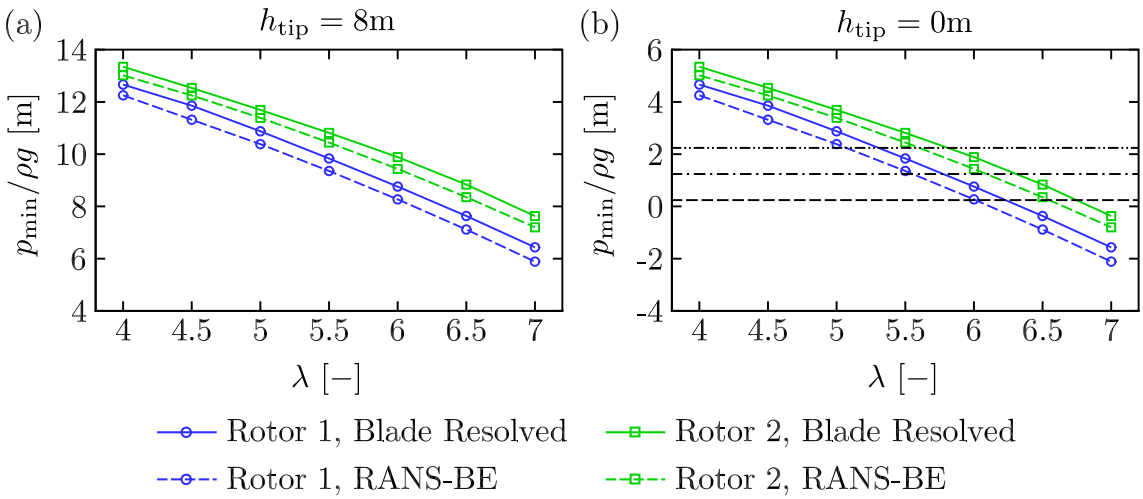

Figure 5.18: Minimum static pressure head on the blade suction surface for tip submersion depths of (a) 8m and (b) 0m. The horizontal dashed, dashed dotted and dashed double dotted lines indicate safety margin of 0m, 1m and 2m respectively, relative to the vapour pressure head of seawater (0.24m).

approach, while maintaining the same safety margin. Alternatively, if the submersion depth of the device is fixed, then the maximum permissible tip-speed-ratio of the rotor computed with the RANS-BE approach can be increased by approximately 0.21, while maintaining the same safety margin.

5.6 Summary

At higher blockage ratios, rotors exert more thrust on the flow and are able to extract more power, when operating at the same tip-speed-ratio. This increase arises from the additional acceleration of the bypass flow, which increases the static pressure drop across the rotor plane and draws a greater mass flow rate through the swept area of the rotor. A further increase in power can be achieved at higher blockage ratios, by increasing the thrust that the rotor applies to the flow. This additional thrust can be applied by either increasing the tip-speed-ratio of the rotor (spinning the rotor faster) or by re-designing the rotor itself to apply greater thrust to the flow (principally by increasing the solidity of the rotor). In some cases, it may not be possible to increase

the tip-speed-ratio of the rotor, as the strength of the blade suction peak increases with tip-speed-ratio and the rotor is more likely to cavitate. Under these conditions, high solidity rotors are preferable as they can apply the additional thrust required to maximise the power coefficient naturally and do not need such high tip-speed-ratios to apply the necessary thrust.

Recent design guidelines state that cavitation inception must be avoided completely during tidal turbine operation. Therefore it may be necessary to either increase the submersion depth or limit the maximum tip-speed-ratio of the rotor, in order to limit the minimum static pressure developed on the blade surface and avoid cavitation inception. Both of these restrictions adversely affect the performance of the rotor. When the submersion depth of the device is increased, the kinetic energy flux that is available to the device for energy extraction may reduce significantly if the velocity profile is highly sheared. In contrast, when the maximum tip-speed-ratio is limited, it may not be possible to achieve the maximum power coefficients that are available at higher blockage ratios by spinning the rotor faster.

The majority of the cavitation analyses that have been carried out in the literature are based on the blade element method. In this work it has been shown that blade element based cavitation analyses are (currently) overly conservative, as the minimum static pressure computed with these methods is too low (they are closer to cavitation in the simulations than they are in reality). This discrepancy arises because tip flow effects (which reduce the strength of the suction peak) are not sufficiently accounted for in blade element based methods and the strength of the suction peak is over-predicted. Hence, new tip flow corrections are required to improve the accuracy of cavitation analyses which are based on the blade element method.

Chapter 6

Actuator Disc Performance on a Streamwise Bed Slope

When carrying out experimental investigations of tidal turbine rotors in towing tanks and flumes, the bottom of the tank is often horizontal and uniform. Likewise, in computational studies of tidal turbine rotors, the sea bed is often assumed to be horizontal and uniform, to simplify the analysis. However, at many sites that are currently under consideration for device installation, the sea bed is not uniform and slopes considerably in the streamwise and lateral directions. At the MeyGen site (Phase 1a) for example, the local depth varies from around 30m to around 35m in the immediate vicinity of the devices (over a few hundred metres) (MeyGen Ltd. 2016). While the effect of sloping bathymetry on the depth-averaged velocity can be readily captured in regional scale computations (by varying the local depth in the depth-averaged shallow water equations), the effect of sloping bathymetry on the local flow field at device scale is less well understood and is often ignored. To address this deficiency, the affect of a (non-horizontal) sloping seabed on the performance of a tidal energy device will be considered in this chapter, in a series of computational studies.

As shown in Fig. 6.1, a first approximation to the sloping bathymetry at real tidal energy sites can be made by a constant (positive or negative) slope in the streamwise direction. Large bathymetric features (such as ridges, troughs and mounds) may also be present at some tidal energy sites. These discrete bathymetric features generate highly energetic turbulent structures, which are shed into the flow and may impact the rotor (see Soto & Escauriaza (2015) and Zangiabadi et al. (2015) for example). However, such bathymetric features will not be analysed in this work, since tidal energy devices are not likely to be installed in the immediate vicinity of such bathymetric features, due to the desire to minimise unsteady loading on the rotor.

In this chapter, upwards facing, horizontal and downwards facing bed slopes will be considered and the resulting changes in performance of an actuator disc (representing an ideal energy extracting device) operating on each bed slope, will be examined. Throughout this chapter it should be noted that tidal currents are bi-directional and a tidal energy device operating on a sloping sea bed at a given geographical location will experience both upwards and downwards facing flows over the tidal cycle. However, the upwards and downwards facing cases have been deliberately segregated in this chapter, in order to clarify the presented analysis. In the next chapter, the actuator disc will be replaced with a blade resolved rotor representation, to examine the changes in performance of a more realistic device representation on each bed slope. Similar approximations to the local bathymetry could also be made in the cross-stream (lateral) direction. However, these variations will not be considered in this work.

6.1 Computational Domains

Three separate computational domains were created for the upwards facing, horizontal and downwards facing bed slopes, as shown in Fig. 6.2. To ensure a consistent

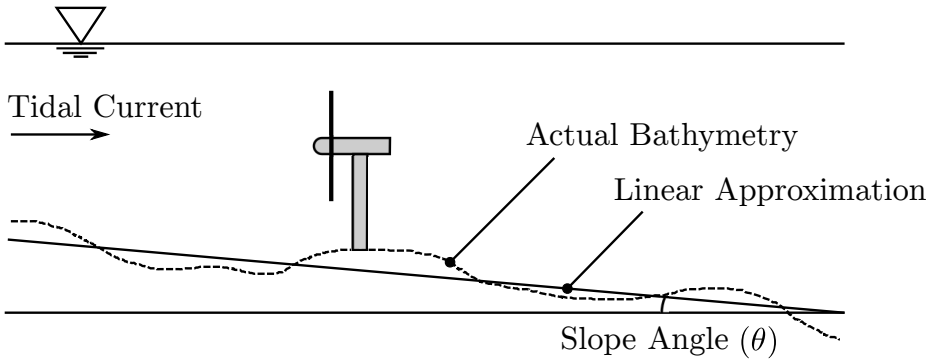

Figure 6.1: Approximating the local bathymetry in the vicinity of a tidal energy device by a constant slope with angle θ.

blockage ratio at the disc plane, a depth of $2D$ (where D is the disc diameter) was adopted at the disc plane on all three bed slopes and the disc was positioned at the mid-depth of the channel (a tip submersion depth of $D/2$). The sloping section was propagated a horizontal distance of $10D$ upstream and $10D$ downstream of the disc plane, at an angle of 5°, to create upwards and downwards facing bed slopes. A slope angle of 5° was chosen for this investigation, as this is likely to be the practical limit for device installation (E.ON 2014). A slope angle of 5° will also be shown later in Section 6.1.3 to be sufficiently shallow for flow separation not to occur on the downwards facing slope. With a disc diameter of 20m (typical of many full-scale tidal energy devices), a slope angle of 5° leads to maximum and minimum water depths of 57.43m and 23.6m respectively, with a depth of 40m at the disc plane. These depths are typical of a variety of tidal energy sites, such as the MeyGen site (MeyGen Ltd. 2011) and the Fall of Warness (Gunn & Stock-Williams 2013).

Two different domain widths were adopted for this investigation, in order to also investigate the effect of blockage at the disc plane. The first domain was assigned a width of $2D$, to yield a relatively high blockage ratio of 0.197. This blockage ratio is representative of the blockage that may be experienced by a device located far from the ends of a sufficiently long fence of closely packed devices (that is arrayed normal to the flow direction), with a tip-to-tip spacing (s) of $1D$. The second domain was

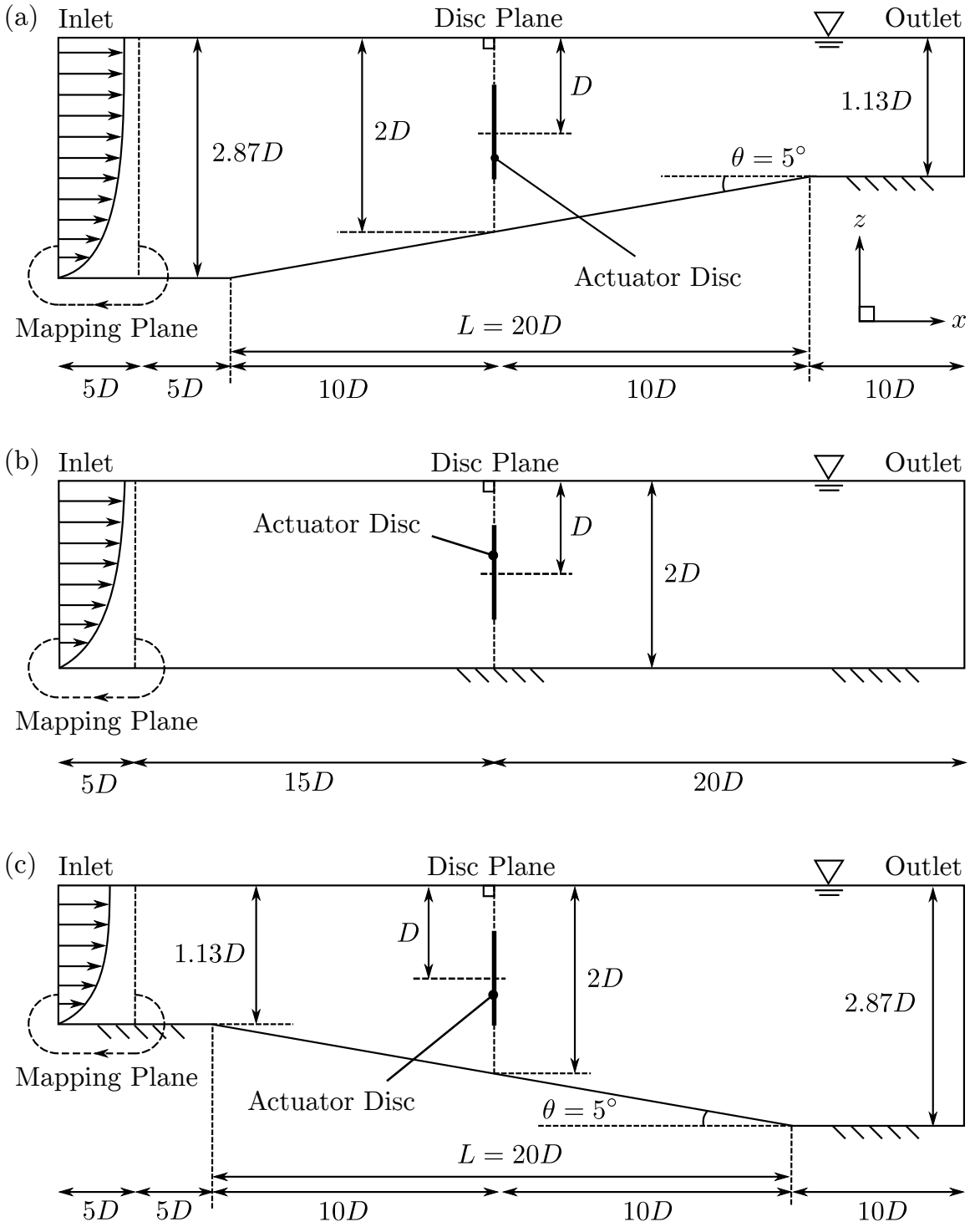

Figure 6.2: Schematic diagram of the computational domain adopted for the (a) upwards facing, (b) horizontal and (c) downwards facing bed slopes. This diagram shows a lateral (side-on) view in the $x - z$ plane.

assigned a width of $6D$, to yield a much lower blockage ratio of 0.065. This blockage ratio is representative of the blockage that may be experienced by a device placed within a more widely spaced fence of devices, with a tip-to-tip spacing of $5D$.

6.1.1 Actuator Disc

An actuator disc is an ideal energy extractor, which only extracts linear momentum from the flow. Energy losses from viscous drag and wake rotation (that are inherent to real rotors) are not captured by the actuator disc, so the energy extracted by the disc represents an upper limit to the maximum theoretical power that can be extracted by a real device. The actuator disc extracts linear momentum from the flow by applying a static pressure drop (Δp) across the cell faces that make up the disc. The strength of the static pressure drop is proportional to the local velocity normal to the cell face (u_x) and is computed using equation 6.1,

$$\Delta p = \frac{1}{2}\rho K u_x^2 \tag{6.1}$$

where ρ is the density of seawater (1025 kg/m^3) and K is the momentum loss factor. The momentum loss factor is equivalent to the local thrust coefficient (C_{TL}) that is used in linear momentum actuator disc theory (Garrett & Cummins 2007, Houlsby et al. 2008) and is related to the porosity of physical porous discs that may be used in flume experiments (Taylor 1944). In this investigation, separate computations were carried out over a range of momentum loss factors, to simulate a range of disc resistances. Table 6.1 provides a summary of the parameter space that was investigated.

As the actuator disc does not impart any swirl or rotation on the flow, the computed flow field (in this investigation) will be symmetric about the mid-width of the domain ($y = 0$). Hence, to reduce the computational time, symmetry boundary conditions were applied along the mid-width of the domain and only half the domain was

Table 6.1: Summary of the parameter space investigated for the actuator disc computations.

Bed Slope	s	B	K
Downwards	D	0.197	0, 0.5, 1, ... 5.5, 6.0
Horizontal	D	0.197	0, 0.5, 1, ... 5.5, 6.0
Upwards	D	0.197	0, 0.5, 1, ... 5.5, 6.0
Downwards	$5D$	0.065	0, 0.5, 1, ... 5.5, 6.0
Horizontal	$5D$	0.065	0, 0.5, 1, ... 5.5, 6.0
Upwards	$5D$	0.065	0, 0.5, 1, ... 5.5, 6.0

computed explicitly.

6.1.2 Free Surface Modelling

In this investigation, the free surface was assumed to be flat and horizontal and any deformation due to energy extraction was neglected (a rigid lid model), as shown in Fig. 6.2. This free surface treatment also implicitly sets the downstream fluid depth and therefore the total energy extracted from the flow (both by the bed friction and the device). In reality, the downstream fluid depth varies in response to both the upstream Froude number and the total energy removed from the flow. As the total energy removed from the flow is strongly dependent on the thrust applied by the device (and hence the device operating point), the downstream fluid depth cannot strictly be specified *a priori* as a boundary condition to the simulations. The rigid lid model adopted in this work is therefore equivalent to assuming an upstream Froude number of 0, when in reality the Froude number based on the bulk velocity and depth at the device plane is actually ~ 0.1 without the device present.

In this investigation it is likely that free surface deformation affects are significantly, particularly due to the bed elevation change between the inlet and the outlet planes on the upwards and downwards facing bed slopes. However, free surface deformation effects are deliberately neglected in this investigation so that the predominant

flow physics associated with the disc performance (particularly the core and bypass flow accelerations and changes in axial velocity shear) can be isolated and identified. An additional analysis is clearly required in future to include the additional acceleration of the core and bypass flows from the free surface deformation, which may then impact device performance. To quantify the uncertainty associated with the neglected free surface deformation, the neglected change in free surface height was estimated after the rigid lid computations were carried out. Firstly, the total energy flux removed from the flow (ΔE) between the domain inlet (subscript 1) and the domain outlet (subscript 2) by both the disc and the resistance provided by the bed slope, was computed numerically using equation 6.2.

$$\Delta E = \int_0^{h_1} \left(p_1 + \frac{1}{2}\rho|\boldsymbol{U_1}|^2 \right) U_1 \mathrm{d}S_1 - \int_0^{h_2} \left(p_2 + \frac{1}{2}\rho|\boldsymbol{U_2}|^2 \right) U_2 \mathrm{d}S_2 \tag{6.2}$$

In equation 6.2, h represents the local fluid depth and $\mathrm{d}S$ integration over the channel cross-sectional area. Neglecting the energy dissipated to wake mixing downstream of the computational domain outlet, the neglected change in free surface height (Δh) between the inlet and outlet was estimated using equation 6.3.

$$\Delta h = \frac{\Delta E}{\dot{m} g} \tag{6.3}$$

In equation 6.3, $\dot{m}$ represents the mass flow rate through the channel and g the acceleration due to gravity (9.81 m/s^2). For the actuator disc in the high blockage domain operating at the highest thrust ($K = 6$), the estimated change in free surface height between the inlet and outlet (Δh) was only 0.24% of the undisturbed water depth at the disc plane ($2D$ = 40 m). Hence, free surface deformation affects are likely to be second order but still significant and will need to be considered in a later analysis.

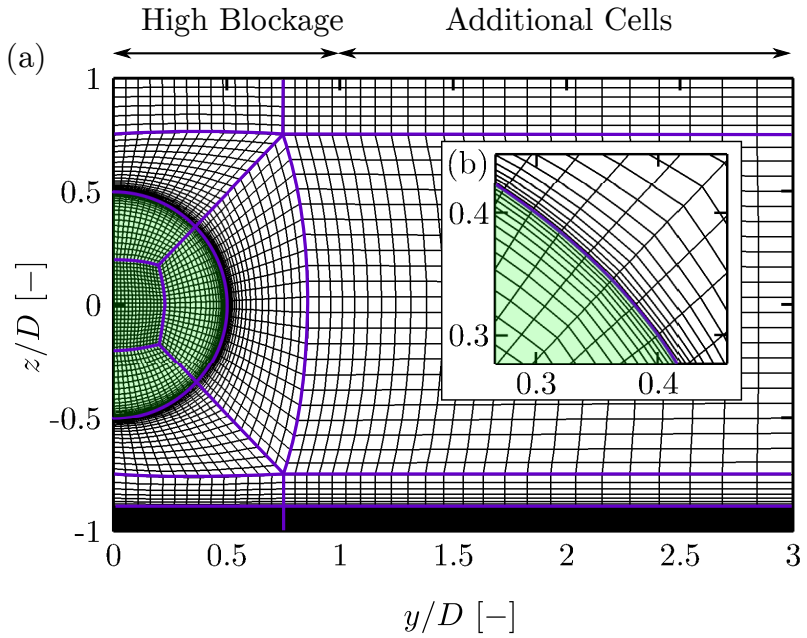

Figure 6.3: A slice through the block structured mesh of the low blockage domain ($B = 0.065$) at the disc plane ($x/D = 0$), normal to the streamwise (x) direction. The cells between $y/D = 1$ and $y/D = 3$ are removed for the high blockage domain ($B = 0.197$). A close up of the disc edge is shown in (b). The blocking edges are highlighted in purple and the cells that make up the disc are shaded in green.

6.1.3 Meshing Strategy

A block structured mesh with all hexahedral cells was generated for each of the computational domains. An O-grid type blocking topology was adopted around the disc region, in order to capture the steep velocity gradients in the radial direction away from the edge of the disc. In order to show the adopted blocking structure, Fig. 6.3 shows a slice through the mesh of the low blockage domain ($B = 0.065$) at the disc plane ($x/D = 0$), normal to the streamwise (x) direction. For the high blockage domain ($B = 0.197$), the additional cells between $y/D = 1$ and $y/D = 3$ were removed, in order to preserve the mesh structure and resolution between cases. The radial grid dimension at the edge of the disc ($\Delta r = D/400$) corresponds with the medium mesh resolution of Nishino & Willden (2012*a*), who showed that it was sufficient to capture the shear layer that develops between the core and bypass flow passages downstream of the disc.

The cells at the disc plane were assigned a length of $D/200$ in the streamwise direction. These cells were expanded in the streamwise direction upstream and downstream of the disc (maintaining the same blocking structure shown in Fig. 6.3), with a growth ratio of 1.02 up to distance of $D/2$ away from the disc. Further upstream and downstream of the disc, the cells were expanded with a growth ratio of 1.1 until they reached the inlet and outlet of the domain.

The wall adjacent cell centroids on the bed surface were assigned a distance of $1.25 \times 10^{-4}D$ normal to the wall, such that y^+ was everywhere in the logarithmic law region of the universal law of the wall ($30 < y^+ < 200$). Due to the total streamwise length of the bed surface ($40D$), it was not possible to reduce the wall normal distance and place these cells within the viscous sub-layer, without producing high aspect ratio cells that would have lead to an unstable computation. Hence the velocity profile between the wall adjacent cell centroid and the wall was modelled with the standard logarithmic law velocity profile (discussed in Chapter 2), which was assumed to be sufficient, even for the downwards facing bed slope (with an adverse pressure gradient). This assumption was expected to provide an acceptable prediction of the wall shear stress and the velocity profile away from the wall, as long as flow separation does not occur.

To investigate the consequences of this assumption, an additional computation was carried out on the downwards facing bed slope with no disc present and with the wall adjacent cell centroids placed in the viscous sub-layer ($y^+ < 5$) over the entire surface. As this domain did not include a disc, the domain was collapsed along the lateral (y) axis into the $x - z$ plane, to enable a 2D computation to be carried out. This approach allowed the high aspect ratio limitation to be overcome by increasing the streamwise resolution (along the x axis), so that a viscous sub-layer resolved computation could be undertaken for comparison.

As shown in Fig. 6.4, the skin friction coefficient was positive over the entire bed

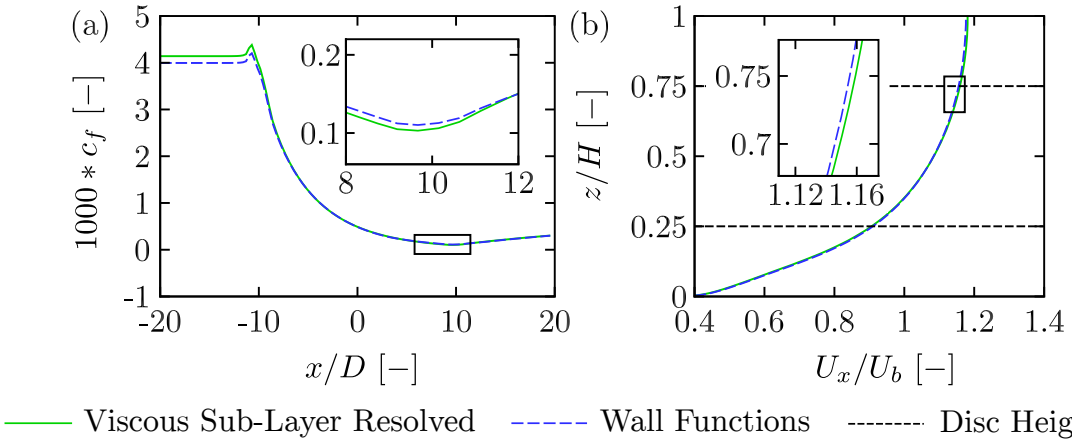

Figure 6.4: (a) Skin friction coefficient on the bed slope and (b) the axial velocity profile at the disc plane ($x/D = 0$), for the downwards facing slope ($\theta = 5°$) with no disc present ($K = 0$). The horizontal dashed lines indicates the height of the actuator disc (to be included).

surface and therefore flow separation did not occur, although if the bed slope had continued further downstream, it would have eventually occurred due to the adverse pressure gradient. Therefore, the logarithmic law velocity profile was likely to be an acceptable assumption for this geometry and inflow conditions. However, it should be noted that for bed slopes greater than 5° (not considered in this work), flow separation is more likely to occur and the logarithmic law velocity profile may be insufficient.

6.1.4 Inlet Conditions

To correctly capture the development of the velocity and turbulence scalar (k and ω) profiles on the bed slope, the velocity and turbulent scalar profiles must be fully developed when they encounter the bed slope. Hence, the inlet boundary conditions must be carefully chosen to ensure that the profiles are fully developed and numerically consistent. In the literature, different methods have been proposed to generate inlet profiles with high levels of velocity shear and ambient turbulence, in order to mimic site specific conditions (McNaughton 2013, Mason-Jones et al. 2013). However, the profiles generated using these methods are not numerically consistent, so the profiles will collapse between the inlet and the start of the bed slope. While an alternative

technique has been proposed by Fleming (2014) to generate numerically consistent profiles, this technique requires the wall shear stress on the seabed to be specified explicitly as a boundary condition (replacing the no-slip condition). This approach cannot be applied to the computations carried out in this work, as the seabed is inclined and the wall shear stress on the seabed develops as part of the solution.

In this investigation, fully developed axial velocity and turbulence scalar profiles were generated at the computational domain inlet using the mapping plane technique described by Tabor & Baba-Ahmadi (2010). In this method, the velocity and turbulence scalar profiles are sampled downstream of the domain inlet (see Fig. 6.2) at the end of each SIMPLE iteration and are applied as the inlet boundary condition during the next iteration. Hence, the sheared axial velocity and turbulent scalar profiles are developed numerically as the simulation converges, in a manner that is conceptually similar to precursor simulations that are used for Large Eddy Simulation (LES) of fully developed turbulent channel flow.

The fully developed profiles that are developed by the mapping plane technique are functions of the mass flow rate, local depth and bed roughness alone. In this investigation, the mass flow rate is already set by the requirement to have a consistent bulk velocity (U_b) of 2.0 m/s at the disc plane and the local depth is already set by the geometry of the domain. Therefore, the bed roughness height (K_s) was used to control the degree of velocity shear instead, by modifying the logarithmic law intercept of the universal law of the wall. Following Cebeci & Bradshaw (1977), the velocity wall function (discussed in Chapter 2) was modified by ΔB,

$$u^+ = \frac{1}{\kappa} \ln\left(Ey^+\right) - \Delta B \tag{6.4}$$

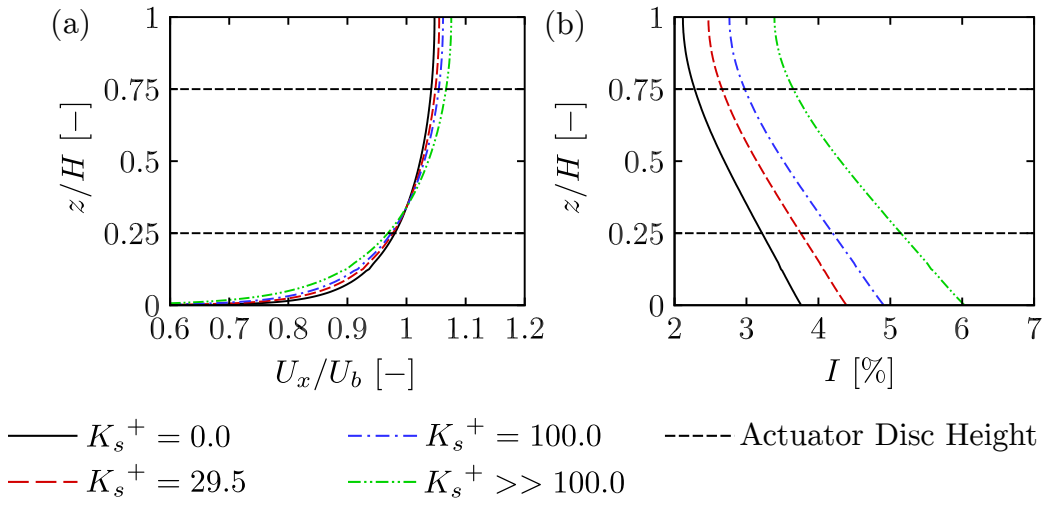

Figure 6.5: Fully developed axial velocity and turbulence intensity profiles at the computational domain inlet ($x/D = -20$) for the horizontal bed slope ($\theta = 0°$), for hydrodynamically smooth, transitional and rough bed surfaces. The horizontal dashed lines indicate the height of the actuator disc (to be included).

$$\Delta B = \begin{cases} 0 & K_s^+ < 2.25 \\ \frac{1}{\kappa} \ln\left(\frac{K_s^+ - 2.25}{87.75} + C_s K_s^+\right) & \\ \times \sin(0.4258 \ln(K_s^+ - 0.811)) & 2.25 < K_s^+ < 90.0 \\ \frac{1}{\kappa} \ln(1 + C_s K_s^+). & K_s^+ > 90.0 \end{cases} \tag{6.5}$$

where E and κ are empirical constants (9.81 and 0.41 respectively), C_s is the roughness constant (taken as 0.5 for uniform roughness elements) and K_s^+ is the dimensionless roughness height (based on the wall shear stress τ_w).

$$K_s^+ = \frac{K_s u_\tau}{\nu} \qquad u_\tau = \sqrt{\frac{\tau_w}{\rho}} \tag{6.6}$$

The dimensionless roughness height represents the height of the roughness elements in wall units and can be used to distinguish between hydrodynamically smooth ($K_s^+ = 0$), transitional ($2.25 < K_s^+ < 90.0$) and rough ($K_s^+ > 90.0$) surfaces. Fig. 6.5 shows the resulting fully developed axial velocity and turbulence intensity profiles for hydrodynamically smooth ($K_s^+ = 0$), transitional ($K_s^+ = 29.5$), rough

($K_s{}^+ = 100$) and fully rough ($K_s{}^+ >> 100$) surfaces on the horizontal bed slope. For consistency, the turbulence intensity has been computed using the bulk velocity at the disc plane ($U_b = 2.0$ m/s), which is the same for all computations carried out in this chapter.

$$I = \sqrt{\frac{2k}{3U_b^2}} \tag{6.7}$$

Fig. 6.5 shows that both the degree of velocity shear (across the disc face) and the ambient turbulence intensity increase with increasing roughness height. As a result, the hydrodynamically fully rough surface experiences the greatest velocity shear across the disc face and also the highest ambient turbulence intensity (up to 6% at the wall). Unfortunately, it was not possible to achieve higher turbulence intensities (that are characteristic of some highly energetic tidal energy sites) by further modifying the wall roughness. To achieve greater turbulence intensities, an unsteady inlet condition would be required, such as the synthetic eddy method of Jarrin et al. (2006). Such an approach was not applied in this investigation, due to the desire to maintain a steady computation.

6.2 Undisturbed Profiles

Before carrying out the actuator disc computations, a separate set of computations were carried out on each bed slope without the disc present. Fig. 6.6 shows the axial velocity and turbulence intensity profiles that were computed at the disc plane without the disc present.

On the downwards facing slope, the adverse pressure gradient leads to a reduction in wall shear stress (and hence velocity gradient) at the wall. To conserve mass, the axial velocity must increase away from the wall, which results in an increase in velocity shear across the disc face. With increased velocity shear, the (undisturbed)

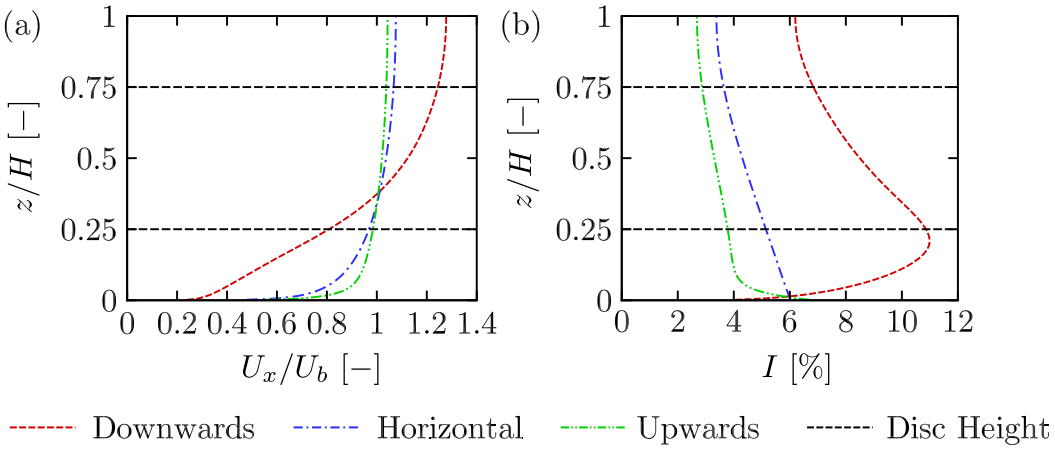

Figure 6.6: (a) Axial velocity and (b) turbulence intensity profiles at the disc plane ($x/D = 0$) with no disc present. The horizontal dashed lines indicate the height of the actuator disc (to be included in later simulations).

dynamic pressure and kinetic energy flux incident on the disc also increase, increasing the power available for extraction. Table 6.2 shows the spatial average of the axial velocity ($\langle u_{x0} \rangle$), axial velocity squared ($\langle u_{x0}^2 \rangle$) and axial velocity cubed ($\langle u_{x0}^3 \rangle$) over the disc area, with no disc present. These quantities are representative of the undisturbed mass flow rate ($\rho \langle u_{x0} \rangle A$), dynamic pressure ($1/2 \rho \langle u_{x0}^2 \rangle$) and kinetic energy flux ($1/2 \rho \langle u_{x0}^3 \rangle$) that is available to the disc on each bed slope.

Table 6.2: Axial velocity, axial velocity squared and axial velocity cubed averaged over the disc area with no disc present, in dimensional and dimensionless form, for the downwards facing, horizontal and upwards facing bed slopes.

Bed Slope	$\langle u_{x0} \rangle$ [m/s]	$\langle {u_{x0}}^2 \rangle$ [m^2/s^2]	$\langle {u_{x0}}^3 \rangle$ [m^3/s^3]	$\langle u_{x0} \rangle / U_b$ [-]	$\langle {u_{x0}}^2 \rangle^{1/2} / U_b$ [-]	$\langle {u_{x0}}^3 \rangle^{1/3} / U_b$ [-]
Downwards	2.1837	4.8336	10.8279	1.092	1.099	1.106
Horizontal	2.0647	4.2654	8.8162	1.033	1.033	1.033
Upwards	2.0363	4.1475	8.4489	1.018	1.018	1.018

As shown in Table 6.2, the kinetic energy flux that is available to the disc on the downwards facing bed slope is 22.8% greater than on the horizontal bed slope. Hence, devices installed on downwards facing bed slopes have a greater potential for power extraction, regardless of the type of device that is installed or how it is operated.

Conversely, on the upwards facing slope the axial velocity profile is less strongly sheared across the projected area of the disc due to the favourable pressure gradient. Despite the reduced kinetic energy flux available for extraction, this may be beneficial from a loading perspective (as will be discussed in section 6.4).

6.3 Thrust and Power Coefficients

Fig. 6.7 shows the variation in the disc thrust and power coefficients (C_T and C_P respectively) with momentum loss factor, on each bed slope. To account for the different degree of velocity shear on each bed slope, the disc thrust (T) and power (P) have been normalised by the dynamic pressure and kinetic energy flux incident on the disc area, without the disc present (indicated by the subscript 0).

$$C_T = \frac{T}{\frac{1}{2}\rho \int_A ({u_{x0}}^2)\,\mathrm{d}A} \tag{6.8}$$

$$C_P = \frac{P}{\frac{1}{2}\rho \int_A ({u_{x0}}^3)\,\mathrm{d}A} \tag{6.9}$$

With the normalisation adopted in equation 6.9, the power coefficient represents the fraction of the available kinetic energy flux that is extracted by the disc. Hence, this definition of the power coefficient can be used as a measure of the efficiency of the disc. However, it should be noted that this is not the only method of normalising C_T and C_P in sheared flows. Draper et al. (2016) and Fleming (2014) adopt the spatial average of the axial velocity squared and cubed (for thrust and power respectively) far upstream of the device, in their normalisation. Unfortunately this definition cannot be reliably adopted in this work, since the sheared velocity profile develops in the streamwise direction along the bed slope and it is not clear how far upstream to sample the flow field. Normalisations using the hub-height velocity were also deemed to be inappropriate, since the hub-height velocity does not capture the degree of shear across the rotor swept-area as accurately as the spatial average (McNaughton

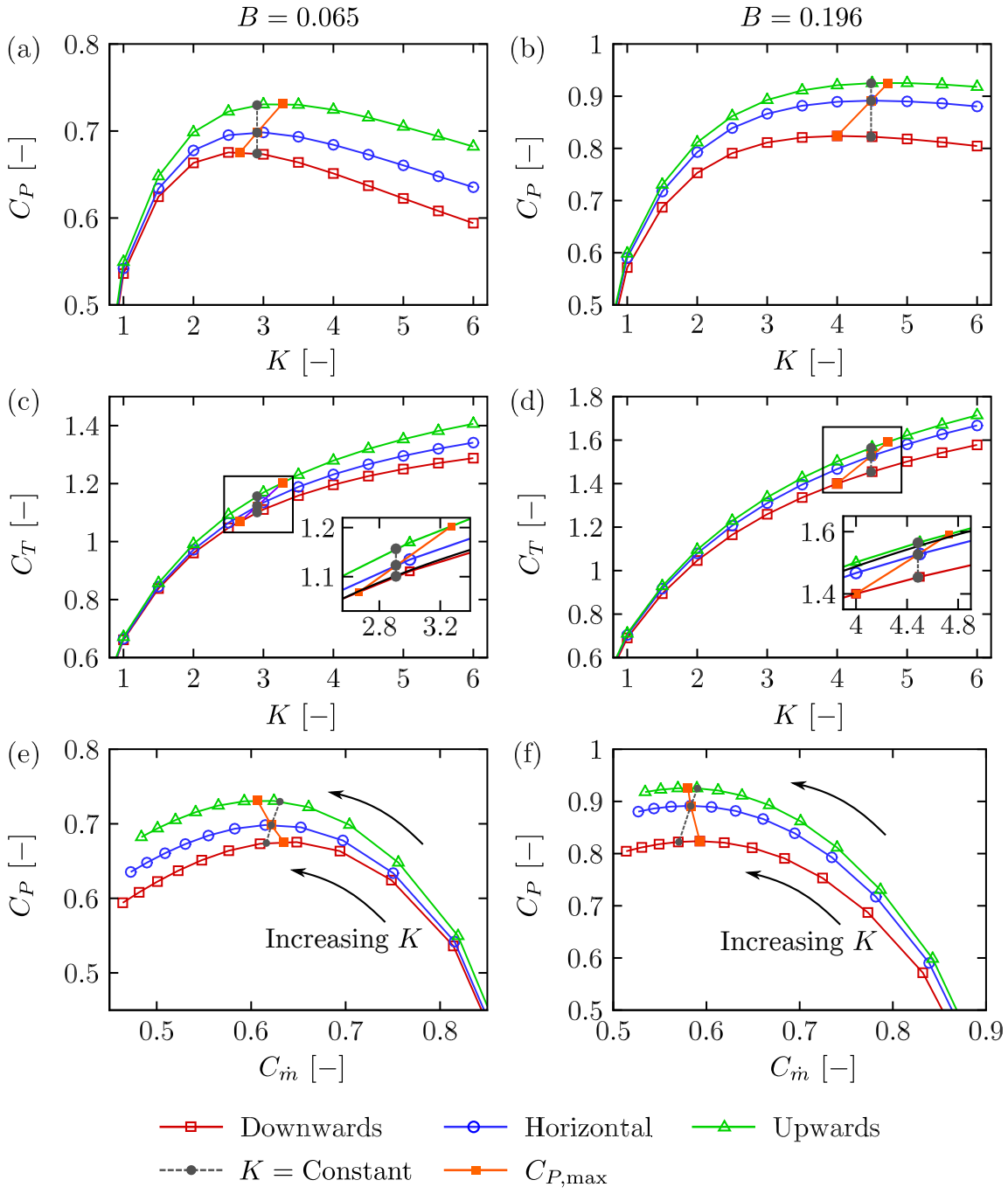

Figure 6.7: Variation in the disc thrust and power coefficients with momentum loss factor and mass flow rate coefficient on each bed slope. The maximum power coefficients ($C_{P,\max}$) were estimated using polynomial curve fits.

2013). Therefore the undisturbed shear profile at the disc plane is adopted for the normalisations in this work.

The power coefficient has also been plotted against the mass flow rate coefficient ($C_{\dot{m}}$) in Fig. 6.7 to aid in the ensuing discussion. The mass flow rate coefficient represents the ratio of the mass flow rate through the swept area of the disc, to the mass flow rate through the swept area of the disc without the disc present.

$$C_{\dot{m}} = \frac{\int_A (\rho u_x)\,\mathrm{d}A}{\int_A (\rho u_{x0})\,\mathrm{d}A} \tag{6.10}$$

With this definition, the mass flow rate coefficient can also be interpreted as $1-\bar{a}$, where $\bar{a}$ is the spatial average of the axial induction factor over the disc area.

As shown in Fig. 6.7, the disc achieves greater thrust and power coefficients on the upwards facing slope than on the horizontal and downwards facing slopes, when operating at the same momentum loss factor (by traversing along the grey dashed line). The physical mechanism that allows the disc to achieve greater thrust and power coefficients on the upwards facing slope will now be described and the observations of the local flow field that accompany it will be presented in sections 6.5.1 and 6.5.2.

The thrust and power coefficients are greater on the upwards facing slope because the bypass flow (the flow which passes around the disc) is accelerated by the downstream constriction, which leads to a greater static pressure drop in the bypass flow passage. As the static pressure must equalise between the core flow (the flow which passes through the disc) and the bypass flow, both far upstream and downstream of the disc, a greater static pressure drop is also developed across the core flow passage. The increased static pressure drop across the core flow passage then draws a greater mass flow rate through the disc (traversing along the grey dashed line in Fig. 6.7 (e and f)). As the disc is operating at the same momentum loss factor, the increased mass flow rate allows the disc to exert a greater static pressure drop on the flow (as $\Delta p = \frac{1}{2}\rho K u_x^2$). Hence, the disc exerts more thrust on the flow (as $T = \Delta p \times A$) and

is able to extract more power (as $P = T \times u_x$), which is manifested as an increase in the thrust and power coefficients in Fig. 6.7.

6.3.1 Maximising the Power Coefficient

Fig. 6.7 also shows an estimate of the maximum power coefficient that can be achieved on each bed slope and the momentum loss factor that it occurs at. These values were estimated using polynomial curve fits and are joined in Fig. 6.7 by a solid orange line. Fig. 6.7 shows that on the upwards facing slope, the momentum loss factor can be increased slightly above the momentum loss factor that maximises the power coefficient on the horizontal slope (traversing along the orange line in Fig. 6.7). By increasing the momentum loss factor, the thrust applied to the flow by the disc increases, which reduces the mass flow rate through the disc area. Hence, a greater fraction of the incident flow is diverted into the bypass flow passage, further accelerating the bypass flow. With a greater acceleration of the bypass flow, a greater static pressure drop develops across the bypass flow passage. As the static pressure in the core and bypass flow passages must equalise both far upstream and downstream of the disc, a greater static pressure drop is also developed across the core flow, which balances the increased disc thrust. Hence, the disc is able to achieve a slightly greater power coefficient on the upwards facing slope when the momentum loss factor is increased, as the increase in disc thrust outweighs the slight reduction in mass flow rate through the disc area (as $P = T \times u_x$). It follows that upwards facing slopes (similarly to high blockage domains), require higher levels of thrust to maximise the power coefficient.

6.3.2 Alternative Normalisation

The normalisations adopted in equations 6.8 and 6.9 aim to isolate the effect of the downstream flow passage constriction from the sheared velocity profile. However,

the actual power extracted from the flow by the disc will depend on both the degree of velocity shear and the downstream flow passage constriction. In order to demonstrate the combined effect of the sheared velocity profile and the downstream flow passage constriction, alternative normalisations were adopted for the thrust and power coefficients ($C_T{}'$ and $C_P{}'$ respectively).

$$C_T{}' = \frac{T}{\frac{1}{2}\rho U_b^2 A} \tag{6.11}$$

$$C_P{}' = \frac{P}{\frac{1}{2}\rho U_b^3 A} \tag{6.12}$$

These definitions are based on the bulk velocity at the disc plane ($U_b = 2.0$ m/s), which is consistent between the bed slopes. Hence, the alternative thrust and power coefficients are a direct representation of the thrust exerted on the flow by the disc and the power extracted from the flow by the disc.

As shown in Fig. 6.8, the disc on the downwards facing slope exerts the most thrust on the flow and extracts the most power at a given momentum loss factor. This is because the increased kinetic energy flux available to the disc (from the sheared velocity profile) exceeds the reduced efficiency that arises from the downstream flow passage expansion (shown in Fig. 6.7). However, on the upwards facing slope, the small reduction in kinetic energy flux available to the disc (from the sheared velocity profile) is approximately balanced by the increased efficiency from the downstream flow passage constriction. Hence, these results suggest that both the degree of velocity shear and downstream flow passage constriction may affect the performance of tidal energy devices to a similar degree. In order to draw a more substantive conclusion that is applicable to real tidal energy devices, both of these effects will be examined in more detail in the next chapter, by adopting a blade resolved rotor representation.

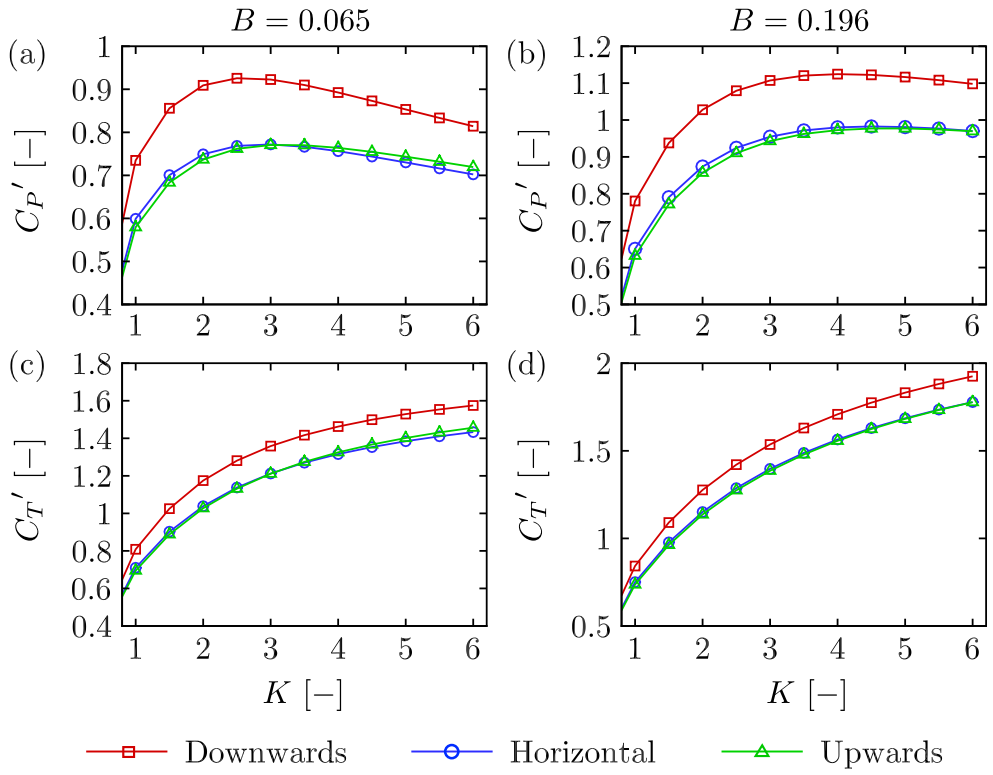

Figure 6.8: Variation in the alternative disc thrust and power coefficients with momentum loss factor.

6.4 Disc Loading

As the disc extracts more power from the flow on the downwards facing slope (when operating at a given momentum loss factor), it might appear to be preferable to install tidal energy devices on downwards facing slopes. However, the increased velocity shear on the downwards facing slope also leads to a greater thrust variation across the disc face, as shown in Fig. 6.9. For the downwards facing slope, Fig. 6.9 shows that the maximum disc thrust is up to 15% greater than the mean thrust, while the minimum is up to 30% lower than the mean thrust. Hence, despite the increased kinetic energy flux that is available for extraction, a downwards facing slope may actually be less desirable for device installation, due to the greater thrust variation across the frontal projected area of the device.

For a real device operating on a downwards facing slope, the greater thrust vari-

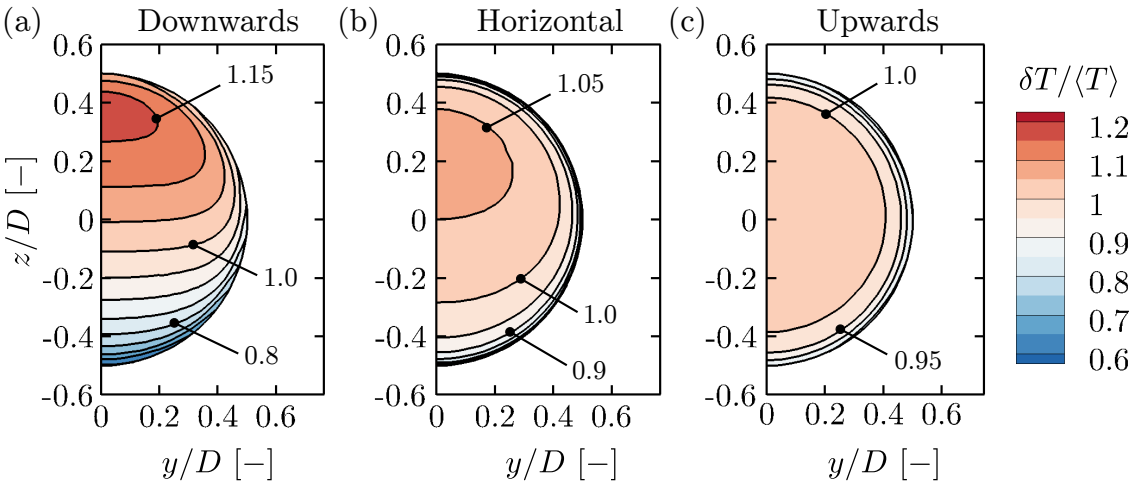

Figure 6.9: Local thrust variation over the disc face at a momentum loss factor of 5 and a blockage ratio of 0.197. The incremental thrust $\delta T = \frac{1}{2}\rho u_x^2 \delta A$ acting on an incremental area of disc δA, has been divided by the mean thrust for that disc $\langle T \rangle$, to highlight the thrust variation across the disc face.

ation corresponds with a more severe cyclical blade loading fluctuation, as the blade rotates through the sheared velocity profile. This blade loading fluctuation will be investigated directly in Chapter 7, by replacing the actuator disc with a blade resolved rotor representation.

6.5 Wake Development

In this section, the local flow field downstream of the disc will be examined, in order to further investigate the mechanism that allows greater thrust and power coefficients to be developed on the upwards facing bed slope at a fixed momentum loss factor.

6.5.1 Axial Velocity

Fig. 6.10 shows vertical and lateral profiles of axial velocity downstream of the disc, at a momentum loss factor of 5 and a blockage ratio of 0.197. The vertical profiles were taken along the mid-width of the channel ($y/S = 0$), while the lateral profiles were taken at the local mid-depth of the channel (which varies in the streamwise

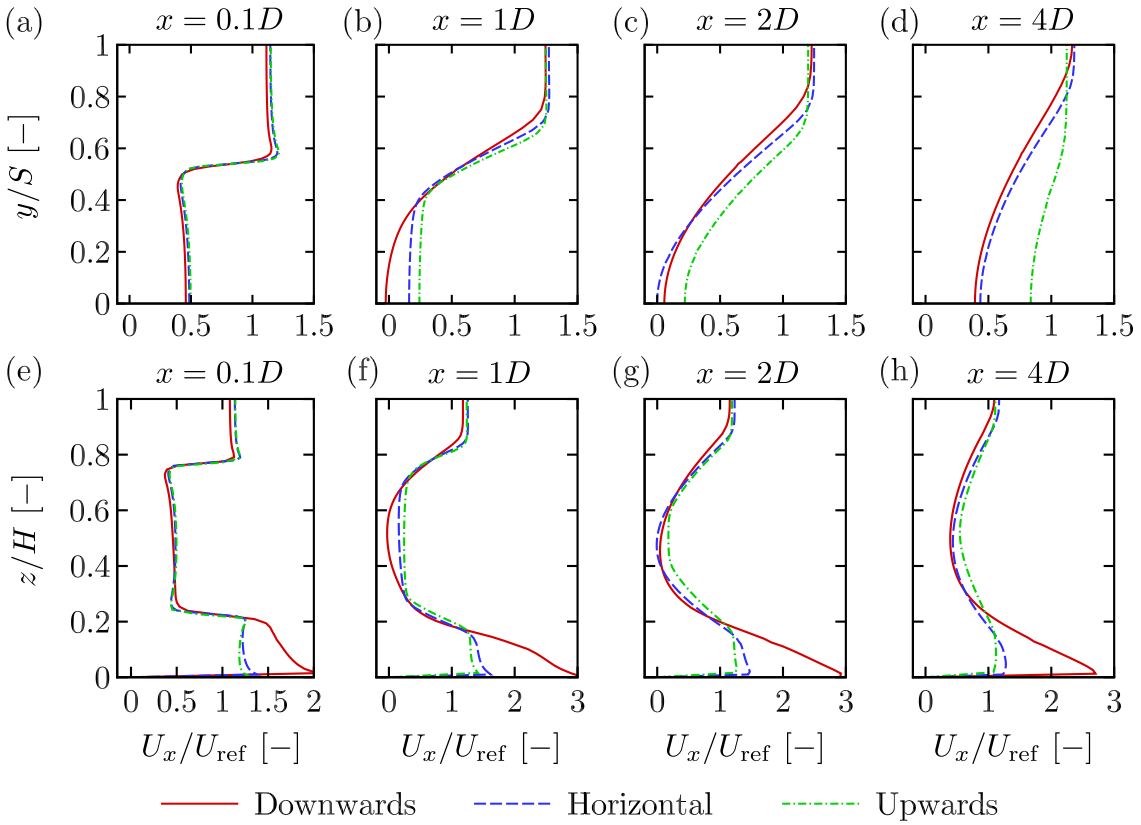

Figure 6.10: Axial velocity profiles in the lateral (a, b, c and d) and vertical (e, f, g, and h) directions downstream of the disc, at a momentum loss factor of 5 and a blockage ratio of 0.197. S represents the width of the domain and H represents the local depth of the domain. The vertical profiles were taken along the channel centreline, while the lateral profiles were taken along the local mid-depth.

direction). To isolate the velocity deficit induced by the disc from the undisturbed sheared velocity profile, the axial velocity in Fig. 6.10 has been normalised by the axial velocity at the same location in the channel without the disc present (U_{ref}). With this normalisation, it should be noted that the normalised axial velocity beneath the disc (particularly on the downwards facing slope) is exaggerated, due to the low values of the reference velocity near the bottom of the sheared velocity profile. Hence, the vertical velocity profiles shown in Fig. 6.10 (e - h) should be interpreted carefully. To aid with the interpretation of the vertical velocity profiles, contours of normalised axial velocity on a vertical plane along the centreline of the domain ($y/S = 0$) are shown in Fig. 6.11.

Immediately downstream of the disc ($x/D = 0.1$), Fig. 6.10 shows that the bypass flow velocity is greater on the upwards facing slope than on the horizontal and downwards facing slopes. The additional acceleration of the bypass flow is generated by the reduced cross-sectional area of the channel downstream of the disc. With an increased bypass flow acceleration, a greater static pressure drop is developed across the bypass flow passage (this will be shown explicitly in section 6.5.2). As the static pressure must equalise between the core and bypass flow passages, both far upstream and downstream of the disc, a greater static pressure drop also develops across the core flow passage. The increased static pressure drop across the core flow passage then draws a greater mass flow rate through the disc, which is manifested as an acceleration of the core flow just downstream of the disc (at $x/D = 0.1$).

Continuing downstream of the disc plane to $x/D = 1$, the expansion of the core flow streamtube leads to a further reduction of the core flow velocity and a further acceleration of the bypass flow velocity. On the downwards facing slope, the adverse pressure gradient augments the deceleration of the core flow velocity, leading to a small region of reversed flow at $x/D = 1$. While such reversed flow is not expected to occur downstream of real rotors, it can occur downstream of actuator discs operating under high thrust conditions. Fig. 6.11 shows that reversed flow can even occur on horizontal bed slopes (where the additional deceleration from the adverse pressure gradient is not present), if sufficient thrust is applied. Nevertheless, the small region of reversed flow is rapidly mixed out by $x/D = 2$, as the core flow velocity is accelerated by the contracting streamtube. Hence, the small region of reversed flow at $x/D = 1$ does not significantly impact the results of this investigation and will not be investigated further.

Further downstream of the disc, the axial velocity continues to recover faster on the upwards facing slope than on the horizontal and downwards facing slopes, due to the favourable pressure gradient. In a tidal array with multiple rows of turbines,

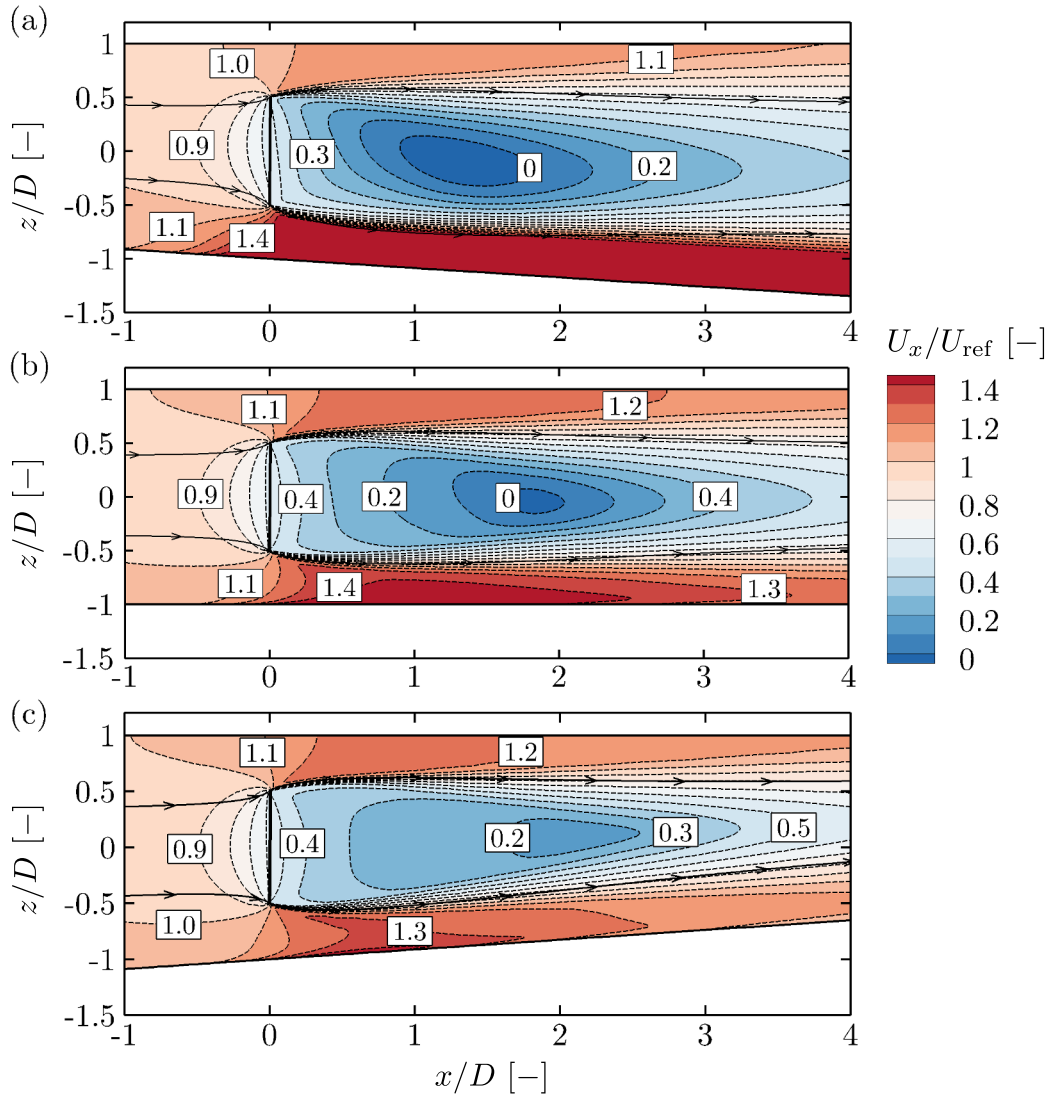

Figure 6.11: Contours of axial velocity along the mid-width of the domain ($y/S = 0$), at a momentum loss factor of 5 and a blockage ratio of 0.197. The solid vertical line at $x/D = 0$ indicates the actuator disc location.

it may therefore be possible to place downstream devices closer to upstream devices when the bed slope is upwards facing (due to the faster wake recovery), as long as the tip clearance of the downstream devices is still sufficient to satisfy shipping and cavitation restrictions.

6.5.2 Static Pressure Coefficient

To examine the static pressure changes that accompany the core and bypass flow accelerations, Fig. 6.12 shows contours of static pressure coefficient (C_{pre}) along the vertical centre plane of the domain ($y/S = 0$), at a momentum loss factor of 5 and a blockage ratio of 0.197. The dividing streamlines are also shown, to indicate the extent of the core and bypass flow passages. In these plots, the static pressure coefficient has been defined by normalising the static pressure with the undisturbed dynamic pressure incident on the disc area ($\frac{1}{2}\rho\langle {u_{x0}}^2\rangle$),

$$C_{\text{pre}} = \frac{p - p_{\text{ref}}}{\frac{1}{2}\rho\langle {u_{x0}}^2\rangle} \tag{6.13}$$

and the reference static pressure (p_{ref}) has been taken as the static pressure at the computational domain outlet (zero in all cases). This normalisation was adopted to account for the increased dynamic pressure incident on the disc from the sheared velocity profile and is therefore consistent with the thrust and power coefficients in Fig. 6.7.

The contour plots in Fig. 6.12 allow the static pressure changes in the immediate vicinity of the disc to be quantified and compared between bed slopes. For example, the downwards facing bed slope experiences the lowest drop in static pressure coefficient in the bypass flow passage (≈ 0.3 between $x/D = -2$ and $x/D = 2$), while the upwards facing slope experiences the greatest drop in static pressure coefficient in the bypass flow passage (≈ 0.8 between $x/D = -2$ and $x/D = 2$). This trend is consistent with the bypass flow accelerations shown in Fig. 6.10. More specifically, the increased acceleration of the bypass flow on the upwards facing slope leads to the greater static pressure coefficient drop across the bypass flow passage in Fig. 6.12.

Far upstream and downstream of the disc, the core and bypass flow static pressures must equalise. While the static pressure may still develop in the streamwise direction

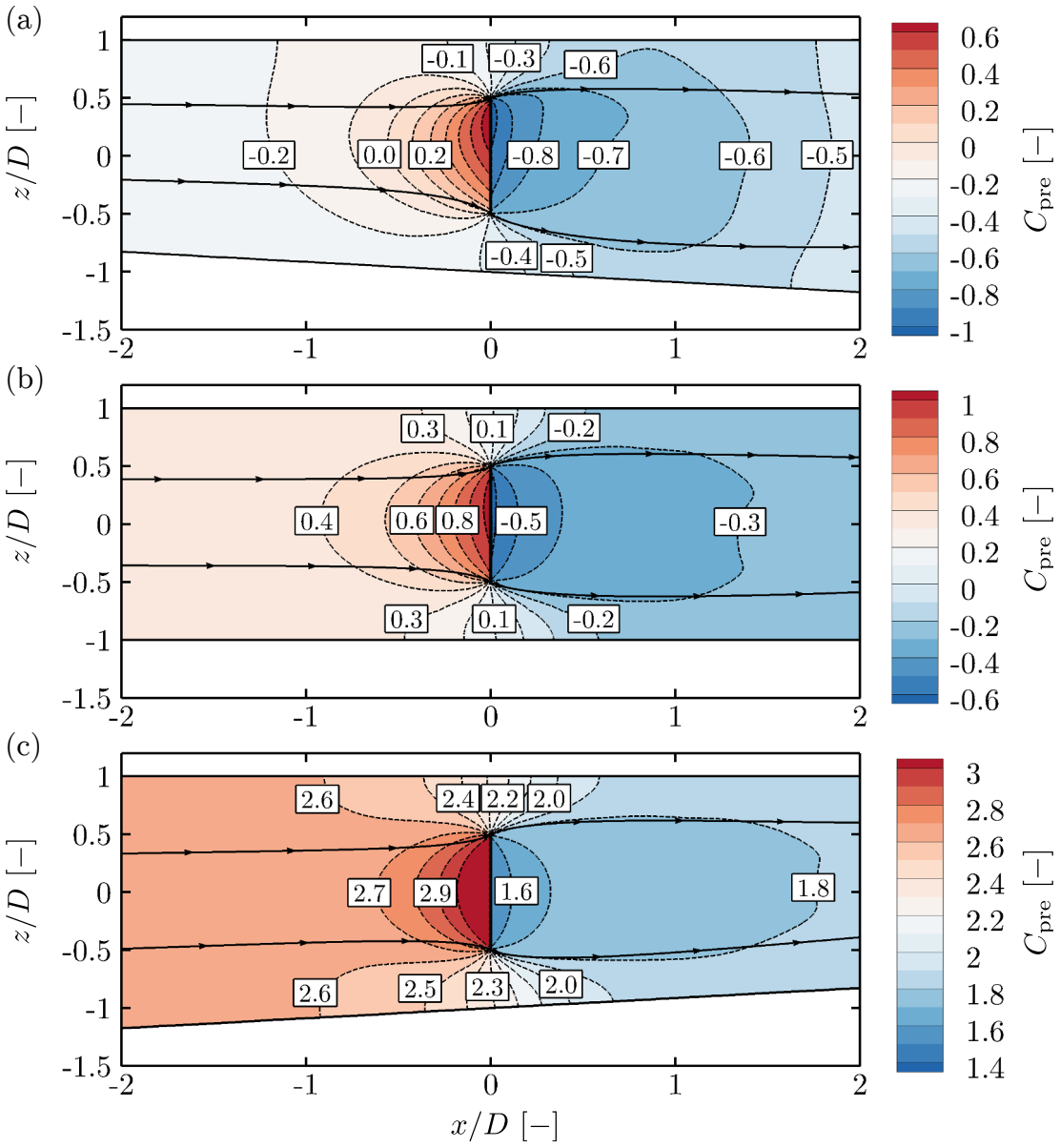

Figure 6.12: Contours of static pressure coefficient along the mid-width of the domain ($y/S = 0$), at a momentum loss factor of 5 and a blockage ratio of 0.197. The solid vertical line at $x/D = 0$ indicates the actuator disc location.

(due to the bed slope and other resistive flow features) the static pressure must still equalise between the core and bypass flow passages. As a result, the static pressure coefficient drop in the bypass flow passage must also be consistent with the static pressure coefficient drop across the core flow passage. Hence, the increased static pressure coefficient drop across the bypass flow passage on the upwards facing slope results in a greater static pressure coefficient drop across the core flow passage. The

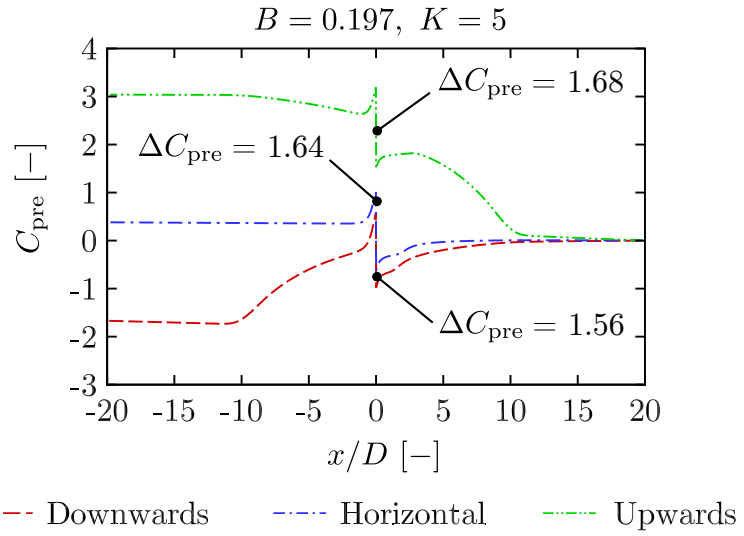

Figure 6.13: Static pressure coefficient variation along the mid-depth of the channel, at a momentum loss factor of 5 and a blockage ratio of 0.197.

increased static pressure coefficient drop across the core flow passage then draws a greater mass flow rate through the disc on the upwards facing slope (as discussed in section 6.3), which allows the disc to exert greater thrust on the flow and extract more power at the same momentum loss factor.

However, it is difficult to observe the static pressure coefficient drop across the disc itself using the contour plots in Fig. 6.12, due to the large gradients in the vicinity of the disc. As an alternative, Fig. 6.13 shows the static pressure coefficient variation along the local mid-depth of the channel, through the centre of the disc. The magnitude of the discontinuities (ΔC_{pre}) have been labelled explicitly in Fig. 6.13, to aid in the ensuing discussion.

As shown in Fig. 6.13, the upwards facing slope exhibits the greatest static pressure coefficient drop across the disc ($\Delta C_{\mathrm{pre}} = 1.68$), whilst the horizontal and downwards facing slopes exhibit lower static pressure coefficient drops across the disc ($\Delta C_{\mathrm{pre}} = 1.64$ and 1.56 respectively). The increased static pressure coefficient drop across the disc on the upwards facing slop is consistent with the static pressure coefficient drop across the core flow passage, the bypass flow passage and hence also the bypass flow acceleration (shown in Fig. 6.10). The proposed mechanism for achieving

greater thrust and power coefficients on the upwards facing bed slope (at the same momentum loss factor), is therefore fully consistent with the local velocity and static pressure fields in the vicinity of the disc.

6.6 Length of the Sloping Section

For the blade resolved simulations that are carried out in the next chapter, the horizontal length of the bed slope (L) is reduced from $20D$ to $12D$ (while maintaining the same slope angle), to reduce the overall cell count and reduce the computational cost of the simulations. As each of these simulations is computationally expensive, it is not feasible to investigate the effect of reducing the slope length (in addition to investigating different tip-speed-ratios and the three different slope orientations) with a blade resolved rotor representation. Therefore, the effect of reducing the horizontal length of the sloping section will be briefly investigated in this chapter instead, with an actuator disc instead of a rotor.

New computational domains with shorter sloping sections were created for the upwards and downwards facing bed slopes. The slope angle (5°), depth at the device plane ($2D$) and the domain width ($2D$) were not modified in the new domains, to allow the horizontal length of the sloping section to be investigated in isolation from the other geometric parameters. To highlight the resulting changes to the overall domain geometry, Fig. 6.14 shows a comparison of the new and original domains adopted for the upwards facing bed slope. The new domain adopted for the downwards facing bed slope is identical to the new domain adopted for the upwards facing slope (Fig. 6.14 (b)), with the flow direction reversed.

By reducing the slope length, the axial velocity profile has a shorter distance to develop before encountering the device. Hence, the degree of shear in the undisturbed axial velocity profiles at the device plane is reduced on the downwards facing slope

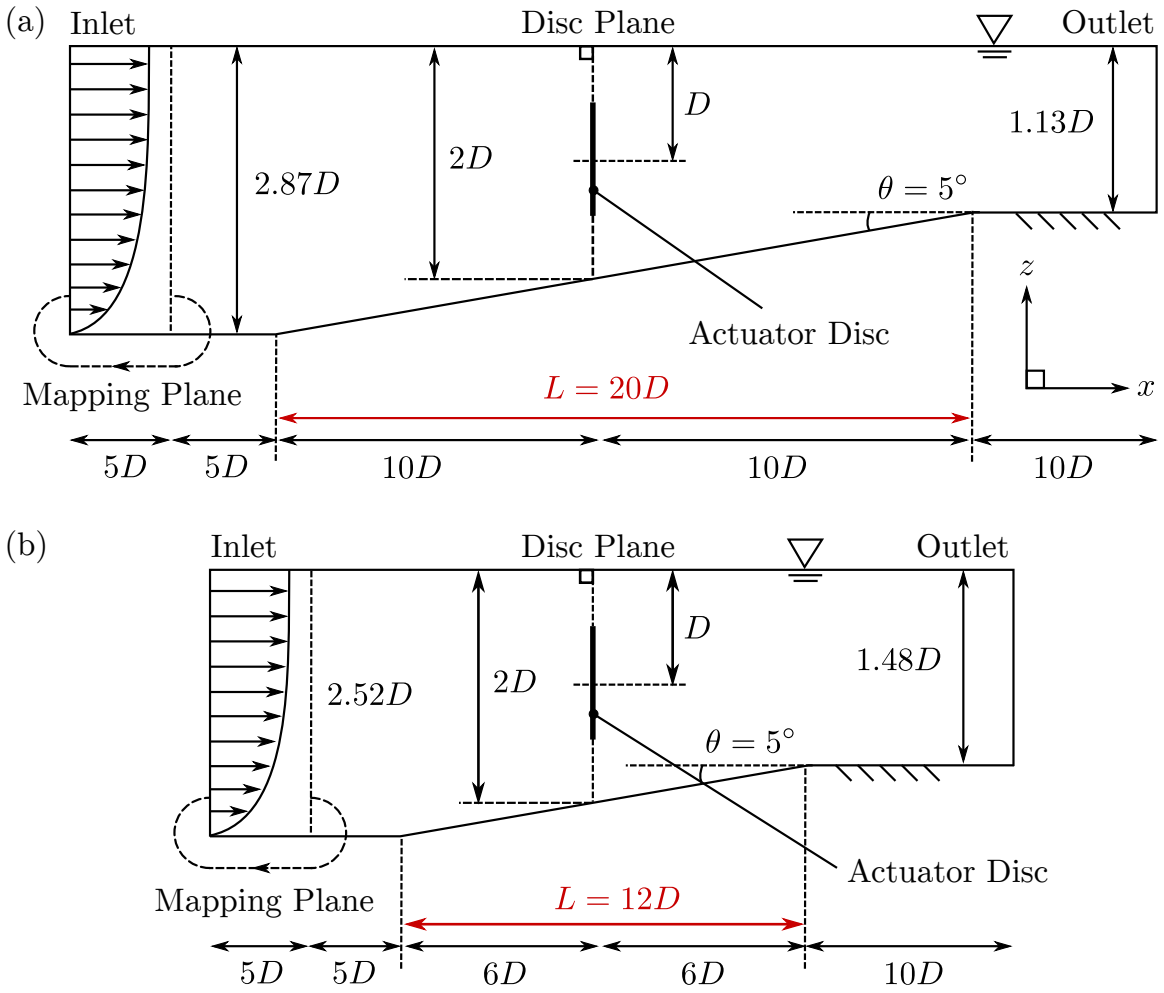

Figure 6.14: Schematic diagram of the computational domains adopted for the upwards facing bed slope with (a) the original slope length ($20D$) and (b) the shorter slope length ($12D$). This diagram shows a lateral (side-on) view in the $x - z$ plane.

and increased on the upwards facing slope (the profiles are more similar), as shown in Fig. 6.15. However, the slope angle is the same in both sets of computations, so the strength of the adverse pressure gradient on the downwards facing bed slope and the strength of the favourable pressure gradient on the upwards facing bed slope remains approximately the same. Hence, the thrust and power coefficients (shown in Fig. 6.16) are almost identical on the original bed slope and the shorter bed slope. Fig. 6.16 therefore confirms that it is the slope angle that determines the strength of the streamwise pressure gradient (and hence the efficiency of energy extraction), rather than the slope length. For the blade resolved computations carried out in Chapter

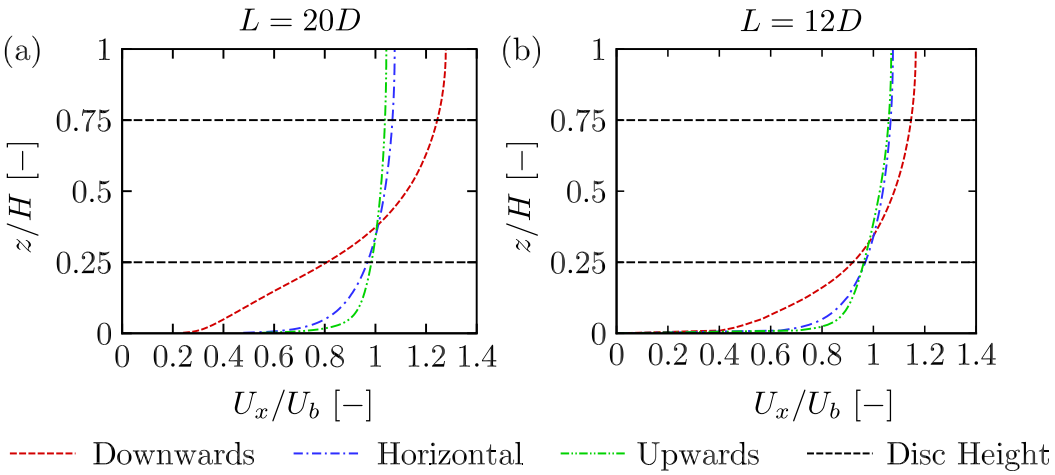

Figure 6.15: Axial velocity profiles at the disc plane ($x/D = 0$) with no disc present, for the original slope length ($20D$) and the shorter slope length ($12D$). The horizontal dashed lines indicate the height of the actuator disc.

7, it is therefore perfectly reasonable to reduce the horizontal length of the bed slope from $20D$ to $12D$, as long as a slope angle of 5° is maintained.

Fig. 6.17 shows the alternative thrust and power coefficients developed on each bed slope. As the alternative thrust and power coefficients are normalised by the bulk velocity, they show the combined effects of the sheared axial velocity profile and the streamwise pressure gradient. Hence, they are a direct reflection of the thrust exerted on the flow by the disc and the power extracted from the flow by the disc. For the original slope length ($20D$), the disc on the downwards facing bed slope exerts more thrust on the flow and extracts more power from the flow than the disc operating on the horizontal and upwards facing bed slopes, at the same momentum loss factor. This is primarily due to the degree of shear in the undisturbed axial velocity profile (shown in Fig. 6.15 (a)). However, when the length of the sloping section is reduced, the difference in the degree of shear between the undisturbed axial velocity profiles is reduced, while the strength of the streamwise pressure gradient remains approximately the same (as the slope angle is the same). Hence, the difference in the alternative thrust and power coefficients between the bed slopes is smaller on the shorter bed slope, as shown in Fig. 6.17.

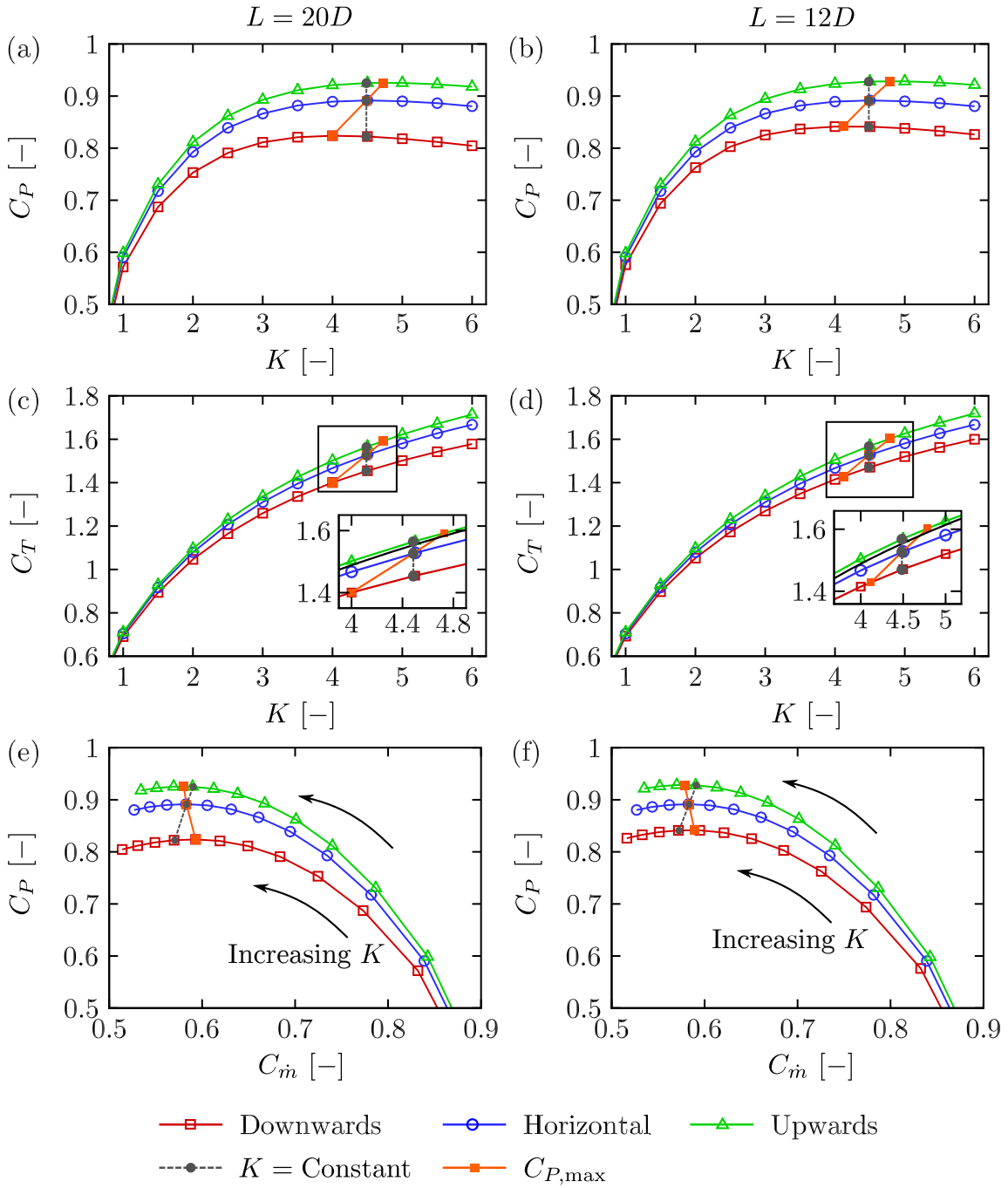

Figure 6.16: Variation in the disc thrust and power coefficients with momentum loss factor and mass flow rate coefficient, for the original slope length ($20D$) and the shorter slope length ($12D$). The maximum power coefficients ($C_{P,\max}$) were estimated using polynomial curve fits.

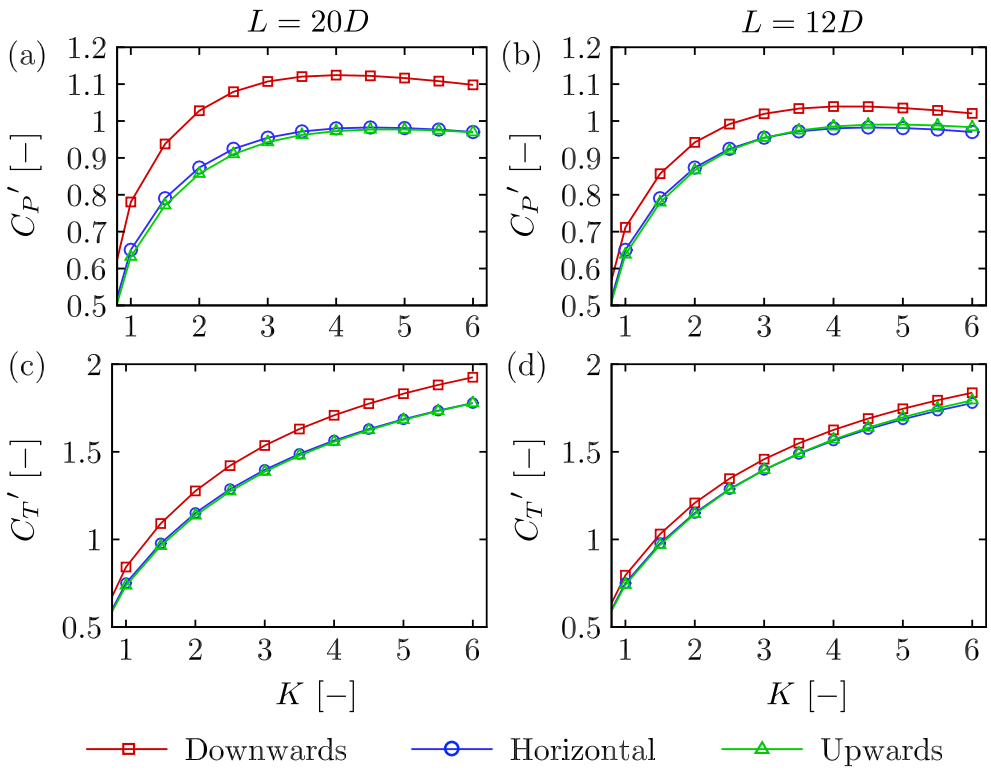

Figure 6.17: Variation in the alternative disc thrust and power coefficients with momentum loss factor, for the original slope length ($20D$) and the shorter slope length ($12D$).

Fig. 6.17 also shows that the disc on the downwards facing bed slope exerts the most thrust on the flow and extracts the most power from the flow at the same momentum loss factor, for both slope lengths. A real tidal energy device operating on a downwards facing 5° bed slope will therefore be able to exert more thrust on the flow and have a greater kinetic energy flux available to it for extraction, at a given tip-speed-ratio. However, due to the dependency on the degree of shear (which was generated artificially in this investigation), this should not be taken as a general result and the performance of devices operating in sloping bathymetries must be analysed on a case-by-case basis.

6.7 Summary

Actuator disc computations have been carried out in a computational domain that slopes in the streamwise direction, over a range of momentum loss factors. On the downwards facing bed slope, the adverse pressure gradient leads to an increase in velocity shear across the disc face. The increased velocity shear increases the kinetic energy flux that is available to the disc for extraction and implies that energy extraction would be increased with a downwards facing flow. However, the increased velocity shear also increases the thrust variation across the disc face. For a real rotor, this corresponds with an increase in the magnitude of the cyclical blade loading fluctuation as the blade rotates through the sheared velocity profile, which may be detrimental to the fatigue life of the device. Hence, despite the increased potential for energy extraction, device lifespan may be reduced with a downwards facing flow.

Despite the reduced kinetic energy flux that is available for extraction, the actuator disc on the upwards facing bed slope is able to extract a greater fraction of the kinetic energy flux that is available to it as useful power, when operating at the same momentum loss factor. This increase occurs because the bypass flow is accelerated by the downstream flow passage constriction, which leads to a greater static pressure drop across the bypass flow passage. As the static pressure in the bypass flow must equalise with the static pressure in the core flow, both far upstream and downstream of the disc, a greater static pressure drop also develops across the core flow passage (on the upwards facing slope). Hence, a greater mass flow rate is drawn through the disc, which increases the thrust exerted on the flow by the disc and increases the power extracted from the flow by the disc, at the same momentum loss factor.

On the upwards facing bed slope, a further increase in the power coefficient is available by slightly increasing the momentum loss factor of the disc. This allows the disc to exert more thrust on the flow, reducing the mass flow rate through the disc and diverting a greater mass flow rate around the disc into the bypass flow passage.

As the increased thrust outweighs the slight reduction in axial velocity through the disc, the disc is able to extract slightly more power from the flow. For a real rotor, the increased momentum loss factor can be achieved by either spinning the rotor faster or by re-designing the rotor itself, to present greater thrust to the flow. These changes will be examined in more detail in the next chapter.

Chapter 7

Tidal Turbine Performance on a Streamwise Bed Slope

In this chapter, blade resolved computations of a tidal turbine rotor will be carried out in a computational domain that slopes in the streamwise direction. This chapter builds on the results of the previous actuator disc computations that were carried out in Chapter 6, by adopting a more realistic rotor representation. The thrust and power coefficients developed by the rotor will be shown to follow the same qualitative behaviour as the actuator disc, demonstrating that the performance changes experienced by the actuator disc can also be realised by real rotors. In addition, the blade resolved rotor representation allows the periodic blade loading fluctuation to be investigated directly. This periodic loading fluctuation is induced by the blade rotating through the sheared axial velocity profile and could not be examined directly in the previous actuator disc computations.

7.1 Computational Domains

In the same manner as the actuator disc computations, three separate computational domains were created for the upwards facing, horizontal and downwards facing bed

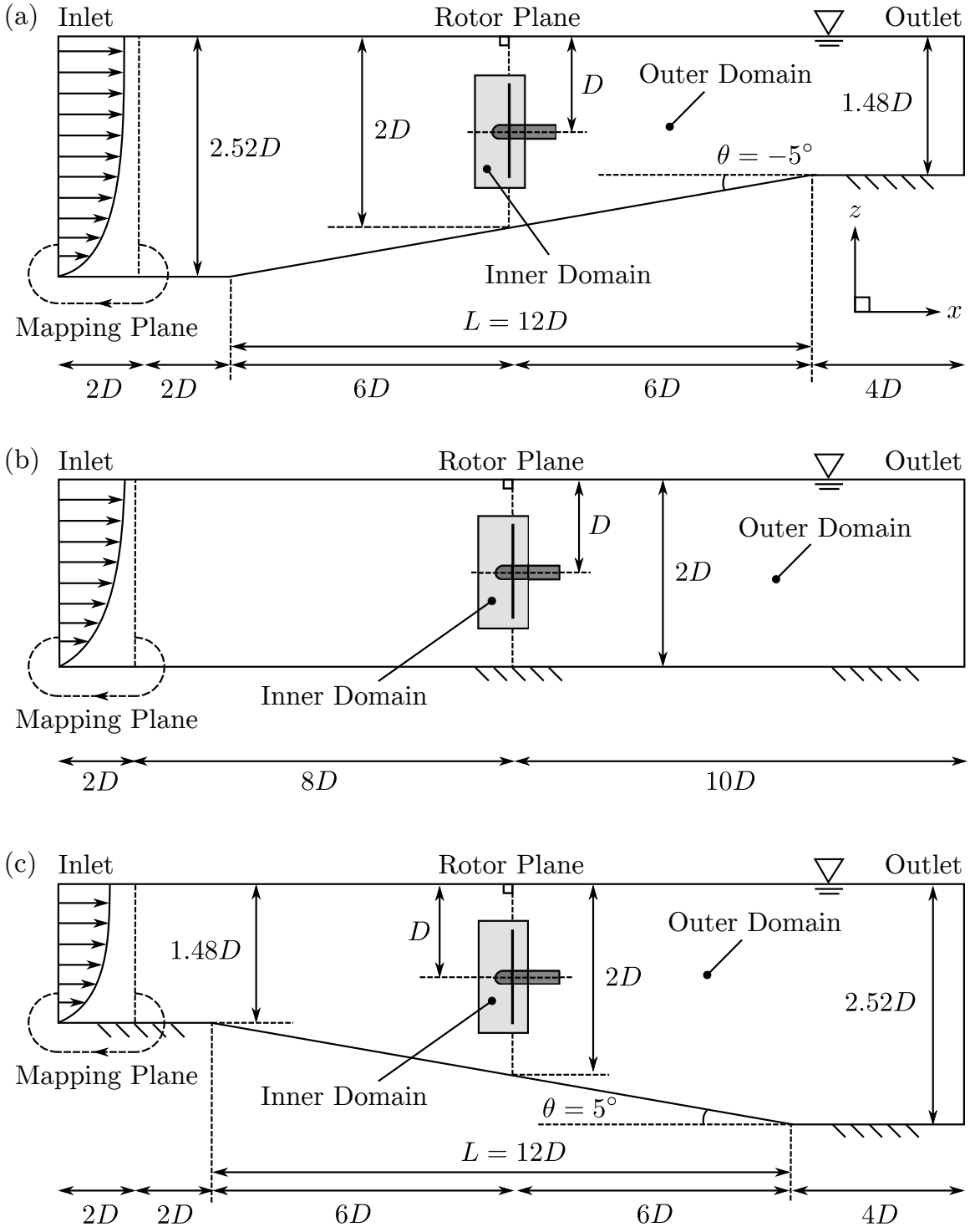

Figure 7.1: Schematic diagram of the computational domains adopted for the (a) upwards facing, (b) horizontal and (c) downwards facing bed slopes. The diagrams show a lateral view in the $x - z$ plane. The coin shaped inner domain (shaded in grey) has length $0.7R$ and radius $1.2R$.

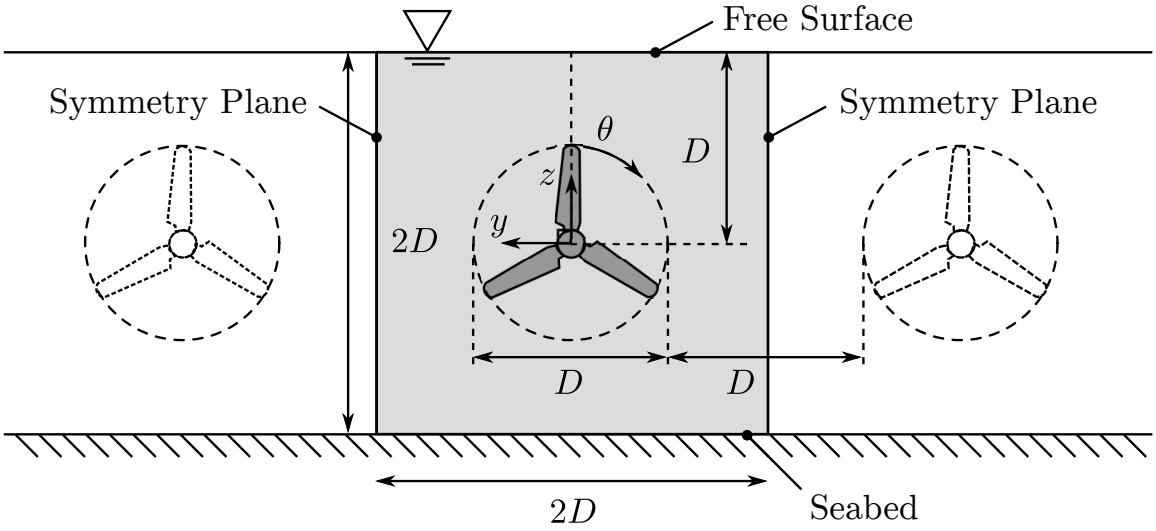

Figure 7.2: A cross-sectional view of the computational domain (indicated by the grey shaded area) and the tidal fence that the rotor is assumed to reside in. The azimuthal position of the blade (θ) is measured clockwise from top dead centre and the streamwise (x) direction is into the page.

slopes, as shown in Fig. 7.1. All three computational domains were assigned a width of $2D$ and a depth of $2D$ at the rotor plane (where D is the rotor diameter), in order to yield a consistent blockage ratio of 0.197 at the rotor plane. Physically, a blockage ratio of 0.197 corresponds with the blockage that may be experienced by a tidal energy device operating far from the ends of a sufficiently long fence of devices (arrayed normal to the flow direction), with a tip-to-tip spacing of $1D$ in a fluid of depth $2D$. A cross-sectional view of the rotor plane is shown in Fig. 7.2, to demonstrate these key dimensions. In all three domains, the rotor plane was aligned perpendicular to the free surface (rather than the bed slope) and the nacelle was placed at the mid-depth of the water column ($1D$ below the free surface). For a 20m diameter rotor, this configuration physically corresponds with a tip-submersion depth of 10m, which is 2m greater than the minimum tip clearance required at the MeyGen site (MeyGen Ltd. 2016).

For consistency with the actuator disc computations, a slope angle of 5° was adopted for the upwards and downwards facing bed slopes, with a horizontal length (L) of $12D$ for the sloping section.

7.2 Meshing Strategy

All three computational domains were constructed from two separate block structured meshes, which are labelled 'inner domain' and 'outer domain' in Fig. 7.1. The coin shaped inner domain contains the rotor and is identical on all three bed slopes. It was constructed from the 120° wedge shaped domain that was developed in Chapter 5, by copying, rotating and merging the wedge twice to form a complete cylinder. Using this approach, the boundary layer resolution adopted in Chapter 5 was maintained exactly and was consistent between the three bed slopes. Rotor 2 (the high solidity rotor design) was chosen for these computations, as it was deemed to be more appropriate than Rotor 1 for operation in highly blocked conditions.

The outer domain was constructed from an O-grid type topology, which was wrapped around the coin shaped inner domain and contained approximately 800 thousand cells. When combined with the inner domain mesh, the overall mesh for each bed slope contained approximately 5.2 million cells.

7.3 Numerical Method

Before carrying out the unsteady sliding mesh computations, a steady Multiple Reference Frame (MRF) computation was carried out using the approach discussed in Chapter 2. This computation was used to generate an improved initial condition for the sliding mesh computations and hence reduce the number of rotor revolutions required to converge the blade loading. As part of this computation, the fully developed axial velocity (U_x), turbulent kinetic energy (k) and specific dissipation rate (ω) profiles were generated at the domain inlet, using the same mapping plane approach that was adopted for the actuator disc computations in Chapter 6.

In the unsteady sliding mesh computations, the inner domain was rotated by a fixed angular increment of 0.2° at the start of each time step. Within each of these

time steps, 15 iterations of the SIMPLE algorithm were carried out. 15 iterations were found to be sufficient to reduce the initial residual of the governing equations for velocity, turbulent kinetic energy and specific dissipation rate by at least 6 orders of magnitude and the Poisson equation for pressure by 4 orders of magnitude.

Temporal convergence was primarily assessed by observing the integrated rotor forces and by placing point probes in the near wake of the rotor. After carrying out the MRF computation to generate an improved initial condition, 5 rotor revolutions were found to be sufficient to converge the blade loading in the unsteady computations. An additional 2 revolutions were then simulated and used for time averaging.

Separate computations were carried out at rotational speeds (Ω) of 0.9, 1.0, 1.1 and 1.2 rad/s on each bed slope (a total of 12 computations). These rotational speeds were specifically chosen to capture the rotor performance around the maximum power coefficient, which was previously determined in Chapter 5 to occur at a rotational speed of approximately 1.04 rad/s in uniform flow at 2.0 m/s (a tip-speed-ratio of 5.2).

7.4 Undisturbed Profiles

Before examining the thrust and power coefficients, Fig. 7.3 shows the undisturbed axial velocity (U_{x0}) and turbulence intensity (I) profiles that were developed at the rotor plane on each bed slope without the rotor present. These profiles were extracted from a separate set of computations that were carried out on each bed slope without the rotor present and are practically identical to the undisturbed profiles that were generated in the actuator disc computations with the shorter bed slope ($L = 12D$). It should be recalled that the axial velocity profile is more strongly sheared across the swept area of the rotor on the downwards facing bed slope because the adverse pressure gradient leads to a reduction in wall shear stress (and hence velocity gradient)

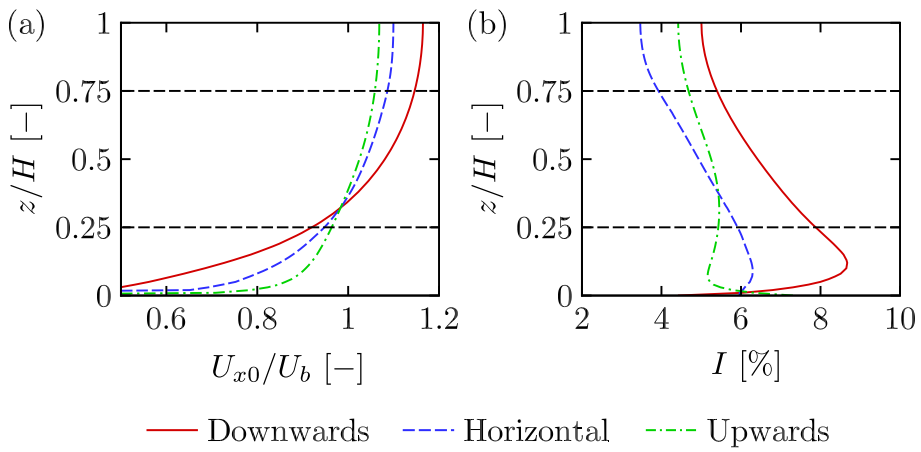

Figure 7.3: Fully developed (a) axial velocity and (b) turbulence intensity profiles at the rotor plane (with no device present) on the downwards, horizontal and upwards facing bed slopes. The black dashed lines indicate the vertical extent of the rotor in the water column.

at the wall. To conserve mass flow rate, the axial velocity away from the wall must increase, which results in increased velocity shear across the swept area of the rotor. The increased velocity shear across the swept area of the rotor increases the kinetic energy flux that is available to the device for extraction, regardless of the type of device or its operation. The opposite changes occur on the upwards facing bed slope, with the favourable pressure gradient reducing the degree of velocity shear across the swept area of the rotor and reducing the kinetic energy flux that is available for extraction.

7.5 Rotor Performance

Fig. 7.4 shows the (time-averaged) rotor thrust and power coefficients (C_T and C_P respectively) on each bed slope. To account for the different degree of velocity shear on each bed slope, the thrust (T) and power (P) have been normalised by the dynamic pressure and kinetic energy flux incident on the swept area of the rotor, without the rotor present.

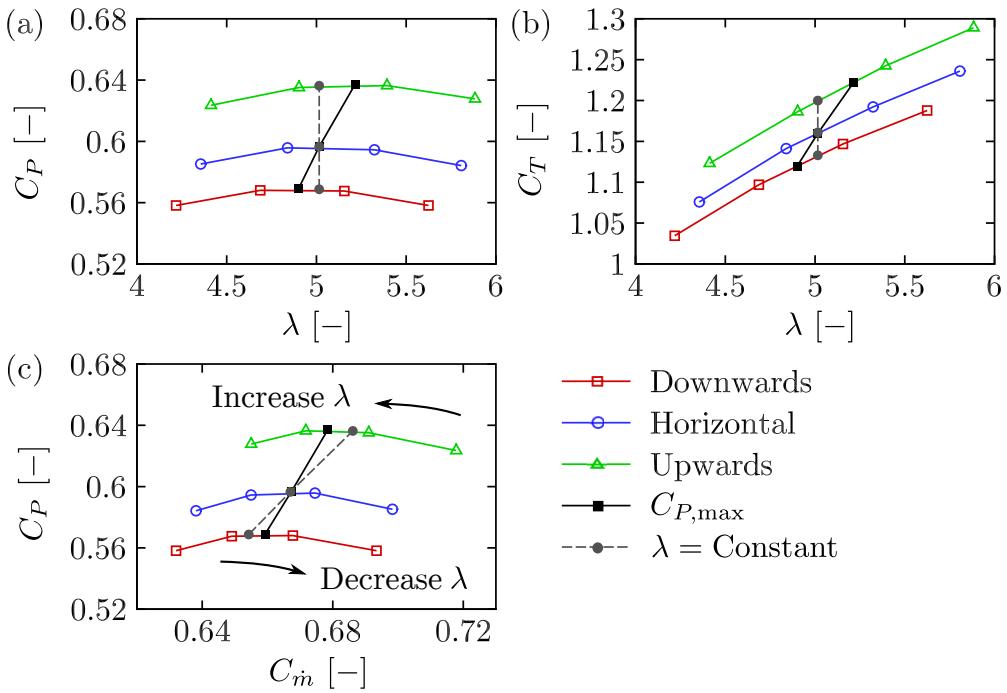

Figure 7.4: Variation in the rotor thrust and power coefficients with tip-speed-ratio and mass flow rate coefficient. The location of the maximum power coefficient ($C_{P,\max}$) has been estimated with a cubic polynomial curve fit.

$$C_T = \frac{T}{\frac{1}{2}\rho \int_A \left({U_{x0}}^2\right) \mathrm{d}A} \tag{7.1}$$

$$C_P = \frac{P}{\frac{1}{2}\rho \int_A \left({U_{x0}}^3\right) \mathrm{d}A} \tag{7.2}$$

In these normalisations, ρ represents the density of seawater (1025 kg/m^3) and A represents the swept area of the rotor. The tip-speed-ratio (λ) has been defined in a similar manner and represents the rotational speed of the rotor relative to the spatial average of the undisturbed axial velocity incident on the swept area of the rotor.

$$\lambda = \frac{\Omega R}{\frac{1}{A} \int_A \left(U_{x0}\right) \mathrm{d}A} \tag{7.3}$$

The power coefficient has also been plotted against the mass flow rate coefficient ($C_{\dot{m}}$) in Fig. 7.4 (c) to aid in the ensuing discussion. The mass flow rate coefficient represents the ratio of the mass flow rate through the swept area of the rotor, to the

mass flow rate through the swept area of the rotor without the rotor present.

$$C_{\dot{m}} = \frac{\int_A (\rho U_x) \mathrm{d}A}{\int_A (\rho U_{x0}) \mathrm{d}A_0} \tag{7.4}$$

With this definition, the mass flow rate coefficient can also be interpreted as $1 - \bar{a}$, where $\bar{a}$ is the spatial average of the axial induction factor over the rotor swept area. To remove the physical presence of the blades when computing the axial velocity at the rotor plane (U_x in equation 7.4), the axial velocity has been approximated as the average of the axial velocity just upstream and just downstream of the rotor plane ($0.1D$ from the rotor plane).

As shown in Fig. 7.4, the rotor on the upwards facing bed slope is able to achieve a greater power coefficient than the same rotor operating on the horizontal and downwards facing bed slopes, when operating at the same tip-speed-ratio (by traversing along the dashed grey line). This increase occurs because the bypass flow (the flow which passes around the rotor swept area) experiences a greater acceleration on the upwards facing bed slope, which arises from the reduced cross-sectional area of the channel downstream of the rotor. With an increased bypass flow acceleration, a greater static pressure drop is developed across the bypass flow passage. As the static pressure in the bypass flow must equalise with the static pressure in the core flow, both far upstream and downstream of the device, a greater static pressure drop also develops across the core flow passage. The increased static pressure drop across the core flow passage then draws a greater mass flow rate through the rotor swept area (as shown in Fig. 7.4 (c)), which is manifested as an increase in the axial velocity at the rotor plane (U_x). So far, this behaviour is consistent with the actuator disc analysis carried out in Chapter 6.

With an actuator disc, the increased axial velocity (U_x) through the disc directly results in an increased static pressure drop across the disc ($\Delta p = \frac{1}{2}\rho K U_x^2$), as the momentum loss factor K (representing the porosity of the disc) is constant. The

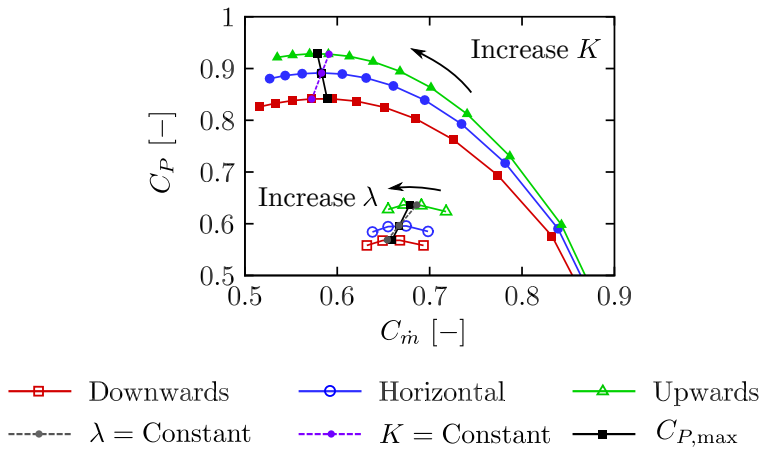

Figure 7.5: Variation in the power coefficient with mass flow rate coefficient for the actuator disc and blade resolved computations. The filled symbols indicate the actuator disc computations while the empty symbols indicate the blade resolved computations.

increased static pressure drop allows the disc to exert more thrust on the flow and extract more power, at the same momentum loss factor. However, with the blade resolved rotor representation, the increased axial velocity increases the angle of attack (α) and relative velocity magnitude (U_{rel}) incident on the blades instead. The increased angle of attack and relative velocity magnitude are manifested as a change in the static pressure distribution on the surface of the blades (as will be shown in section 7.5.1), which increases the lift and drag forces acting on the blades. With increased lift and drag forces acting on the blades, the rotor is able to exert more thrust and extract more power from the flow at the same tip-speed-ratio (traversing along the dashed grey line in Fig. 7.4).

For reference, Fig. 7.5 shows a direct comparison of the power coefficients computed with the actuator disc and blade resolved approaches at a blockage ratio of 0.197. While the power coefficient is naturally much lower for all the blade resolved computations than the actuator disc computations (the actuator disc is an ideal energy extractor), the qualitative differences between the bed slopes are the same. More specifically, a greater power coefficient is achieved at the same operating condition on the upwards facing bed slope (constant K or λ) than on the horizontal and down-

wards facing bed slopes. In addition, a further increase in power coefficient can be achieved on the upwards facing bed slope by increasing the resistance provided by the device (increasing K or λ).

7.5.1 Uniform Flow Computations

In order to examine the changes in the static pressure distribution on the surface of the blades that lead to the increased thrust and power coefficients shown in Fig. 7.4, it is necessary to remove the effect of the sheared velocity profile from the static pressure distribution. However, unlike the thrust and power coefficients, it is not possible to remove the effect of the sheared velocity profile from the static pressure distribution on the surface of the blades by normalisation alone. Hence, an additional set of computations were carried out in uniform flow instead, to directly remove the effect of the sheared velocity profile. To carry out these computations, the no-slip condition on the seabed was replaced with a slip condition (zero gradient normal to the wall) for all flow variables. The inlet velocity and turbulence scalar profiles were then replaced with uniform profiles based on a bulk velocity of 2.0 m/s (at the rotor plane), a turbulence intensity of 5% and a turbulence length scale of 0.7 times the hub height of 20m (following the recommendations by Gant & Stallard (2008)). This turbulence intensity roughly matches the turbulence intensity at the rotor plane in the no-slip computations (see Fig. 7.3 (b)), while the large length scale ensures that the intensity does not decay significantly between the inlet and the rotor plane.

Fig. 7.6 shows the thrust and power coefficients computed on each bed slope in uniform flow. Consistent with Fig. 7.4, Fig. 7.6 shows that the rotor operating on the upwards facing bed slope is able to achieve greater thrust and power coefficients than the same rotor operating on horizontal and downwards facing bed slopes at the same tip-speed-ratio (by traversing along the grey dashed line). The increased thrust and power coefficients are once again facilitated by the increased bypass flow acceleration,

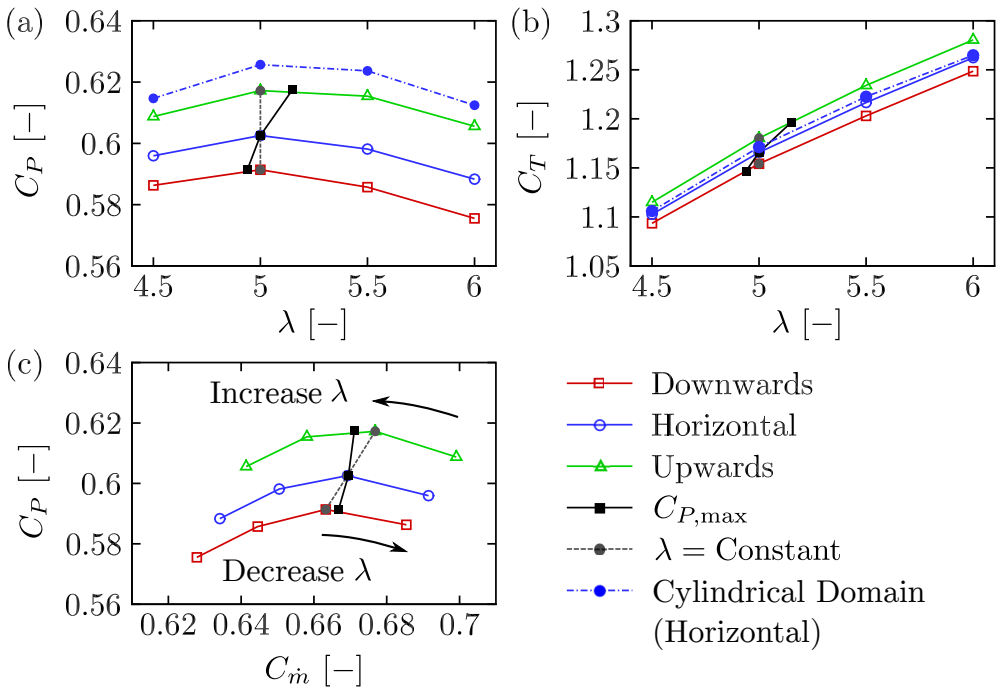

Figure 7.6: Variation in rotor thrust and power coefficients with tip-speed-ratio and mass flow rate coefficient, when operating in uniform flow. The location of the maximum power coefficient ($C_{P,\max}$) has been estimated with a cubic polynomial curve fit and is shown with a black solid line. The blue dashed line shows the thrust and power coefficients computed in a cylindrical domain with equivalent blockage (0.197) from Chapter 5. This case effectively uses a horizontal bed slope.

which leads to a greater static pressure drop across the bypass flow passage and hence also across the core flow passage. The increased static pressure drop across the core flow passage then draws a greater mass flow rate through the rotor swept area, as shown in Fig. 7.6 (c), resulting in greater thrust and power coefficients. These uniform flow computations therefore confirm that the increase in efficiency (power coefficient) that is achieved on the upwards facing bed slope arises from the channel geometry and is not associated with the degree of shear in the undisturbed velocity profiles.

Fig. 7.6 also shows the thrust and power coefficients that were computed with the same rotor in a cylindrical domain with an equivalent blockage of 0.197 in Chapter 5. These computations can be directly compared with the horizontal bed slope computations (from this chapter), to assess the accuracy of the cylindrical domain assumption

that was adopted in Chapter 5. The horizontal bed slope computations carried out here (in a rectangular domain) show that the thrust and power coefficients are reasonably well predicted by a cylindrical domain with an equivalent area blockage ratio. More specifically, the thrust and power coefficients at a tip-speed-ratio of 5 (close to the maximum power coefficient) are 0.5% and 3.8% greater (respectively) than the values computed in the rectangular domain. While some of this discrepancy can be attributed to the shape of the outer domain, it should be noted that the computations carried out in this chapter use an unsteady flow solver and experience a lower turbulence intensity at the rotor plane ($\sim 5\%$ rather than $\sim 10\%$), in order to better match the sheared flow computations. With further investigation of these factors it is likely that the cylindrical domain adopted in Chapter 5 will provide an even better approximation to the rectangular channel adopted in this chapter, as long as rotor blockage is sufficiently low, the channel cross-section is not highly asymmetric and the rotor is not placed close to the channel boundaries. Under these conditions a rectangular domain is essential to capture the asymmetry of the bypass flow as the blades rotate through each rotor revolution.

At this stage, it would be desirable to directly compare the static pressure distribution on the surface of the blades on each bed slope. However, despite the removal of the sheared velocity profile, the static pressure distribution still varies over the rotor revolution. To demonstrate this variation, Fig. 7.7 shows the static pressure coefficient distribution on a slice through the rotor blade (normal to the blade axis) at $r/R = 0.8$, for rotor azimuthal positions of 0°, 120° and 240° (measured clockwise from top-dead-centre). In Fig. 7.7, the static pressure coefficient (C_{pre}) has been defined as,

$$C_{\text{pre}} = \frac{p - p_\infty}{\frac{1}{2}\rho(U_\infty^2 + (\Omega r)^2)} \tag{7.5}$$

where p is the local static pressure, p_∞ is the freestream static pressure and U_∞ is

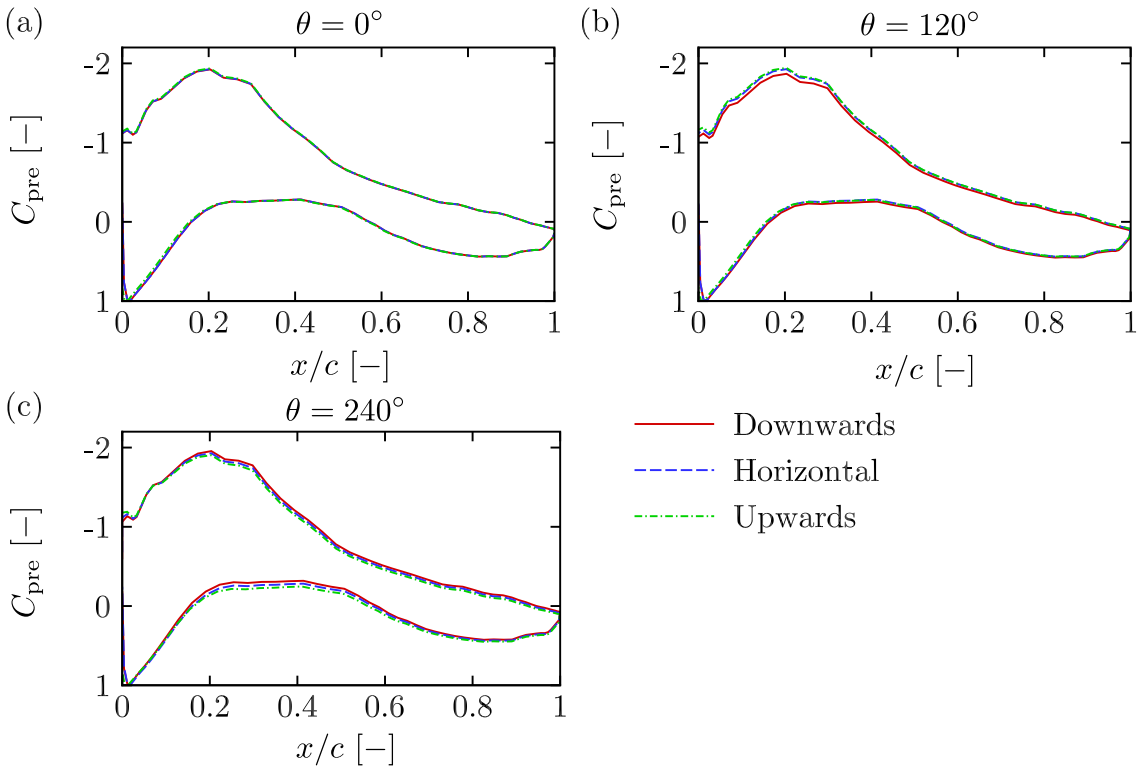

Figure 7.7: Static pressure coefficient on a slice through the rotor blade (normal to the blade axis) at $r/R = 0.8$ and $\lambda = 5$, in uniform flow for different rotor azimuthal positions (θ).

the freestream velocity.

The variation in the static pressure distribution over the rotor revolution arises from the vertical velocity component (U_z), which is generated by the non-horizontal bed slope (even when the sheared axial velocity profile is removed). This vertical velocity component was not analysed in the actuator disc computations carried out in Chapter 6, as the actuator disc develops a static pressure drop using only the velocity component normal to the disc face. As the actuator discs (and the rotors considered in this chapter) are oriented normal to the free surface, the vertical velocity component did not affect the performance of the actuator discs in Chapter 6, so it was neglected in the analysis. Fig. 7.8 shows the undisturbed profiles of the vertical velocity component at the rotor plane, on each bed slope. Regardless of whether a no-slip or a slip boundary is adopted on the seabed, Fig. 7.8 shows that a vertical

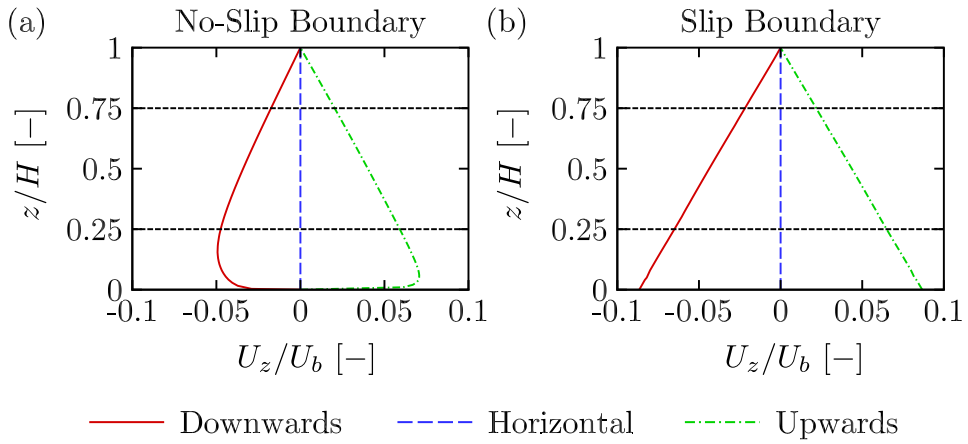

Figure 7.8: Undisturbed profiles of vertical velocity at the rotor plane (without the rotor present) for (a) no-slip and (b) slip boundary conditions on the seabed.

velocity component that is 2-6% of the bulk velocity is developed across the swept area of the rotor. This vertical velocity component results in the small fluctuations in the surface pressure distribution which are shown in Fig. 7.7.

To quantify the effect of the vertical velocity component on the unsteady blade loading, Table 7.1 compares the mean thrust and power coefficients (for a single blade) and the root-mean-square of the fluctuations, over the final rotor revolution at a tip-speed-ratio of 5 (in uniform flow). On the horizontal bed slope, the undisturbed vertical velocity component is zero. Hence, the root-mean-square of the fluctuations is small ($\sim$ 0.2% of the mean) and is likely to be due to a combination of noise and unsteadiness at the blade root. On the upwards and downwards facing bed slopes, the root-mean-square of the fluctuations in the thrust coefficient increases to $\sim$ 0.5% of the mean, while the root-mean-square of the fluctuations in the power coefficient increases to $\sim$ 1.2% of the mean. Table 7.1 shows that the magnitude of these fluctuations is approximately 4 times smaller than the corresponding root-mean-square of the fluctuations in the thrust and power coefficients when the axial velocity profile is sheared. Hence, for a 5° bed slope, the axial velocity shear appears to be a greater contributor to the unsteady blade loading than the vertical velocity component induced by the bed slope.

Table 7.1: Mean and root-mean-square of the fluctuations in C_T and C_P (for a single blade) over the final rotor revolution at a tip-speed-ratio of 5. The over bar indicates the mean, while the subscript $_{\text{RMS}}$ indicates the root-mean-square, which is given as a percentage of the mean value.

Slope	Seabed Boundary	$\overline{C_T}$ [-]	$C_{T,\text{RMS}}$ [%]	$\overline{C_P}$ [-]	$C_{P,\text{RMS}}$ [%]
Upwards	Slip	0.393	0.50	0.206	1.12
Horizontal	Slip	0.389	0.20	0.201	0.28
Downwards	Slip	0.385	0.52	0.197	1.19
Upwards	No-slip	0.395	2.00	0.212	4.00
Horizontal	No-slip	0.380	2.86	0.199	5.74
Downwards	No-slip	0.366	4.84	0.189	9.74

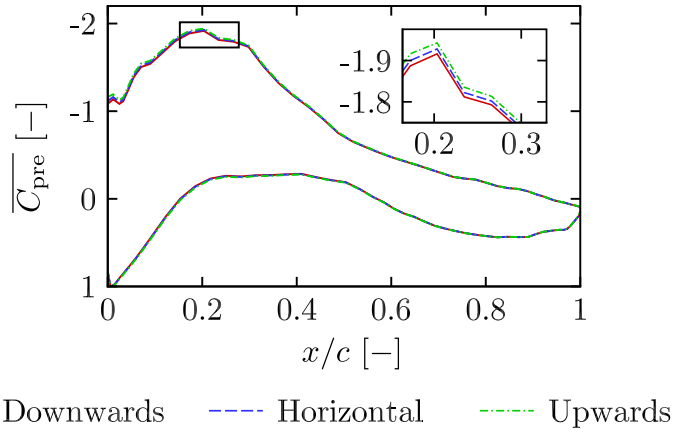

Figure 7.9: Static pressure coefficient distribution on a slice through the rotor blade (normal to the blade axis) at $r/R = 0.8$ and $\lambda = 5$, averaged over the final rotor revolution in uniform flow.

Returning to the mechanism for the increased thrust and power coefficients on the upwards facing bed slope, Fig. 7.9 shows the static pressure coefficient distribution on the same slice through the rotor blade (normal to the blade axis) at $r/R = 0.8$, but averaged over the final rotor revolution ($\overline{C_{\text{pre}}}$). The rotor on the upwards facing bed slope experiences greater suction (on average over a complete rotor revolution) than the same rotor operating on the horizontal and downwards facing bed slopes, at the same tip-speed-ratio. The stronger suction peak (in particular) is consistent with the increased mass flow rate through the rotor swept area (due to the increased

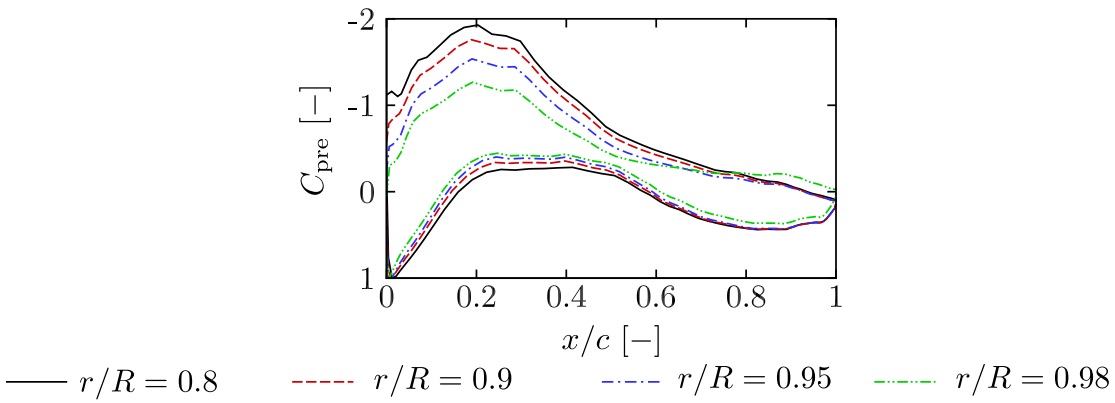

Figure 7.10: Static pressure coefficient distribution on several slices through the rotor blade (normal to the blade axis), in uniform flow on the horizontal bed slope. The tip-speed-ratio is 5 and the blockage ratio is 0.197.

static pressure drop across the core flow passage), which leads to an increase in the relative velocity magnitude and angle of attack incident on the blades. Hence, the mechanism that allows rotors operating on upwards facing bed slopes to achieve greater thrust and power coefficients (when operating at the same tip-speed-ratio), is slightly different but is still consistent with the actuator disc analysis carried out in Chapter 6.

7.5.2 Tip Flow Observations

Fig. 7.10 shows the static pressure coefficient distribution on several slices through the outboard sections of the rotor blade (normal to the blade axis), in uniform flow on the horizontal bed slope. For these computations, the blockage ratio (0.197) is significantly higher than the unblocked tip-flow analysis carried out in Chapter 4. Nevertheless, the static pressure distributions show similar qualitative behaviour to the static pressure distributions in Chapter 4, as the tip of the blade is approached. More specifically, the strength of the suction peak significantly reduces, while the static pressure on the pressure surface generally increases, as the tip of the blade is approached. These changes are indicative of a reduction in the angle of attack and spanwise flow accelerations along the pressure and suction surfaces of the blade,

suggesting that the same characteristics of the tip-loss mechanism are present at a blockage ratio of 0.197. However, the degree to which the angle of attack reduction and spanwise flow accelerations coincide with the unblocked tip-flow analysis in Chapter 4 remains uncertain, until further analysis is carried out.

At higher blockage ratios than the blockage ratio considered here, it is likely that the tip flow behaviour will diverge significantly from the tip flow behaviour under unblocked conditions. In particular, in the limit that the blockage ratio approaches 1, or the rotor is placed adjacent to a domain boundary, duct or shroud, the flow around the tip from the pressure surface to the suction surface will be completely blocked. Under these conditions the tip flow behaviour will be completely different to the tip flow behaviour in unblocked conditions and a different tip correction is required altogether.

7.5.3 Maximising the Power Coefficient

Fig. 7.4 also shows an estimate of the maximum power coefficient that can be achieved on each bed slope and the tip-speed-ratio that it occurs at. These maximum power coefficients were computed using cubic polynomial curve fits and are joined in Fig. 7.4 by a solid black line. To achieve the maximum power coefficient on the upwards facing bed slope, a greater tip-speed-ratio is required than on the horizontal slope. This is because the mass flow rate through the rotor swept area is initially higher on the upwards facing bed slope than on the horizontal slope, when operating at the same tip-speed-ratio. Hence, the azimuthally-averaged angle of attack on the upwards facing bed slope is initially higher than the azimuthally-averaged angle of attack that maximises the lift to drag ratio on the outboard aerofoil sections. It follows that the tip-speed-ratio can be increased slightly on the upwards facing bed slope, reducing the mass flow rate through the rotor swept area (by increasing the rotor thrust) and returning the relative flow vector back towards the optimum angle of attack that

maximises the lift to drag ratio on the outboard aerofoil sections.

Conversely, on the downwards facing bed slope a slightly lower tip-speed-ratio is required to maximise the power coefficient. This is because the mass flow rate through the rotor swept area on the downwards facing bed slope is initially lower than the mass flow rate through the rotor swept area on the horizontal slope, when operating at the same tip-speed-ratio. Hence, the azimuthally-averaged angle of attack on the downwards facing bed slope is initially too low to maximise the lift to drag ratio of the outboard aerofoil sections. By reducing the tip-speed-ratio, the mass flow rate through the swept area of the rotor increases (as the rotor thrust reduces), which increases the angle of attack and returns the relative flow vector back towards the optimum angle of attack that maximises the lift to drag ratio on the outboard aerofoil sections.

By comparing this analysis with the actuator disc analysis that was carried out in Chapter 6, it appears that the same mechanism (increasing device thrust) allows a greater maximum power coefficient to be achieved on upwards facing bed slopes. This increased thrust is similar to the increased thrust that is required in non-sloping domains to maximise the power coefficient at higher blockage ratios (see Schluntz & Willden (2015)). Hence, the analysis carried out here suggests that the downstream flow passage constriction (which can alternatively be thought of as downstream blockage) should be considered as well as the blockage at the device plane, when predicting device performance. However, when making this comparison it should be recalled that the bed slope also modifies the degree of velocity shear at the device plane, which does not occur if the blockage ratio at the device plane is varied in a non-sloping domain.

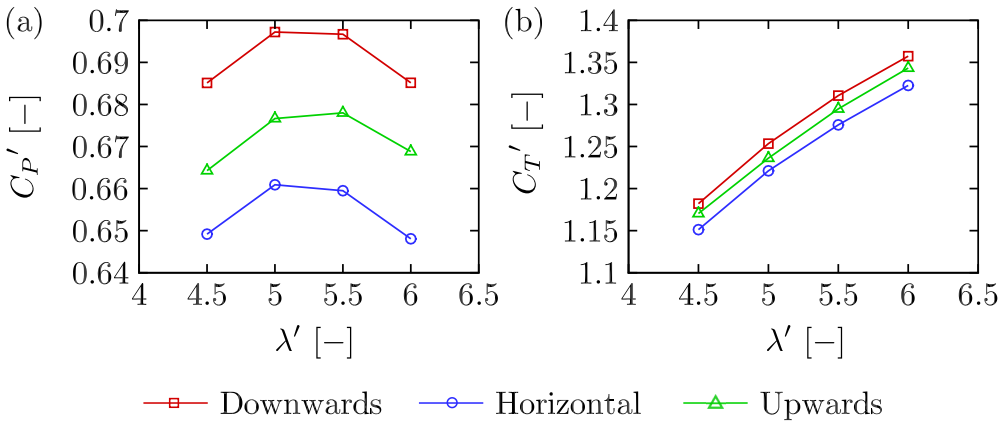

Figure 7.11: The variation in (alternative) thrust and power coefficients with (alternative) tip-speed-ratio.

7.5.4 Alternative Normalisation

The mean thrust and power developed by the rotor in practice will depend on both the degree of velocity shear and the downstream flow passage constriction. In order to demonstrate the combined effect of the sheared velocity profile and the downstream flow passage constriction, alternative normalisations were adopted for the thrust coefficient ($C_T{}'$), power coefficient ($C_P{}'$) and tip-speed-ratio (λ').

$$C_T{}' = \frac{T}{\frac{1}{2}\rho U_b^2 A} \tag{7.6}$$

$$C_P{}' = \frac{P}{\frac{1}{2}\rho U_b^3 A} \tag{7.7}$$

$$\lambda' = \frac{\Omega R}{U_b} \tag{7.8}$$

These definitions are based on the bulk velocity at the rotor plane ($U_b = 2.0$ m/s), which is consistent between bed slopes. Hence, the alternative thrust and power coefficients are a direct representation of the thrust and power that can be developed by the rotor and the alternative tip-speed-ratio is a direct representation of the rotational speed of the rotor.

As shown in Fig. 7.11, the rotor on the downwards facing bed slope exerts the most thrust on the flow and also extracts the most power from the flow at a given

tip-speed-ratio. This is because the increased kinetic energy flux available to the rotor (from the increased velocity shear), dominates the reduced efficiency (lower C_P) that arises from the flow passage expansion downstream of the rotor. However, Fig. 7.11 also shows that the rotor on the upwards facing bed slope does not exert the least thrust on the flow and extract the least power at a given tip-speed-ratio. This is because the small reduction in kinetic energy flux that is available to the rotor (due to the reduced velocity shear) is outweighed by the increase in efficiency (greater C_P) that arises from the downstream flow passage constriction. Hence, these results suggest that for 5° bed slopes, both the degree of velocity shear and downstream flow passage constriction affect the rotor thrust and power to a similar degree. In this instance, the overall power generated by the device is expected to be greater on the downwards facing bed slope than on the horizontal and upwards facing bed slopes.

7.6 Safety Margins for Cavitation

The blade resolved computations carried out in this chapter can also be used to investigate the order of magnitude of the safety margin that is likely to be required to account for sheared flow in the cavitation analysis presented in Chapter 5. To do this, the minimum static pressure was extracted from the blade resolved computations on the horizontal bed slope in both uniform and sheared flow, with the blade at top-dead-centre (since the static pressure reaches a minimum here). Hydrostatic and atmospheric pressure components were then added, as described in Chapter 5. Fig. 7.12 (a) shows the static pressure coefficient distribution on a slice through the blade at $r/R = 0.94$, which corresponds with the approximate location where the static pressure reaches a minimum and hence cavitation is most likely to occur.

Due to the increased axial velocity incident on the blade at top-dead-centre in the sheared flow, the strength of the blade suction peak is increased and hence the

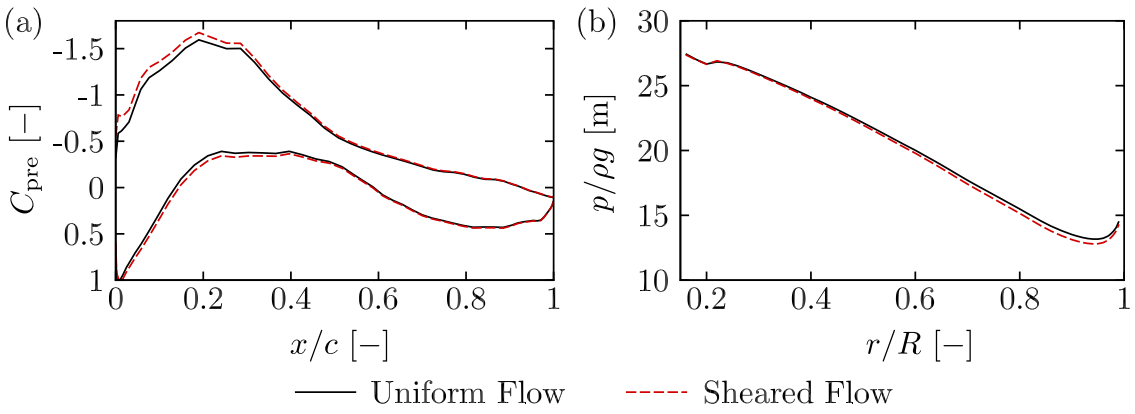

Figure 7.12: (a) Static pressure coefficient distribution on a slice through the rotor blade (normal to the axis) at $r/R = 0.94$ on the horizontal bed slope, in uniform and sheared flow. (b) Minimum sectional static pressure along the blade span span on the horizontal bed slope in uniform and sheared flow. The tip-speed-ratio is 5 and the blockage ratio is 0.197.

minimum static pressure is $\sim$ 0.37m lower than in the uniform flow (as shown in Fig. 7.12 (b)). Hence, to account for the additional reduction in minimum static pressure from the sheared velocity profile, a safety margin of $\sim$ 0.37m would be appropriate for the cavitation analysis. However, as discussed in Chapter 5, an additional safety margin is still required to account for the unsteady pressure fluctuations induced by surface waves and ambient turbulence, which are not included here.

It should also be emphasised that the safety margin suggested here is specific to the profile considered in this work (in this case the horizontal bed slope) and more highly sheared velocity profiles will require a larger safety margin. For instance, repeating the analysis with the downwards facing and upwards facing bed slopes leads to minimum static pressures that are $\sim$ 0.7m and $\sim$ 0.18m (respectively) lower than the minimum static pressure computed in uniform flow on the horizontal bed slope (due to the significantly different shear profiles). Hence, the downwards and upwards facing bed slopes will require safety margins of $\sim$ 0.7m and $\sim$ 0.18m respectively. The magnitude of the difference in the required safety margins between bed slopes further emphasises the need for case-by-case assessment of the required safety margin to account for sheared flow in cavitation analyses.

7.7 Near Wake Development

In order to investigate the development of the near wake, an additional 7 rotor revolutions were simulated on each bed slope at a rotational speed of 1.0 rad/s (to give a total of 14 revolutions). These additional revolutions were found to be sufficient to converge the near wake structure up to $4D$ downstream of the rotor plane. Fig. 7.13 shows horizontal and vertical profiles of axial velocity ($\overline{U_x}$) downstream of the rotor plane, where the axial velocity has been averaged over the final rotor revolution and normalised by the undisturbed axial velocity at the same location in the channel (U_{ref}). This normalisation was adopted to isolate the velocity deficit from the effect of shear in the undisturbed channel. Before examining the wake profiles, it should be noted that this normalisation does amplify the differences in the axial velocity profiles beneath the rotor ($z/H < 0.2$), due to the low values of the reference velocity near the bottom of the sheared velocity profile.

Fig. 7.13 shows that immediately downstream of the rotor plane ($x/D = 0.1$), the bypass flow velocity is greater on the upwards facing bed slope than on the horizontal and downwards facing bed slopes (except beneath the rotor due to the normalisation adopted). The increased bypass flow acceleration exhibited on the upwards facing bed slope arises from the reduced cross-sectional area of the channel downstream of the rotor (by mass conservation). The increased bypass flow acceleration leads to a greater static pressure drop across the bypass flow passage and hence also across the core flow passage (as the static pressure must equalise between the core and bypass flow passages both far upstream and downstream of the rotor). With an increased static pressure drop across the core flow passage, a greater mass flow rate is drawn through the swept area of the rotor on the upwards facing bed slope. In Fig. 7.13, this is manifested as an acceleration of the core flow velocity just downstream of the rotor (at $x/D = 0.1$). Further downstream of the rotor, the axial velocity in the core and bypass flow streams continues to recover faster on the upwards facing bed slope,

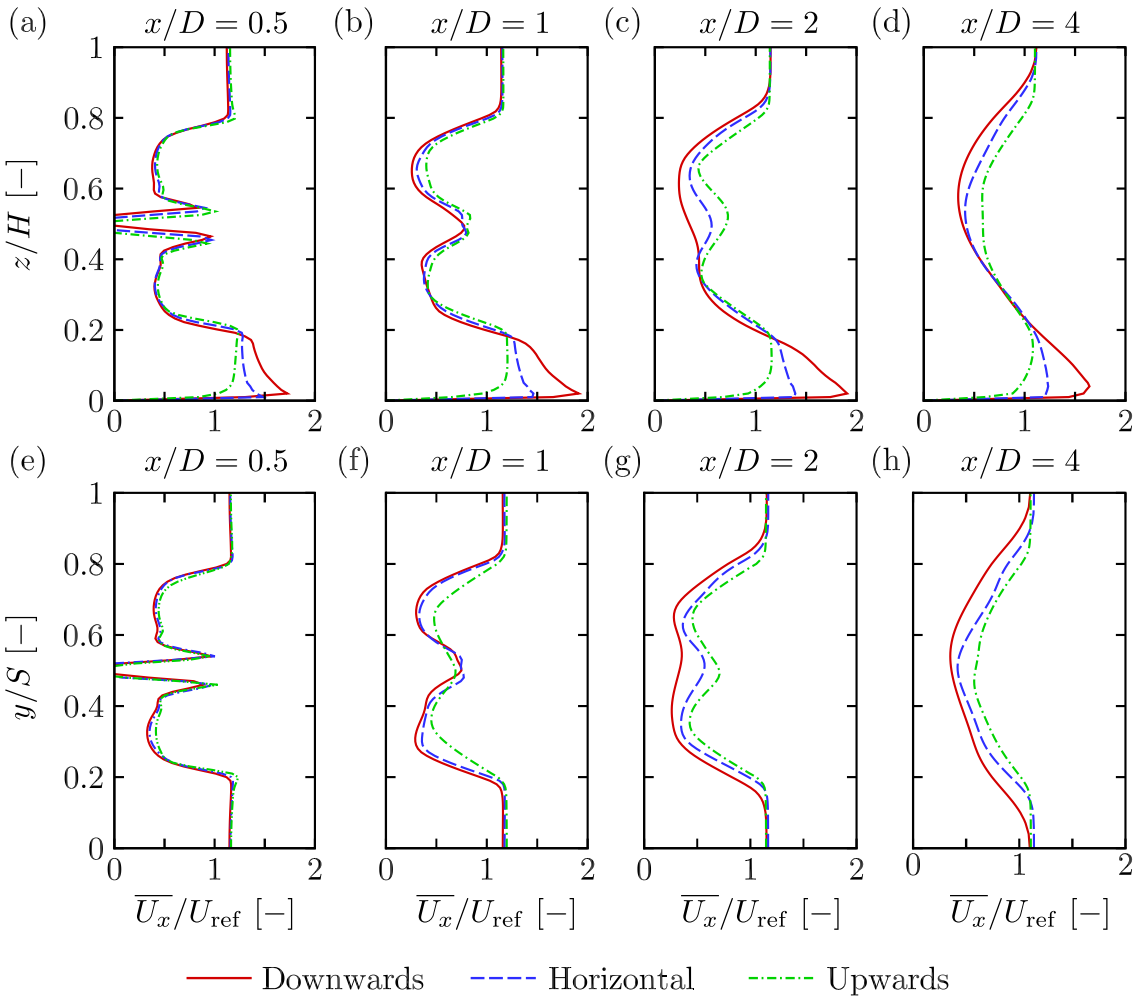

Figure 7.13: Time averaged axial velocity in the vertical (a, b, c d) and lateral (e, f, g, h) directions downstream of the rotor plane at a rotational speed of 1.0 rad/s. The reference velocity has been taken as the local velocity at the same location in the channel with no device present. H represents the local depth of the domain and S represents the width of the domain. The vertical profiles were taken on the channel centreline ($y = 0$), while the lateral profiles were taken along the local mid-depth.

due to the favourable pressure gradient.

To compare the rate of wake expansion in the channel, Fig. 7.14 shows the edge of the wake in a vertical plane along the centreline of the domain ($y/S = 0$) and along a lateral plane through the local mid-depth of the domain. Following Masters et al. (2013), the edge of the wake has been taken as the location where the axial velocity reaches 95% of the undisturbed axial velocity at the same location in the channel (where $\overline{U_x}/U_{\text{ref}} = 0.95$). In both the lateral and vertical directions, the rate

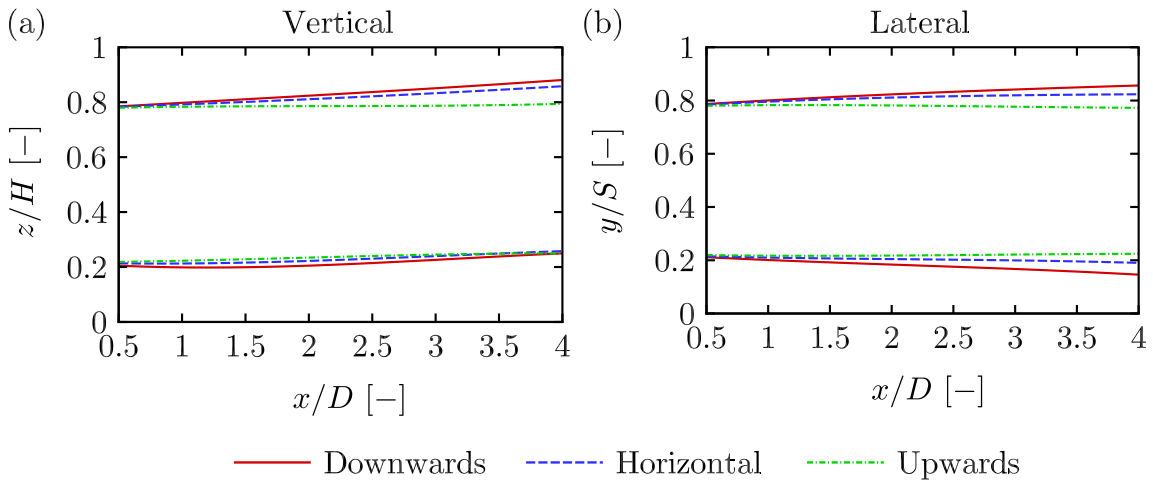

Figure 7.14: Edge of the wake in the (a) vertical and (b) lateral directions, at a rotational speed of 1.0 rad/s. The edge of the wake has been taken as the location where $\overline{U_x}/U_{\text{ref}} = 0.95$.

of wake expansion is slower on the upwards facing bed slope than on the horizontal and downwards facing bed slopes. Hence, when the rotor is operating at the same tip-speed-ratio, the wake on the upwards facing bed slope is smaller both in absolute size and also relative to the local cross-sectional area of the channel. The slower rate of wake expansion arises because the axial velocity difference between the core and the bypass flow streams is smaller on the upwards facing bed slope than on the horizontal and downwards facing bed slopes, as shown in Fig. 7.13. With a smaller velocity difference between the core and bypass flow streams, the static pressure difference between the core and bypass flow streams (which drives the wake expansion) is also smaller and hence the rate of wake expansion is slower on the upwards facing bed slope.

Fig. 7.14 also shows that the wake drifts upwards towards the free surface on all three bed slopes. This upwards drift has also been observed in experimental measurements of an isolated tidal turbine rotor in sheared flow by Stallard et al. (2015) and arises because of the different rates of mixing above and below the turbine in a sheared flow. As shown in Fig. 7.3 (b), the undisturbed turbulence intensity is

stronger below the turbine than above the turbine (on all three bed slopes), which promotes stronger mixing below the turbine than above the turbine. Hence, the flow recovers faster below the turbine than above the turbine and the wake drifts upwards towards the free surface. As the undisturbed axial velocity profile is more strongly sheared on the downwards facing bed slope (and the undisturbed turbulence intensity is stronger), it follows that the upwards drift towards the free surface is more pronounced on the downwards facing bed slope than on the horizontal and upwards facing bed slopes.

7.8 Summary

Blade resolved computations have been undertaken in three different computational domains that slope in the streamwise direction. On the downwards facing bed slope, the adverse pressure gradient increases the degree of velocity shear across the rotor swept area, which increases the kinetic energy flux that is available for extraction. Hence, devices operating on downwards facing bed slopes are able to exert more thrust on the flow and extract more power, when operating at the same tip-speed-ratio. However, the increased velocity shear also increases the blade loading fluctuation as the blades rotate through the sheared velocity profile, which may be detrimental to the fatigue life of the device.

On upwards facing bed slopes, devices generate less power due to the reduced kinetic energy flux that is available for extraction. However, the devices are more efficient at extracting the power that is available to them, when operating at the same tip-speed-ratio. This is because the reduced cross-sectional area downstream of the rotor leads to an increased acceleration of the bypass flow. The increased acceleration of the bypass flow increases the static pressure drop across the bypass flow passage and hence also across the core flow passage (as the static pressure must

equalise between the core and bypass flow streams both far upstream and downstream of the rotor). Hence, a greater mass flow rate is drawn through the rotor swept area, increasing the the thrust exerted on the flow by the rotor and the power extracted from the flow by the rotor, at a fixed rotational speed. On upwards facing bed slopes, a further increase in efficiency (power coefficient) is also possible by increasing the tip-speed-ratio (and hence the thrust) of the rotor. With an increased tip-speed-ratio, the mass flow rate through the rotor swept area reduces, which reduces the angle of attack back towards the angle of attack that maximises the sectional lift to drag ratio of the outboard aerofoil sections.

Downstream of the rotor, wake recovery is faster on the upwards facing bed slope due to the favourable pressure gradient. Hence, the wake itself occupies a smaller fraction of the cross-sectional area of the channel on the upwards facing bed slope than the horizontal and downwards facing bed slopes. The wake has also been observed to drift upwards towards the free surface on all three bed slopes. This upwards drift has been attributed to the different rates of mixing above and below the rotor due to the sheared axial velocity profile.

Chapter 8

Conclusions and Future Work

In this chapter, a brief summary of the main conclusions drawn in this thesis will be presented. Potential areas of future work will then be highlighted.

8.1 Conclusions

8.1.1 Tip Flow Corrections for Horizontal Axis Rotors

On the outboard sections of rotating blades, the blade loading drops off as the tip is approached. This drop off in blade loading can be attributed to a combination of downwash at the rotor plane (which reduces the angle of attack) and spanwise flow accelerations on the pressure and suction surfaces of the blade. Both of these tip flow effects are induced by vorticity that is shed from the blade and result in a modification of the static pressure distribution on the blade surface. It has been shown that as the tip of the blade is approached, the changing surface pressure distribution causes the sectional force vector to reduce in magnitude and rotate away from the rotor plane, towards the streamwise direction. To account for this behaviour, low order rotor models that are based on the blade element method require a tip flow correction with the capacity for anisotropy in the thrust and torque producing directions.

In this thesis, two different tip flow correction methods have been analysed. In the first method, the lift and drag polars (that are used as a sub-grid model to compute the blade loading) are modified. By allowing the sectional lift coefficient to decrease while the sectional drag coefficient increases, the sectional force vector can reduce in magnitude and rotate towards the streamwise direction as the tip of the blade is approached. In the second method, a correction factor is applied directly to the thrust and torque producing forces (independently) before they are applied to the flow field. By applying a stronger correction to the torque producing force than the thrust producing force, the sectional force vector can reduce in magnitude and rotate towards the streamwise direction as the tip of the blade is approached. Both correction methods have been shown to achieve similar levels of accuracy when applied to actuator line computations of a 4.5m diameter wind turbine rotor (the MEXICO rotor).

However, both correction methods experience distinct limitations. The method of modifying the lift and drag polars requires the angle of attack and relative velocity magnitude to be extracted from blade resolved computations or experimental measurements of the complete (3D) rotor. This can lead to errors near the root and tip, as the spanwise flow component is significant and the flow is not strictly in the plane of the aerofoil section. Conversely, the method of applying a correction factor to the blade forces is currently limited by the functional form of the correction factor and a lack of empirical data for calibration.

It should be emphasised that the near-tip analysis presented in this thesis is limited to cases where the flow field local to the blade sections is steady. Hence, the proposed corrections are not applicable in sheared flow, domains with significant anisotropy or when blade-tower interaction effects are strong. Furthermore, the applicability of the analysis to blocked flow conditions remains uncertain, as the spanwise pressure gradients and trajectory of the shed vorticity are likely to be modified by the presence

of domain boundaries. For these flow scenarios, further analysis of the near-tip flow is required before a tip flow correction can be applied with confidence.

8.1.2 Cavitation Restrictions on Tidal Turbine Performance

Increasing the blockage ratio and the tip-speed-ratio of tidal turbine rotors increases the strength of the suction peak developed on the outboard blade sections. Hence, the minimum static pressure in the fluid decreases and the rotor is pushed closer to cavitation as the blockage ratio and tip-speed-ratio are increased. Furthermore, when tip flow effects are not adequately accounted for, blade element based cavitation analyses over-predict the strength of the suction peak developed on the outboard blade sections. Hence, these (industry standard) cavitation analyses are currently overly conservative.

As cavitation inception must be avoided entirely during rotor operation, device developers can choose to either limit the maximum tip-speed-ratio of the rotor or increase the submersion depth, in order to increase the minimum static pressure in the fluid and avoid cavitation inception. Both of these restrictions limit the maximum power coefficient that can be developed by the rotor. However, it has been shown that rotors which are specifically designed for blockage (they exert higher thrust at a given tip-speed-ratio) can operate at higher tip-speed-ratios before cavitation limits are reached. They can therefore achieve higher maximum power coefficients than rotors which are not designed specifically for blockage.

The cavitation analysis in this thesis was carried out in a cylindrical domain with equivalent area blockage to reduce the computation cost of the simulations. This assumption was investigated and found to be reasonably accurate over the range of blockage ratios considered, as long as the rotor is not located close to the free surface. Under these conditions, the bypass flow around the device becomes highly anisotropic and a cylindrical domain is no longer an acceptable approximation.

8.1.3 Tidal Power Extraction on a Streamwise Bed Slope

Tidal power extraction has been considered in a computational domain that slopes in the streamwise direction. Downwards facing bed slopes increase the kinetic energy flux that is available to devices for extraction, by increasing the degree of velocity shear across the swept area of the device. However, the increased velocity shear also increases the magnitude of the unsteady blade loading fluctuations, which may be detrimental to the fatigue life of the device. Conversely, devices on upwards facing slopes experience reduced unsteady blade loading fluctuations, due to a reduction in velocity shear across the swept area of the device. In addition, devices placed on upwards facing slopes extract power more efficiently, despite the reduced kinetic energy flux that is available to them for extraction. This increase in efficiency can be attributed to the downstream constriction of the flow by the seabed and free surface, which leads to an increased acceleration of the bypass flow (the flow which passes around the device) at a fixed tip-speed-ratio. The increased acceleration of the bypass flow leads to a greater static pressure drop across the bypass flow passage and hence also across the core flow passage (as the static pressure must equalise between the core and bypass flow passages both far upstream and downstream of the device). The increased static pressure drop across the core flow passage then draws a greater mass flow rate through the swept area of the device, increasing the power extracted at a fixed tip-speed-ratio.

In this thesis, a rigid lid model was adopted for the free surface in all computations. The rigid lid model neglects the free surface deformation that must accompany energy extraction (equivalent to assuming $Fr = 0$) and sets the fluid depth at the downstream boundary, thus implicitly prescribing the energy removed from the flow. Hence, the rigid lid model does not account for the additional acceleration of the core and bypass flow streams that are induced by the drop in free surface height across the rotor. These effects were deliberately neglected in this thesis, in order to isolate the effects

of velocity shear and downstream flow passage constriction on device performance. However, a future analysis is essential to quantify the neglected effects of free surface deformation on device performance.

8.2 Future Work

8.2.1 Tip Flow Corrections for Horizontal Axis Rotors

Now that detailed observations of the tip loss mechanism have been carried out and two different tip flow correction methods have been analysed in detail, a new tip flow correction can be proposed. This new tip flow correction should fulfil several criteria in order to fully account for the tip loss mechanism. Firstly (and most importantly), the correction should allow the sectional force vector to reduce in magnitude and rotate towards the streamwise direction as the tip of the blade is approached. Furthermore, the sectional force vector should be able to rotate past 90°, in order to capture the negative sectional torque that some rotors exhibit at high tip-speed-ratios. The new tip flow correction should also include some blade shape dependency, which will allow a more aggressive correction to be applied to high solidity tidal turbine rotors. However, in order to propose and parametrise such a dependency, more rotors need to be analysed, as the current dataset is very limited. Ideally, these rotors should have a variety of blade and tip geometries, so that the blade shape dependency can be both better understood and more accurately parameterised.

Furthermore, the applicability of the tip-flow analysis to flow conditions where the blade tip passes close to domain boundaries (i.e. blocked flow conditions), needs to be investigated. This is of particular importance for tidal turbine rotors, as tidal turbines are likely to be installed in closely packed arrays of turbines in relatively shallow flows. Tidal flows are also often highly sheared and the applicability of the tip-flow analysis to conditions where the flow field local to the blade motion is unsteady, also

remains unclear. Such tip-flow analyses could be carried out using the same procedure described in this thesis and would be particularly useful for simulations of arrays of devices where tip-flow corrected reduced order rotor models are often employed.

8.2.2 Cavitation Restrictions on Tidal Turbine Performance

At a tip submersion depth of 8m and a design tip-speed-ratio of 5, both rotor designs adopted in this work are not likely to cavitate. This can be attributed to a combination of the broad suction peak of the RISØ-A1-24 aerofoil and the relatively low design tip-speed-ratio of the rotor. However, the maximum power coefficient of these rotors is relatively low due to the maximum lift to drag ratio of the RISØ-A1-24 aerofoil (around 60). In order to increase the maximum power coefficient, future rotor designs are likely to be less conservative, with a higher design tip-speed ratio. These rotors are likely to utilise thinner aerofoils with a higher maximum lift to drag ratio on the outboard blade sections. The increased lift to drag ratio is usually accompanied by a sharper suction peak. Hence, these rotor designs may be much closer to cavitation than the relatively conservative rotor designs investigated in this work. Hence, the cavitation analysis will need to be repeated for new rotor designs.

A hydrodynamic safety margin was introduced in this thesis to account for the dynamic pressure fluctuations from free surface waves, ambient turbulence and velocity shear, that were not directly included in the computations. While the magnitude of this safety margin is likely to be imposed on a case-by-case basis to account for site specific conditions, further work is required to quantify the likely order of magnitude of this safety margin, which currently remains unknown.

The cavitation analyses in this thesis have all been carried out at the design condition, before rated power is achieved. However, for flow speeds above rated power, load control mechanisms are employed, which alter the static pressure distribution on the blade surface and change the likelihood of cavitation inception. Overspeed

control for example, increases the strength of the blade suction peak, pushing the rotor closer to cavitation. A new cavitation analysis will need to be carried out to ensure that cavitation inception does not occur above rated power when specific load control mechanisms are adopted.

The cavitation analysis presented in this thesis could also be used as a design tool to select a suitable submersion depth for a given device to be installed at a given tidal energy site. By identifying the lowest atmospheric tide and maximum tidal current at a given site, a submersion depth can be selected to ensure that the minimum static pressure remains greater than the vapour pressure of seawater (with an appropriate safety margin) over the entire range of operating conditions. Alternatively, it may be desirable to select a shut-down speed that limits the minimum static pressure on the surface of the rotor blades. Such design decisions are clearly multifaceted and will need to be considered in future studies.

Cavitation limits will be more restrictive for devices installed close to the free surface due to the reduced hydrostatic pressure contribution. However, the simplified analysis carried out in a cylindrical domain in this thesis is not appropriate for these installation conditions, due to the asymmetry of the bypass flow. Local free surface deformation effects and the wave induced pressure fluctuations will also become increasingly significant as the tip of the blade approaches the free surface. Under these conditions, blade resolved computations should be carried out directly (that include surface waves and free surface deformation effects) in order to more accurately compute the blade surface pressure distribution. However, the analysis presented in this thesis can still be used as a useful first approximation for these conditions.

References

Adcock, T. A. A., Draper, S., Houlsby, G. T., Borthwick, A. G. L. & Serhadlioğlu, S. (2014), 'The available power from tidal stream turbines in the Pentland Firth', *Proc. R. Soc. A* **469**, 20130072.

Adcock, T. A. A., Draper, S. & Nishino, T. (2015), 'Tidal power generation - a review of hydrodynamic modelling', *Proc IMechE Part A: J Power and Energy* **229**(7), 755771.

Ahmed, M. (2012), 'Blade sections for wind turbine and tidal current turbine applications - current status and future challenges', *International Journal on Energy Research* **36**, 829–844.

Apsley, D. D. & Leschziner, M. A. (2000), 'Advanced turbulence modelling of separated flow in a diffuser', *Flow, Turbulence and Combustion* **63**, 81–112.

Atlantis Resources (2017), 'Tidal Turbines', `https://www.atlantisresourcesltd.com/services/turbines`. Accessed: January 2018.

Bardina, J. E., Huang, P. G. & Coakley, T. J. (1997), 'Turbulence modeling validation, testing, and development'. NASA Technical Memorandum 110446.

Batten, W., Bahaj, A. & Molland, A. (2008), 'The prediction of the hydrodynamic performance of marine current turbines', *Renewable Energy* **33**(5), 1085–1096.

Bechmann, A., Sørenson, N. & Zahle, F. (2011), 'CFD simulations of the MEXICO rotor', *Wind Energy* **14**, 677–689.

Belloni, C. S. K. (2013), 'Hydrodynamics of Ducted and Open-Centre Tidal Turbines'. DPhil Thesis, University of Oxford.

Bertagnolio, F., Sørensen, N., Johansen, J. & Fuglsang, P. (2001), Wind turbine airfoil catalogue, Technical Report Risø-R-1280(EN), Risø National Laboratory, Roskilde, Denmark.

Betz, A. (1919), 'Schraubenpropeller mit geringstem Energieverlust. Mit einem Zusatz von L. Prandtl', *Nachrichten von der Gesellschaft der Wissenschaften zu Göttingen, Mathematisch-Physikalische Klasse* pp. 193–217.

Betz, A. (1920), 'Das Maximum der theoretisch moglichen Ausnutzung des Windes durch Windmotoren', *Zeit ges Turbinenwesen* **26**, 307–309.

Black and Veatch Ltd. (2005), Phase II UK tidal stream energy resource assessment, Technical Report 107799/D/2200/03, Carbon Trust.

Black and Veatch Ltd. (2011), UK tidal current resource & economics, Technical report, Carbon Trust.

Blackmore, T., Gaurier, B., Myers, L., Germain, G. & Bahaj, A. (2015), The effect of freestream turbulence on tidal turbines, *in* '12th European Wave and Tidal Energy Conference (EWTEC 2015)', Nantes, France.

Blunden, L. S. & Bahaj, A. S. (2006), 'Initial evaluation of the tidal stream resource of the Portland Bill UK', *Renewable Energy* **31**, 121–132.

Boorsma, K. & Schepers, J. G. (2009), Description of experimental setup, MEXICO measurements, Technical Report ECN-X–09-0XX, Energy Research Centre of the Netherlands (ECN).

Boorsma, K. & Schepers, J. G. (2014), New MEXICO experiment: Preliminary overview with initial validation, Technical Report ECN-E–14-048, Energy Research Centre of the Netherlands (ECN).

Boussinesq, J. (1878), 'Essai sur la th'eorie des eaux courantes', *Journal de math 'ematiques pures et appliqu'ees* p. 335376.

Branlard, E. (2011), Wind turbine tip-loss corrections: Review, implementation and investigation of new models, Master's thesis, Technical University of Denmark.

Buckland, H., Masters, I., Orme, J. & Baker, T. (2013), 'Cavitation inception and simulation in blade element momentum theory for modelling tidal stream turbines', *Proc. IMechE Part A: J. Power and Energy* **227**(4), 479–485.

Carlton, J. S. (1994), *Marine Propellers and Propulsion*, Butterworth–Heinemann, Burlington, USA.

Cebeci, T. & Bradshaw, P. (1977), *Momentum Transfer in Boundary Layers*, Hemisphere Publishing Corporation, New York, USA.

Chaviaropoulos, P. K. & Hansen, M. O. L. (2000), 'Investigating three-dimensional and rotational effects on wind turbine blades by means of a quasi-3d navier-stokes solver', *Journal of Fluids Engineering* **122**, 330–336.

Churchfield, M., Li, Y. & Moriarty, P. (2013), 'A large-eddy simulation study of wake propagation and power production in an array of tidal-current turbines', *Phil. Trans. R. Soc. A* **371**(1985).

Consul, C., Willden, R. H. J. & McIntosh, S. C. (2013), 'Blockage effects on the hydrodynamic performance of a marine cross flow turbine', *Phil. Trans. R. Soc. A.* **371**.

Cooke, S., Willden, R. H. J. & Byrne., B. W. (2015), Power and thrust behaviour in a porous disc fence array experiment, *in* '4th Oxford Tidal Energy Workshop', Oxford, UK.

Cooke, S., Willden, R. H. J., Byrne, B. W. & Stallard, T. (2014), An experimental investigation of blockage in a short fence array of tidal turbines, *in* 'Proceedings of the 1st International Conference on Renewable Energies Offshore (RENEW)', Lisbon, Portugal.

Department for Business, Energy & Industrial Strategy (2016*a*), 'Electricity Generation Costs (November 2016)'.

Department for Business, Energy & Industrial Strategy (2016*b*), 'Hinkley Point C: contractual documents'.

Department for Business, Energy & Industrial Strategy (2017), 'Contracts for Difference (CFD) Second Allocation Round Results'.

Department of Energy and Climate Change (2008), 'Climate Change Act (c.27)', `http://www.legislation.gov.uk/ukpga/2008/27/pdfs/ukpga_20080027_en.pdf`. Accessed: January 2018.

Department of Energy and Climate Change (2017), 'Electricity: Chapter 5, Digest of United Kingdom Energy Statistics (DUKES)'.

DNV GL (2015), Tidal Turbines - Rules and Standards, Technical Report DNVGL-ST-0164.

Draper, S., Houlsby, G. T., Oldfield, M. L. G. & Borthwick, A. G. L. (2010), 'Modelling tidal energy extraction in a depth-averaged coastal domain', *IET Renewable Power Generation* **4(6)**, 545–554.

Draper, S. & Nishino, T. (2014), 'Centred and staggered arrangements of tidal turbines', *Journal of Fluid Mechanics* **739**, 72–93.

Draper, S., Nishino, T., Adcock, T. A. A. & Taylor, P. H. (2016), 'Performance of an ideal turbine in an inviscid shear flow', *Journal of Fluid Mechanics* **796**, 86–112.

Du, Z. & Selig, M. (1998), 'A 3-D stall-delay model for horizontal axis wind turbine performance prediction', *AIAA Paper* **21**, 9–19.

Eckelmann, H. (1974), 'The structure of the viscous sublayer and the adjacent wall region in a turbulent channel flow', *Journal of Fluid Mechanics* **65**(3), 439–459.

EMEC (2016), 'European Marine Energy Centre Website', `http://www.emec.org.uk/`. Accessed: January 2018.

E.ON (2014), Private Communication.

European Parliament (2009), 'Directive 2009/28/EC of the European Parliament and of the Council of 23 April 2009 on the promotion of the use of energy from renewable sources and amending and subsequently repealing directive', *Official Journal of the European Union* (QJ L 140), 16–62.

Eurostat (2017), 'Energy from renewable sources', `http://ec.europa.eu/eurostat/web/energy/data/shares`. Dataset [Code: nrg_ ind_335a], Accessed: December 2017.

Farrell, P. E. & Maddison, J. R. (2011), 'Conservative interpolation between volume meshes by local Galerkin projection', *Comput. Methods Appl. Mech. Engrg.* **200**, 89–100.

Ferrer, E. & Munduate, X. (2007), 'Wind turbine blade tip computations using CFD', *Journal of Physics: Conference Series* **75**, 012005.

Ferziger, J. H. & Perić, M. (1995), *Computational methods for fluid dynamics*, Springer-Verlag, Berlin Heidelberg NewYork.

Fleming, C. (2014), 'Tidal turbine performance in an offshore environment'. DPhil Thesis, University of Oxford.

Fraser, S., Nikora, V., Williamson, B. & Scott, B. (2017), 'Hydrodynamic impacts of a marine renewable energy installation on the benthic boundary layer in a tidal channel', *Energy Procedia* **250–259**.

Galloway, P., Myers, L. & Bahaj, A. (2010), Studies of a scale tidal turbine in close proximity to waves, *in* '3rd International Conference on Ocean Energy', Bilbao, Spain.

Gant, S. & Stallard, T. (2008), Modelling a tidal turbine in unsteady flow, *in* 'The Proceedings of The Eighteenth (2008) International Offshore and Polar Engineering Conference', Vancouver, Canada, pp. 473–479.

Garrett, C. & Cummins, P. (2005), 'The power potential of tidal currents in channels', *Proc. R. Soc. A* **461**, 2563–2572.

Garrett, C. & Cummins, P. (2007), 'The efficiency of a turbine in a tidal channel', *Journal of Fluid Mechanics* **588**, 243–251.

Glauert, H. (1935), Airplane propellers, *in* 'Aerodynamic Theory', Julius Springer, Berlin, pp. 169–360.

Goldstein, S. (1929), 'On the vortex theory of screw propellers', *Proc. R. Soc. A* **123**(792), 440–465.

Gosman, A. (1998), 'Developments in industrial computational fluid dynamics', *Chem. Eng. Res. Des.* **76**(2), 153–161.

Goundar, J. & Ahmed, M. (2013), 'Design of a horizontal axis tidal current turbine', *Applied Energy* **111**, 161–174.

Gunn, K. & Stock-Williams, C. (2013), 'On validating numerical hydrodynamic models of complex tidal flow', *International Journal of Marine Energy* **3–4**, e82–e97.

Gunn, K., Stock-Williams, C., Burke, M., Willden, R., Vogel, C., Hunter, W., Stallard, T., Robinson, N. & Schmidt, S. R. (2016), 'Limitations to the validity of single wake superposition in wind farm yield assessment', *Journal of Physics: Conference Series* **749**, 012003.

Guntur, S., Bak, C. & Sørensen, N. (2011), Analysis of 3D stall models for wind turbine blades using data from the MEXICO experiment, *in* '13th International conference on wind engineering', ICWE, Amsterdam, Netherlands.

Guntur, S. & Sørensen, N. (2015), 'A study of rotational augmentation using CFD analysis of flow in the inboard region of the MEXICO rotor blades', *Wind Energy* **18**, 745–756.

Hand, M. M., Simms, D. A., Fingersh, L. J., Jager, D. W., Cotrell, J. R., Schreck, S. & Larwood, S. M. (2001), Unsteady aerodynamic experiment phase VI: Wind tunnel test configurations and available data campaigns, Technical Report NREL/TP-500-29955, National Renewable Energy Laboratory (NREL).

Hansen, M. & Johansen, J. (2004), 'Tip studies using CFD and comparison with tip loss models', *Wind Energy* **7**, 343–356.

Herraez, I., Medjroubi, W., Stoevesandt, B. & Peinke, J. (2012), 'Aerodynamic simulation of the MEXICO rotor', *Journal of Physics: Conference Series* **555**, 012051.

Herrig, J., Emery, J. & Erwin, J. (1951), Effect of section thickness and trailing edge radius on the performance of NACA 65-series compressor blades in cascade at low speeds, Technical Report RM L51J16, NASA.

Himmelskamp, H. (1945), Profile investigations on a rotating airscrew, PhD thesis, Gottingen University, Germany.

Houlsby, G. T., Draper, S. & Oldfield, M. L. G. (2008), Application of linear momentum actuator disc theory to open channel flow, Technical Report OUEL 2296/08, Department of Engineering Science, Univerity of Oxford.

Hu, J. & Willden, R. (2016), Unsteady load relief of an axial flow tidal turbine in sheared flow by individual pitch control, *in* 'Proceedings of the 5th Oxford Tidal Energy Workshop', Oxford, UK.

Hunter, W. (2016), 'Actuator disk methods for tidal turbine arrays'. DPhil Thesis, University of Oxford.

Hunter, W., Nishino, T. & Willden, R. (2014), Implementation and validation of an actuator line class for wind and tidal turbines, *in* '9th OpenFOAM Workshop', Zagreb, Croatia.

Hunter, W., Nishino, T. & Willden., R. (2015), 'Investigation of tidal turbine array tuning using 3D Reynolds-Averaged NavierStokes Simulations', *International Journal of Marine Energy* **10**, 39–51.

Ivanell, S., Sørensen, J., Mikkelsen, R. & Henningson, D. (2009), 'Analysis of numerically generated wake structures', *Wind Energy* **12**(1), 63–80.

Jarrin, N., Benhamadouche, S., Laurence, D. & Prosser, R. (2006), 'A synthetic-eddy-method for generating inflow conditions for large-eddy simulations', *International Journal of Heat and Fluid Flow* **27**(4), 585–593.

Jasak, H. (1996), Error analysis and estimation for the finite volume method with applications to fluid flows, PhD thesis, Imperial College London, Department of Mechanical Engineering.

Jha, P., Churchfield, M., Moriarty, P. & Schmitz, S. (2013), Accuracy of state–of–the–art actuator-line modeling for wind turbine wakes, *in* '51st AIAA Aerospace Sciences Meeting', Dallas, Texas.

Johansen, J. & Sørenson, N. N. (2004), 'Aerofoil characteristics from 3D CFD rotor computations', *Wind Energy* **7**, 283–294.

Kalitzin, G., Medic, G., Iaccarino, G. & Durbin, P. (2005), 'Near-wall behaviour of RANS turbulence models and implications for wall functions', *Journal of Computational Physics* **204**, 265–291.

Kirby, R. & Retiere, C. (2009), 'Comparing environmental effects of Rance and Severn barrages', *Proceedings of the Institution of Civil Engineers – Maritime Engineering* **162**(1), 11– 26.

Lanchester, F. (1915), 'A contribution to the theory of propulsion and the screw propeller', *Trans Inst Naval Architects* **57**, 98–116.

Lande-Sudall, D., Stallard, T. & Stansby, P. (2017), Experimental study of the wakes due to tidal rotors and a shared cylindrical support, *in* 'Twelfth European Wave and Tidal Energy Conference (EWTEC 2017)', Cork, Ireland.

Lindenburg, C. (2003), Investigation into rotor blade aerodynamics, Technical Report ECN–C–03–025, Energy Research Centre of the Netherlands (ECN).

Lindenburg, C. (2004), Modelling of rotational augmentation based on engineering considerations and measurements, *in* 'European Wind Energy Conference', London, UK.

Low Carbon Innovation Coordination Group (2012), Technology Innovation Needs Assessment (TINA) Marine Energy Summary Report, Technical report.

Luo, J. Y., Issa, R. I. & Gosman, A. D. (1994), Prediction of impeller-induced flows in mixing vessels using multiple frames of reference, *in* 'IChemE Symposium Series', 136, pp. 549–556.

Luznik, L., Flack, K., Lust, E. & Taylor, K. (2013), 'The effect of surface waves on the performance characteristics of a model tidal turbine', *Renewable Energy* **58**, 108–114.

MacEnri, J., Reed, M. & Thiringer, T. (2013), 'Influence of tidal parameters on SeaGen flicker performance', *Phil. Trans. R. Soc. A* **371**(2013), 829–844.

Machefaux, E., Larsen, G. & Murcia-Leon, J. (2015), 'Engineering models for merging wakes in wind farm optimization applications', *Journal of Physics: Conference Series* **625**, 012037.

Malki, R., Masters, I., Williams, A. & Croft, T. (2014), 'Planning tidal stream turbine array layouts using a coupled blade element momentum - computational fluid dynamics model', *Renewable Energy* **63**(46–54).

Martínez-Tossas, L., Churchfield, M. & Leonardi, S. (2015), 'Large eddy simulations of the flow past wind turbines: actuator line and actuator disc modelling', *Wind Energy* **18**, 1047–1060.

Mason-Jones, A., O'Doherty, D., Morris, C. & O'Doherty, T. (2013), 'Influence of velocity profile & support structure on tidal stream turbine performance', *Renewable Energy* **52**, 23–30.

Masters, I., Malki, R., Williams, A. & Croft, T. (2013), 'The influence of flow acceleration on tidal stream wake dynamics: a numerical study using a coupled BEM-CFD model.', *Applied Mathematical Modelling* **37**(16–17), 7905 – 7918.

McIntosh, S., Fleming, C. & Willden, R. (2011), Embedded RANS-BEM tidal turbine design, *in* 'The Proceedings of the Ninth European Wave and Tidal Energy Conference (EWTEC 2011)', Southampton UK.

McNaughton, J. (2013), Turbulence modelling in the near-field of an axial flow tidal turbine using *Code_Saturne*, PhD thesis, University of Manchester.

Menter, F. R. (1994), 'Two-equation eddy-viscosity turbulence models for engineering applications', *AIAA Journal* **32(8)**, 1598–1605.

MeyGen Ltd. (2011), MeyGen Phase 1 EIA Scoping Document, Technical Report MEYGEN-ER-002-EIA Scoping Document 1.7.

MeyGen Ltd. (2014), Decommissioning programme, Technical Report MEY–10–70–HSE–002–D–.

MeyGen Ltd. (2016), MeyGen Tidal Energy Project Phase 1. Project Environmental Monitoring Programme, Technical Report MEY-1A-70-HSE-018-I-PEMP.

Mikkelsen, R. (2003), Actuator disc methods applied to wind turbines, PhD thesis, Technical University of Denmark.

Milne, I., Sharma, R., Flay, R. & Bickerton, S. (2013), 'Characteristics of the turbulence in the flow at a tidal stream power site', *Phil. Trans. Roy. Soc. A* **371**(1985).

Moser, R., Kim, J. & Mansour, N. (1999), 'DNS of turbulent channel flow up to $\mathrm{Re}_\tau = 590$', *Physics of Fluids* **11**, 943–945.

Muchala, S. (2017), 'Tidal turbine support structures'. DPhil Thesis, University of Oxford.

Mycek, P., Gaurier, B., Germain, G., Pinon, G. & Rivoalen, E. (2014), 'Experimental study of the turbulence intensity effects on marine current turbines behaviour. Part 1: one single turbine', *Renewable Energy* **66**, 729–746.

Ning, A. & Dykes, K. (2014), 'Understanding the benefits and limitations of increasing maximum rotor tip speed for utility scale wind turbines', *Journal of Physics: Conference Series* **524**, 012087.

Nishino, T. & Willden, R. H. J. (2012*a*), 'Effects of 3-D channel blockage and turbulent wake mixing on the limit of power extraction by tidal turbines', *International Journal of Heat and Fluid Flow* **37**, 123–135.

Nishino, T. & Willden, R. H. J. (2012*b*), 'The efficiency of an array of tidal turbines partially blocking a wide channel', *Journal of Fluid Mechanics* **708**, 596–606.

Nishino, T. & Willden, R. H. J. (2013), 'Two-scale dynamics of flow past a partial cross-stream array of tidal turbines', *Journal of Fluid Mechanics* **730**, 220–244.

Olczak, A., Stallard, T., Feng, T. & Stansby, P. (2016), 'Comparison of a RANS blade element model for tidal turbine arrays with laboratory scale measurements of wake velocity and rotor thrust', *Journal of Fluids and Structures* **64**, 87–106.

OpenHydro (2017), 'The Open-Centre Turbine', http://www.openhydro.com/Technology/Open-Centre-Turbine. Accessed: January 2018.

Patankar, S. V. (1980), *Numerical Heat Transfer and Fluid Flow*, Hemisphere Publishing Corporation, Washington DC USA.

Plaza, B., Bardera, R. & Visiedo, S. (2015), 'Comparison of BEM and CFD results for MEXICO rotor aerodynamics', *Journal of Wind Engineering and Industrial Aerodynamics* **145**, 115–122.

Renewables Advisory Board (2008), 2020 Vision - How the UK can meet its target of 15% renewable energy, Technical Report RAB (2008) 0226.

Rusche, H. (2002), Computational Fluid Dynamics of dispersed two-phase flows at high phase fraction, PhD thesis, Imperial College London.

Saad, Y. (1993), *Iterative Methods for Sparse Linear Systems*, Society for Industrial and Applied Mathematics. Second Edition.

Sant, T. (2007), Improving BEM–based aerodynamics models in Wind turbine design codes, PhD thesis, DU Wind - Delft University Wind Energy Research Institute.

Sant, T., van Kuik, G. & van Bussel, G. (2006), 'Estimating the angle of attack from blade pressure measurements on the NREL Phase VI rotor using a free wake vortex model: axial conditions', *Wind Energy* **9**(6), 549–577.

Schepers, J. G., Boorsma, K., Cho, T., Gomez-Iradi, S., Schaffarczyk, P., Jeromin, A., Shen, W. Z., Lutz, T., Meister, K., Stoevesandt, B., Schreck, S., Micallef, D., Pereira, R., Sant, T., Madsen, H. A. & Sørensen, N. (2012), Final report of IEA task 29, Mexnext (phase 1): Analysis of MEXICO wind tunnel measurements, Technical Report ECN-E12-004, Energy Research Centre of the Netherlands (ECN).

Schlichting, H. & Gersten, K. (2000), *Boundary Layer Theory*, Springer-Verlag. 8th Edition.

Schluntz, J., Vogel, C. & Willden, R. (2014), Blockage–enhanced performance of tidal turbine arrays, *in* 'The Proceedings of the 2nd Asian Wave and Tidal Energy Conference (AWTEC 2014)', Tokyo, Japan.

Schluntz, J. & Willden, R. (2014), 'An actuator line based method with novel blade flow field coupling based on potential flow equivalence', *Wind Energy* **18**(8), 1469 – 1485.

Schluntz, J. & Willden, R. H. J. (2015), 'The effect of blockage on tidal turbine rotor design and performance', *Renewable Energy* **81**, 432–441.

Serhadlioğlu, S., Adcock, T. A., Houlsby, G. T., Draper, S. & Borthwick, A. G. L. (2013), 'Tidal stream energy resource assessment of the Anglesey Skerries', *International Journal of Marine Energy* **3-4**, e99–e111.

Shen, W., Hansen, M. & Sørenson, J. (2009), 'Determination of the angle of attack on rotor blades', *Wind Energy* **12**, 91–98.

Shen, W., Mikkelsen, R., Sørenson, J. & Bak, C. (2005), 'Tip loss corrections for wind turbine computations', *Wind Energy* **8**, 457–475.

Shen, W. & Sørensen, J. (1999), 'Quasi–3D Navier–Stokes model for a rotating airfoil', *Journal of Computational Physics* **150**, 518–548.

Shen, W. Z., Zhu, W. J. & Sørenson, J. N. (2012), 'Actuator line/Navier-Stokes computations for the MEXICO rotor: comparison with detailed measurements', *Wind Energy* **15**, 811–825.

Shives, M. & Crawford, C. (2013), 'Mesh and load distribution requirements for actuator line CFD simulations', *Wind Energy* **16**(8), 1183–1196.

Snel, H. & Van Holten, T. (1994), Review of recent aerodynamic research on wind turbines with relevance to rotorcraft, *in* 'Aerodynamics and Aeroacoustics of Rotorcraft', AGARD CP-552, Berlin, Germany, pp. 139–149.

Sørensen, N., Michelsen, J. & Schreck, S. (2002), 'Navier–Stokes predictions of the NREL Phase VI rotor in the NASA Ames 80 ft x 120 ft wind tunnel', *Wind Energy* **5**(2-3), 151–169.

Sørenson, J. N. & Shen, W. Z. (2002), 'Numerical modelling of wind turbine wakes', *Journal of Fluids Engineering* **124(2)**, 393–399.

Soto, K. & Escauriaza, C. (2015), Numerical simulations of marine hydrokinetic devices in complex bathymetries, *in* 'The Proceedings of the 11th European Wave and Tidal Energy Conference (EWTEC 2015)', Nantes, France.

Stallard, T., Collings, R., Feng, T. & Whelan, J. (2013), 'Interactions between tidal turbine wakes: experimental study of a group of three-bladed rotors', *Phil. Trans. R. Soc. A* **371**(1985).

Stallard, T., Feng, T. & Stansby, P. K. (2015), 'Experimental study of the mean wake of a tidal stream rotor in a shallow turbulent flow', *Journal of Fluids and Structures* **54**, 235–246.

Stansby, P. & Stallard, T. (2016), 'Fast optimisation of tidal stream turbine positions for power generation in small arrays with low blockage based on superposition of self-similar far-wake velocity deficit profiles', *Renewable Energy* **92**(366–375).

Sweby, P. K. (1984), 'High resolution schemes using flux limiters for hyperbolic conservation laws', *SIAM Journal on Numerical Analysis* **21**, 995–1011.

Tabor, G. R. & Baba-Ahmadi, M. (2010), 'Inlet conditions for large eddy simulation: A review', *Computers & Fluids* **39**(4), 553–567.

Taylor, G. I. (1944), Air resistance of a flat plate of very porous material, Technical Report 2236, ARC Reports and Memoranda.

Troldborg, N. (2009), Actuator Line Modeling of Wind Turbine Wakes, PhD thesis, Technical University of Denmark.

Turnock, S. R., Phillips, A. B., Banks, J. & Nicholls-Lee, R. (2011), 'Modelling tidal current turbine wakes using a coupled RANS-BEMT approach as a tool for analysing power capture of arrays of turbines', *Ocean Engineering* **38**, 1300–1307.

Vennel, R., Funke, S., Draper, S., Stevens, C. & Divett, T. (2015), 'Designing large arrays of tidal turbines: a synthesis and review', *Renewable and Sustainable Energy Reviews* **41**, 454–472.

Versteeg, H. K. & Malalasekera, W. (1995), *An Introduction to Computational Fluid Dynamics: The Finite Volume Method*, Pearson Education Ltd.

Vogel, C. (2014), 'Theoretical limits to tidal stream energy extraction'. DPhil Thesis, University of Oxford.

Vogel, C. R., Willden, R. H. J. & Houlsby, G. T. (2013), A correction for depth-averaged simulations of tidal turbine arrays, *in* 'The Proceedings of the 10th European Wave and Tidal Energy Conference (EWTEC 2013)', Aaldborg, Denmark.

von Kárman, T. (1930), 'Mechanische ähnlichkeit und turbulenz', *Nachrichten von der Gesellschaft der Wissenschaften zu Göttingen, Fachgruppe 1* **5**, 58–76.

Wimshurst, A. & Willden, R. (2016*a*), 'Tidal power extraction on a streamwise bed slope', *Ocean Engineering* **125**(1), 70–81.

Wimshurst, A. & Willden, R. H. J. (2016*b*), Validation of an actuator line method for tidal turbine rotors, *in* 'The 26th International Ocean and Polar Engineering Conference', ISOPE, Rhodes (Rodos), Greece. TPC-2016-0825.

Yang, H., Shen, W., Sørensen, J. & Zhu, W. (2011), 'Extraction of airfoil data using PIV and pressure measurements', *Wind Energy* **14**, 539–556.

Zangiabadi, E., Edmunds, M., Fairley, I., Togneri, M., Williams, A., Masters, I. & Croft, N. (2015), 'Computational fluid dynamics and visualisation of coastal flows in tidal channels supporting ocean energy development', *Energies* **8**, 5997–6012.

Zhang, Y., van Zuijlen, A. & van Bussel, G. (2017), 'The MEXICO rotor aerodynamic loads prediction: ZigZag tape effects and laminar–turbulent transition modeling in CFD', *Journal of Wind Engineering and Industrial Aerodynamics* **168**, 152–163.

Appendix A

Publications

Wimshurst, A. & Willden, R. H. J. (2016), 'Validation of an Actuator Line Method for Tidal Turbine Rotors', *in* 'Proceedings of the 26th International Ocean and Polar Engineering Conference (ISOPE)', TPC-2016-0825.

Wimshurst, A. & Willden, R. H. J. (2016), Tidal power extraction on a streamwise bed slope, *Ocean Engineering* 125(1), 70–81.

Wimshurst, A. & Willden, R. H. J. (2016), 'Computational analysis of blockage designed tidal turbine rotors', in 'Proceedings of the 2nd International Conference on Renewable Energies Offshore (RENEW 2016)', Lisbon, Portugal, pp. 587–597.

Wimshurst, A. & Willden, R. H. J. (2017), 'Extracting lift and drag polars from blade resolved computational fluid dynamics for use in actuator line modelling of horizontal axis turbines', *Wind Energy* 20(5), 815–833.

Wimshurst, A. & Willden, R. H. J. (2017), 'Analysis of a tip correction for horizontal axis turbines', *Wind Energy.* 20(9): 1515–1528.

Wimshurst, A. & Willden, R. H. J. (2017), 'Spanwise flow corrections for tidal turbines', in '12th European Wave and Tidal Energy Conference (EWTEC 2017)', Cork, Ireland.

Wimshurst, A., Vogel, C. & Willden, R. H. J. (2017), 'Cavitation limits on tidal turbine performance', *Ocean Engineering.* 152(1), 223–233

Wimshurst, A. & Willden, R. H. J., 'Computational Observations of the Tip Loss Mechanism Experienced by Horizontal Axis Rotors', *Wind Energy.* Accepted.

Wimshurst, A. & Willden, R. H. J. (2017), Tidal turbine blade loading on a streamwise bed slope, *Renewable Energy.* Under Review.